
Biomechanical Controls of Epithelial Morphostasis

Augusto Borges



München 2024

Biomechanical Controls of Epithelial Morphostasis

Augusto Borges

Dissertation
an der Fakultät Physik
der Ludwig-Maximilians-Universität
München

vorgelegt von
Augusto Borges
aus La Plata, Argentinien

München, den 22.10.2024

Erstgutachter: Prof. Dr. Joachim Rädler

Zweitgutachter: Prof. Dr. Hernán López-Schier

Tag der mündlichen Prüfung: 05.12.2024

Inhaltsverzeichnis

Summary	xvii
Zusammenfassung	xix
1 Introduction	1
1.1 Mechanobiology	1
1.2 Stress Inference	4
1.2.1 Dynamic Stress Inference	6
1.3 The Zebrafish: Lateral line and Neuromasts	8
1.3.1 The lateral line	8
1.3.2 The posterior lateral line migratory primordia	10
1.3.3 Neuromasts and the Hair Cells	10
1.3.4 Neuromast patterning: The Planar Cell Polarity (PCP)	11
1.3.5 Planar Cell Inversions: PCI	12
1.4 Motivation	13
2 Dynamic Mechanical State Inference	15
2.1 Introduction	15
2.1.1 Geometrical stress inference	16
2.2 Incorporating dynamical information in a inference pipeline	19
2.3 The relation between the viscous and elastic scale	22
2.4 Evaluation of goodness of fit	23
2.5 Theoretical scale value	25
3 ForSys: Open Source stress and pressure inference	29
3.1 ForSys inference in <i>in silico</i> static images	31
3.2 ForSys inference in an <i>in silico</i> dynamical setting	33
3.3 <i>In vivo</i> validation in the Mucociliary epithelium of Xenopus embryos	37
3.4 Characterizing the mechanical state of the zebrafish neuromast	39
3.4.1 Stress and pressure distribution in the migrating primordium	39
3.4.2 The mechanical state of the neuromast	41

4	Planar Cell Inversion	45
4.1	Introduction	45
4.2	<i>In vivo</i> Planar Cell Inversion	48
4.3	Phenotypic differences in the PCI process	51
4.3.1	Mutants delayed the initiation of their inversion	51
4.3.2	The final angle of the hair cell pair depends on the mutation	53
4.3.3	<i>Emx2</i> and <i>Notch1a</i> mutants affect the progression of the cell rotation	53
4.4	Computational model	55
4.4.1	The symmetrical and asymmetrical models	57
4.4.2	The Metropolis-Hastings algorithm	58
4.4.3	Model implementation	59
4.4.4	Models results comparison against <i>in vivo</i> rotations	60
5	Discussion	63
5.1	Inferring mechanical states through time	63
5.2	ForSys: A software to infer dynamic states	64
5.3	Finding the East: Polarity Cell Inversion	65
5.4	Final words	66
A	seapipy: Automatic generation of <i>in silico</i> tissues	69
B	Inertia of the rotating pair	73
	Danksagung	87

Abbildungsverzeichnis

- 1.1 **Modern view of developmental stages.** From a zygote, the embryo undergoes cell division without growth, named cleavage. After approximately ten division rounds, cells organize around the yolk in the *blastula*, and the three germ layers appear (ectoderm, mesoderm, endoderm). During *gastrulation*, the three germ layers rearrange and start to specialize into different structures. In particular, the ectoderm forms the basis for the neural tube, which will form the brain during the *Neurulation* process. Finally, the *organogenesis* process finishes the development of the more specialized structures, such as muscle and neurons. The figure summarizes these last two stages by the grey-shaded region between the gastrula stage and the early embryo. Dark orange areas in the embryo represent the yolk, while lighter areas show the position of the cell mass. Icons used in the figure are taken from <https://togotv.dbcls.jp/en/pics.html> by DBCLS, which is licensed under CC-BY 4.0 Unported <https://creativecommons.org/licenses/by/4.0/> 2

- 1.2 **Dynamic inference methods.** (A) DLITE assumes that the forces (\vec{F}_i) in the system are tangent to the membranes (\hat{r}_{ij}) at the tricellular junctions, scaled by the tension value (λ). It tracks each system element through time and assigns the previous time solution as an initial guess for the next time point. Here $[M_\lambda]$ is the matrix representation of the system. (B) VFM Finite Element Mesh is built from the microscopy images of the system. Tensions are inferred by using the relationship between the forces of the system ($[F]$) and the velocity of the nodes ($[v]$), mediated by a damping matrix ($[D]$). (C) ForSys uses the velocity of the junctions ($[b]$), modulated by a scale parameter ($[b]$) relating the spatial and time scales. The microscopy images correspond to a primordium (A and C) and a neuromast (B). In both cases, membranes were tagged using claudnb:lyn-EGFP. Image reproduced from Borges and Chara, 2024 (submitted). 9

2.1	Geometry as an observable. (A) The orientation of rods in a magnetic field is a proxy for the underlying field. Black rods are simulated iron filings orientation with a small Gaussian noise. Continuous red lines show the underlying field. (B) Analogously, the form of the membranes can be used to estimate the stress that shaped them. The color of the membranes and cells indicates stress and pressure, respectively. The color scale is relative in both cases.	16
2.2	Membranes and tricellular junctions. (A) Scheme of a four-cell system with two tricellular junctions (1 and 2). A common edge between them joins both junctions. At each one of these junctions, the contact angles are α_1, β_1 and γ_1 and α_2, β_2 and γ_2 for the TJs 1 and 2 respectively. Different approximations exist for the contact angles. (B) In a polygonal approximation, the two tricellular junctions are joined by a straight line whose angle is used in the calculations. (C) On the other hand, curved edges allow a closer following of the shape. In (B) and (C) vectors \vec{r}_* , with $*$, represent the two cells at each side of the junction and show the resulting approximation. Image adapted from Borges and Chara, 2024 (submitted). .	20
2.3	Exploration of the scale parameter. (A) Heatmaps of the saturated score function as a function of the scale parameter ($1/Wi$) and the velocity at each frame. (B) Boxplots with the best scale parameter for the examples. Each individual boxplot shows all repetitions and frames. The best values is taken as the median of each boxplot. The distribution medians are summarized in table 2.1. Figure adapted from [15].	24
2.4	Fitting of the damping coefficient Square Distance from the theoretical value for the scale parameter to the maximum in the saturated score function in the sweeps. The distance is calculated for a damping coefficient $\eta = 1$ (blue lines) and the best-fitted values. The best values are in each legend. $\eta_{x\text{-furrow}} = 2.2, \eta_{y\text{-furrow}} = 2.4, \eta_{\text{circular-furrow}} = 2.5,$ and $\eta_{\text{random-tensions}} = 3.1.$.	27
3.1	The stress inference pipeline. (A) The static inference is performed on a microscopy image by creating a skeletonized tissue representation. Then, ForSys reads it and builds the system of equations according to the geometrical properties of the tissue. Lastly, the system is solved, and the intracellular pressures and intercellular stresses are inferred. (B) Similarly, the dynamical inference uses a time series of images to add dynamical information to the system of equations used in the static case. A time mesh is generated from the succession of microscopy images, and pivot vertices are tracked through time. Then, the velocity of these vertices from frame to frame is used to modify the system of equations, allowing non-static tissues to be analyzed by stress inference. Image reproduced from [15].	30

3.2 **Comparison between static ForSys and other force inference methods.** I tested whether the static implementation of ForSys differed from the values of DLITE and CellFIT. Each column represents one of the examples. **(A)** I show that the inferred stress versus the ground truth follows the $y=x$ line, plotted as a solid black line as a visual aid, for the three methods at the last simulated frame. **(B)** Moreover, the distribution of stresses of all methods has similar behaviors in the histograms. Both panels **(A)** and **(B)** are for a selected representative simulation. **(C)** Then, the result for all inferred tensions versus ground truth repetitions is shown for each condition at the last simulated frame. The black dashed line is the $y=x$ line and is a visual aid. The score function's values are in the lower right corner of each plot. ForSys, in its static modality, has better results in the three first examples and comparable results in the random tension case. Figure reproduced from [15]. 32

3.3 **In silico qualitative validation for tissues in static equilibrium.** Four different conditions were generated with seapipy to test the static equilibrium condition. Each column shows a representative repetition per example. The ground truth **(A)** can be compared to the values for the DLITE predictions **(B)** and the Static ForSys **(C)**. The three rows shown correspond to the final time. The color bar shows the order of the colormap for both the stresses and the pressures. Figure adapted from [15] 33

3.4 **In silico quantitative validation for tissues in static equilibrium.** Four different conditions were generated with seapipy to test the static equilibrium condition. Each column shows a representative repetition per example. The mean absolute percentage error **(A)** and the saturated score function **(B)** for all simulations are represented in two boxplots, DLITE and Static inference with ForSys, paired by condition. Dots show the result for individual repetitions. Figure adapted from [15] 34

3.5 **In silico validation of ForSys for tissues in dynamical equilibrium.** I generated four examples with seapipy to test dynamical equilibrium conditions. Each column shows a representative repetition per example. The first row **(A)** shows the ground truth values for the stress and the pressures, the static inference made by ForSys is in the second row **(B)**, and the dynamical ForSys inference is in **(C)**. I show each example at one time point after the system's tensions changed. The color bar shows the order of the colormap for both the stresses and the pressures. Figure adapted from [15]. 35

- 3.6 **Dynamic inference outperforms the static pipeline.** The mean absolute percentage error **(A)** and the saturated score function value **(B)** for all simulations are represented in two boxplots, Static and Dynamical inference, paired by condition. Dots show the result for individual repetitions. **(C)** Dependence of the MAPE on the velocity $|v|_2$. The scattered dots are the median for all experiments with a velocity corresponding to the current $|v|_2$ bin. Error bars in the y-axis are one standard deviation, and error bars in the x-axis represent the size of the velocity bin. **(D)** Dynamic to static score function ratio ($r = \log(\frac{\text{dynamic}}{\text{static}})$) as a function of the $|v|_2$ bin. A ratio bigger than zero shows that the dynamic solutions performed better (Red zone), and a negative value (Green Zone) favors the static solution. The black dashed line at $r = 0$ separates both zones. All velocity bins favor the dynamic solution. Figure adapted from [15] 36
- 3.7 **Comparison of ForSys-derived stress with myosin II measurements in the *Xenopus* embryo mucociliary epithelium.** **(A)** Scheme of the *Xenopus* embryo and position of the mucociliary epithelium. **(B)** Five examples of inference in *Xenopus* embryos. The microscopy image is shown alongside the myosin intensity map and the ForSys inference result. The color code in the maps represents the myosin sensor intensity and the stress prediction. The scale was saturated at tension values of two. The highlighted region in the microscopies shows the area that was analyzed. **(C)** Relationship between myosin sensor intensity and stress inferred for the five examples. Each scatter point shows the value for a particular membrane in that example. The dashed black line represents the $y = x$ line. Each color corresponds to the rounded rectangle around the embryo and its font color in panel (B). The average Pearson correlation coefficient is $R=0.56 \pm 0.11$; (mean \pm std) **(D)** Quantification of stresses and myosin sensor intensity for the five examples. Inferred stresses and myosin intensities are not significantly different ($p=0.76$; Mann-Whitney U test; $N=154$). Figure reproduced from [15]. 38
- 3.8 **ForSys inference of a moving epithelium in the zebrafish lateral line at 2 dpf.** **(A)** Schematic of the biological model. The neuromasts of the posterior lateral line are formed by detaching from a primordium that migrates from the anterior to the posterior of the fish. **(B)** Frames 0, 7, and 15 of the primordium migration in which cell membranes are fluorescently marked with Claudnb:lyn-EGFP. **(B')** The membrane signal is used for segmentation, which ForSys uses to predict cell membrane tension and intracellular pressure. **(C, C')** Consecutive frames show cell division. The membrane tension in the cell just about to divide is considerably higher than the surrounding membranes. After division, the dividing membrane retains a high tension. Figure adapted from [15]. 40

3.9 **ForSys inference predicts localization of epithelial rosettes.** (A) Schematic of the primordium orientation and the position of the optical planes. (B) Microscopy image of fluorescently marked membranes with Claudnb:lyn-EGFP. Constriction of the cell membranes in rosettes is evident in the apical plane. The asterisks show the anteroposterior location of rosettes. Cell segmentation was done on a Z-plane at a more basal plane than the one shown. (C) Ridgeline plots of cell densities along the anteroposterior axis were performed over 16 frames for a representative primordium. Time goes from bottom to top. The direction of primordium migration is to the right. The asterisks show the positions of the manually annotated rosettes. (D) Anteroposterior position of the manually tracked rosette against the inferred position by taking the local maxima of the density of pressure values from (B). The diagonal line marks $y=x$ as a reference for comparing predicted and manually annotated values. Figure adapted from [15]. . . . 42

3.10 ***In vivo* ForSys inference in an epithelium with rotating cells.** (A) Schematic of cell composition in a zebrafish lateral line neuromast. Sensory hair cells are located in the middle and surrounded by different support cells. (B) Microscopy image of a neuromast whose cells can be tracked by membrane-tethered EGFP. (B') Below is the ForSys tension prediction after membrane segmentation. (C) The tension predicted for membranes is classified by the type of cell-cell contact. The homotypic contacts between hair cells show the highest predicted tension, while the homotypic contacts between support cells show the lowest on average. Each data point is the mean of the predicted tension values for each membrane type in one frame. The frames come from N=7 videomicroscopy experiments. (D) Schematic of the planar cell inversions occurring in 50% of the nascent hair cell pairs: sibling hair cells perform a 180° rotation to exchange positions along the anterior-posterior axis. (E) Time-lapse frames showing the *in vivo* rotation process: around 100 minutes after mitosis, the nascent hair cells exchange anteroposterior positions by rotating in the epithelial plane. The sibling cells remain attached during the rotation, while the surrounding cells do not actively participate in the movement. (F) Homotypic tensions between the young rotating hair cells are significantly lower than their contacts with the surrounding cells. Figure reproduced from [15]. 44

- 4.1 **The neuromast organ and the polarity of the hair cells.**(A) Neuro-mast microscopy with its membranes tagged using *claudnb:lyn-EGFP*. (B) Neuromasts comprise two types of supporting cells: sustentacular (in blue) and mantle cells (in red), and hair cells (in dark green) in the middle. (C) After hair cells are born from a Unipotent Hair Cell Progenitor, they undergo a symmetry-breaking event, which consists of a bistable switch and determines their identity to be either *emx2* positive or *emx2* negative. (D) Cellular identity defines the orientation of the hair in the hair cells, with *Emx2* positive cells pointing to the posterior side and the *Emx2* negative cells in the anterior direction. The color represents the identity, and the black dot represents the position of the hair. 47
- 4.2 **Inversions as a three-phase rotational homotypic movement.**(A) Example of a pair of hair cells in a wild-type neuromast inverting in the center of mass reference frame. Smaller points represent earlier times. The arrows in the middle illustrate the direction of movement. (B) The angle of the cell pair is defined as the angle between the horizontal axis and a line that passes through the centroids of the sibling cells. (C) Trajectories for all the 70 experiments as gray dots. The red line shows a representative example. The green line and the shaded region are the mean and one standard deviation of all the trajectories. (D) All trajectories are depicted in cumulative angle, and after fitting a sigmoid function, three phases are identified. The two green and blue cells represent the movement's relative state. (E) Distance between the inverting pair during the three phases of the movement. (F) The Pearson correlation coefficient for the movement of cells (N=10). 49
- 4.3 **Mutants and wild type present differences in the phases and final pattern** (A) Scheme of the final pattern achieved by the hair cells after neuromast development. The axis is Antero-Posterior from left to right. Green cells represent *emx2* negative cells, and red cells *emx2* positive. The gray circle shows the position of the hair bundle. (B, C, D), Boxplots showing the time spent by the process in each of the three phases (Onset, progression, and stoppage, respectively) for the wild type and each mutant. Dots represent individual experiments (N=40, N=23 and N=9 for wild type, *Emx2* *-/-* and *Notch1a* *-/-* respectively). 52
- 4.4 **Initial and final distribution of angles** (A) Initial distribution of angles for the wild type, *emx2* *-/-* and *notch1a* *-/-*.(B) Distribution of final angles for the three presented conditions. The distributions are significantly different between the wild type and the other two, with $p=0.004$ for wild type and *emx2* knockout and $p=0.01$ between wild type and *notch1a* knockout. Each of the distributions in both panels have $N_{wt} = 71$, $N_{emx2^{-/-}} = 42$ and $N_{notch1a^{-/-}} = 22$ 54

4.5	<p>Mutations affect cell rotation differently. (A) Boxplot of the noise during the planar cell inversion in the wild types and mutants, the p-values come from an Anderson-Darling test comparing distributions. (B) Inversion frequency shown as a difference to an equal probability situation, i.e., 50% chance. (C) Handedness of the rotational movement for the three experimental conditions.</p>	55
4.6	<p>Computational modeling of the Planar Cell Inversion. (A) Sketch of the model. Solid blue balls represent each of the cells, and the arrows are the possible clockwise or anticlockwise movement around the horizontal axis. Each of the cells' positions is tracked through their angle with respect to that axis. The gradient coloring represents the possible asymmetry between the anterior and posterior regions. (B) In the asymmetrical model, both cells, shown as a green and a blue ball, have an attractive well on opposite sides of the AP axis, represented by a dashed ball of corresponding colors. (C) In the symmetrical model, each attractive well is on the same side of the axis.</p>	56
4.7	<p>Computational model relationship with the phenotypes. (A, B) Representative cumulative angle trajectory of the inverting pair for a wild type and a notch1a knockout. The colored regions represent the three phases of the process: onset (blue), progression (orange), and stoppage (green). (C, D) Similarly, the asymmetrical and symmetrical models are represented in the same configuration for a depth of 50 and 0 (C) and a depth of 50 and 20 (D). (E) Final angle achieved by the inverting pair as a function of the relative depth of the wells for the symmetrical (red) and asymmetrical (blue) model. The dashed line represents the mean value, and the shadowed area is one standard deviation. (F) Noise predicted by both models as a function of the relative well depth. (G, G') final angles achieved by the asymmetrical (well depth of 50 and 0, panel G) and symmetrical (well depth of 50 and 20, panel G') models.</p>	61
A.1	<p>Seapipy image generation. (A) Four different conditions were generated with Surface Evolver through the seapipy package. (B) Afterward, tissue stresses and pressures are inferred with ForSys. Figure reproduced from [15].</p>	71

- B.1 Moment of inertia of the rotating pair.** **(A)** After the Unipotent Cell Hair Progenitor division, cells separate during the onset phase, and after a small period, they start to join together. The Polarity Cell Inversion process starts around the time that a rounding appears. During the rotation, the two-cell system has the maximum circularity. The left side of the panel shows a sketch of the movement, and the right side shows a microscopy image to illustrate the step. **(B)** The two-cell system can be studied as the dependence of the distance D with the length of the interface l . **(C)** Moment of inertia of the two-cell system as a function of the bond length l . The moment of inertia for two circular bodies through their contact point is shown as the dashed line on the top of the plot. The dashed line at the bottom shows the moment of inertia for a circle in the axis through its center. In panels (A) and (C), the brightness of the circles shows their density after mass relocation. 74

Tabellenverzeichnis

1.1	Current stress inference methods. Currently, seven stress inference methods exist. Only three are currently available to the public, of which only one has dynamic capabilities. DLITE has an asterisk in its static status due to its usage of the previous frame's information, as discussed in the main text. Table reproduced from Borges and Chara, 2024 (submitted).	7
1.2	Developmental stages of the Zebrafish. Table adapted from Kimmel <i>et al.</i> , [79].	8
2.1	Best scale parameter's values and fitted damping coefficient. After sweeping values from 0 to 0.5, the best scale parameter is chosen as the median of the best values for each of the twenty-five repetitions for each example separately. The fitting of the damping coefficient is performed by minimizing the distance of the theoretical scale parameter to the maximum score in each condition	25

Summary

Interactions in biological systems are myriad. Attempting to understand them provides valuable insights with broader bearing in biology, bioengineering, and medicine. Notwithstanding this immense realm of applications, biology presents unique characteristics that are not present in other “traditional” physical systems, making Biological Physics an exciting area of research that has the possibility of introducing new physics. This thesis will be guided by the leitmotif of understanding the coordination that allows functional patterns to arise in biological matter. In other words, what is the interplay between mechanics and signaling that underlies tissue shape?

The shape of biological tissue arises during development through the combination of morphogenetic signals and local mechanical interactions of the tissues’ minimal units, the cells. Measuring mechanical observables such as stress and stiffness is crucial to understanding the shaping that occurs. Direct experimental manipulation of biological samples allows access to these observables at the cost of altering their natural course of development at best and destroying them irreversibly at worst. This restricts the type of phenomena that can be studied using these techniques, as investigating processes taking place over longer time scales would be challenging.

Computational methods such as Stress Inference can overcome these problems. These methods do not require further interaction with the sample aside from microscopy imaging. Nonetheless, no publicly available methods exist to apply Stress Inference to time-dependent systems. In this thesis, I develop an innovative method to infer physical forces from a time series of microscopy images, which enables me to address shape generation (morphogenesis) and maintenance (morphostasis) *in vivo*. I introduce a formalism to incorporate dynamic information into the inference pipeline and model the cells as a viscoelastic material. With that assumption, I derive a relationship between the elastic and viscous scales for the first time in this type of model.

I introduce ForSys as a new tool that utilizes dynamic microscopic information. I have made ForSys Open Source to enhance its usability and impact in the field of tissue biophysics. Tissues can be represented as a collection of geometrical entities. Vertex models use this approach to simulate the evolution of tissues by changing the position of vertices, representing tricellular junctions of the cells. I also introduce seapipy as a tool to create *in silico* ground truths of stress distributions from vertex models. Aided by this tool, I streamline the validation of ForSys in static and dynamic *in silico* settings before moving to *in vivo* systems. I test ForSys in three different systems belonging to two model organisms.

I first show that ForSys' static predictions correlate with Myosin II fluorescence measurements in the *Xenopus* mucociliary epithelium. Then, I use it to investigate the formation of protoneuromasts in the zebrafish lateral line in the early hours of its development. I find that weighted inferred pressures are a good predictor of rosette formation prior to neuromast deposition. Finally, with ForSys, I study the stress distributions between homotypical and heterotypical cell-cell boundaries in the mechanosensory neuromasts of the zebrafish lateral line. There, ForSys predictions show asymmetries in the stress distributions between different cell types.

I then turn my attention to the process by which sensory hair cells in the neuromast acquire their pattern, the Planar Cell Inversion process (PCI). Through careful quantitative measurements, I show that PCI can be divided into three phases with distinct features. Moreover, I study the process in two mutant lines with knockouts of the *Emx2* transcription factor and the *Notch1a* gene, which are suspected to be involved in the Planar Cell Polarity pathway in the organ. My results show that the mutants have distinctive characteristics to the wild type. Then, I present a simple two-agent model to simulate PCI. I implement a one-dimensional Monte Carlo model that evolves using Metropolis-Hastings importance sampling, with a simple Hamiltonian that incorporates a soft spheres repulsion and attractive wells for each agent. Using the position of the wells, I propose two model alternatives: a symmetrical and an asymmetrical model. I show that the asymmetrical model qualitatively matches the wild-type observations, while the symmetrical model does so with the mutants. Using ForSys, I also show that the stress in homotypic hair cell tight junctions is lower than in the heterotypic junctions between them and the surrounding cells, hinting at adhesion differences consistent with experimental observations.

I introduce two new software tools to aid in the experimental exploration of the mechanical state of biological matter. I apply them to study the PCI process and shed some light on the underlying biology that drives it. I believe that the formalism and tools I made available will push forward the development of better and more complete means to measure mechanical quantities in biological systems, aiding our understanding of morphogenesis and morphostasis at the mesoscopic scale.

Zusammenfassung

Wechselwirkungen in biologischen Systemen sind vielfältig. Der Versuch, sie zu verstehen, liefert wertvolle Erkenntnisse, die in der Biologie, der Biotechnik und der Medizin von weitreichender Bedeutung sind. Ungeachtet dieses immensen Anwendungsbereichs weist Biologie einzigartige Merkmale auf, die in anderen “traditionellen” physikalischen Systemen nicht vorhanden sind. Die Biologische Physik ist somit ein spannendes Forschungsgebiet, welches möglicherweise neue Physik bietet. Das Leitmotiv der vorliegenden Arbeit ist das Verständnis der Koordination, die die Entstehung funktioneller Strukturen in biologischem Gewebe ermöglicht. Mit anderen Worten: Wie spielen Mechanik und Signalübertragung zusammen, um die Struktur von Gewebe zu bestimmen?

Die Form von biologischem Gewebe entsteht während seiner Entwicklung durch die Kombination von morphogenetischen Signalen und lokalen mechanischen Wechselwirkungen zwischen den kleinsten Einheiten des Gewebes, den Zellen. Die Messung mechanischer Größen wie Spannung und Steifigkeit ist äußerst wichtig für das Verständnis dieser Formgebung. Direkte experimentelle Manipulation biologischer Proben ermöglicht den Zugang zu diesen Messgrößen, allerdings mit der Gefahr, dass der natürliche Entwicklungsverlauf im besten Fall verändert und im schlimmsten Fall irreversibel zerstört wird. Dies beschränkt die Arten von Phänomenen, die mithilfe dieser Techniken erforscht werden können, da länger andauernde Prozesse mit diesen Techniken nur schwer untersuchbar sind.

Computergestützte Methoden wie die Spannungsinferenz können diese Probleme überwinden. Diese Methoden erfordern neben mikroskopischer Bildgebung keine weitere Interaktion mit der Probe. Dennoch gibt es keine öffentlich zugänglichen Methoden, um Spannungsinferenz auf zeitabhängige Systeme anzuwenden. In dieser Arbeit entwickle ich eine innovative Methode zur Ableitung physikalischer Kräfte aus einer Zeitreihe von Mikroskopiebildern, die es ermöglicht, die Formbildung (Morphogenese) und -erhaltung (Morphostase) *in vivo* zu untersuchen. Ich führe einen Formalismus ein, um dynamische Informationen in die Inferenzpipeline einzubeziehen und modelliere die Zellen als ein viskoelastisches Material. Aus dieser Annahme leite ich zum ersten Mal in dieser Art von Modell eine Beziehung zwischen der elastischen und der viskosen Skala ab.

Ich stelle mit ForSys ein neues Tool vor, das dynamische mikroskopische Information nutzt. Ich habe ForSys Open Source zur Verfügung gestellt, um seine Anwendbarkeit zu erhöhen und seinen Beitrag zur Gewebebiophysik zu optimieren. Gewebe können als eine Sammlung von geometrischen Einheiten dargestellt werden. Vertex-Modelle nutzen diesen Ansatz, um die Entwicklung von Geweben zu simulieren, indem sie die Position

von Vertices, also trizellulären Verbindungen, verändern. Außerdem präsentiere ich *seapipy*, ein Softwaretool, mit dem sich aus Vertex-Modellen *in silico Ground Truths* von Spannungsverteilungen erstellen lassen. Mithilfe dieses Tools optimiere ich die Validierung von ForSys in statischen und dynamischen *in silico* Konfigurationen, bevor ich zu *in vivo* Systemen übergehe. Ich teste ForSys in drei verschiedenen Systemen aus zwei Modellorganismen. Zunächst zeige ich, dass die statischen Vorhersagen von ForSys mit Myosin-II-Fluoreszenzmessungen im mukoziliären Epithel von *Xenopus* korrelieren. Anschließend untersuche ich mit ForSys die Bildung von Protoneuromasten im Seitenlinienorgan des Zebrafisches in den ersten Stunden seiner Entwicklung. Ich stelle fest, dass der gewichtete abgeleitete Druck ein guter Prädiktor für die Rosettenbildung vor der Ablagerung von Neuromasten ist. Schließlich nutze ich ForSys, um die Spannungsverteilung zwischen homotypischen und heterotypischen Zell-Zell-Grenzen in den mechanosensorischen Neuromasten des Zebrafisch-Seitenlinienorgans zu untersuchen. Dort zeigen die Vorhersagen von ForSys Asymmetrien in der Spannungsverteilung zwischen verschiedenen Zelltypen.

Danach betrachte ich den Prozess, durch den die Haarsinneszellen im Neuromast ihre Struktur erhalten, die ebene Zellumkehr (PCI, *Planar Cell Inversion*). Durch sorgfältige quantitative Messungen zeige ich, dass PCI in drei Phasen mit unterschiedlichen Merkmalen unterteilt werden kann. Darüberhinaus untersuche ich den Prozess in zwei Mutantenlinien mit Knockouts des Transkriptionsfaktors *Emx2* und des Gens *Notch1a*, von denen man annimmt, dass sie an der planaren Zellpolarität (*planar cell polarity*) in diesem Organ beteiligt sind. Meine Ergebnisse zeigen, dass der Prozess in den Mutanten andere Merkmale aufweist als im Wildtyp. Anschließend stelle ich ein einfaches Zwei-Agenten-Modell zur Simulation von PCI vor. Ich implementiere ein eindimensionales Monte-Carlo-Modell, das sich mithilfe des Metropolis-Hastings *Importance Sampling* anhand einer einfachen Hamilton-Funktion entwickelt. Diese besteht aus einer weiche-Kugeln-Abstoßung und Potentialtöpfen für jeden Agenten. Anhand der Position der Töpfe schlage ich zwei Modellalternativen vor: ein symmetrisches und ein asymmetrisches Modell. Ich zeige, dass das asymmetrische Modell qualitativ mit den Beobachtungen des Wildtyps, und das symmetrische mit denen der Mutanten übereinstimmt. Mit Hilfe von ForSys zeige ich außerdem, dass der Stress in homotypischen Haarzellen-*Tight Junctions* geringer ist als in heterotypischen Verbindungen zwischen ihnen und den sie umgebenden Zellen, was auf Adhäsionsunterschiede hinweist, die mit experimentellen Beobachtungen übereinstimmen.

Ich stelle zwei neue Software-Tools vor, die bei der experimentellen Erforschung des mechanischen Zustands biologischer Gewebe helfen. Ich wende sie an, um den PCI-Prozess zu untersuchen und die zugrundeliegende Biologie, die ihn antreibt, zu beleuchten. Ich glaube, dass der Formalismus und die Werkzeuge, die ich zur Verfügung gestellt habe, die Entwicklung besserer und umfassenderer Mittel zur Messung mechanischer Größen in biologischen Systemen vorantreiben und unser Verständnis von Morphogenese und Morphostase auf der mesoskopischen Skala unterstützen werden.

List of publications

During my PhD, I participated in the following publications and software packages.

Publications relevant to this thesis

1. Kozak, E.L., Miranda-Rodríguez, J.R., **Borges, A.**, Dierkes, K., Mineo, A., Pinto-Teixeira, F., Viader-Llargués, O., Solon, J., Chara, O. and López-Schier, H. (2023). Quantitative videomicroscopy reveals latent control of cell-pair rotations in vivo. **Development** 150, dev200975.
2. **Borges, A.**, Miranda-Rodríguez, J.R., Ceccarelli, A.S., Ventura, G., Sedzinski, J., López-Schier, H. and Chara, O. (2024). ForSys: non-invasive stress inference from time-lapse microscopy. **bioRxiv**.
3. **Borges, A.**, Pinto-Teixeira, F., Wibowo, I., Pogoda, H.-M., Hammerschmidt, M., Kawakami, K. and López-Schier, H., Miranda-Rodríguez, J.R. (2024). Incoherent collective cell chemotaxis in a zebrafish model of branchio-oto-renal syndrome. **microPublication Biology**.
4. **Borges, A.**, Chara O. (2024) Peeking into the future: Inferring mechanics in dynamical tissues. Under review

Other publications

1. Ceccarelli, A.S., **Borges, A.** and Chara, O. (2022). Size matters: tissue size as a marker for a transition between reaction–diffusion regimes in spatio-temporal distribution of morphogens. **R. Soc. open sci.** 9, 211112.
2. Lavalle, N.G., Miranda-Rodríguez J.R., Cura Costa E., **Borges, A.**, Viader-Llargués O., López-Schier H., Chara O. Local control of cellular proliferation underlies neuro-mast regeneration in zebrafish. In preparation.
3. Aldecoa Rodrigo N., **Borges A.**, Chara O. StressNET: An adaptable AI model for stress inference. In preparation.

Software packages

1. **Borges, A.** (2024). borgesaugusto/seapipy: v0.2.0-alpha.
2. **Borges, A.**, Ceccarelli, A.S. and Chara, O. (2024). ForSys software.

Kapitel 1

Introduction

1.1 Mechanobiology

The study of forces in biology and their relationship with the evolution of tissues can be traced back to the late nineteenth-century works by His, Roux, Driesch, and Spemann, synthesized in the *Entwicklungsmechanik* movement [78]. This movement tried to understand the shaping of the embryo from a mechanical lens. Before this movement, in the late eighteenth century and beginning of the nineteenth, the study of organism development, or embryology, was transverse by debates about the merits of preformation vs. epigenesis, in a time before the publication of Darwin’s “On the Origin of the Species” in 1859 [40]. Naturalists such as Etienne Geoffroy Saint-Hilaire (1772-1844) had a profoundly theological interpretation of organism development anchored in Transcendental Anatomy. In his view, all organisms develop from an idealized system of a divine origin. His primary interest lies in how the external environment affects the development of the chicken. Studying the effect of external factors on development was common in the nascent embryological discipline. Due to the lack of specialized tools, results were more challenging to replicate. This led many researchers to create their own tools, accelerating experiments in the next generation.

During this period, much focus was on *teratology*, the study of physiological abnormalities. This was studied by performing experiments on the embryos during their development and, through them, learning how to cause them. Experiments like refrigerating or varnishing chick eggs performed by Camille Dareste (1822-1899) are among the first examples [39]. Different refinements were introduced to only affect part of the egg, such as precise incisions to sear specific sites in the embryo [156, 50, 155], which inaugurated a “causal” developmental biology [26]. A little before the advent of *Entwicklungsmechanik*, different parts of the embryo were recognized and studied; for example, the germ layers were identified by Heinz Christian Pander (1794-1865) in 1817 [53, 5]. Different germ layers could be followed until they eventually transformed into new structures during the development cycle of different animals. The main stages of embryological development are summarized in figure 1.1.

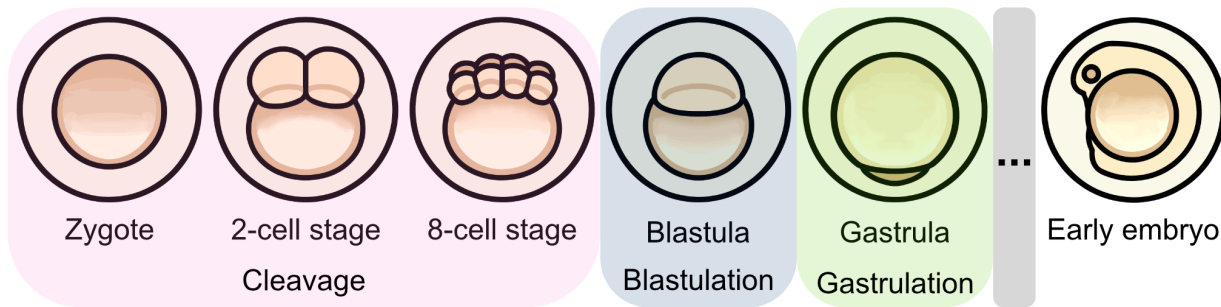


Abbildung 1.1: **Modern view of developmental stages.** From a zygote, the embryo undergoes cell division without growth, named cleavage. After approximately ten division rounds, cells organize around the yolk in the *blastula*, and the three germ layers appear (ectoderm, mesoderm, endoderm). During *gastrulation*, the three germ layers rearrange and start to specialize into different structures. In particular, the ectoderm forms the basis for the neural tube, which will form the brain during the *Neurulation* process. Finally, the *organogenesis* process finishes the development of the more specialized structures, such as muscle and neurons. The figure summarizes these last two stages by the grey-shaded region between the gastrula stage and the early embryo. Dark orange areas in the embryo represent the yolk, while lighter areas show the position of the cell mass. Icons used in the figure are taken from <https://togotv.dbcls.jp/en/pics.html> by DBCLS, which is licensed under CC-BY 4.0 Unported <https://creativecommons.org/licenses/by/4.0/>

These studies gave experimental insights into the preformation vs. epigenesis debate. In preformation theory, the embryo is construed as a “miniature” version of the full adult that grows during development. In contrast, epigenesis provides a picture where the embryo is formed through successive small changes [146]. Moreover, another competing explanation for the development of the organisms was the *embryological parallelism*, where the different stages of embryological development go through the adult stages of the organism’s phylogenetic ancestors [53]. One of its main proponents, Ernst Haeckel (1834-1919), summarizes it as “Ontogeny recapitulates Phylogeny” [53]. Ontogeny refers to the organism’s development from the egg’s fertilization to its adult form. Phylogeny, on the other hand, refers to the history of the evolution of a certain species. This idea is also called *recapitulation theory*, or *biogenetic law*. He proposed the existence of the *Gastraea* as an original, ancestral form from which all animals evolved. In his view, it was only during gastrulation that his *Urform* was truly visible [138].

In an attempt to settle the debate between these competing ideas, Karl Ernst von Baer (1792-1876) postulated the Laws of Embryology [7]. He studied germ layer formation, especially in chick embryos, cataloging their development from day zero to hatching and noting the changes that the germ layers underwent, among other contributions. His four laws deal with the pillars of preformation and recapitulation theory. The laws can be stated, as summarized by Huxley in 1853 [65], as:

1. The more general characters of a large group appear earlier in the embryo than the more special characters.
2. From the most general forms the less general are developed, and so on, until finally the most special arises.
3. Every embryo of a given animal form, instead of passing through the other forms, rather becomes separated from them.
4. The embryo of a higher form never resembles any other form, but only its embryo.

These laws, taken in pairs, reveal much about the existing debates in the area at the time. The first two address the preformationists' ideas. In them, von Baer establishes that the embryo develops from general to specific, and it is the more general, perhaps in modern terms, more "potent" structures that give rise to evermore specialized tissues. On the other hand, the last two laws pitch into the recapitulation theory. There, von Baer highlights that during development, rather than similarities, the differences between different species get accentuated.

The *Entwicklungsmechanik* gained traction amid this debate. Development cannot be studied only through manipulations of the embryo's external environment or by explaining the different structures beginning to be characterized teleologically. Wilhelm His (1831-1904) proposed that the embryo should be studied through the causal links that arise from the mechanics of its development rather than focusing on how its past might have affected it [67]. At first glance, this was a "Markovian" approach, although thirty years before Markov's paper [63]. In this view, evolution led to the structural changes that allowed the embryo to form, but the developmental process of the embryo could be studied independently.

Later, Wilhelm Roux (1850-1924) studied frog embryos and worked on how cell division affected development. His most popular experiment involved killing one cell at the two-cell stage with a needle to establish how that would affect the embryo as a whole. Even though he did not remove the killed cell, and therefore its results might still be affected by the interplay between the two cells, he observed that those embryos that survived reached other stages as a 'half-embryo'. This led him to propose a *Mosaic theory* of epigenesis. Cells have unique roles, becoming increasingly determined after cell division. His influence in the Mechanics of Development movement extends far beyond his scientific contributions. He also created the *Archiv für Entwicklungsmechanik der Organismen* journal in 1894 and later in 1925 the *Wilhelm Roux' Archiv für Entwicklungsmechanik der Organismen*.

Similarly, Hans Driesch (1867-1941) conducted experiments on sea urchins, separating the two blastomeres by agitating the animal in suspension. This separation did not halt development but resulted in animals half the expected size. Having lost half of the embryo during the early blastomere stages, the animals were able to arrive at the larvae stage. Driesch interpreted this result as not only the specialization of cells in a mosaic pattern but also as involving some regulatory activity that allows for compensation of the lost half.

At the beginning of the twentieth century, while working at the University of Munich, the embryologist Johannes Holtfreter (1901-1992) proposed a new idea to account for the morphogenetic movements observed during development. He showed that certain tissues favor association with other tissues (tissue affinity, “Gewebeaffinität”), even after complete dissociation of the cells [75, 145]. Moreover, together with Phillip Townes (1927-2017), they postulated that directed cell migration might spawn from differences in the rate of recovery of cell membranes [145], a concept known as “timing hypothesis” [137].

After this work, the meaning of “mechanistic” interpretation shifted. Due to improvements in genetic techniques and a better understanding of the molecular basis of heredity and regulation, the physical aspects of development took a secondary role, whereas molecular explanations were preferred [138]. Perhaps the best example is the works by Lewis, Nüsslein-Volhard, and Wieschaus, leading to the 1995 Nobel Prize in medicine, where they studied how different genes affected the development of the *Drosophila* fly and the specialization of its organs [92, 112].

Most recently, mechanics, in the physical sense, has resurfaced in the study of different biological processes, especially development [117, 64, 30] and regeneration [131, 142, 89]. Tissue shapes are not only consequences of the biochemical signaling pathways regulating tissue activity but also result from a complex interaction between the regulatory network and the population of cells [29, 31, 48, 57].

Studies of tissue rheology have been used to answer quantitatively different open questions in the field, using physical and biological explanations. For example, elastic properties during the zebrafish’s body elongation were investigated using deformable magnetic droplets [132, 103]. Optical traps [109], and laser ablation [12, 48, 143] are popular methods for probing elastic properties *in vivo*. For an exhaustive description of existing methods of experimental tissue rheology, I would like to refer to the excellent review articles by Sugimura *et al.* [140], Rosa Cusachs *et al.* [126], and Gómez-Gonzalez *et al.* [58],

An alternative to experimental manipulation of a system is to use the widespread availability of computer resources to estimate its mechanical state. Generally, these methods are called Stress Inference tools [59, 127]. This approach allows an inexpensive and quick overview that might guide further experimentation. In the next section, I will describe them in detail. Moreover, I have compiled Table 1.1 to summarize all the existent stress inference methods.

1.2 Stress Inference

Using the shape of a tissue to estimate the force present in it was applied by Stein and Gordon in the 1980s [136] for the first time [127]. The conceptual idea behind this method is to encode the topological information in a set of linear equations that are simultaneously solved to render the tensions and pressures in the system. Whether to solve for stress, pressure, or both depends on the technique used and will be reviewed in the following paragraphs. Another critical part of these models is the algorithm used to estimate the shape itself, which will be briefly described in this introduction. A detailed description

of the methods will appear at the beginning of Chapter 2. Currently, these methods are referred to as Stress Inference methods, as suggested by several authors [127, 33, 111, 15], as the inference outcomes are scalar values representing the stress components in each of the cell membranes. Perhaps the more general term Mechanical State Inference (or estimation) would be more appropriate. I will use force, tension, and stress, depending on which term is used by the authors of the original work being discussed.

Over more than a decade of work [21, 20, 32, 157], Brodland and colleagues created an inference method that could follow a Finite Element mesh through time and use the shape of the mesh to estimate the tensions in the arrangement, they called their technique Cinemechanometry [37]. A unique characteristic of this method is that the mesh does not need to coincide with the membranes, and sub- and supra-cellular structures could be addressed. They successfully applied it to account for the tensions during the furrow invagination of *Drosophila* and renamed their tool Video Force Microscopy (VFM) [22]. Importantly, this method uses video microscopy, not only a still image, to estimate the tensions in the mesh.

One of the main limitations of force inference techniques is the quality of the source images. Not long after VFM was released, Ishihara and Sugimura created a Bayesian inference tool [71]. The advantage of using a Bayesian approach lies in the ability to reconstruct the pressures and tension in the systems even when the image quality does not allow for discerning the curvatures of the membranes faithfully. These early implementations of force inference had the intracellular pressures, as well as the intercellular tension, intermixed into one system of equations, whose solution would describe the mechanical state of the system. They also had a polygonal approach to the shape of the cells. In this approach, all cell junctions are approximated by a straight edge drawn from the tricellular junction to the tricellular junction. Similarly, Chiou, Hufnagel, and Shraiman published a method that also uses a polygonal approach and a mixed representation of pressures and forces [33]. In their method, instead of using a Bayesian solver, Chiou and colleagues found the solution through inverting the system of equations.

Some years later, Brodland and collaborators released the Cellular Force Inference Toolkit (CellFIT) [23] as a new method to estimate forces in the system. There, the authors make two technical innovations. Firstly, they separated the pressure from the stresses in the mathematical description of the system and introduced the possibility of curved edges. By allowing curved edges, the stability of the solution is increased by providing independent equations at both vertices of each membrane. An increased stability means that slight variations of the initial data affect the model's outcome less. On the other hand, separating pressure and tension estimation allowed a better understanding of the origin of intracellular pressures, with all models to date using the Young-Laplace equation.

At the end of the 2010s, an innovation came from using video microscopies. VFM was less stable than its static counterpart, CellFIT. However, Vasan and colleagues used the new curved edges idea and separated equations for stress and pressure in combination with time series information, introducing DLITE (Dynamic Local Intercellular Tension Estimator) [147]. In their approach, vertices, edges, and cells are tracked in time, and the values for the tensions in the edges in a previous time point are used to inform the solver

method in the subsequent inference. This increases the solution’s robustness compared to CellFIT [147].

Finally, Noll, Streichan, and Shraiman proposed a clever idea to estimate not only the tensions in the system but also the shape of the cells simultaneously [111]. They named this method VMSI (Variational Method of Stress Inference). The main idea is to concurrently calculate the tension and the geometry by imposing the equilibrium condition at each tricellular junction. They found the method to be much more robust than its predecessors. However, this method is more challenging to implement and has not been made publicly available.

Three-dimensional stress inference presents a unique set of challenges particular to the new geometry. In this thesis, I will only address two-dimensional stress inference in a tissue monolayer; currently, two methods work in a three-dimensional setting [148, 70].

1.2.1 Dynamic Stress Inference

During developmental processes, morphogenetic flows shape organisms into their functional forms [129, 128] in species such as Zebrafish [160, 9, 120, 130, 119] and Drosophila [99, 80, 57, 35]. Most Stress inference methods rely on the spatial relationship between the vertices of the system, usually taken as the tricellular junctions [17]. However, if there is a time series of images, how can we incorporate that information effectively into the inference pipeline?

To my knowledge, only three methods in the literature tackle his problem. 1) DLITE uses the time series to improve the robustness of the solution by giving an informed guess of the tension to the system solver (Figure 1.2A)[147]. 2) Video Force Microscopy (VFM), in which the tension of the Finite Element Mesh edges is found using a damping matrix (Figure 1.2B) [22]. And 3) ForSys, where the system is modeled as viscoelastic, and the movements are incorporated directly into the equations(Figure 1.2C) [15]. Methods that use movement details to inform the solution are called Dynamic inference, contrasting with Static inference.

It should be noted that DLITE is not a fully Dynamic algorithm because it only uses the movement to inform the next step of the solver method, as pointed out by other authors [127]. Video Force Microscopy, on the other hand, uses a damping matrix to calculate the force from the velocity of the mesh movement. However, it is less robust than CellFIT due to its straight-edge approach and inherent arbitrariness in the mesh choice. Moreover, its source code, or binary files, were never made available to the community. The ForSys method is a product of this thesis and will be explained in Chapter 3, and it is available as Open Source software on GitHub.

I have compiled a table describing all existing stress inference software 1.1. In the table, I sketch the algorithm for each method, whether it is a dynamic or static method, and show which system they were initially applied to, along with their availability.

Method	Type	2D / 3D	Algorithm	Originally applied to	Availability	Publication
VFM	Dynamic	2D	Finite element mesh; Straight edges; Stress/pressure together; Least Squares solver	Ventral furrow formation in <i>Drosophila</i> , in vivo	Not available	2010 [22, 37]
Chiou <i>et al.</i>	Static	2D	Straight edges; Stress/pressure together; Inverse solution	Ventral furrow formation in <i>Drosophila</i> , in vivo	Not available	2012 [33]
Bayesian	Static	2D	Straight edges; Stress/pressure together; Bayesian solver	<i>Drosophila</i> pupal wing, in vivo	Open Source on GitHub	2012 [71]
CellFIT	Static	2D	Curved edges; Stress/pressures separated; Least Squares solver	Dorsal closure and imaginal disk in <i>Drosophila</i> , in vivo; Dragonfly wing	Not available	2014 [23]
CellFIT-3D	static	3D	Curved edges; Only stress; Least squares solver	Murine embryos, in vivo	Not available	2017 [148]
DLITE	Static*	2D	Curved edges; Stress/pressure separated; Least Square solver	Human stem cell colonies, in vitro	Open Source on GitHub	2019 [147]
VMSI	Static	2D	Fitted curved edges; Stress/pressure separated; Variational solver	<i>Drosophila</i> embryogenesis, in vivo	Not available	2020 [111]
foambryo	static	3D	Curved edges; Stress/pressure separated; Least Square solver	Ascidian embryo (<i>P. mammillata</i>), in vivo; <i>C. elegans</i> embryo, in vivo	Open Source on GitHub	2023 [70]
ForSys	Static and Dynamic	2D	Curved edges; Stress/pressure separated; Least-square solver	Zebrafish Lateral Line, in vivo; <i>Xenopus</i> Mucociliary epithelium, in vivo	Open Source on GitHub	2024 [15]

Table 1.1: **Current stress inference methods.** Currently, seven stress inference methods exist. Only three are currently available to the public, of which only one has dynamic capabilities. DLITE has an asterisk in its static status due to its usage of the previous frame’s information, as discussed in the main text. Table reproduced from Borges and Chara, 2024 (submitted).

Period	Duration in hours post fertilization (hpf)
Zygote	0 to 0.75 hpf
Cleavage	0.75 to 2.25 hpf
Blastula	2.25 to 5.25 hpf
Gastrula	5.25 to 10 hpf
Segmentation period	10 to 24 hpf
Pharyngula period	24 to 48 hpf
Hatching period	48 to 72 hpf
Larval period	>72 hpf

Tabelle 1.2: **Developmental stages of the Zebrafish.** Table adapted from Kimmel *et al.*, [79].

Having briefly described the evolution of mechanobiology and what stress inference algorithms are, in the next section, I will describe the experimental system that will be used in most of the present work, that is, the zebrafish and its lateral line organs: The Neuromasts. All other results of this thesis spawned from the scientific questions posed about the development and regeneration of this organism.

1.3 The Zebrafish: Lateral line and Neuromasts

The zebrafish (*Danio rerio*), a tropical freshwater fish native to South Asia, will be used as an experimental system through this thesis. Zebrafish is an easy-to-maintain and cost-effective model organism [158, 38]. It is a common model organism in development and regeneration. Females lay approximately one hundred eggs, allowing a good sample for screening and experiment planning. Zebrafish are sexually mature at three to four months, allowing for the fast establishment of mutant lines. Under normal conditions, establishing a new mutant line takes approximately 6 months. Breeding can be repeated weekly. Moreover, they have a rapid development, entering the larval period after approximately seventy-two hours post fertilization (hpf) and until 30 days post fertilization (dpf) to become an adult [79](for details see table 1.2). During its development laboratory, zebrafish are traslucent, facilitating the accessibility of imaging techniques.

This species has homologs for approximately $\sim 70\%$ of human genes. Moreover, much of its physiology is similar to the corresponding mammalian functions. They are a common system in regeneration studies. They can regenerate different organs, such as the heart, fin, hair cells, and spinal cord, among others [76, 91] [118] [121, 151][10, 124, 123].

1.3.1 The lateral line

To sense the environment around them, zebrafish, as well as other aquatic vertebrates, possess a series of mechanosensory organs whose function is to regulate the so-called “touch-at-a-distance” sense [44]. These organs are organized in a line from head to tail, called the

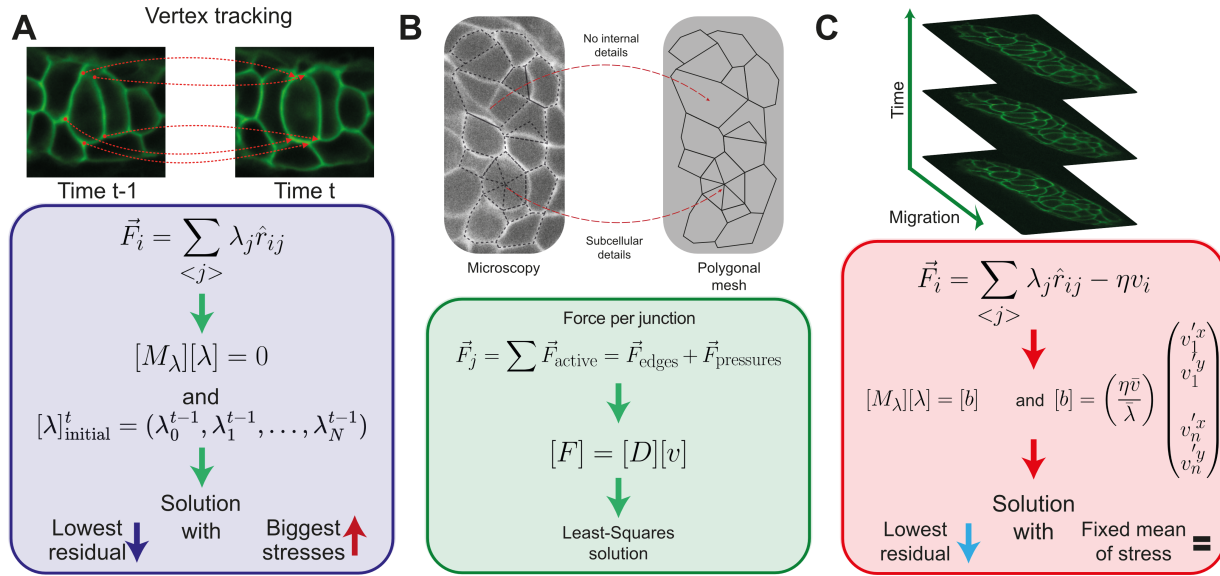


Abbildung 1.2: **Dynamic inference methods.** **(A)** DLITE assumes that the forces (\vec{F}_i) in the system are tangent to the membranes (\hat{r}_{ij}) at the tricellular junctions, scaled by the tension value (λ). It tracks each system element through time and assigns the previous time solution as an initial guess for the next time point. Here $[M_\lambda]$ is the matrix representation of the system. **(B)** VFM Finite Element Mesh is built from the microscopy images of the system. Tensions are inferred by using the relationship between the forces of the system ($[F]$) and the velocity of the nodes ($[v]$), mediated by a damping matrix ($[D]$). **(C)** ForSys uses the velocity of the junctions ($[b]$), modulated by a scale parameter ($[b]$) relating the spatial and time scales. The microscopy images correspond to a primordium (A and C) and a neuromast (B). In both cases, membranes were tagged using claudnb:lyn-EGFP. Image reproduced from Borges and Chara, 2024 (submitted).

lateral line. They influence rheotaxis, predator/prey dynamics, schooling, and reproduction [77, 114, 139]. The organs that form the lateral line, the neuromasts, contain the sensing cells. These cells are commonly referred to as Hair Cells, and their function is similar to the mammalian inner ear [52].

Two lines are formed at different developmental stages during the fish's development. First, the Posterior Lateral Line (PLL), going from head to tail, forms starting behind the ear and sequentially dotting the side of the animal until the tail. The neuromasts that form the lateral line are deposited by a cluster of around one hundred cells that migrate along the line called primordium. At approximately 22 hpf, the first primordium starts migrating behind the fish's ear and gives rise to the horizontal neuromasts (prim1) [51, 107]. Their orientation mimics the direction of the primordium migration [98]. Afterward, a second primordium (prim2) appears ~ 16 hours after prim1 to deposit the vertical neuromasts [100]. The impact of the anatomical differences between these two sets of organs will become apparent in section 1.3.3. At approximately 38 hpf, the Anterior Lateral Line (ALL) starts

forming by the migration of two primordia that appear above and below the eye [72]. In this work, the Lateral Line refers only to the Posterior Lateral Line and its primordia.

In larval fish, the posterior lateral line has less than ten neuromasts on each side of the body [54]. A scheme of this set of organs will be shown in Chapter 3 and figure 3.8. The number of organs increases during adulthood through stitching by budding or inter-neuromast proliferation [56, 154, 88]. This organ system is easily accessible, as the neuromasts are on the skin's surface. This allows straightforward imaging and pharmacological manipulation to study the different processes during its development.

1.3.2 The posterior lateral line migratory primordia

The first primordium migrates below the skin from the head to the tail in the span of approximately twenty-four hours, originating from the posterior placode behind the fish's ear [100]. Cyclically, clusters of cells detach from the primordium, staying in the deposited position and forming the neuromast at the site. The front of the primordium consists of mesenchymal leader cells that migrate. In contrast, in the trunk of the primordium, trailing cells are constricted in the apical region, forming epithelial rosettes before the proto-neuromast is deposited [87].

Primordium migration is a complex process maintained by a regulatory network with the Wnt/ β catenin and FGF as primary contributors. FGF is expressed in the trailing region, and Wnt appears mainly at the leading edge where the β catenin is activated [6, 87, 107, 96]. Even though the activator is unknown, the Wnt inhibitor Dkk1 has been shown to regulate it [6]. Moreover, the chemokine receptors 4b and 7b (CXCR4b and CXCR7b, respectively) regulate the movement. CXCR4b is expressed in the leading cells of the migratory cluster, while CXCR7b localizes in the trailing cells. Interestingly, the boundary between mesenchymal cells and epithelial tissue undergoing rosetogenesis coincides with the FGF / Wnt boundary. A study of this complex reaction network might shed light on the specific regulation that underlies primordium migration and neuromast deposition [3, 133, 16].

Neuromasts derived from the first primordium of the posterior lateral line generate horizontal neuromasts, whose hair cells are oriented following the anteroposterior axis. The second primordium gives rise to vertical neuromasts oriented toward the dorsoventral axis [98].

1.3.3 Neuromasts and the Hair Cells

The mechanosensory organs in the lateral line are the *neuromasts*. Adult organs comprise approximately 70 cells [51, 97, 66], with four main cell types being identified. The mantle cells of the organ provide structural support and are located in the outer rim of the neuromast. Recently, neuromast ionocytes have been identified to have a role in hair cell function in adult fish [115]. Sustentacular cells provide support, have the highest proliferative power [151], and surround the mechanosensory hair cells. The hair cells are the sensory cells of the organ, having a hair bundle projecting outward from the fish's body. The bundle is formed

by actin-rich stereocilia whose order, from shorter to taller, gives each hair cell a distinctive polarity. Next to the tallest stereocilia, a single kinocilium microtubule protrudes.

Supporting cells in the neuromast transform into a Unipotent Hair Cell Progenitor (UHCP), giving rise to two sibling hair cells through mitotic division. Upon damage, the hair cell population can replenish even in the presence of extensive damage [151], recovering both functionality and topology.

Each hair cell is innervated by neurons that transmit to the central nervous system. Water movements around the fish affect the direction of the bundle, triggering either a hyperpolarization or a depolarization of the hair cell, depending on the direction of the movement. When the bundle deforms towards the microtubule, the ion channel opens, depolarizing the hair cell. Neuromasts have around 20 hair cells stereotypically located at the center of the organ, surrounded by the other cell types. The hair cell population orders in a mirror-symmetric organization aligned with either the anteroposterior axis in horizontal neuromasts or the dorsoventral axis in vertical neuromasts, with half of the population facing opposite directions. Due to pressure differences in the alignment axis, this symmetry allows half of the population to depolarize and the other half to hyperpolarize, giving the organ equal sensitivity in both axis directions. Therefore, correct organ patterning is essential for the organ's function. Cells in the neuromast undergo an intriguing process in which cells rotate around a common center to reposition themselves in their functionally necessary positions, called Planar Cell Inversion (PCI).

1.3.4 Neuromast patterning: The Planar Cell Polarity (PCP)

In epithelial tissues, cells order through a signaling pathway called the Planar Cell Polarity (PCP) pathway [27]. Patterns grow gradually through the different stages of animal development. The PCP pathway has been extensively studied in *Drosophila melanogaster*, which led to the identification of key genes such as Van Gogh, Diego, and Frizzled. Genetic and pharmacological manipulation of the PCP pathway leads to deformed patterns due mainly to changes in cell orientation [82, 106, 104].

Even though a complete picture of how the PCP pathway affects orientation in the neuromast is lacking, it intervenes in the orientation of the hair cell population [141]. In wild-type conditions, horizontal neuromasts have hair cells located on the anterior side of the organ facing caudally, while cells in the posterior region face rostrally. Mutations in some of the intervening genes cause major changes in the cell orientation. Mutations in *vangl2*, or *frizzle* in a smaller amount, produce isotropic orientation of the cells in the organ [106]. Interestingly, Wnt mutations create a concentric pattern, with sibling cells still oppositely oriented, effectively breaking the mirror symmetry to a line through the center of the organ and perpendicular to the organizing axis [106].

The main factor contributing to orientation in zebrafish hair cells is the Emx2 (Empty spiracles homeobox 2) transcription factor [74, 68]. After the mitotic division of the UHCP, sibling hair cells enter a bistable switch to determine their genotypic identity for the rest of their life [73]. This switch is a competence between Emx2 and Notch levels in each cell, leading to a definite identity as Emx2 positive or Emx2 negative cell. Experimentally, Emx2

is present in hair cells of the posterior region, oriented caudally, and therefore, anterior cells facing rostrally are *Emx2* negative [74]. It has been proposed that *Emx2* affects the position of the hair within the cell but not the final position of the cell in the organ [113].

1.3.5 Planar Cell Inversions: PCI

Collective cell migration is pervasive in many biological processes, such as cancer invasion, immune response, wound healing, and during the development of organisms [85, 125, 84]. Recently, different methods have been developed to study cell-cell interactions in the presence of strong confinement and controlled conditions [24, 25]. There, a two-cell system's movement was restricted *in vitro* by localizing the cells inside wells, and the cells interacted through a common bridge.

Neuromasts in the zebrafish lateral line present a minimal model to study cell migration *in vivo*. During the development of the organ, hair cells rearrange after the Unipotent Hair Cell Progenitor division [159]. These movements are not well understood, with only a handful of mechanistic models addressing, at times, different aspects of the process [47, 113], one of which is part of this thesis [82]. The benefits of using this particular system lie in the ease of access to the organs as they lie on the fish's skin and the existing wealth of knowledge about the fish itself that allows for genetic and pharmacological alterations if necessary.

After the division of the UHCP, sibling hair cells rotate around an axis that passes through a common point of contact to exchange positions. After the rotation, hair cell pairs drift away. As cells invert their original positions and always align with the Planar Polarity axis, this process is called Planar Cell Inversion (PCI). During this process, cells must start the rotation, maintain the circular motion, and stop after a rotation of approximately 180° .

Additionally, PCI does not occur for every nascent hair cell pair. Different bodies of work have reported inversion rates of wild-type hair cells, chronologically: 60% [159]; 71% [102] and 60.8% [106]. In section 4.3.3 (And figure 4.5B), I will present the quantification published by Kozak *et al.*, with inversion happening in 56% of the cases [82]. Those cell dyads that do not undergo PCI still conform to the mirror symmetry of the orientation pattern without rearranging. Notably, inversions are observed even when the Planar Polarity pathway has been disrupted by mutations of genes such as *vangl2* and *drizzle* [106]. Other typical genetic mutations to study this process are the orientation-defining *emx2* and its antagonist *notch1a*.

PCI-like behavior has not yet been seen in mammals [43]. However, similar dynamics have been reported in other organs of the fish, flies, and *in vitro* studies of mammalian cells [94, 95]. This minimal cell migration model, where only two cells rotate around a common axis perpendicular to the epithelial sheet, could help understand cell-cell interactions during migration. Moreover, understanding these phenomena might prove helpful for medicine, as contrary to human hair cells, in zebrafish, they can regenerate.

1.4 Motivation

The organization of biological phenomena around the constraints given by nature is a remarkable event. Biological systems are organized through a myriad of relations, feedback, and feedforwards, influencing their environment and themselves far beyond the scale where they are constrained. With their interactions, they can build complex processes that start microscopically but, taken together, allow incredible achievements, such as the coordination of cells “species” to parsimoniously create tissues, organs, systems, animals, and beyond. In turn, cells are the fruit of the interactions of smaller parts, such as proteins, formed by molecules and atoms, and so forth.

Studying how different levels of organization complement each other and coordinate their behaviors to increase the capabilities of the isolated parts is a worthy task. In particular, biological systems can showcase phenomena that do not appear in “inert” matter, allowing for the investigation of *new* physics. As there are many scales involved, researchers set the scale with the scientific question being pursued at hand. In the present thesis, by and large, I will focus on tissue-level phenomena, where the smallest “particles” are the cells.

My main interest lies in understanding how patterns form in biological systems, that is, how the individual agents of the system can arrive at a definite pattern replicable by the organism. As a model system, I studied the zebrafish lateral line and its organs, such as the neuromast. These organs reliably arrive at the same mirror-symmetric pattern during development and regeneration, a pattern necessary for the organism’s correct functioning. If the mirror symmetry is disturbed, the fish will be disadvantaged.

As a first attempt, I decided to look into the mechanical interactions occurring in the organ. Therefore, I created a computational tool that allows the characterization of the mechanical stress of the system through the inference of the stress present in the cortex of the cells in the epithelial layer. As was mentioned in Section 1.3.5, in Zebrafish, sometimes there is a reversal of the cell’s polarity just after cell division. Accordingly, I had to develop this algorithm to work not only in static images but in dynamic conditions. I analyzed the Planar Cell Inversion process from data Dr. Kozak and Dr. Miranda-Rodriguez acquired. Finally, I developed a pipeline to analyze the inversion data systematically and used it to create a phenomenological model of the movement.

In chapter 2, I will introduce the formalism used to create the stress inference algorithm, as well as an interesting relationship that arises linking the time and space scale in Mechanical Inference Models. Then, I will present, in Chapter 3, the software I developed, ForSys, to infer the stresses and pressures. I will show the Planar Cell Inversion quantification results, the modeling strategy, and the implications of such a formalism in Chapter 4. Afterward, I will show the accompanying software developed to aid in validating ForSys in appendix A. Finally, in appendix B, I will present the calculation of the moment of inertia of a pair of cells that approach each other as a proxy for the inertia in the Planar Cell Inversion movement.

Kapitel 2

Dynamic Mechanical State Inference

In this chapter, I will propose a formalism to incorporate time into the stress inference models. This will allow valuable information about the movement to refine the inference techniques.

2.1 Introduction

Different experimental techniques allow stress measurements in biological tissues. Techniques such as light traps that allowed probing of viscoelastic properties in *Drosophila* development [8], magnetic droplets that were used to measure differences in the properties of the zebrafish body during elongation [103, 132], or laser ablation, to measure membrane stress through recoil [12, 48, 143]. Distinct methods have varying degrees of complexity and different hypotheses that should be met. Performing an experiment like the ones described above influences the tissue, most often irreversibly. For instance, magnetic droplets are added to the embryo at around 12 hours post fertilization (4-6 somites stage [103]), which then develops normally. In laser ablation, the tissue is damaged irreparably by cutting membranes using a high-power laser.

Another avenue for determining the mechanical state of a biological system can be computationally aided. Inference techniques allow estimating the relationship between stresses and pressures in a system without operating on the sample. Their algorithm is applied to microscopy images of the tissue of interest. These methods require three main characteristics to perform well

1. **Details of the microscopy:** The user must decide on the level of detail at which the inference is applied. The relevant structures must be visible in the microscopy to reconstruct it computationally.
2. **Theoretical framework:** All techniques have a set of assumptions. In computational approaches, this becomes central. The choice of the underlying model influences the result of the inference. It also might affect the level of detail required for the experimental image.

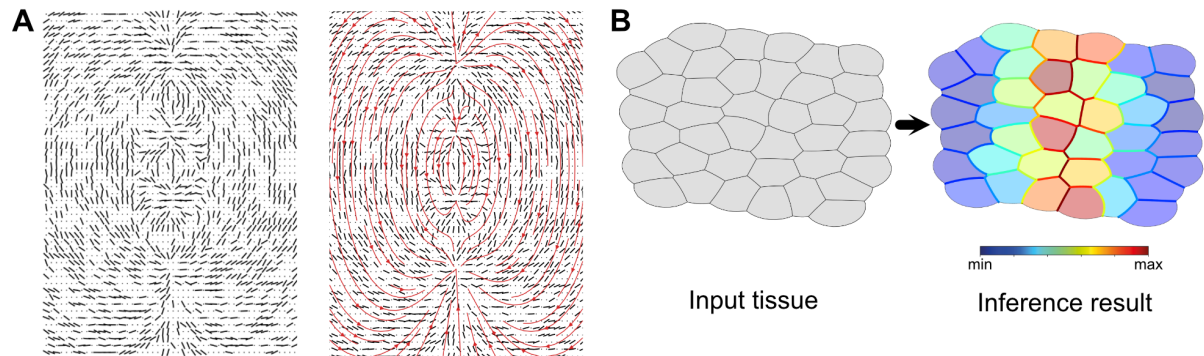


Abbildung 2.1: **Geometry as an observable.** (A) The orientation of rods in a magnetic field is a proxy for the underlying field. Black rods are simulated iron filings orientation with a small Gaussian noise. Continuous red lines show the underlying field. (B) Analogously, the form of the membranes can be used to estimate the stress that shaped them. The color of the membranes and cells indicates stress and pressure, respectively. The color scale is relative in both cases.

3. **Knowledge of the relationship between different scales:** In almost all current stress inference models, only the relative positions and orientations of the cells' membranes or the velocity of the cells in continuous strain models are relevant, but not both simultaneously. When both are present in the model, the relation between the scales must be tuned.

Understanding morphogenetic movements is central to unveiling the role that cell mechanics play in biology. In the present chapter, I will propose a method to infer the mechanical state of a tissue from a combination of its topology and dynamics. First, I will describe the static algorithm by which single microscopy images can be inferred. Then, I will introduce how to add dynamic information from the apparent cell movements into the inference. Finally, I will analyze how this interplay between the spatial and temporal scales impacts the analysis. All the analyses presented in this work will pertain to two-dimensional inferences.

2.1.1 Geometrical stress inference

Here, I will describe stress inference from static images, which uses only the geometry of the cells' arrangements. I will call this *static inference* or *geometric stress inference*. These methods calculate scalar quantities that serve as a measurement of the stress acting on a membrane. Originally, they were called force inference methods, but stress inference is more appropriate due to the scalar nature of their results [127, 33, 111].

In a magnetic field, iron filings will align with the underlying field, making it possible to predict its direction at each position by measuring the relative displacement of the rods 2.1A. Similarly, geometrical stress inference uses the relative orientation of the tissue's membranes to predict the stress field that originated such geometry 2.1B.

In two dimensions, the tissue is reconstructed computationally into vertices, joined by edges defining cells in a monolayer. In particular, the protagonists in this approach are those vertices where three membranes meet, called tricellular junctions, triple junctions (TJs) [17] or pivot vertices (Marked as i and j in figure 2.2A). The importance of these elements lies in that at each junction, the contact angle between the cells' membranes carries information about the energy of the interfaces [41]. In this type of inference, each triple junction is assumed to be in mechanical equilibrium, which allows the formulation of a system of equations representing the mechanical state of the system.

Each edge is defined as a straight line joining two vertices. Cells are then created by a collection of joined vertices with the edges as their boundaries. At every tricellular junction, the mechanical equilibrium hypothesis leads to a force equation whose terms depend on the stress model. Each edge's contribution is in the direction of the membrane, scaled by the stress. This originates from the vertex model definition of *line tension* where the potential energy of the interface is proportional to the length of the edge (first term of equation A.2) [23, 22, 71, 147, 22]. Similarly, different authors have added terms inspired by the vertex model, such as cell elasticity and contractility [105, 4, 49]. At each pivot vertex, the equilibrium is then defined as

$$\sum_j \lambda_j \tilde{r}_j^i = 0 \quad (2.1)$$

where the sum is over all the membranes (j) connecting to the pivot (i), λ_j is the stress of membrane j , \tilde{r}_j^i is the versor representing the membrane j from vertex i .

Using equation 2.1 in all pivot vertices of the system leads to a homogeneous system of equations relating the versors that describe the geometry, with their relative strengths, given by the stress λ . Namely, at each of the V pivot vertices, the equation will read

$$\lambda_1 \tilde{r}_1^i + \lambda_2 \tilde{r}_2^i + \lambda_3 \tilde{r}_3^i = 0 \quad (2.2)$$

for the i th vertex. In these equations, each one of the versors is known from the geometry, and only the stresses λ_* are unknown.

The solutions to these equations depend on correctly determining the shape of membranes. Membranes' shapes can be approximated as either straight or curved. In the straight-edge formalism, the only vertices in the system are those that define tricellular junctions, effectively approximating each cell as a polygon (Figure 2.2B).

This method has the advantage that it can be used even for insufficiently defined microscopies, where the boundaries of the cells are not clearly defined. This, in turn, means that the details pertaining to the membrane's curvature are not visible. However, the straight-edged approximation makes the system less robust. This is because, in this situation, each versor will contribute the same magnitude, with opposite sign, at each end of the membrane (Figure 2.2B). On the other hand, curved edges add independent information to the system of equations as they might have different values at each end of the membrane (Figure 2.2C).

In the curved-edge approach, each vertex that is not a tricellular junction is considered virtual. The cell's membranes are then composed of a collection of internal edges that

join virtual vertices. Virtual vertices are not directly involved in the calculation insofar as they only change the membrane's angle and contribute to the level of detail in calculating the curvature. In this setting, the versors \hat{r} are calculated using the limiting angle at the tricellular junctions, considering the curvature of the interfaces. The limiting angle is calculated by the circular fitting of all the virtual edges that compose a cellular boundary.

Each tricellular junction will contribute one equation per spatial dimension to the system and approximately three unknowns. The number of unknowns may vary as membranes connect two pivots, or it could also happen that a pivot vertex has more than three membranes connecting. This can be summarized in a *geometrical matrix* $[M_\lambda]$ where each row will represent a pivot component and each column a membrane. In a system with V pivot vertices and E membranes, this reads

$$[M_\lambda][\lambda] = 0 \quad (2.3)$$

here, $[M_\lambda] \in \mathbb{R}^{2V \times E}$ and $[\lambda] \in \mathbb{R}^{1 \times E}$. Brodland *et al.* have pointed out that generally, this definition leads to an overdetermined system of equations [23], i.e., with more equations than unknowns. However, there can be underdetermined systems, especially when the edges can not be fully resolved [71, 127]. In principle, junctions with more than three joining membranes, such as four-fold vertices, can be pivot vertices. However, they are less energetically stable [135], a fact that was pointed out by Thompson more than half a century ago [144, 55]. Moreover, each four-fold vertex contributes fewer equations (two) than unknowns (four), which could eventually lead to an underdetermined system of equations, as mentioned above.

Importantly, equation 2.3, as it is a homogenous equation, allows for the trivial solution where all stresses in the tissue are identically null. There are two prevalent methods to avoid this; other authors and I have used a Lagrange multiplier to establish a relation among the stresses by introducing a normalization for the average value of the stress [23, 22, 37, 15]. This is incorporated by adding an additional equation to the system, fixing the average value of the stresses

$$\sum_j \lambda_j = \bar{\lambda}$$

Even though all stress inference algorithms set the average to one ($\bar{\lambda} = 1$), this is a free hyperparameter of the model. This has the additional advantage of adding an equation to the system, which increases its stability. A different method deals with the null solution by penalizing it through a regularizer in the cost function associated with the algorithm used to find the solution [147]. Vasan *et al.* implement this by requiring the simultaneous minimization of the equation's residual and the maximization of the stresses at each pivot vertex.

Usually, an approximate solution for the system is found through the Least Square method. For this, a new system of equations is created as

$$[M_\lambda]^T [M_\lambda] [\lambda] = 0 \quad (2.4)$$

Notably, equation 2.4 could have a solution with negative values for some of the λ stresses. Physically, this implies that the direction of the force in the system of equations

2.2 is in the opposite direction to the versor; that is, the membrane would be pushing instead of pulling. Typically, these problems arise from elements incompatible with the stress inference model being used, such as four-fold junctions, membranes with more than one concavity, or membranes at near right angles [127, 135, 149]. Therefore, it is possible to avoid these situations altogether by skipping problematic membranes and junctions. Another possibility is to use a constrained solution, such as the Non-Negative Least Squares method [86, 153, 108]. Other methods can be used to solve the system of equations, such as direct inversion of the system, aided by pseudoinverses, such as the Moore-Penrose pseudoinverse, which will be discussed below [116, 33, 45].

Pressures can be estimated using the Young-Laplace equation. This equation relates the difference in the pressure difference between two cells (ΔP) with the shape of the membrane that separates them and its stress as,

$$\Delta P = \lambda_{ij}\rho_{ij} \quad (2.5)$$

where λ_{ij} is the stress of the membrane that joins vertices i and j , and ρ_{ij} is the curvature of the shared membrane. This leads to an inhomogeneous system of linear equations. In matrix form,

$$[M_P][P] = [b_P] \quad (2.6)$$

In the $[M_P]$ matrix, each row represents a shared interface between two cells with a +1 and a -1 in the columns corresponding to the two cells. The $[P]$ column vector has all the unknown pressures, and the right-hand side $[b_P]$ column vector contains the product between the curvature and the stress of each membrane, as detailed in equation 2.5. Similarly to stresses, it is common to incorporate a Lagrange multiplier to establish an ambient pressure, usually set to zero. The effect of changing this constraint on the pressure solutions has not been addressed in any inference model. Measuring the pressure of biological systems is an under-explored topic. Recently, Campàs *et al.* determined the osmotic contributions to the intracellular pressure in zebrafish *in vivo* [152].

The stress distribution is then inferred by solving a system of equations constructed from the constitutive equation 2.1 by Least Square minimization [23, 147, 33], variational [111] or Bayesian methods [71]. As none of these methods allows inference during morphogenetic movements, it is worthwhile to wonder how it would be possible to expand them to work under those conditions.

2.2 Incorporating dynamical information in a inference pipeline

Previously, I presented the three main characteristics a dynamic inference model should fulfill. The first of these points was the determination of the *details of the microscopy*. Brodland and colleagues have argued that the elements of the tissue can be divided into two categories: Passive components, such as cytoplasm and extracellular matrix, and active elements, such as the actomyosin network and the cell membranes [22, 37]. Passive elements

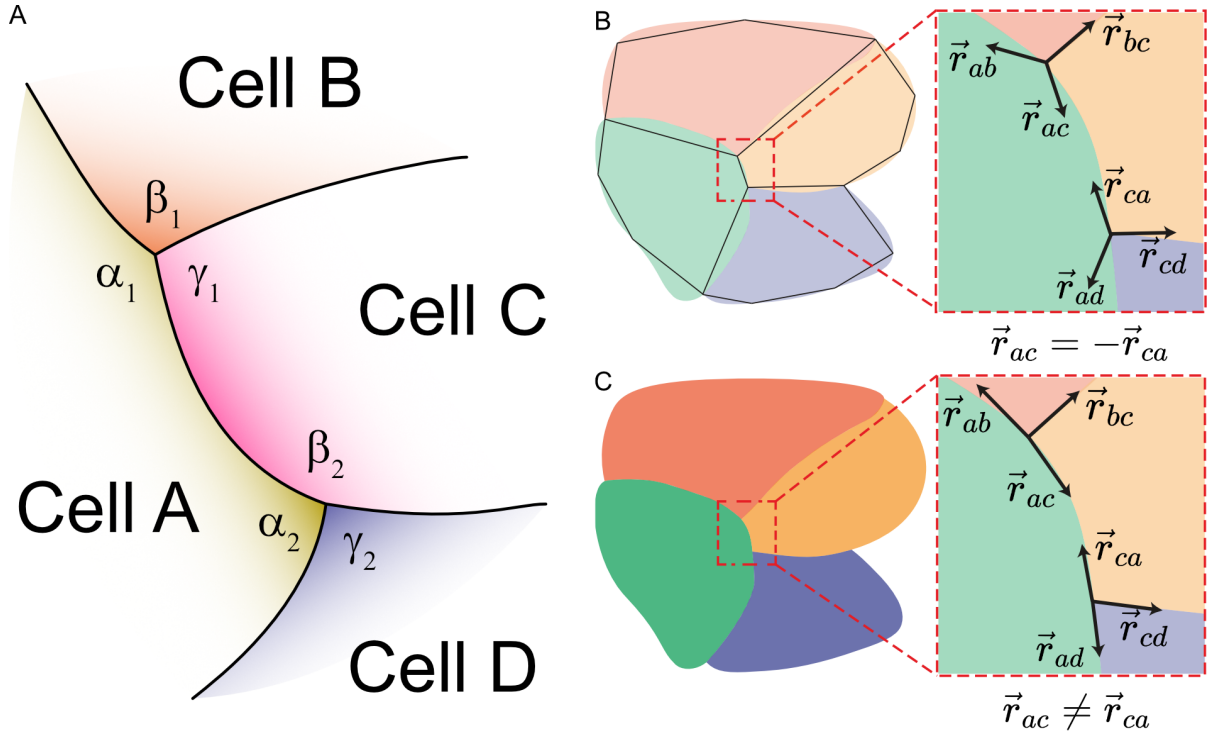


Abbildung 2.2: **Membranes and tricellular junctions.** (A) Scheme of a four-cell system with two tricellular junctions (1 and 2). A common edge between them joins both junctions. At each one of these junctions, the contact angles are α_1 , β_1 and γ_1 and α_2 , β_2 and γ_2 for the TJs 1 and 2 respectively. Different approximations exist for the contact angles. (B) In a polygonal approximation, the two tricellular junctions are joined by a straight line whose angle is used in the calculations. (C) On the other hand, curved edges allow a closer following of the shape. In (B) and (C) vectors \vec{r}_* , with *, represent the two cells at each side of the junction and show the resulting approximation. Image adapted from Borges and Chara, 2024 (submitted).

dissipate energy, while active components generate work. Therefore, the relevant structures, such as the cells' boundaries, must be well-defined in the microscopy for the inference to be effective. However, some methods may allow sub and supra-cellular levels of detail [22].

In the present work, the level of detail will be constrained to the shape of cells' membranes; I will ignore the subcellular details that account for the stress generation machinery itself. The next point was the underlying *assumptions of the model*. I will only use the vertex model line tension approximation as presented above in equation 2.2. Finally, as for the third consideration about the *scale relation*, I will show a method to incorporate the dynamic information into the inference pipeline. This will inevitably add the time scale to the algorithm, profoundly changing the character of the model. Then, in section 2.3, I will show how to deal with this arising issue.

I will suppose that the system evolves through a series of quasistatic states in an over-

damped regime [122]. Physically, this is equivalent to introducing a viscoelastic response to membrane deformations [8, 34], effectively modeling the cell as a viscoelastic material. I do this by adding a damping term proportional to the velocity of each junction to all equations. This transforms the equation for the i th vertex (as shown in equation 2.2) into

$$\sum_j \lambda_j \tilde{r}_j^i = \eta \vec{v}^i \quad (2.7)$$

where η is the damping coefficient and \vec{v}^i is the velocity of vertex i .

This addition transforms the system presented in equation 2.3 into a nonhomogeneous system of equations as

$$[M_\lambda][\lambda] = [B] \quad (2.8)$$

where $[M_\lambda]$ is the geometric matrix introduced in section 2.1.1, and $[\lambda]$ is the column vector of the stresses. Now, the system adds the $[B] \in \mathbb{R}^{1 \times V}$ matrix. Each two rows of this matrix contains the two spatial coordinates of the velocity for a given junction as

$$[B] = \begin{bmatrix} v_x^1 \\ v_y^1 \\ \vdots \\ v_x^V \\ v_y^V \end{bmatrix}$$

Different methods can be used to solve this inhomogeneous system of equations. A Least Squares approximation can be made as

$$[M_\lambda]^\top [M_\lambda][\lambda] = [M_\lambda]^\top [B] \quad (2.9)$$

Another strategy is to directly invert the system of equations. As this is not generally possible, a pseudoinverse such as the Moore-Penrose [116] can be calculated. The pseudoinverse is defined as

$$[A]^\ddagger = ([A]^\top [A])^{-1} A^\top$$

where $[A] \in \mathbb{R}^{n \times m}$. Therefore, the solution to the system in equation 2.9 becomes

$$[\lambda] = ([M_\lambda]^\top [M_\lambda])^{-1} [M_\lambda]^\top [B] \quad (2.10)$$

In Python, numerical solutions can be found by leveraging the `lmfit` package [108]. This package implements a wrapper around the SciPy implementation of the Least Square minimizer, adding additional parameters to the numerical algorithm. It is possible to calculate the residuals at each junction in the system, i.e., $[M_\lambda][\lambda] - [B]$, and pass them to the `lmfit` algorithm, which calculates the least squares system. This is equivalent to calculating the least squares systems directly on the system, as described in equation 2.9. To demonstrate this, we can see that the minimum value of the residual function is the same as the solution 2.10. For this, let the residual function be

$$D = \|[M_\lambda][\lambda] - [B]\|^2$$

Then, by expanding the product this is equivalent to

$$([M_\lambda][\lambda] - [B])^\top([M_\lambda][\lambda] - [B]) = [\lambda]^\top[M]^\top[M][\lambda] - [\lambda]^\top[M]^\top[B] - [B]^\top[M][\lambda] + [B]^\top B$$

The solution will be an extreme of the residuals, therefore we have to find the minima. Taking the derivative of the residual with respect to $[\lambda]$, we find that

$$\frac{\partial D}{\partial[\lambda]} = 2[M]^\top[M][\lambda] - 2[M]^\top[B] \quad (2.11)$$

which after setting $\frac{\partial D}{\partial[\lambda]} = 0$ leads to the same solution as 2.10.

I have shown that by modeling the cell as a viscoelastic material whose state evolves through quasistatic snapshots, the movement of the tricellular junctions can be incorporated to the inference problem. This leads to a linear inhomogeneous system of equations, with no additional unknowns than in the static case. To solve this, different algorithms can be used. In the present work, I have always attempted direct inversion, and when this was not possible or when negative values were found, a Non-Negative Least Squares algorithm was used.

2.3 The relation between the viscous and elastic scale

In section 2.2, I introduced changes to equation 2.2 that incorporated a drag term, as shown in equation 2.7. Importantly, this addition brings a new scale into the model: time. In static stress inference, forces along the membranes are described with their magnitude only being carried in the stress λ , while the direction has a unitary norm. On the contrary, while the constant η might be adjusted, the velocity carries the units with which it was measured. This impels the necessity of tailoring the system in the correct scale relationship between time and space.

Through a back-of-the-envelope calculation, I can show the expected units for η , set by the relations in equation 2.7. In that equation (2.7), the left-hand side has the versors, which carry no units, and the stress λ_j , which has units of N/m^2 . Taken together with the right-hand side, the damping units are $[\eta] = \frac{Ns}{m} \frac{1}{m^2} = \frac{Ns}{m^3}$. On the contrary, if λ is instead taken to be the magnitude of the force, this would make the coefficient have the usual damping units of $[\eta] = \frac{Ns}{m}$. I recognize that a deeper dimensional analysis of the different implications of the mental model behind stress inference is lacking in the literature.

We can transform the constitutive equations into a nondimensional form by taking a reference stress and velocity. Both quantities can, in principle, be taken from diverse observables in the system. Here, I chose to rescale the stress using the system's average stress as

$$\lambda'_j = \frac{\lambda_j}{\bar{\lambda}}$$

where λ'_j is the nondimensional stress of the membrane j and $\bar{\lambda}$ is the average stress in the system. Furthermore, I can use the time average, which is performed over all frames of the

mean junction velocity, to obtain a reference velocity. Mathematically,

$$\bar{v} = \frac{1}{N_{\text{frames}}} \sum_{t=t_i}^{t_f} \frac{\sum_j N_{\text{junctions}}^t \|\vec{v}_t^i\|}{N_{\text{junctions}}^t}$$

where the time average is performed over the N_{frames} ($= t_f - t_i$) from frames t_i to t_f , and the average velocity in each frame is over all the N_v^t junctions at frame t .

We can incorporate the described reference stress and velocity in equation 2.7 to obtain its non-dimensional form, which appears after rearranging the dimensional factors discussed in the preceding paragraph to the right-hand side

$$\sum_j \lambda_j' \tilde{r}_j^i = \left(\frac{\eta \bar{v}}{\bar{\lambda}} \right) \frac{\vec{v}'^{i,j}}{\bar{v}} \quad (2.12)$$

Significantly, the number $\frac{\eta \bar{v}}{\bar{\lambda}}$ provokes an interesting interpretation. Both the numerator and denominator of the number have units of force. However, the denominator expresses the average stress of the membranes in the system, while the denominator is the stress coming from the junction's movements. In essence, this number sets a relation between the two different scales of the system. Therefore, it could be interpreted as the reciprocal of the Weissenberg number (Wi), which relates the elastic ($\bar{\lambda}$) and viscous scales ($\eta \bar{v}$) in the system [42]. Although I note a difference between the viscous definition and my usage of the damping coefficient, going forward, this scale constant will be written as $\frac{1}{Wi}$.

This implies that to solve the system as presented in equation 2.9, the right-hand side has to be modified by normalizing by the reference velocity (\bar{v}) and multiplying by the scale constant $\frac{1}{Wi}$,

$$[M_\lambda]^\top [M_\lambda] [\lambda] = \frac{1}{Wi} \frac{1}{\bar{v}} [M_\lambda]^\top [B] \quad (2.13)$$

and hereafter I will define the $[B']$ matrix as $[B'] = \frac{1}{Wi} \frac{1}{\bar{v}} [B]$.

We found a non-dimensional expression of the constitutive equations needed for inferring stress in dynamic environments. Realizing that the emerging non-dimensional number $\frac{1}{Wi} = \frac{\eta \bar{v}}{\bar{\lambda}}$ accounts for the relation between viscous and elastic forces in the system, I will investigate how to tune this number in these models to correctly estimate the scales.

2.4 Evaluation of goodness of fit

We require a systematic procedure to measure the degree of similarity of the methods' results with the ground truth obtained by experimental or computational approaches. I decided to use a combination of three measurable quantities: the Pearson correlation coefficient, the Mean Absolute Percentage Error (MAPE), and the coefficient of determination. In all cases, I apply these statistics to the ground truth and the inference generated by the software.

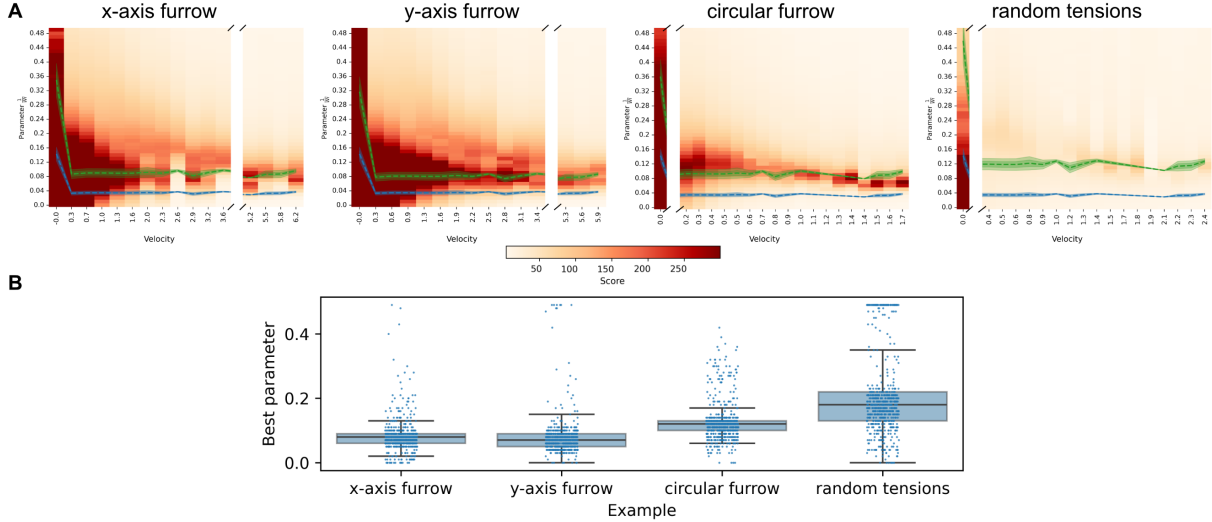


Abbildung 2.3: **Exploration of the scale parameter.** (A) Heatmaps of the saturated score function as a function of the scale parameter ($1/W_i$) and the velocity at each frame. (B) Boxplots with the best scale parameter for the examples. Each individual boxplot shows all repetitions and frames. The best values is taken as the median of each boxplot. The distribution medians are summarized in table 2.1. Figure adapted from [15].

In this way, the different characteristics these observables measure are combined. The Pearson coefficient measures the degree of covariance between the inference and the expected value. It is defined between 1, for perfect correlation to -1 for perfect anti-correlation, with zero indicating no correlation. The Coefficient of Determination measures the variability of the inference to the ground truth, with its values varying from 1 for a perfect match to $-\infty$ for the worst case. Finally, the MAPE indicates how much the inferred values differ from the expected ground truth, having a zero value for a perfect match and $+\infty$ as a worst case. Combining these three quantities allows for a measurement of precision and accuracy in one observable.

The score I propose takes a zero value when the system is maximally different from the ground truth and is unbounded from above if a perfect match occurs. Therefore, the score function is defined as

$$s(M, p, r) = \frac{\alpha}{M} + \frac{\beta}{2} \frac{1+p}{1-p} + \frac{\gamma}{1-r} \quad (2.14)$$

where M , p , and r are the MAPE, Pearson coefficient, and coefficient of determination, respectively. The coefficients α , β , and γ allow changing each statistic's relative importance in the score calculation. Hereafter, these three parameters will always be taken as one ($\alpha = \beta = \gamma = 1$).

I introduced a cut-off as the score function in 2.14 is unbounded from above. This cut-off saturates the function at the value for which the error would be around 1 %

$$s(0.01, 0.99, 0.99) = 299.5$$

Example	Scale parameter ($\frac{1}{W_i}$)	η_{fit}
x-axis furrow	0.08	2.2
y-axis furrow	0.07	2.4
circular furrow	0.12	2.5
Random tensions	0.18	3.1
Combined examples	0.09	2.3

Table 2.1: **Best scale parameter’s values and fitted damping coefficient.** After sweeping values from 0 to 0.5, the best scale parameter is chosen as the median of the best values for each of the twenty-five repetitions for each example separately. The fitting of the damping coefficient is performed by minimizing the distance of the theoretical scale parameter to the maximum score in each condition

When the saturated score function is used, 299.5 will be assigned to those scores higher than the cut-off. This is done in figures 2.3, 3.4 and 3.6.

Next, I used this score to find the best scale parameter in each example. For this, I performed a sweep of the possible values for the scale parameter ($\frac{1}{W_i}$), starting from a value of 0 up until 0.5. A zero value is equivalent to a static inference, as the right-hand side of equation 2.13 becomes zero. Moreover, a scale parameter value of 0.5 implies that the elastic scale is twice as strong as the viscous. The sweep was performed separately in all repetitions of the four examples (Figure 2.3A). Initially, a bigger parameter space exploration was performed to arrive at the best search interval.

After aggregating the repetitions by example, the best scale parameter was chosen as the median of the values for which the score is maximal (Figure 2.3B). In every case, the value of the median coincided with the mode of the parameter’s distributions. The values are summarized in table 2.1.

2.5 Theoretical scale value

Equation 2.12 shows that the scale parameter ($\frac{1}{W_i}$) depends on the reference stress ($\bar{\lambda}$), the reference velocity (\bar{v}), and the damping coefficient (η). Both reference values can be measured from the system in the *in silico* cases. By construction, the stresses coming from the solution of the stresses equations will have a mean of one ($\bar{\lambda} = 1$), and the velocities can be calculated according to equation 2.3. Therefore, it is possible to estimate the theoretical scale parameter’s value for different drag values η .

The simulations to create the tissues were performed using the Surface Evolver [18] (as described in appendix A), and according to the selected implementation, the value for the damping should be $\eta = 1$. I then plotted the theoretical values from the simulations in the heatmaps of figure 2.3A (Blue lines). To this end, the velocity was defined as the norm of the vector containing the components of the velocity of the junctions in each row; I will call this *dimensional velocity*. Then, the dimensional velocity was sorted into twenty bins, shown as the x-axis in the heatmaps of figure 2.3A. Intriguingly, in all cases, the theoretical

value for the scale parameter appears below the optimal value per the simulations. Given that the other two values involved in the calculation are measured from the simulations, this implies that the damping coefficient, which is the only free parameter, is bigger than one.

Therefore, I created a fitting routine to estimate the optimal value for the η coefficient so that it is closer to the seen results from the parameter sweep. Using the `scipy` package [153], I minimized the distance between the calculated value and the scale parameter corresponding to the maximum score function. The minimization is then performed over the sum of the distances of the velocity bins. As the score function was saturated, the highest score degenerated in the scale parameter in some cases. Therefore, I use the median of the degenerated values in the scale parameter as its optimal value. The fitting was performed five times, one for each of the four prescribed conditions and once for the sum of all the conditions. The resulting theoretical scale parameters for the adjusted damping coefficient are shown in figure 2.3A (Green line) and summarized in table 2.1. Interestingly, the optimal value for the damping coefficient in the prescribed examples improves the accuracy of the theoretical scale parameter for almost all velocities in every case (Figure 2.4 Orange lines), compared with the assumption of a damping of 1 (Figure 2.4 Blue lines).

In this section, I have analyzed the theoretical value of the scale parameter and compared it with the optimal value that arises from the maximum score. The theoretical value was lower than expected by this comparison. Thus, I performed a fitting routine on the only free parameter: the damping coefficient η . This coefficient was found to be higher than the expected value of $\eta = 1$ as summarized in table 2.1. Taken together, these results show that in the *in silico* ground truths generated, the scale of the elastic stresses is an order of magnitude above the viscous one.

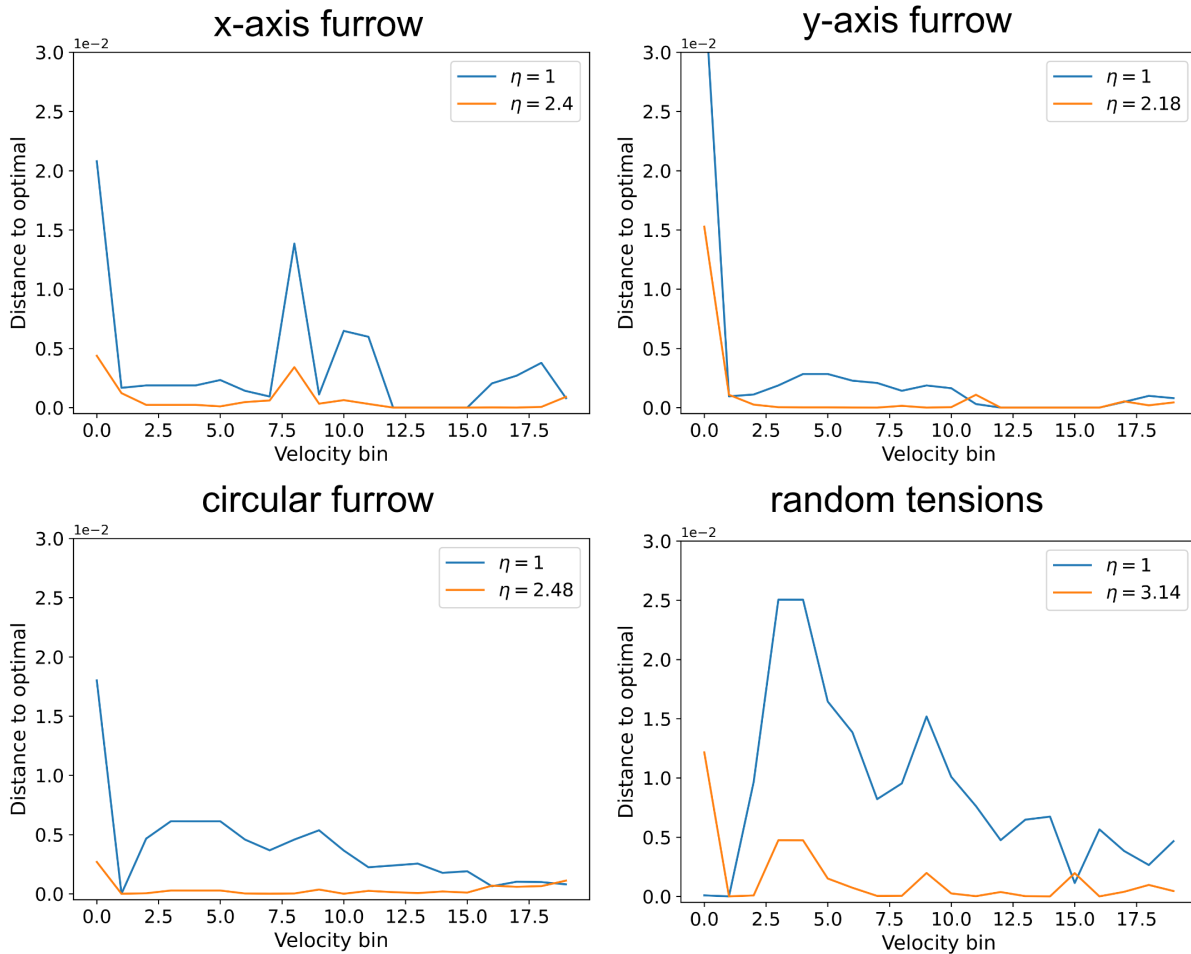


Abbildung 2.4: **Fitting of the damping coefficient** Square Distance from the theoretical value for the scale parameter to the maximum in the saturated score function in the sweeps. The distance is calculated for a damping coefficient $\eta = 1$ (blue lines) and the best-fitted values. The best values are in each legend. $\eta_{x\text{-furrow}} = 2.2$, $\eta_{y\text{-furrow}} = 2.4$, $\eta_{\text{circular-furrow}} = 2.5$, and $\eta_{\text{random-tensions}} = 3.1$.

Kapitel 3

ForSys: Open Source stress and pressure inference

ForSys is an Open Source inference algorithm developed in Python specifically tailored to manage dynamic information from video microscopy. In a nutshell, ForSys utilizes the topology of the membranes and the velocity of the cell's boundaries to deduce the stress distributions. As was discussed above (chapter 2), the algorithm starts from a microscopy image and converts it into a polygonal structure that allows curved edges. The software's static modality heeds what was described in section 2.1.1, following other authors closely [23, 147]. ForSys's dynamic model's details were presented in section 2.2. The user may define whether the inference should be performed with a Static or a Dynamic algorithm.

To use this tool, the user converts static microscopy or a time series of microscopies into skeleton images of the cell boundaries through image segmentation [1, 2] or skeletonization. This segmented image is read by ForSys and converted into a polygonal structure with curved edges. This later is transformed into a system of equations depending on the input and the chosen modality. Finally, the inference results are presented as color codes in the membranes for the stress values and in the cell's faces for estimated intracellular pressures. A scheme of this pipeline is presented for the static (Figure 3.1A) and the dynamic modes (Figure 3.1B).

Before using the tool I developed to study the mechanical state of a real-world biological system like the zebrafish neuromasts, I must validate it against a known ground truth. To this end, I created another package called seapipy [13]. seapipy is a Python package that allows the generation of Surface Evolver-compatible files through a simple interface, allowing a fast and easy integration within the ForSys environment. A detailed description of the seapipy software will be presented in appendix A. First, to perform the validation, I generated four different ground truths archetypes with seapipy that were used to test the accuracy of the static and dynamic modes. Later, I tested the capabilities of ForSys to estimate the stresses in a published set of *in vivo* data: the mucociliary epithelium of *Xenopus* embryos [150]. Afterward, I applied the software to the migrating primordium in the zebrafish's lateral line and studied the generation of the protoneuromasts. Finally, I studied the mechanical state of the different cell types in maturing neuromasts.

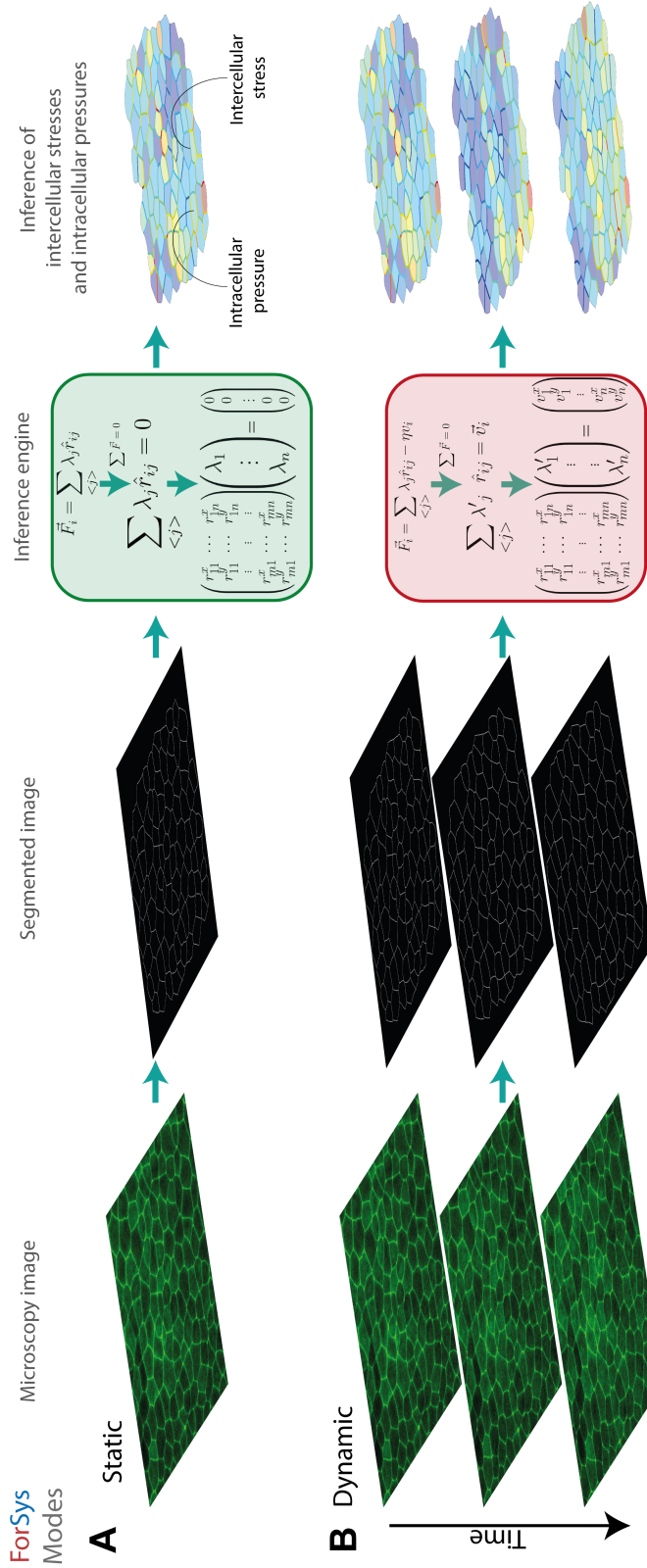


Abbildung 3.1: **The stress inference pipeline.** (A) The static inference is performed on a microscopy image by creating a skeletonized tissue representation. Then, ForSys reads it and builds the system of equations according to the geometrical properties of the tissue. Lastly, the system is solved, and the intracellular pressures and intercellular stresses are inferred. (B) Similarly, the dynamical inference uses a time series of images to add dynamical information to the system of equations used in the static case. A time mesh is generated from the succession of microscopy images, and pivot vertices are tracked through time. Then, the velocity of these vertices from frame to frame is used to modify the system of equations, allowing non-static tissues to be analyzed by stress inference. Image reproduced from [15].

3.1 ForSys inference in *in silico* static images

The static modality of ForSys was implemented following the description of chapter 2. The main difference between ForSys’s static modality and other methods such as CellFIT [23] or DLITE [147] stems from the imposition of the average constraint before transforming the system into its least-square form. In this section, I will compare the accuracy of ForSys simulations with the DLITE and CellFIT solutions. The authors of the DLITE method have added a CellFIT modality to their software, which I will use when referring to the CellFIT results. This is because CellFIT is not open source, so its integration into the analysis pipeline would be challenging for direct comparison between membranes. Moreover, its binary files are no longer available.

First, I investigated how similar the inference solutions for the three methods, CellFIT, DLITE, and ForSys’s static modality, are. This analysis showed that the accuracy of the methods is very similar, as seen by their closeness to the $y = x$ line (Figure 3.2A). Furthermore, the distributions of stress values arising from the inferences are nearly identical (Figure 3.2B). Finally, the accumulated solutions for all repetitions at the last frame of the simulations display remarkable similarity (Figure 3.2C). The comparison between the score function values for the static modality of ForSys and DLITE shows that ForSys, even in its static modality, outperforms other methods in all but the random tension scenario.

To further analyze the differences between distributions of stresses found through inference, I measured the distance between distributions in the Wasserstein sense. As the distance value gives a number that might be difficult to interpret by itself, I also generated an artificial normal distribution with a mean of $\mu = 1$ and a standard deviation of $\sigma = 0.2$. The Wasserstein distance is zero if and only if the two distributions being compared are equal, and it can be arbitrarily large for increasingly different sets of data. The distance was almost zero in all pairwise comparisons among the three algorithms. To make it comparable, I defined the relative distance as the ratio between the distance between the methods’ solutions and the distance with the random distribution. This analysis showed that the vertical and horizontal furrow are ~ 30 times, the circular furrow is ~ 10 times, and the random stresses are ~ 5 times more similar between the different methods’ solutions than the random distribution. This shows that the methods’ solutions are remarkably similar. Therefore, in the rest of this section, DLITE implementation will be used to compare closely with ForSys.

To perform a more comprehensive comparison, I used the last frame generated by the simulation in each of the four examples. The ground truth value (Figure 3.3A), DLITE’s estimation (Figure 3.3B), and the inference by ForSys static modality (Figure 3.3C) of the intercellular stresses and intracellular pressures are qualitatively similar. Both methods show a relatively low Mean Absolute Percentage Error (MAPE) ($\sim 10\%$) (Figure 3.4A). ForSys showed a lower value for the MAPE, as compared to DLITE, for all cases except the random stresses. This was tested using the Mann-Whitney U test with the alternative hypothesis that ForSys’s MAPE is stochastically lower than DLITE’s, giving significance scores of $p < 1e-5$, $p < 1e-8$, and $p = 0.01$ for the x-furrow, the y-furrow and the circular furrow respectively. The same test was repeated using the saturated score function (Figure

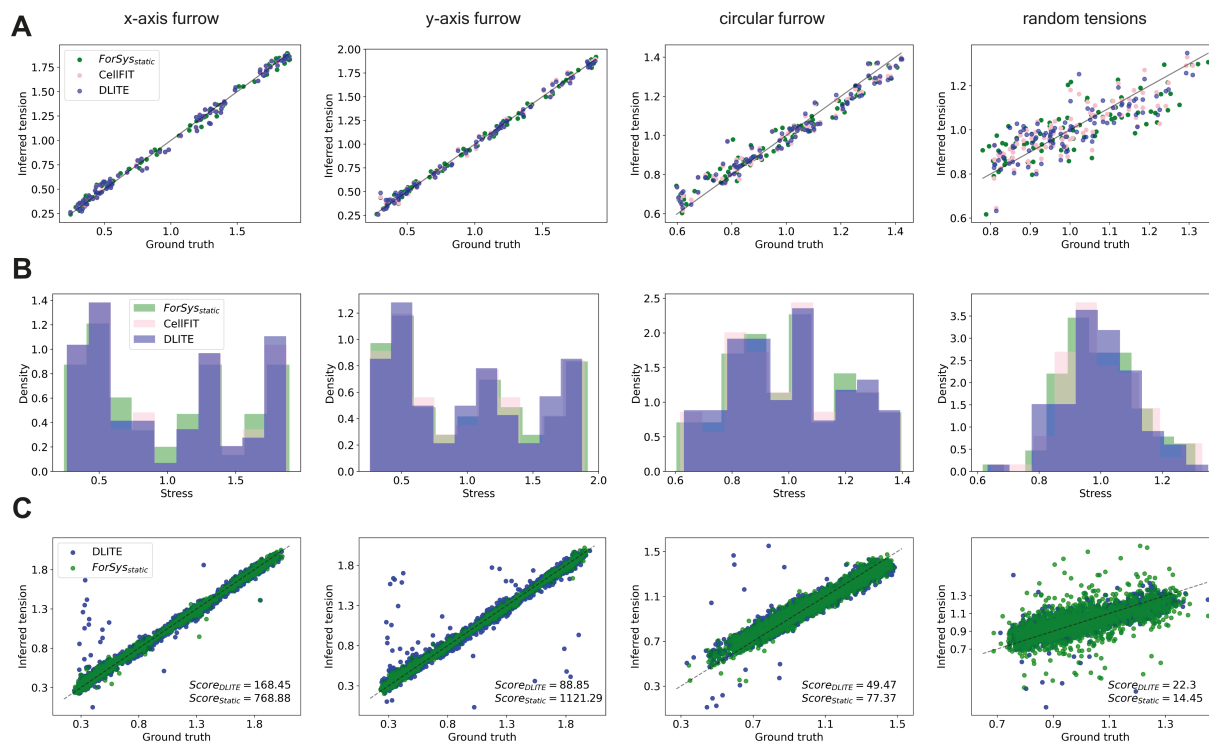


Abbildung 3.2: **Comparison between static ForSys and other force inference methods.** I tested whether the static implementation of ForSys differed from the values of DLITE and CellFIT. Each column represents one of the examples. **(A)** I show that the inferred stress versus the ground truth follows the $y=x$ line, plotted as a solid black line as a visual aid, for the three methods at the last simulated frame. **(B)** Moreover, the distribution of stresses of all methods has similar behaviors in the histograms. Both panels (A) and (B) are for a selected representative simulation. **(C)** Then, the result for all inferred tensions versus ground truth repetitions is shown for each condition at the last simulated frame. The black dashed line is the $y=x$ line and is a visual aid. The score function's values are in the lower right corner of each plot. ForSys, in its static modality, has better results in the three first examples and comparable results in the random tension case. Figure reproduced from [15].

3.4B). This showed that ForSys had a stochastically bigger score value than DLITE in all cases except the random stresses, with a significance of $p < 0.001$, $p < 1e - 4$, and $p < 0.01$ for the x-furrow, the y-furrow and the circular furrow respectively, confirming the previous result. Interestingly, in the random stresses example, the alternative hypothesis that the distributions are equal shows that ForSys and DLITE are not significantly different ($p = 0.01$). Additionally, ForSys displays, on average, a smaller spread of both MAPE and values for the score, as revealed by the smaller interquartile range of the distributions of values.

Taken together, these results show that the static modality of ForSys is accurate and

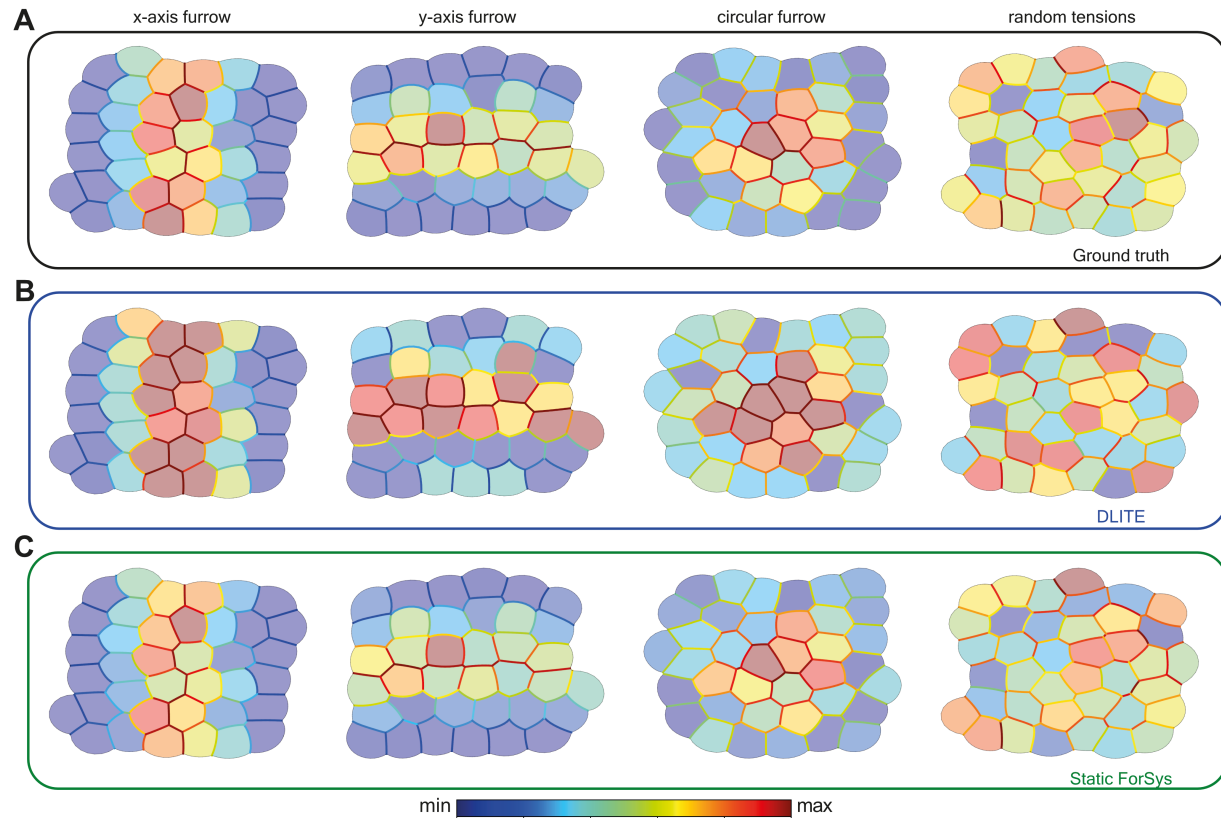


Abbildung 3.3: **In silico qualitative validation for tissues in static equilibrium.** Four different conditions were generated with seapipy to test the static equilibrium condition. Each column shows a representative repetition per example. The ground truth (A) can be compared to the values for the DLITE predictions (B) and the Static ForSys (C). The three rows shown correspond to the final time. The color bar shows the order of the colormap for both the stresses and the pressures. Figure adapted from [15]

precise to effectively recover the *in silico* generated ground truths. Accordingly, in the next section, only the static modality of ForSys will be used to compare with the dynamic results.

3.2 ForSys inference in an *in silico* dynamical setting

I used the time evolution of the *in silico* examples to validate the dynamic modality of ForSys. As introduced in section 2.2, I will assume that the cells in the tissue are in an overdamped regime, in the sense that I model the cells as a viscoelastic material. This was achieved by incorporating the velocity into the equilibrium equations at each junction mediated by a damping coefficient η . Finally, in section 2.3, I showed that this leads to a number related to the rate between viscous and elastic scales in the system, which I named

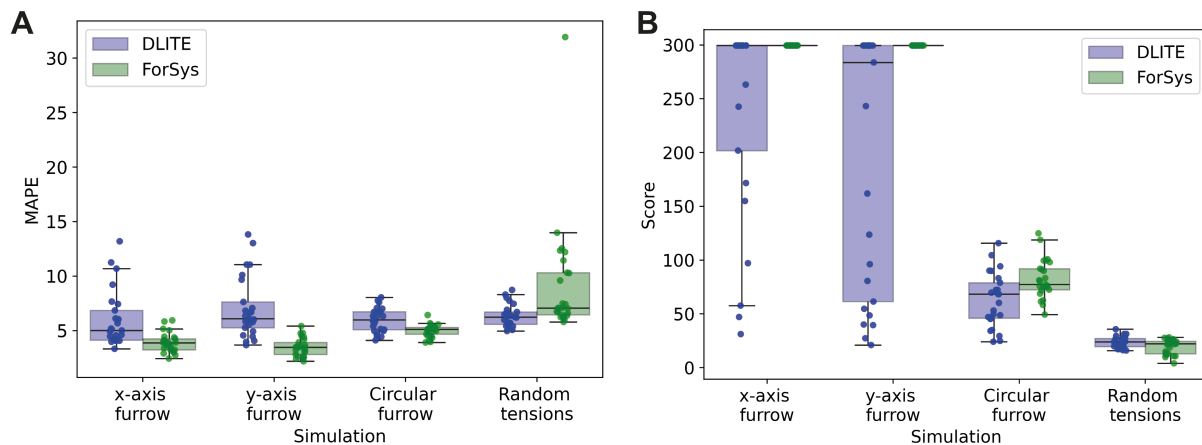


Abbildung 3.4: **In silico quantitative validation for tissues in static equilibrium.** Four different conditions were generated with seapipy to test the static equilibrium condition. Each column shows a representative repetition per example. The mean absolute percentage error (A) and the saturated score function (B) for all simulations are represented in two boxplots, DLITE and Static inference with ForSys, paired by condition. Dots show the result for individual repetitions. Figure adapted from [15]

$$\frac{1}{W_i}$$

ForSys determines the velocity of each junction by tracking them through the time series of images. This is achieved by searching for all the junctions near the original position of the one being tracked in the new frame and joining the closest ones. In those cases that it can not be determined, no future position is assigned to the junction, which is interpreted as a null velocity in the equation. It is also possible to manually assign an initial guess to connect junctions' id through time. Once the junction has been assigned to the previous time point, it is removed from the list of possible futures. Therefore, adding even a small set of initial guesses can lead to a more faithful tracking of the junctions.

In dynamical inference, the inclusion of the velocities made it necessary to create a non-dimensional version of the constitutive equations, which in turn made the system dependent on dimensionless parameter: $\frac{\eta \bar{v}}{\lambda}$. In the dynamic modality, I used the fitted values of this parameter, presented in section 2.2 and table 2.1.

First, I looked into the qualitative differences between the ground truth generated by seapipy and the inference results. I found that the four prescribed conditions (Figure 3.5A) were qualitatively recapitulated by the inference both in the static (Figure 3.5B) and dynamic modality (Figure 3.5C). However, in the three furrow cases, ForSys dynamic shows a better qualitative agreement with the ground truths, as it finds a more defined outline of the furrow sections.

Next, I used the mean absolute percentage error (MAPE) (Figure 3.6A) and the saturated score function (Figure 3.6B) to quantify the accuracy and precision of the method. The dynamic modality has a lower MAPE for all cases except in the random tensions. This was

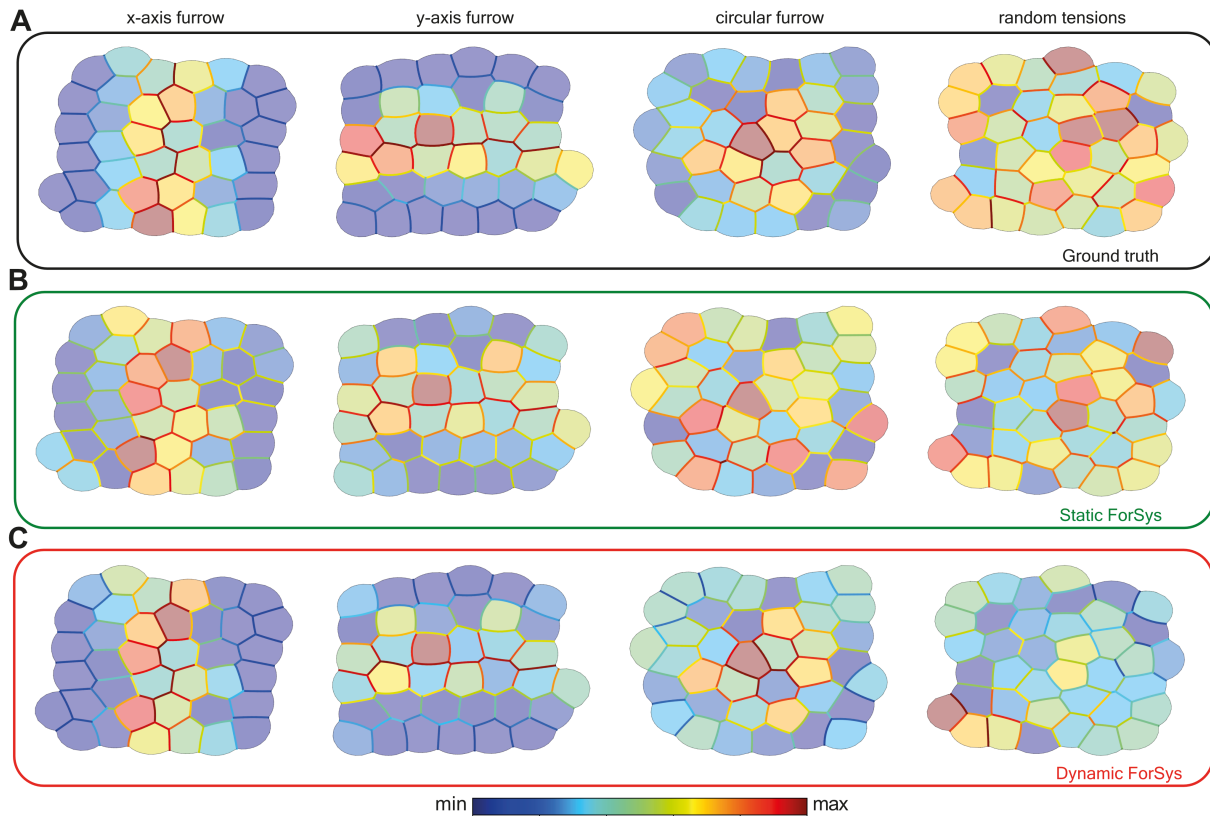


Abbildung 3.5: **In silico validation of ForSys for tissues in dynamical equilibrium.** I generated four examples with seapipy to test dynamical equilibrium conditions. Each column shows a representative repetition per example. The first row (**A**) shows the ground truth values for the stress and the pressures, the static inference made by ForSys is in the second row (**B**), and the dynamical ForSys inference is in (**C**). I show each example at one time point after the system's tensions changed. The color bar shows the order of the colormap for both the stresses and the pressures. Figure adapted from [15].

confirmed by a Mann-Whitney U-test, with the alternative hypothesis that the dynamic modality has a stochastically smaller MAPE ($p < 1e - 9$; $p < 1e - 9$; $p < 1e - 7$, for the x-furrow, y-furrow, and circular furrow, respectively). I applied a similar analysis using the saturated score function and found that the dynamic modality has stochastically larger score values for all four examples ($p < 1e - 8$; $p < 1e - 9$; $p < 1e - 9$; $p = 0.03$, for the x-furrow, y-furrow, circular furrow, and random, respectively). Interestingly, the MAPE value is not significantly different between the static and dynamic modalities ($p = 0.06$).

Notably, the accuracy and precision of both the dynamic and static modalities depend on the degree of motion in the vertices of the tissue. This can be seen in the dependence of MAPE on the dimensional velocity of the system ($|v|_2$) (Figure 3.6C). This implies that both modalities, mainly the dynamic modality, worsen with more movement. Even though this result may seem counter-intuitive, it is important to note that an increase in movement

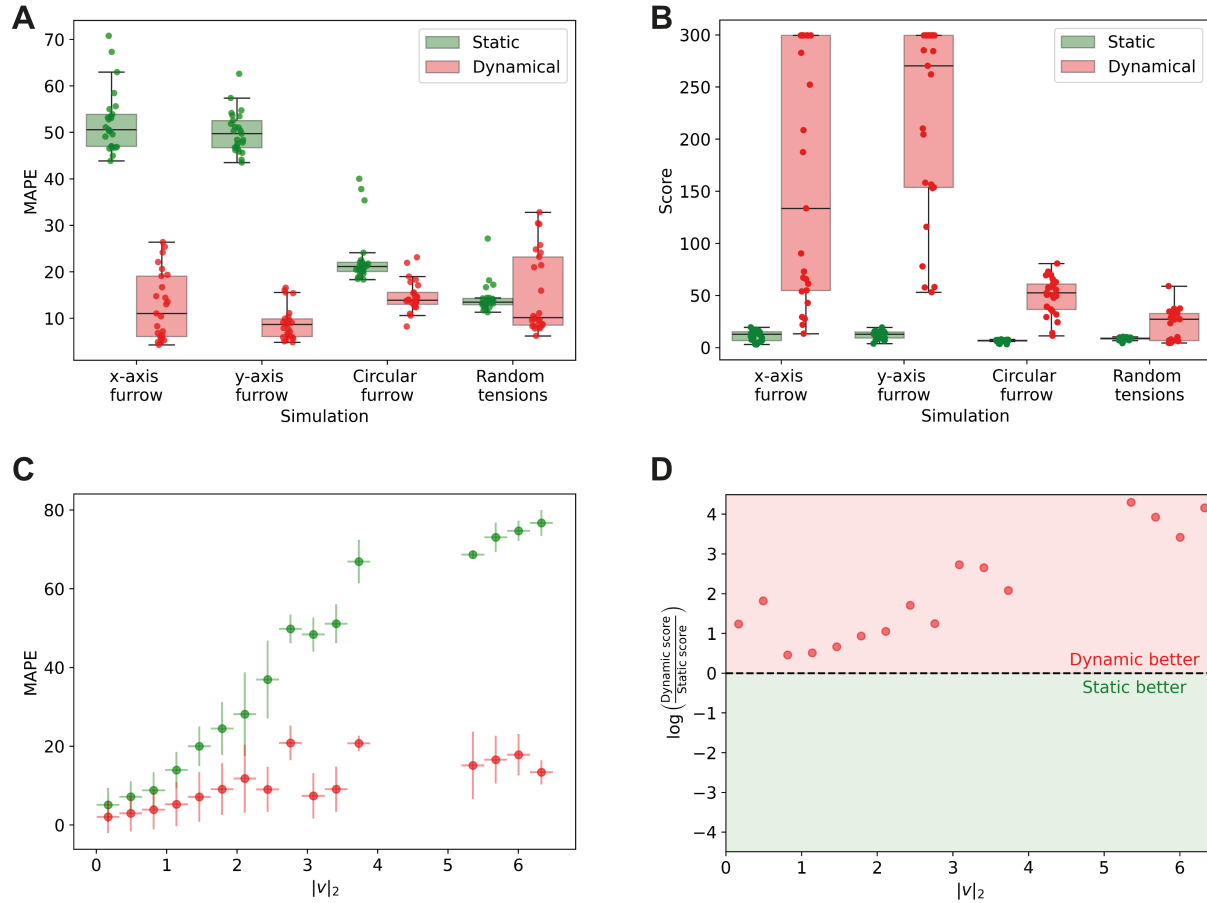


Abbildung 3.6: **Dynamic inference outperforms the static pipeline.** The mean absolute percentage error (A) and the saturated score function value (B) for all simulations are represented in two boxplots, Static and Dynamical inference, paired by condition. Dots show the result for individual repetitions. (C) Dependence of the MAPE on the velocity $|v|_2$. The scattered dots are the median for all experiments with a velocity corresponding to the current $|v|_2$ bin. Error bars in the y-axis are one standard deviation, and error bars in the x-axis represent the size of the velocity bin. (D) Dynamic to static score function ratio ($r = \log(\frac{\text{dynamic}}{\text{static}})$) as a function of the $|v|_2$ bin. A ratio bigger than zero shows that the dynamic solutions performed better (Red zone), and a negative value (Green Zone) favors the static solution. The black dashed line at $r = 0$ separates both zones. All velocity bins favor the dynamic solution. Figure adapted from [15]

translates into a noisier inference. This is because the system of equations is ill-conditioned, as Broadland and colleagues measured in the static case using the condition number [23]. This means that small input changes will get amplified in the solution. However, Figure 3.6C also shows that the static modality worsens rapidly, while the dynamic modality finds a plateau in this velocities' range. For the highest velocity, the mean absolute percentage error in the static modality is $\sim 80\%$ against $\sim 15\%$ in the dynamic's case.

Finally, we can visualize the better modality as a function of the dimensional velocity ($|v|_2$) by calculating the logarithm of the ratio between the saturated score function of both modalities: $r = \log\left(\frac{\text{dynamic score}}{\text{static score}}\right)$ (Figure 3.6D). In this plot, the region with $r > 0$, plotted in red, shows that the dynamic modality performs better, and for $r < 0$, shown as a green shade, the static would be a better algorithm. We can see that the dynamic modality outperforms the static one for all velocity values.

Therefore, I showed that the dynamic algorithm could faithfully recover the ground truth values generated by the *in silico* seapipy pipeline. I have also shown that the accuracy and precision of the method depend on the degree of movement in the tissue, getting worse with increasing velocities. However, the dynamic modality reaches a plateau and is shown to outperform the static variant consistently.

3.3 *In vivo* validation in the Mucociliary epithelium of *Xenopus* embryos

After showing that ForSys correctly recapitulates the *in silico* examples in its static and dynamic modalities, I focused on an *in vivo* system. For this, I used a published data set of the mucociliary epithelium of the *Xenopus* embryo [150](Figure 3.7A). I used the fluorescently tagged myosin II intensity as a proxy for membrane stress. This was quantified using a non-muscle myosin II A-specific intrabody (SF9-3xGFP). This protein has been used as a proxy for active myosin II [60, 110]. Besides, this sensor allows the membrane to be visible to segment the image before the analysis by ForSys.

Using a single microscopy image per epithelium (Figure 3.7A), I segmented the tissue using EPySeg [1] and performed manual corrections with Tissue Analyzer [2]. First, I qualitatively compared five examples (Figure 3.7). I created the myosin maps from the microscopy to plot the ground truth intensities in the same scale as the inferred stress. ForSys could recover information about areas of high stress, such as embryos three and five. Moreover, in embryo 4, ForSys can reproduce a homogeneous stress pattern. In these five experiments, there is a moderate correlation between the inference and the myosin intensity for each embryo ($R = 0.56 \pm 0.11$; mean \pm std)(Figure 3.7C, and mean absolute percentage errors of approximately 20 % (21 ± 5 ; mean \pm std). In addition, stress and myosin intensity distributions are not significantly different ($p = 0.76$; Mann-Whitney U test; $N = 154$)(Figure 3.7D).

In total, I analyzed 127 embryos, many of which had a small number of membranes. Therefore, the following analysis will use only embryos with a significant p-value in the

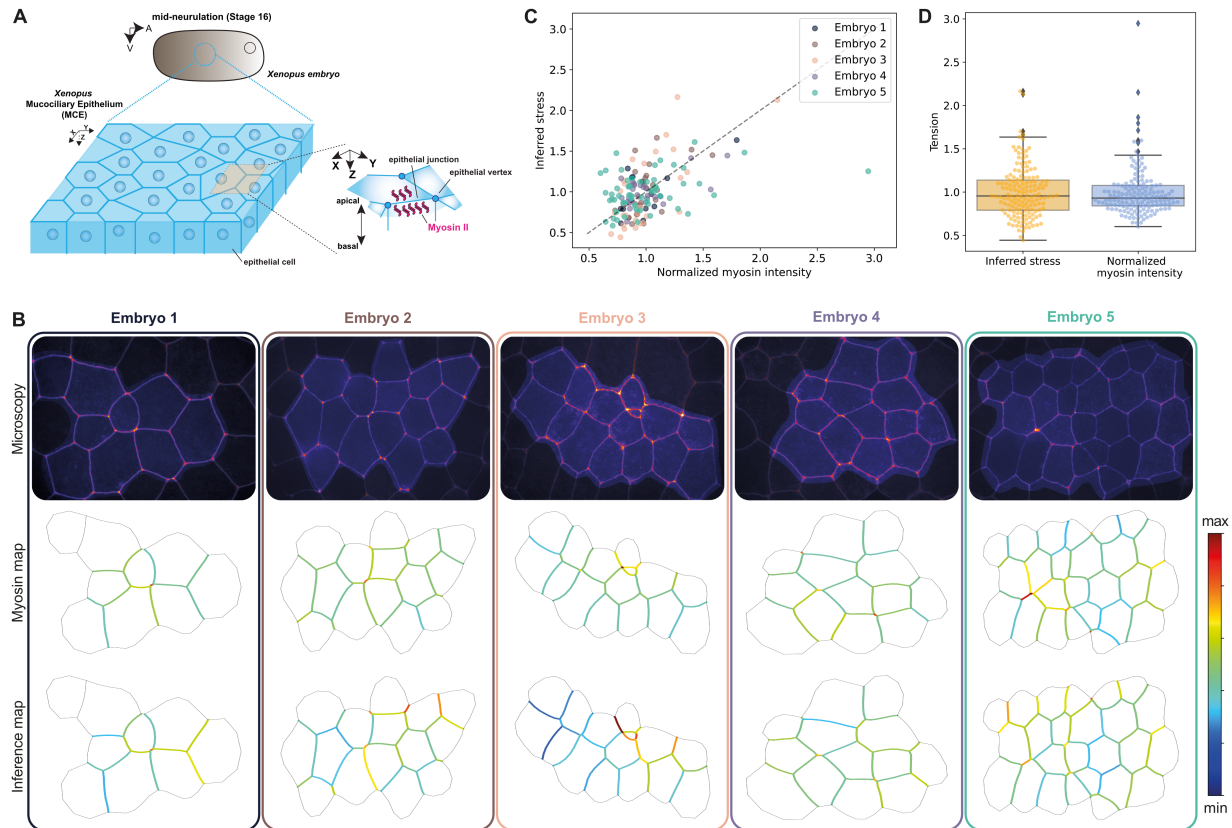


Abbildung 3.7: **Comparison of ForSys-derived stress with myosin II measurements in the Xenopus embryo mucociliary epithelium.** (A) Scheme of the Xenopus embryo and position of the mucociliary epithelium. (B) Five examples of inference in Xenopus embryos. The microscopy image is shown alongside the myosin intensity map and the ForSys inference result. The color code in the maps represents the myosin sensor intensity and the stress prediction. The scale was saturated at tension values of two. The highlighted region in the microscopies shows the area that was analyzed. (C) Relationship between myosin sensor intensity and stress inferred for the five examples. Each scatter point shows the value for a particular membrane in that example. The dashed black line represents the $y = x$ line. Each color corresponds to the rounded rectangle around the embryo and its font color in panel (B). The average Pearson correlation coefficient is $R=0.56 \pm 0.11$; (mean \pm std) (D) Quantification of stresses and myosin sensor intensity for the five examples. Inferred stresses and myosin intensities are not significantly different ($p=0.76$; Mann-Whitney U test; $N=154$). Figure reproduced from [15].

Pearson correlation coefficient. When pulling together all embryos, I found a moderate correlation between the inferred stress in the membranes and their myosin fluorescence ($R = 0.38$ and $p < 1e-40$; $N = 1176$ membranes). Additionally, I quantified the correlation for each embryo separately and found a median correlation of $R = 0.54 \pm 0.19$ (mean \pm std; $p < 0.05$). These correlation values agree with previously reported correlations between Myosin intensity and other stress inference techniques [111, 71].

Therefore, I found that ForSys inference correlates positively with the myosin fluorescence in the membranes of the mucociliary epithelium in *Xenopus* embryos, which is used as a proxy for the membranes' stress. This *in vivo* validation of the tool serves as an important step to apply it to other biological systems, as will be shown in the next sections.

3.4 Characterizing the mechanical state of the zebrafish neuromast

Having validated the tool *in silico* and *in vivo*, I now turned to investigate the mechanical state of the neuromasts in the zebrafish lateral line. The inclusion of dynamic inference now allows the study of the stresses and pressures present during the primordium movement through the zebrafish embryo while forming the lateral line. The migratory primordium comprises approximately one hundred cells that move from the head to the tail of the fish embryo (Figure 3.8A). Periodically, groups of around thirty cells detach from the trailing part of the primordium and are then deposited along the lateral line [52]; these groups of cells are called protoneuromasts.

Each of these deposited structures gives rise to a neuromast. This mechanosensitive organ is a pseudostratified tissue formed by various cell types. For simplicity, in this chapter, I will group the cells into two different categories: sustentacular cells, which support the organ, and hair cells, which provide the sensory function. Hair cells originate after sustentacular cells give rise to a hair-cell progenitor, which divides into a pair of hair cells.

In the present section, I will show how ForSys can be used to predict the localization in space and time of protoneuromasts during primordium migration. Later, I will describe the mechanical state of the neuromast organ during its development, particularly as it relates to the Polarity Cell Inversion movement.

3.4.1 Stress and pressure distribution in the migrating primordium

I will study the migration of the primordial in Zebrafish two days after fertilization (2 dpf). I will use a time series of images with EGFP-labeled plasma membranes (Figure 3.8B). I followed the primordia trajectory for thirty minutes, taking one image every two minutes. In all cases, I segmented the images in the basal plane region. After inputting ForSys with the segmentation, I obtained a stress and pressure map describing the state

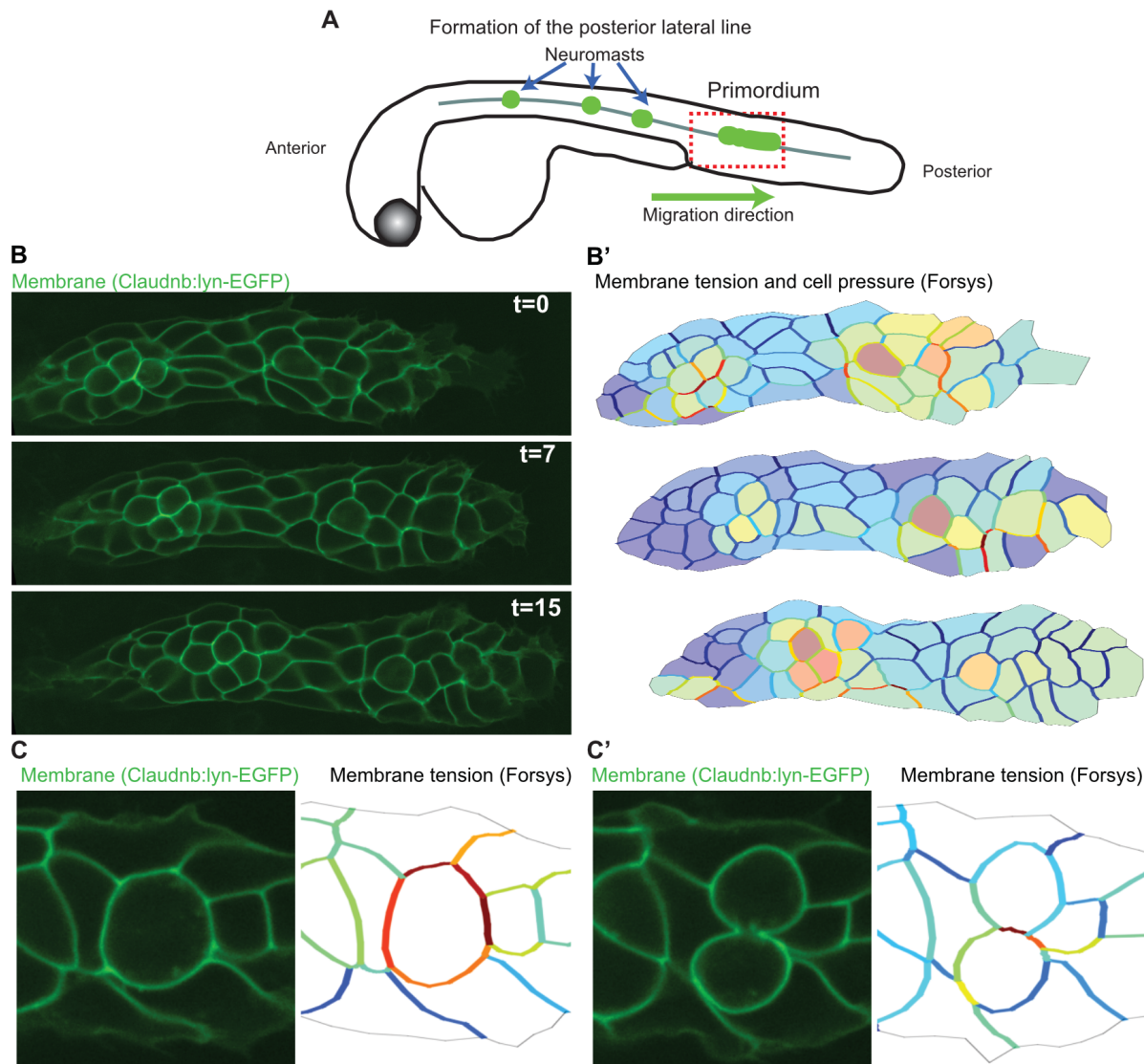


Abbildung 3.8: ForSys inference of a moving epithelium in the zebrafish lateral line at 2 dpf. (A) Schematic of the biological model. The neuromasts of the posterior lateral line are formed by detaching from a primordium that migrates from the anterior to the posterior of the fish. (B) Frames 0, 7, and 15 of the primordium migration in which cell membranes are fluorescently marked with Claudnb:lyn-EGFP. (B') The membrane signal is used for segmentation, which ForSys uses to predict cell membrane tension and intracellular pressure. (C, C') Consecutive frames show cell division. The membrane tension in the cell just about to divide is considerably higher than the surrounding membranes. After division, the dividing membrane retains a high tension. Figure adapted from [15].

of the primordium (Figure 3.8B').

First, I concentrated on qualitatively describing what happened to the stresses found in the membranes just after cell division. I found that cells just before cell division show higher stress than their non-dividing neighbors (Figure 3.8C). Moreover, after cell division, the stress remains higher in the shared membrane between the sibling cells (Figure 3.8C').

Then, I studied the mechanical state of the whole tissue. As mentioned, the primordium creates protoneuromasts in its anterior region while migrating posteriorly. Just before detachment, an epithelial rosette is formed around the center of the soon-to-be separated area. This process involves forming apical constrictions in the epithelial cells [62] (Figure 3.9A and B). Therefore, the constriction can be easily detected by morphological analysis in the apical plane of the epithelium [46]. However, how constrictions in the apical region relate to the morphology of the basal plane is unknown.

First, I located the rosettes by looking at the morphology of the apical plane, shown in asterisks in Figure 3.9B and 3.9C, and manually annotated their position in the anterior-posterior axis (AP-axis). I used the pressure inferred by ForSys in its dynamic modality smoothed using Kernel Density Estimation, using cells' pressures as weights. This resulted in a smooth curve that describes the cells' pressure as a function of the positions in the AP-axis for each time point (Figure 3.9C).

I found that the rosettes' positions, as seen by detecting the constrictions in the apical plane, are spatially correlated with the zones of high pressure inferred by ForSys (Figure 3.9C). Moreover, their predicted positions are highly correlated with the annotated positions ($R = 0.99$ and $p < 1e - 26$, $N = 34$; for the combination of both rosettes) (Figure 3.9D). Notably, in one of the neuromasts, ForSys can predict the presence of a rosette before it is visible in the apical plane.

This analysis revealed that rosette formation might be preceded by mechanical changes in the tissue, which would allow the detection of apical rosettes by changes in the basal region.

3.4.2 The mechanical state of the neuromast

After protoneuromasts detach from the primordium, they are deposited along the zebrafish embryo, forming the lateral line. They later develop to form the mechanosensory neuromast organ. Here, I will study the relation of stresses between different cell types in the neuromast. This organ is composed of a center of mechanosensory hair cells surrounded by supporting cells (Figure 3.10A) [66]. Cells were tagged with a plasma membrane marker, which allowed me to segment them using ilastik [11] and epyseg [1] (Figure 3.10B). After segmentation, ForSys, in its dynamic modality, was used with the time series of images to infer the stresses in the organ (Figure 3.10B).

I will concentrate the efforts on the hair cells and their relation with the supporting cells around them. I observe that hair cells' membranes have a higher stress on average ($p < 1e - 5$) compared to Hair Cell-Supporting cell interfaces. Additionally, the homotypic interfaces between supporting cells have the lowest stress ($p=0.03$) compared to Hair Cell-Supporting cell interfaces (Figure 3.10C).

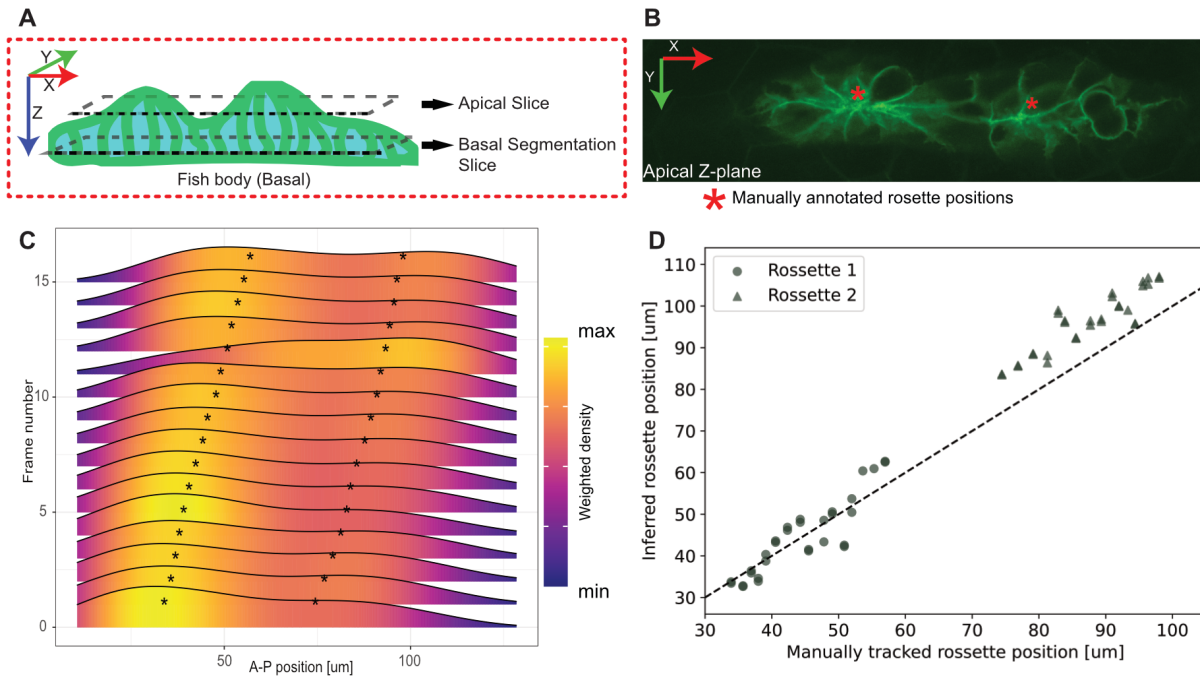


Abbildung 3.9: **ForSys inference predicts localization of epithelial rosettes.** (A) Schematic of the primordium orientation and the position of the optical planes. (B) Microscopy image of fluorescently marked membranes with Claudnb:lyn-EGFP. Constriction of the cell membranes in rosettes is evident in the apical plane. The asterisks show the anteroposterior location of rosettes. Cell segmentation was done on a Z-plane at a more basal plane than the one shown. (C) Ridgeline plots of cell densities along the anteroposterior axis were performed over 16 frames for a representative primordium. Time goes from bottom to top. The direction of primordium migration is to the right. The asterisks show the positions of the manually annotated rosettes. (D) Anteroposterior position of the manually tracked rosette against the inferred position by taking the local maxima of the density of pressure values from (B). The diagonal line marks $y=x$ as a reference for comparing predicted and manually annotated values. Figure adapted from [15].

Next, I looked into the Planar Cell Inversion process (PCI). In PCI, after the division of the Hair Cell Progenitor, the sibling pair rotate around 180° around their centroid (Figure 3.10D and Figure 3.10E). This process happens around half the times [82, 159]. The mechanism that underlies the inversion process remains unknown.

I decided to focus on the membranes of the hair cells during the inversion processes and compare the stress inferred by ForSys between the homotypic hair cell-hair cell and the heterotypic hair cell-sustentacular cell membranes. I found that the interfaces between hair cells and sustentacular cells have significantly smaller stress than the hair cell-hair-cell membranes ($p < 1e - 4$) (Figure 3.10F).

Taken together, this suggests that a cell-type specific adhesion pattern exists that coordinates the remodeling process during PCI. Moreover, due to the inverse relation between adhesion and stress, this result implies that the PCI process is led by a strong adhesion between sibling hair cells and weaker links with the surrounding tissue, which helps in contact remodeling during the pair's rotation.

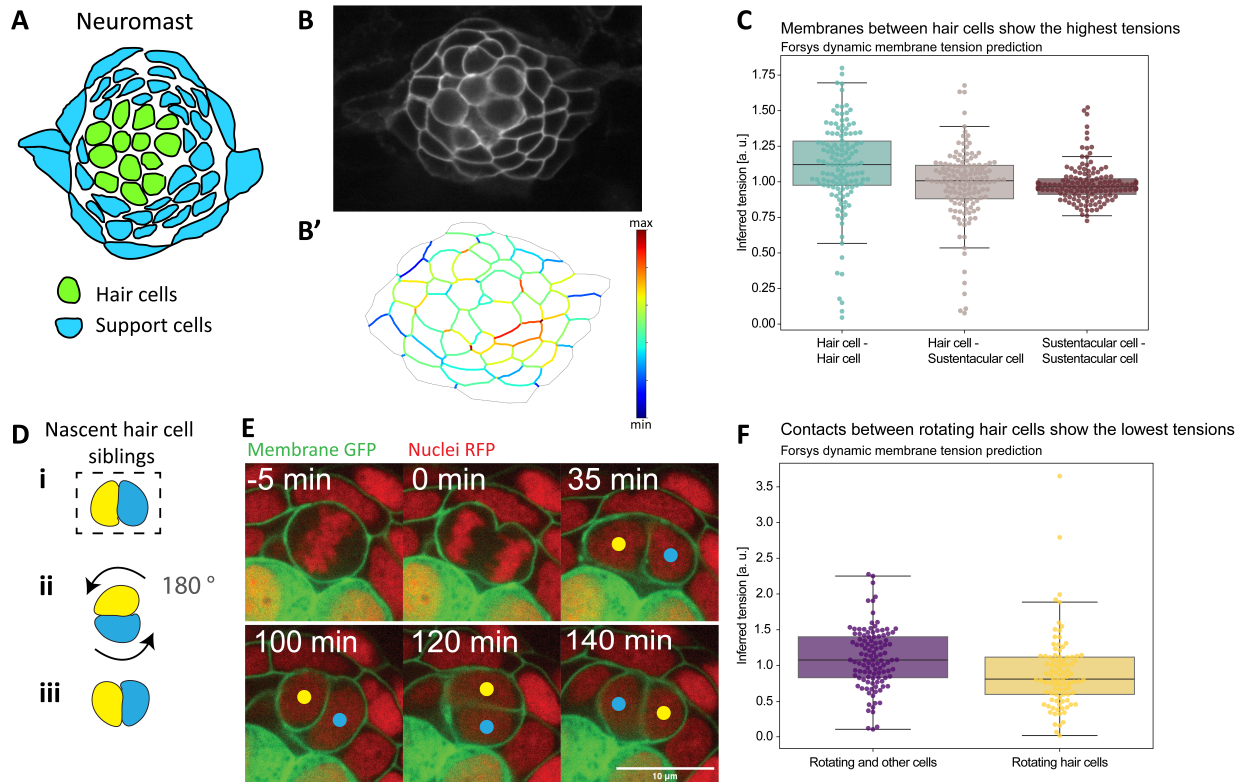


Abbildung 3.10: *In vivo* ForSys inference in an epithelium with rotating cells. (A) Schematic of cell composition in a zebrafish lateral line neuromast. Sensory hair cells are located in the middle and surrounded by different support cells. (B) Microscopy image of a neuromast whose cells can be tracked by membrane-tethered EGFP. (B') Below is the ForSys tension prediction after membrane segmentation. (C) The tension predicted for membranes is classified by the type of cell-cell contact. The homotypic contacts between hair cells show the highest predicted tension, while the homotypic contacts between support cells show the lowest on average. Each data point is the mean of the predicted tension values for each membrane type in one frame. The frames come from N=7 videomicroscopy experiments. (D) Schematic of the planar cell inversions occurring in 50% of the nascent hair cell pairs: sibling hair cells perform a 180° rotation to exchange positions along the anterior-posterior axis. (E) Time-lapse frames showing the *in vivo* rotation process: around 100 minutes after mitosis, the nascent hair cells exchange anteroposterior positions by rotating in the epithelial plane. The sibling cells remain attached during the rotation, while the surrounding cells do not actively participate in the movement. (F) Homotypic tensions between the young rotating hair cells are significantly lower than their contacts with the surrounding cells. Figure reproduced from [15].

Kapitel 4

Planar Cell Inversion

In the previous chapter, I showcased software that allowed me to study distinct processes during the development of the Zebrafish lateral line. I used it to study the formation of the protoneuromasts during the primordium's head-to-tail migration and the asymmetry in the stresses dependent on the nature of the junction. In this chapter, I will concentrate on an intriguing process during neuromast development where two cells are involved in a coordinated movement that eventually gives rise to the patterning of the organ: the Planar Cell Inversion.

4.1 Introduction

Collective cell migration is pervasive in complex biological phenomena such as development and regeneration. For these movements to occur, processes at different scales must operate and coordinate for a robust result. However, the internal functions need not be deterministic or stochastic, and different cogs could behave under different dynamics.

Neuromasts are mechanosensory organs located in the lateral line of the zebrafish (Figure 4.1A). Neuromasts exhibit a circular shape, with the mechanosensory cells in the middle of the organ, surrounded by supporting cells (Figures 3.5A and 4.1B). Mature wild-type neuromasts exhibit a stereotypical patterning on the apical side, where hair cells orient opposite each other. The positioning of the kinocilia measures the orientation of these cells. Interestingly, this pattern exhibits a strong alignment with either the Antero-Posterior axis (AP axis) or the Dorso-Ventral axis (DV axis), depending on its genesis. Those neuromasts derived from the first primordium (prim1) that appears during embryogenesis are aligned with the AP axis, while those deriving from the second primordium (prim2) align with the DV axis [106]. The precise patterning of the organ is crucial to its sensory function.

The kinocilia's orientation characterizes the cell's polarity and can be represented as a vector going from the cell boundary to the hair. Mean-field values can be calculated to estimate the degree of orientation and alignment of the hair cells in the organ. To this end, the organ's polarity can be measured using the dipole moment of the orientation vectors,

mathematically

$$d = \langle \cos \theta \rangle$$

Where θ is the angle between each of the cells' polarity vectors and a director vector, in this context either the AP or DV axis. On the other hand, the alignment can be described using the nematic order parameter S , which measures the average orientation of the cells to the common director axis as

$$S = \left\langle \frac{3 \cos^2 \theta - 1}{2} \right\rangle$$

Using this definition, the angles will be zero for a perfectly aligned sample, and therefore $S = 1$. On the contrary, for an isotropic distribution, the nematic order parameter will be zero.

The organ's patterns are not only robust from a developmental point of view. Neuro-masts lie in the fish's skin and are therefore exposed to harm. Following an injury, they are capable of regenerating the organ even after extreme damage, such as ablating around 95% of the organ's cells [151]. After the regeneration process, the neuromast is not only composed of roughly the same number of cells as a noninjured organ, but its hair cells regain their nematic ordering as well as their polarity.

The process of Planar Cell Inversion is a good model system for studying collective migration because it is a minimal model, with only two cells performing the lion's share of the motion. In their movement, the rotating pair interacts locally with the surrounding cells of the tissue, but the movement of the neighbors is negligible as compared to the dyad. The cell pair appears from a Unipotent Cell Pair Progenitor (UHCP), which develops from a supporting cell. Lateral, a local mechanochemical symmetry-breaking event defines each cell pair's genotype (Figure 4.1C) [73, 47, 83]. During this event, one of the cells in the pair will activate Notch1a receptors, which leads to a loss of the Emx2 transcription factor. The chemical identity acquired by the cells in this process will determine their orientation to the organizing axis. Emx2 positive cells face the posterior and ventral region while Notch1a orient to the anterior and dorsal side for prim1 and prim2 derived neuromasts, respectively (Figure 4.1D). The acquisition of the chemical identity happens through a bistable switch, which makes it impossible to know which cell of the pair will have a particular identity before the symmetry has been broken [73]. Cells of the same orientation cluster on the side opposite to their orientation in the organ.

In Planar Cell Inversion, the hair cell pair rotates around its geometric center after the symmetry-breaking event, effectively inverting its position to the organizing axis. PCI occurs in approximately 60% percent of cases. I hypothesized that this process involves three distinct stages:

1. **Initiation of the movement:** This stage begins just after the hair cells appear from the UHCP, and it mainly involves the symmetry-breaking event. This stage ends when the rotation of the cells starts.
2. **Progression of the movement:** Here, the cells undergo the rotation *per se* and involve the stochastic noise and the deterministic drift towards the end position.

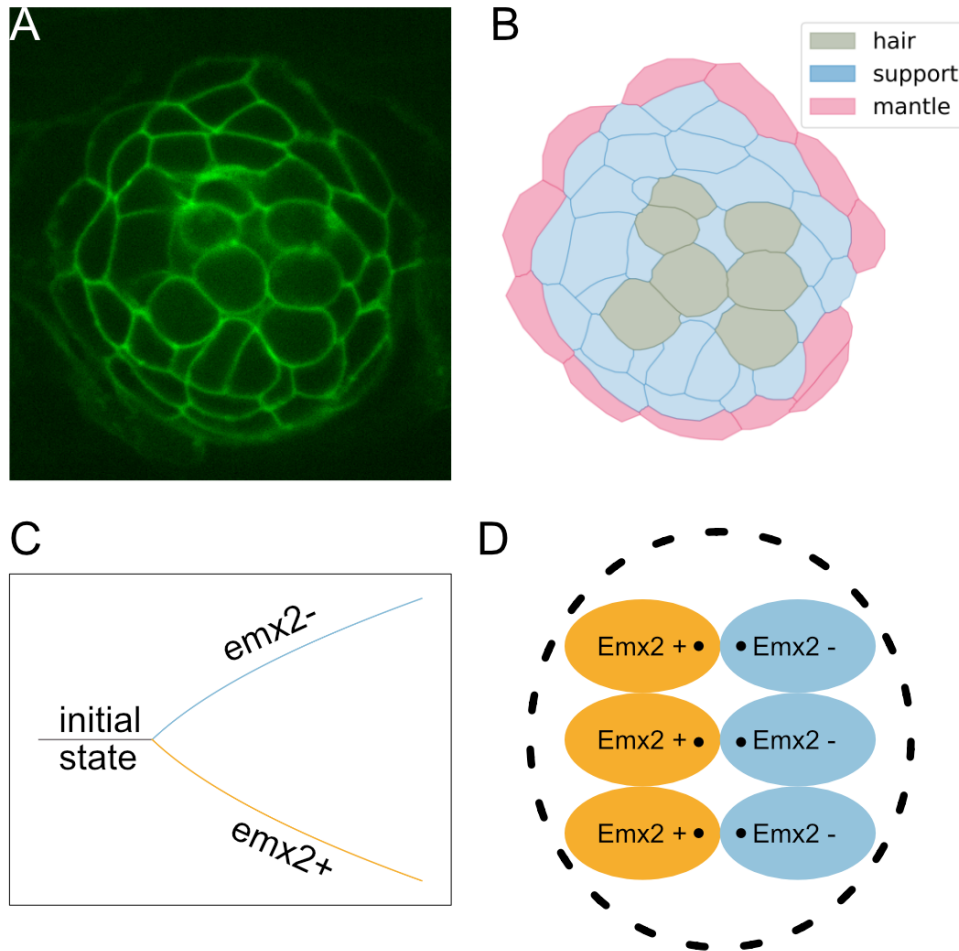


Abbildung 4.1: **The neuromast organ and the polarity of the hair cells.** (A) Neuromast microscopy with its membranes tagged using *claudnb:lyn-EGFP*. (B) Neuromasts comprise two types of supporting cells: sustentacular (in blue) and mantle cells (in red), and hair cells (in dark green) in the middle. (C) After hair cells are born from a Unipotent Hair Cell Progenitor, they undergo a symmetry-breaking event, which consists of a bistable switch and determines their identity to be either *emx2* positive or *emx2* negative. (D) Cellular identity defines the orientation of the hair in the hair cells, with *Emx2* positive cells pointing to the posterior side and the *Emx2* negative cells in the anterior direction. The color represents the identity, and the black dot represents the position of the hair.

3. **The stoppage of the movement:** After the cells have rotated once around their geometric center approximately 180° , the movement stops. This stage should involve the mechanism by which cells sense that their final position has been reached and their arrest of movement.

Interestingly, this process has been studied *in vitro* [19, 69, 25, 24]. Contrary to *in vivo* observations, cell rotation was found always to take place in this context, and the rotational movement does not stop. Other theoretical approaches have used a variety of models to study the process. Camley and colleagues [28] found vital ingredients for the rotation of a pair of cells in a patterned substrate using a Phase Field Model (PFM) [36, 81]. In their PFM, the authors added the dynamics of the nucleus of each cell as additional fields. They were able to show rotational dynamics for some parametrization of the cell-cell interactions. Using Particle dynamics, Leong managed to examine cell rotations in a two-cell system and study the direction of protrusions depending on the direction of rotation. He found that the cell cluster rotates with a characteristic S-shape, or its mirror image, depending on the direction of the movement [90]. Li and Sun used a physical model akin to a vertex model, with a chemical signal modeling the Rho-ROCK pathway, and found a similar correlation between the shape of the interface and the direction of the rotational motion [93]. We could not replicate this observation *in vivo* [82].

In this chapter, I will explore the process of Planar Cell Inversion and propose a framework to study this type of process. To better understand the controlling force behind the movement, I will investigate PCI for the wild-type fish and two knockout mutants: *emx2* and *notch1a*. As previously stated, these two have an antagonistic relationship in which *Notch1a* represses the activity of the *Emx2* transcription factor. Thus, I will explore how PCI occurs in wild-type fish and how these two knockouts affect its onset, progression, and stoppage.

4.2 *In vivo* Planar Cell Inversion

I aim to quantify the process of Planar Cell Inversion (PCI). As a first step, I need to define which observables I will require to represent the movement. In PCI, after a period of noisy movement, cells perform one rotation around their centroid and separate slowly after arriving at their final position. To visualize it, Figure 4.2A shows a representative example, seen from the center of mass of the pair¹. In this picture, the size of the dots in the scatter represents time. Here, both cells start on opposite sides of the x-axis and rotate clockwise once until they exchange positions. After the exchange, cells separate gradually, as shown by the bigger scatter dots. Taken together, this hints at a stochastic period before the inversion, where cells move randomly, followed by a directed migration to rotate and finalized by a slow drift away from their sibling.

¹I will use the center of mass when referring to the center of the cell dyad system, which would be equivalent as taking both cell masses to be equal. Then, the centroid will refer to the geometrical center of an individual cell.

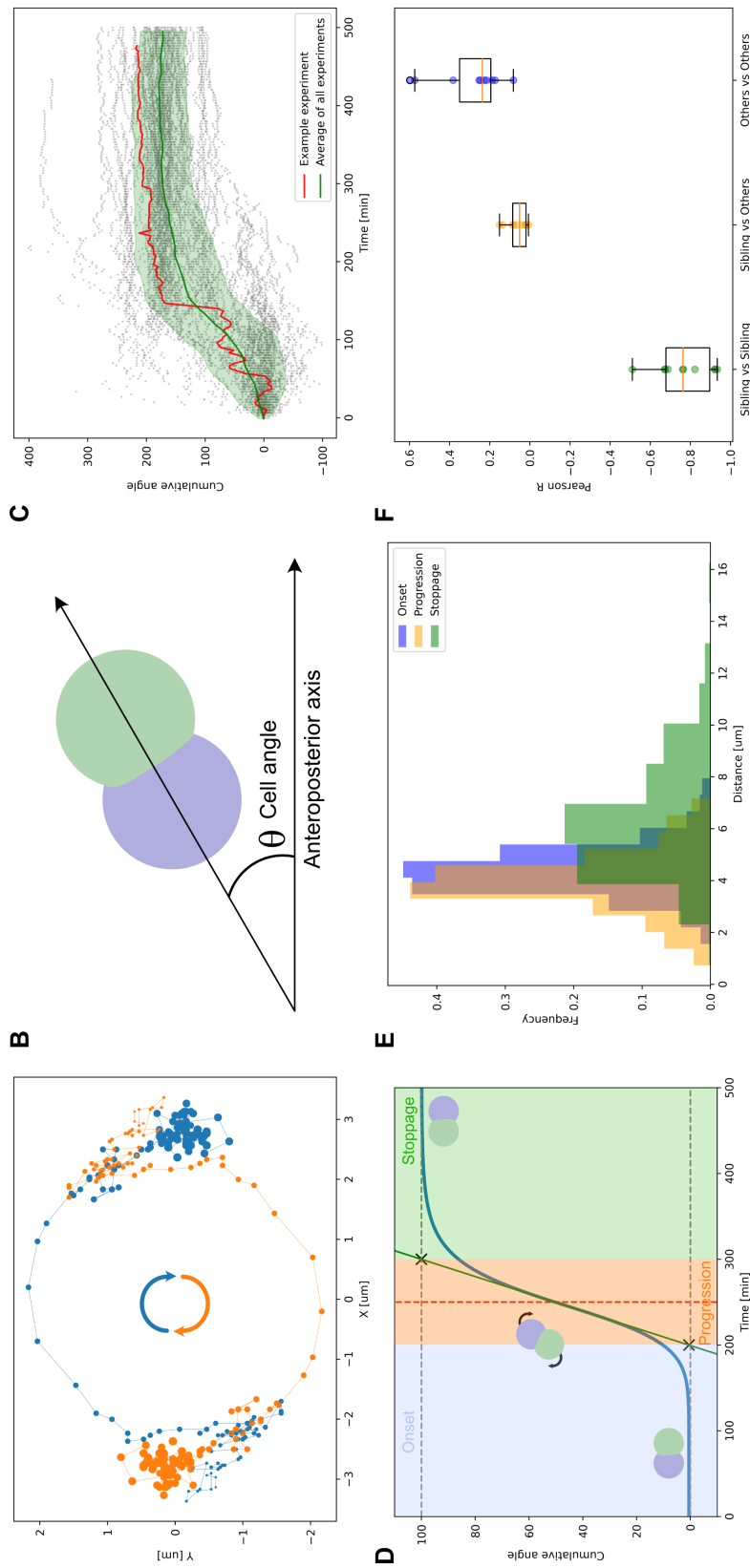


Abbildung 4.2: **Inversions as a three-phase rotational homotypic movement.** (A) Example of a pair of hair cells in a wild-type neuromast inverting in the center of mass reference frame. Smaller points represent earlier times. The arrows in the middle illustrate the direction of movement. (B) The angle of the cell pair is defined as the angle between the horizontal axis and a line that passes through the centroids of the sibling cells. (C) Trajectories for all the 70 experiments as gray dots. The red line and the shaded region are the mean and one standard deviation of all the trajectories. (D) All trajectories are depicted in cumulative angle, and after fitting a sigmoid function, three phases are identified. The two green and blue cells represent the movement's relative state. (E) Distance between the inverting pair during the three phases of the movement. (F) The Pearson correlation coefficient for the movement of cells ($N=10$).

Figure 4.2A showed that the movement seen from the center of mass of the cell dyad has circular symmetry. Therefore, I decided to quantify the rotational movement using the angle of the pair. This is defined as the angle between a line that passes through the centroids of the siblings and the horizontal axis (AP axis) (Figure 4.2B). With this definition, an angle of zero is aligned with the AP axis, and an angle of ninety degrees would represent a pair of hair cells perpendicular to the axis position. No distinction is made between which cells are most anterior or most posterior. Therefore, this definition makes the angles lie between 0 and 180°, being these two angles equivalent. This definition has the additional advantage of giving one quantity for the whole rotational movement of both cells.

Furthermore, I used the cumulative angle, defined as the sum of all angular changes over time, to quantify the pair’s movement. Positive angle changes represent anti-clockwise movement, and negative changes represent a clockwise cell rotation. I defined an inversion event as those pair movements with a cumulative angle of at least ninety degrees. Using this quantification, cell movements for the seventy inverting pairs display a sigmoid-like behavior with a fast angle change during the inversion (Figure 4.2C). Figure 4.2C shows all the trajectories in gray, with a highlighted representative one in red. The average of all trajectories is shown as a solid green inside the shaded region, representing one standard deviation. Not all PCIs last the same time for calculating the mean and standard deviation, so I binned the times in fifty bins, between 0 and 550 minutes. While individual trajectories are shown without binning, the mean and standard deviation in the cumulative angle in figure 4.2C are calculated by taking the mean over repeated values in the bin.

The shape of the trajectories in the cumulative angle space, as well as the biological observations, hint at a sigmoid-like process. Therefore, I used a four-parameter logistic function defined as

$$f(t) = c + \frac{d - c}{1 + (t/a)^b} \quad (4.1)$$

here, t is the time. The a , b , c , and d parameters are the function’s inflection point, steepness, and lower and higher asymptotes, respectively. The resulting curve is shown in Figure 4.2D. This generalization allows me to discuss the three parts of the process, represented in the figure by the stages of the rotations by the blue and green cells. To mathematically define the beginning and the end of the process, I use the intersection between a line going through the inflection point and the asymptotes, also shown as black crosses in Figure 4.2D.

The three parts of the process can be characterized in different ways, and each one presents unique features. For instance, sibling cells are closest together during the Progression phase of the inversion, measured as the distance between their centroids (Figure 4.2E, orange distribution). Therefore, as hair cells are surrounded by sustentacular cells, the homotypic hair cell-hair cell interfaces are maximized during the inversion. This also relates to an increase in the pair’s circularity as a whole. These phenomena are not seen in non-inverting pairs [82]. A physical toy-model explanation of this relates to the moment of inertia of the pair, as it would be minimum for a perfectly circular shape, as opposed to an oblong configuration. Even though the moment of inertia calculation is easy for a circle

and for an ellipse in two dimensions, I derived a continuous representation as a function of the bond length, which can be seen in Appendix B. Finally, in the last phase, siblings drift away from each other, as seen by the green distribution in Figure 4.2D.

Before analyzing the specific characteristics of the inversion process between the mutant genotypes, one last general characteristic of the PCI process involves the existence of confinement. First, I did not observe Hair Cells moving across the tissue, which points to PCI as a local rearrangement process. Then, I quantify the movement of the non-inverting and inverting cells in ten neuromasts by quantifying the movement of all their cells (Figure 4.2F). I calculated the Pearson correlation of the trajectories of all non-inverting cells in the organ against each other, against the inverting pair, and of the inverting pair to each other separately in each experiment. I found that the non-inverting cells are uncorrelated ($R=0.14$), suggesting no organized movement of the non-inverting cells in the organ as a group. I also found that sibling cells performing PCI are uncorrelated with the rest of the cells in the organ ($R=0.07$), which points to their movement being independent of their neighbors. Finally, I also saw that the inverting pair of cells has a strongly anti-correlated movement ($R=-0.77$), consistent with their circular movement to exchange positions.

I have shown that PCI is a three-part process. In this play, the sibling cells exchange their positions by rotating around their center of mass once while the rest of the epithelium surrounds their movement. I also showed that the siblings are closest to each other during the rotation (in the Progression phase) and will drift apart once it stops. Next, I will analyze the differences that appear when studying the Notch1a and Emx2 loss of function mutants in this system before venturing into a modeling approach.

4.3 Phenotypic differences in the PCI process

This section will focus on perturbations of the Planar Cell Polarity pathway through *emx2* and *notch1a* knockouts. By analyzing their behavior with respect to wildtype fish, I found that not only is the final pattern at which the neuromasts arrive different in each case, but there are also differences in the PCI process itself. Understanding these differences may help understand the process as a whole.

4.3.1 Mutants delayed the initiation of their inversion

As I stated at the beginning of the chapter, during the development of the neuromasts, the hair cells acquire a definite polarity, which is dependent on the chemical identity of the cell. Due to the bistable switch mechanism [73], after the symmetry-breaking event, the cells' identity is fixed. In the wild type, *Emx2* positive cells are located on the anterior side preferentially, with their hairs in the opposite direction. In contrast, *Emx2* negative cells are positioned on the posterior side facing opposite to them. Mutant lines with an *Emx2* knockout point all cells caudally, while *Notch1a* knockouts acquire an inverse pattern, with all cells oriented rostrally (Figure 4.3A).

To compare the timing of the genotypes in each phase, I analyzed the distributions for

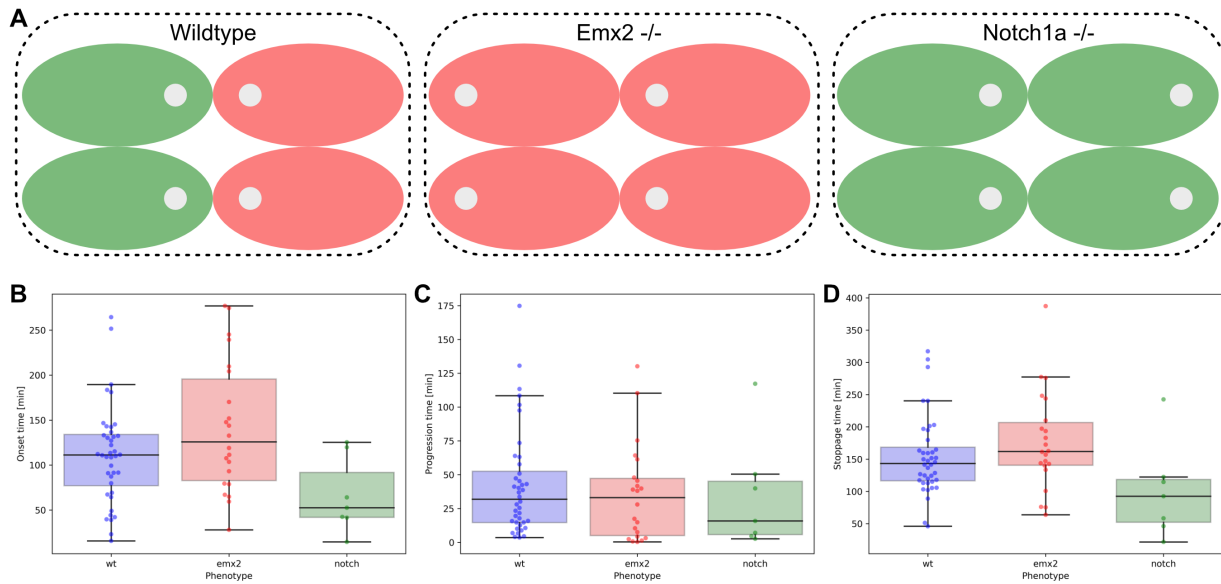


Abbildung 4.3: **Mutants and wild type present differences in the phases and final pattern (A)** Scheme of the final pattern achieved by the hair cells after neuromast development. The axis is Antero-Posterior from left to right. Green cells represent *emx2* negative cells, and red cells *emx2* positive. The gray circle shows the position of the hair bundle. **(B, C, D)**, Boxplots showing the time spent by the process in each of the three phases (Onset, progression, and stoppage, respectively) for the wild type and each mutant. Dots represent individual experiments (N=40, N=23 and N=9 for wild type, *Emx2* *-/-* and *Notch1a* *-/-* respectively).

the 69 experiments. I used the Mann-Whitney U test with a two-sided alternative hypothesis when testing if two distributions are similar and the lesser (or greater) alternative hypothesis when testing for stochastic ordering, using the SciPy implementation of the test [153]. During PCI, hair cells in wild-type fish and in the *Emx2* mutants take longer to start inverting than in the *notch1a* *-/-* mutant ($p = 0.02$ and $p = 0.005$, respectively), while *Emx2* *-/-* mutants take about the same time (Figure 4.3B). I found no differences between the three conditions in the duration of the inversion (Figure 4.3C). However, *Notch1a* mutants reach their final positions faster than wild-type and *Emx2* mutant ($p = 0.01$ and $p = 0.005$, respectively; Figure 4.3D).

Even though I found no statistical difference between the wild-type fish and the *Emx2* mutant in any of the phases, qualitatively, the mutant appears to delay the start of their inversion and its ending. This suggests that *notch1a* and *Emx2* mutants affect the initiation of the process but not its progression. As the effect on the stoppage time is convoluted with the delay in the initiation of the process it is not possible to address whether the mutation affects on the termination time as well.

4.3.2 The final angle of the hair cell pair depends on the mutation

After the division of the Unipotent Hair Cell Progenitor, the sibling cells emerge with an angle approximately aligned with the AP axis, which is valid for the three conditions explored. As the switch that determines the chemical identity of the cells for the remainder of their life occurs sometime after the division, it could be expected that it is not affected by any of the knockouts. I confirm this hypothesis by performing a Mann-Whitney test, which showed no statistical differences between the initial angle distributions (Figure 4.4A).

However, after the progression of the PCI process, cells acquire a new final angle after they stop rotating, which is distinctive for each genotype. I found that the wildtype's final angles are statistically different from the *emx2* and *notch1a* knockouts ($p=0.004$ and $p=0.01$, respectively; Figure 4.4B). I found that the final angles achieved by the wildtype are $18^\circ \pm 15^\circ$, for *emx2* are $28^\circ \pm 21^\circ$ and for *notch1a* $30^\circ \pm 19^\circ$ (in all cases expressed as mean \pm std). However, the angles are not normally distributed. I reasoned that due to the angles being represented only in the first quadrant, they would accumulate at an angle of zero. Therefore, I fitted a Gamma distribution to the angles in each case, which density function is defined as

$$f(x, \alpha; \delta, \beta) = \frac{\beta^\alpha (x - \delta)^{\alpha-1} e^{-\beta(x-\delta)}}{\Gamma(\alpha)}$$

where δ represents the offset, β the scale and α the shape factor. All three conditions have similar scales ($\beta \approx 0.3$) and offsets ($\delta \approx 0$). However, they have different shape parameters. In the wildtype case, the shape parameter is almost equal to one, $\alpha_{wt} = 0.98$. On the contrary, both mutants have a shape parameter of almost two, which represents the more skewed distribution of values ($\alpha_{emx2} = 1.65$ and $\alpha_{notch} = 1.99$). Importantly, a shape of one reduces the Gamma distributions to an exponential ($f(x; \alpha) = \alpha e^{-\alpha x} \Theta(x)$, with Θ the Heaviside function).

Together, these results indicate noticeable differences between the final angles of the wild type and the mutants. As the initial conditions are similar in every case, I suppose that differences in final angles are acquired during the progression. The progression dynamics might be involved, as well as the start and stop “signals” that initiate and terminate this phase.

4.3.3 *Emx2* and *Notch1a* mutants affect the progression of the cell rotation

I first concentrated on the progression of the inversion. During Planar Cell Inversion, each cell in the dyad moves non-monotonically in a stochastic walk to exchange positions. I call the swings in the direction of the movement ‘wobbling.’ To measure wobbling, I calculated the noise as the arc length of the curve defined by the movement. I normalized it to the

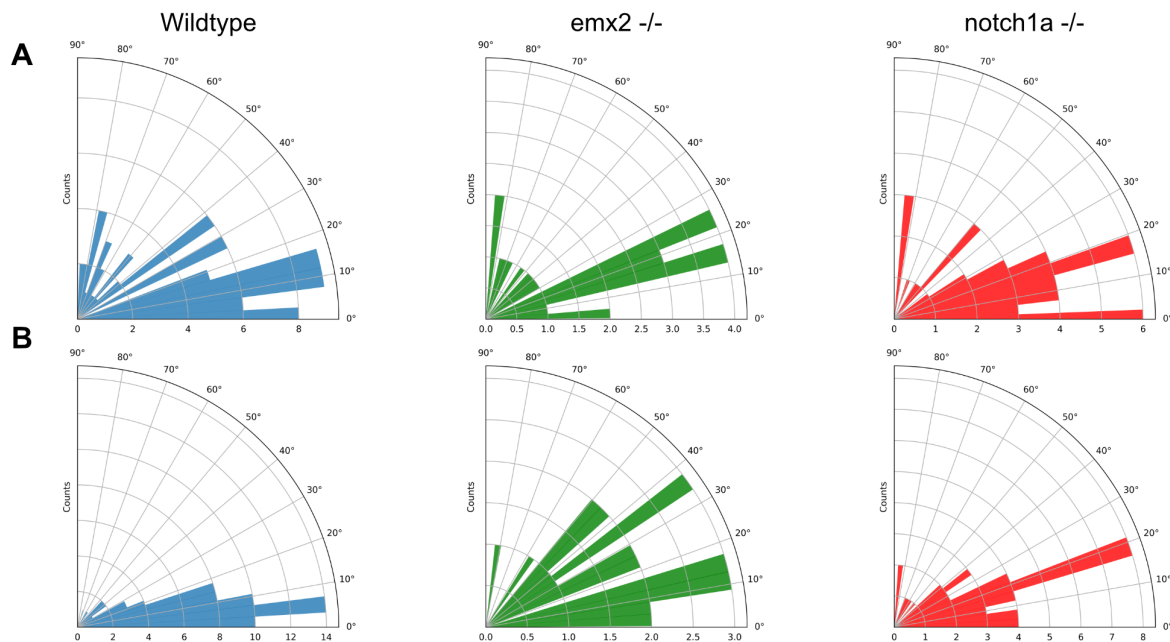


Abbildung 4.4: **Initial and final distribution of angles (A)** Initial distribution of angles for the wild type, *emx2*^{-/-} and *notch1a*^{-/-}. **(B)** Distribution of final angles for the three presented conditions. The distributions are significantly different between the wild type and the other two, with $p=0.004$ for wild type and *emx2* knockout and $p=0.01$ between wild type and *notch1a* knockout. Each of the distributions in both panels have $N_{wt} = 71$, $N_{emx2^{-/-}} = 42$ and $N_{notch1a^{-/-}} = 22$.

shortest distance between the initial and final positions. Symbolically,

$$W_j = \frac{\sum_{t=0}^{N-1} |r_j(t+1) - r_j(t)|}{|r_j(N) - r_j(0)|} \quad (4.2)$$

where r_j is the position of cell j at time t , and the sum is taken for all the times except the last one. This definition has the advantage of being non-dimensional and allows for a direct comparison between experiments with different durations.

I found significant differences in wobbling among the three genotypes (Figure 4.5A). Due to the many outliers present in the distribution, the p-values reported in the figure correspond to the Anderson-Darling test. As expected, the noise in the wild type is the lowest of the three: $p = 0.022$ for wt vs. *emx2*^{-/-}, $p < 0.0001$ for wt vs. *notch1a*^{-/-}. Surprisingly, the Notch1a knockout also has significantly higher noise than the other mutant ($p < 0.0001$, *emx2*^{-/-} vs *notch1a*^{-/-}). Again, I used the Mann-Whitney U test for stochastic ordering.

Next, I investigated whether the proportion of PCIs happening is the same for each genotype. In a purely random initiation, I would expect a fifty percent chance. I found a similar value in the wild type and *emx2* cases (56 % and 55 %, respectively). Even though

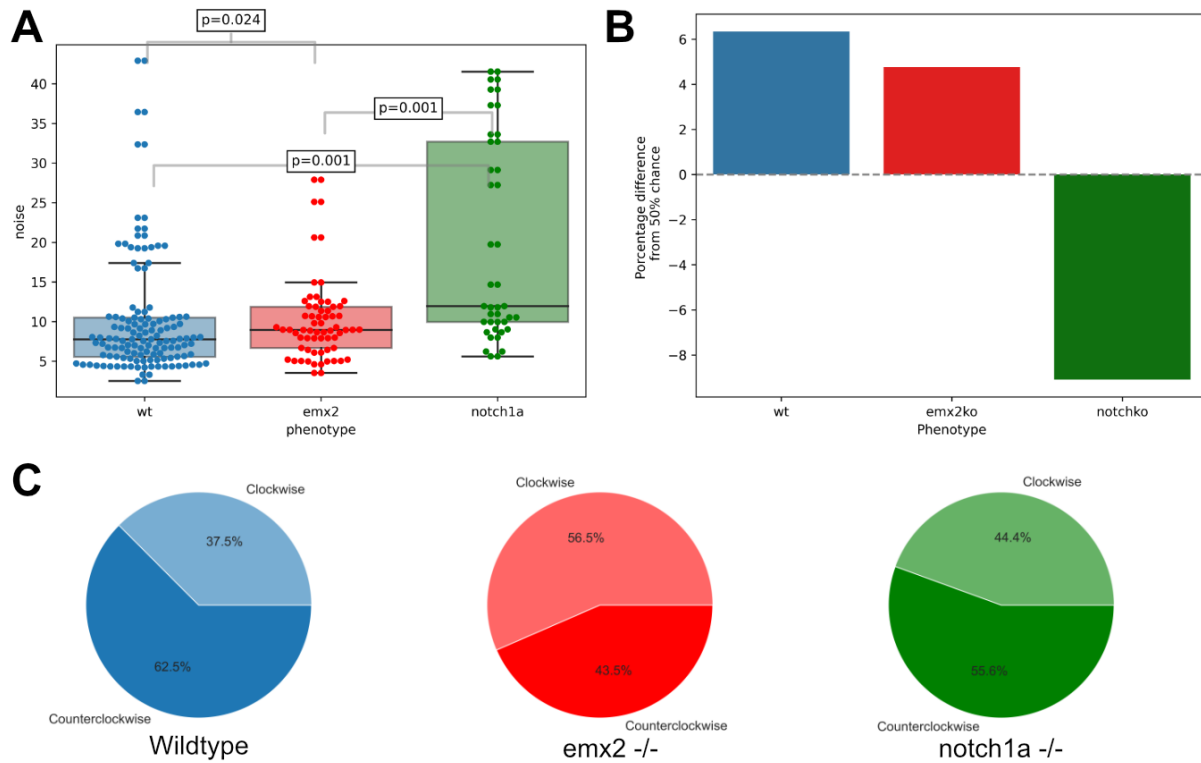


Abbildung 4.5: **Mutations affect cell rotation differently.** (A) Boxplot of the noise during the planar cell inversion in the wild types and mutants, the p-values come from an Anderson-Darling test comparing distributions. (B) Inversion frequency shown as a difference to an equal probability situation, i.e., 50% chance. (C) Handedness of the rotational movement for the three experimental conditions.

inversion happens with a similar frequency between wild types and emx2 mutants, notch1a mutant inversions are less likely to occur (41%) (Figure 4.5B).

Finally, I investigated the handedness of the inversion. I found qualitative differences between the genotypes in the direction of the movement, but they are not significantly different (Figure 4.5C). The handedness of the inversion will be determined by the shortest distance to perform the process. A cell pair that starts with an angle of 20° will probably rotate 180° counterclockwise to 200° instead of 220° clockwise to the same position. Therefore, the process's handedness will depend more on the cell pair's initial angle than on the pair's genotypic identity.

4.4 Computational model

Guided by the previous result, I developed a minimal model to shed light on the characteristic behaviors that the different genotypes exhibit. As the central part of the cell dyad's rotational motion pertains to the process's progression phase, I built the model around

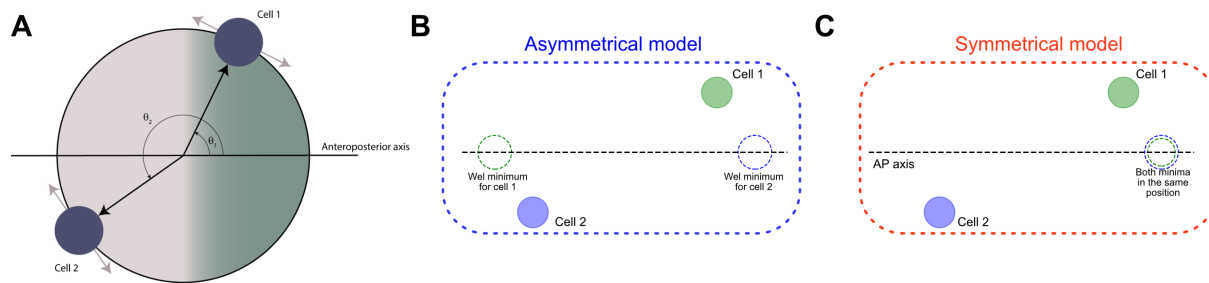


Abbildung 4.6: **Computational modeling of the Planar Cell Inversion.** (A) Sketch of the model. Solid blue balls represent each of the cells, and the arrows are the possible clockwise or anticlockwise movement around the horizontal axis. Each of the cells' positions is tracked through their angle with respect to that axis. The gradient coloring represents the possible asymmetry between the anterior and posterior regions. (B) In the asymmetrical model, both cells, shown as a green and a blue ball, have an attractive well on opposite sides of the AP axis, represented by a dashed ball of corresponding colors. (C) In the symmetrical model, each attractive well is on the same side of the axis.

that phase. Moreover, as described in the previous sections, it is in this phase that the genotypical differences become apparent.

I postulated a one-dimensional problem in which two interacting agents can move freely. This dimension represents the angle the cells' position vector makes with the horizontal axis, which in this problem represents the Anterior-Posterior axis. If the radius at which the two agents lie is fixed, this problem can be described as rotating two agents around a common center (Figure 4.6A). At each discrete time, cells can move a fixed amount either anticlockwise (+1) or clockwise (-1). The reasoning for using a one-dimensional representation of space was based on the assumption that the inversion is a process mainly driven by the two sibling cells. This logic follows from the results presented in Figure 4.2F, where the sibling cells are strongly anti-correlated. At the same time, the movement of the inverting pair versus the movement of the rest of the organ is uncorrelated. Effectively, this corresponds to the PCI of the sibling hair cells on a small circular portion of the organ, delimited by the surrounding cells. I introduced a Hamiltonian energy function to accommodate this and all considerations and explored two different modeling possibilities.

In section 4.3.2, I showed that even though the initial angles do not differ with respect to the mutations, the final angles achieved by the pair do. Therefore, I added potential wells into the model that attract the agents to represent these preferential positions. I decided to use a Gaussian well representation of the potential as

$$\Omega(\theta_j) = -e^{-\frac{(\theta_j - \mu_j)^2}{2\sigma_j^2}} \quad (4.3)$$

where θ_j is the position, μ_j is the well's minimum and σ_j is the potential's standard deviation for cell j . The well's minima can be located at any position in the one-dimensional space and will be the crucial difference between the models presented in the following

section. The standard deviation of the well, σ , represents its steepness and reach. A very steep potential in Gaussian wells will favor a rapid evolution but might not be sensed if far enough apart from the agent. In the system, I fixed this at a value of approximately 288° , which ensures that the agents feel the wells at any position in space.

Cells cannot occupy the same position, so a repulsion must be introduced. To do this, two typical methods involve either hard-sphere or soft-sphere repulsion. In the hard-sphere formalism, cells are not allowed to interpenetrate each other. On the other hand, the soft-spheres formalism provides some degree of elasticity, controlled by the parametrization. I used the well-known Lennard-Jones potential and retained its repulsive part. Therefore, the spheres will have a repulsion given by

$$\phi(\theta_2 - \theta_1) = \begin{cases} \left(\frac{d}{\theta_2 - \theta_1}\right)^{12} & |\theta_2 - \theta_1| \leq d, \\ 0 & \text{otherwise} \end{cases} \quad (4.4)$$

where d is maximum distance of the interaction, and the θ_j the positions of each cell. Equation 4.4 can be transformed into a hard-sphere potential by making the energy in the case that $|\theta_2 - \theta_1| \leq d$ arbitrarily large.

I compiled these interactions, equations 4.3 and 4.4, in an energy function that only depends on the angular position of the cells, θ_1 and θ_2 , as

$$H(\theta_1, \theta_2) = \rho\phi(\theta_2 - \theta_1) + \omega_1\Omega(\theta_1) + \omega_2\Omega(\theta_2) \quad (4.5)$$

where ρ , ω_1 , and ω_2 control the strength of the repulsion and the depth of the wells, respectively. This expression allows the exploration of many modeling possibilities to try to establish which could be the mechanisms behind the dynamics I see experimentally. In particular, this definition of the model has only one free parameter in the repulsion potential once the exponent of the interaction is set, two parameters per Gaussian well, and three parameters in the energy function, or Hamiltonian. Therefore, there are eight free parameters. From the experiments, I decided that the cells must always be in contact, and thus, the d parameter in equation 4.4 is fixed at 180° . I do not expect differences in the repulsion between different models, as it should be a characteristic of the mechanical exclusion of the cells' membranes. Hence, I fixed the repulsion value at $\rho = 0.01$ in all simulations. Moreover, the width of the wells is also chosen so that their effect can be sensed by the cells long-range, at approximately 288° in equation 4.3. Consequently, four free parameters remain in the model, controlling the potential wells' positions (2) and depth (2). I will build two possible scenarios around these parameters to explore.

4.4.1 The symmetrical and asymmetrical models

I created two simple characteristic models with different positions of the Gaussian wells and tested their behavior by varying the depth of said wells, that is, their intensity. In the asymmetrical model, I set the position of the potential well sensed by each cell on opposite sides of the AP axis. The cell's minimum position will be opposite to the side at which it

starts. For example, if a cell begins in the anterior position, its minimum will be located in the posterior region and vice versa. Due to the fact that cells' minima are on opposite sides of the AP axis, I call this model *asymmetrical*. Additionally, I defined a model where the two wells' minima coincide, which I call *symmetrical model*.

The asymmetrical model allows cooperation between the inverting pair of cells as they move. In contrast, the symmetrical model leads to competition for the same position. This last model achieves the final position through a trade-off between the cell-cell exclusion and the well's depth. Notably, both models would coincide if one of the Gaussian wells has zero depth. This last case represents the possibility that only one of the cells is actively moving while the other follows due to the confined nature of the inversion. This possibility is especially relevant as I have shown before that PCI can occur even when an *emx2* symmetry-breaking event has not happened, such as in the case of both knockouts.

4.4.2 The Metropolis-Hastings algorithm

I created Python software to implement the model using a Monte Carlo approach to minimize the energy defined in equation 4.5. As the system's properties will be linked through the Hamiltonian's definition, I expect them to be close together in the system's phase space. Therefore, I decided to use a Metropolis algorithm implementation [101, 61]. In this algorithm, space sampling gives a higher chance of acceptance to more likely states. Detailed balance ensures that the probability distribution only depends on the initial and final energy and requires that all processes are in equilibrium with their inverse at equilibrium,

$$\sum_j^M p_j P(j \rightarrow k) = \sum_k^M p_k P(k \rightarrow j)$$

where $P(l \rightarrow m)$ is the probability of going from an initial state x_l to x_m , and p_l is the probability distribution. This equation can be rearranged by joining probabilities distributions on one side and transition probabilities on the other. Moreover, the probability distributions can be separated into a selection probability and an acceptance probability as

$$\frac{P(j \rightarrow k)}{P(k \rightarrow j)} = \frac{g(j \rightarrow k) A(j \rightarrow k)}{g(k \rightarrow j) A(k \rightarrow j)} \quad (4.6)$$

where g is the selection probability and A is the acceptance probability.

In the Metropolis-Hastings algorithm, the probability of each state is chosen as a Boltzmann distribution ($P(x_j) = \frac{1}{Z} e^{-\frac{H(x_j)}{k_B T}}$), leaving the selection probability as uniform ($g(j \rightarrow k) = 1/M$). Finally, the acceptance probability, defined in equation 4.6, is

$$A(j \rightarrow k) = \begin{cases} e^{-\beta(E_k - E_j)} & E_k > E_j \\ 1 & E_k \leq E_j \end{cases} \quad (4.7)$$

where E_* is the energy of state *. Choosing states in this way guarantees that the distribution in the macroscopic limit approaches the equilibrium distribution.

4.4.3 Model implementation

To create the two models' agents, I used the experimental initial angle distributions of individual cells to randomly allocate the initial positions of one of the cells, creating the second one at exactly 180° apart. The angular position of the first cell is taken from a normal distribution centered at 180° and with a standard deviation of 50° ($\mu \pm \sigma = 180^\circ \pm 50^\circ$). Furthermore, I incorporate the symmetry-breaking event into the simulation by starting with all wells' depths set to zero ($\omega_1 = \omega_2 = 0$), leaving only the repulsion interaction between the cells. After a certain number of steps, defined in a *breaking_time* parameter, the depths of the wells are assigned according to the simulation parameters.

The algorithm follows by letting each cell randomly choose to move one spatial step clockwise or anti-clockwise at each time with uniform probability. The spatial step is set at $\Delta x = 0.25^\circ$. Once a direction is chosen, the cell's position is changed virtually, and the corresponding energy of the new state is calculated. This process is repeated for both cells, and the energy of the two new states is compared to that of the unchanged initial positions. Finally, the system is updated according to equation 4.7. In pseudo-code,

```

1  c1 = Cell(position=random.normal(180, 50))
2  c2 = Cell(position=180-c1.position)
3  cells = [c1, c2]
4  for t in range(0, nsteps):
5      if t > breaking_time:
6          c1.break_symmetry()
7          c2.break_symmetry()
8
9      e0 = get_systems_energy()
10     virtual_velocity = random.choice([1, -1], 2)
11     update = [False, False]
12     for index in range(2):
13         cells[index].virtual_update(virtual_velocity[index])
14         cells[index - 1].restore_to_real()
15         e1 = get_systems_virtual_energy()
16         if check_metropolis(e0, e1, Temperature):
17             update[index] = True
18

```

The Metropolis-Hastings check function is implemented as

```

1  def check_metropolis(e0, e1, temperature):
2      if e1 < e0:
3          return True
4      else:
5          if temperature != 0:

```

```
6         if random.uniform(0, 1) < exp(-temperature * (e1 - e0)):  
7             return True  
8         else:  
9             return False  
10     else:  
11         return False
```

4.4.4 Models results comparison against *in vivo* rotations

As I intend to test the model's hypothesis against the experimental conditions, I first compiled two representative cumulative angle trajectories for a wild type and a notch1a mutant (Figure 4.7A and B, respectively). I only compared the notch1a mutant as they present with more significant differences concerning the wild type than the emx2 mutant. These trajectories will be compared to the ones generated for the *in silico* conditions of the asymmetrical and symmetrical wells introduced in previous sections.

I simulated the model for the asymmetrical and symmetrical parameterizations and qualitatively compared their trajectories to the described experimental curves. In the simulations I show, the asymmetrical model was constructed as a one-well system with a depth of 50 (Figure 4.7C). The symmetrical model consisted of two wells on the posterior side of the axis, with a relative depth of 0.4 (ω_1/ω_2 , meaning depths of 20 and 50 for each cell (Figure 4.7D). I found that the asymmetrical model's trajectories resemble the wild-type experimental ones, while the symmetrical model corresponds to the mutant's result. This resemblance is especially noticeable when looking at the total rotation performed by the cell pair, with the cells in the symmetrical model rotating less than the ones in the asymmetrical. Moreover, cells in the symmetrical model have higher wobbling than those in the asymmetrical model.

The final angle reached by the inverting pair is expected to be crucial for the physiology of the neuromast. I then investigated how the relative depth of the wells impacted the angle at which the inverting agents concluded their process. As presented in the section 4.3.2, the genotypic identity of the system influences the final angles achieved. Similarly, I found that the two model variants have different behaviors, which in turn depend on the relative depth of the wells (Figure 4.7E). I observed that the asymmetrical model is robust with respect to changes in the relative depth with almost no variation, while the symmetrical model has a deviation from the AP axis of 60° for a relative depth of 0.5 ($\omega_1 = 50$; $\omega_2 = 25$).

Furthermore, I found that the wells' relative depth affects the movement's noise, as defined in equation 4.2. Again, the asymmetrical model is robust to the changes in the relative depth, while the symmetrical model's wobbling increases when $\omega_1 \rightarrow \omega_2$. This result points in the direction that the symmetrical model behaves similarly to the mutant genotypes due to the increased noise in the dynamics, as shown in section 4.3.3.

Finally, I explore the final angle distributions by choosing two well parameterizations consistent with the observed final angles. As the asymmetrical model is robust to changes

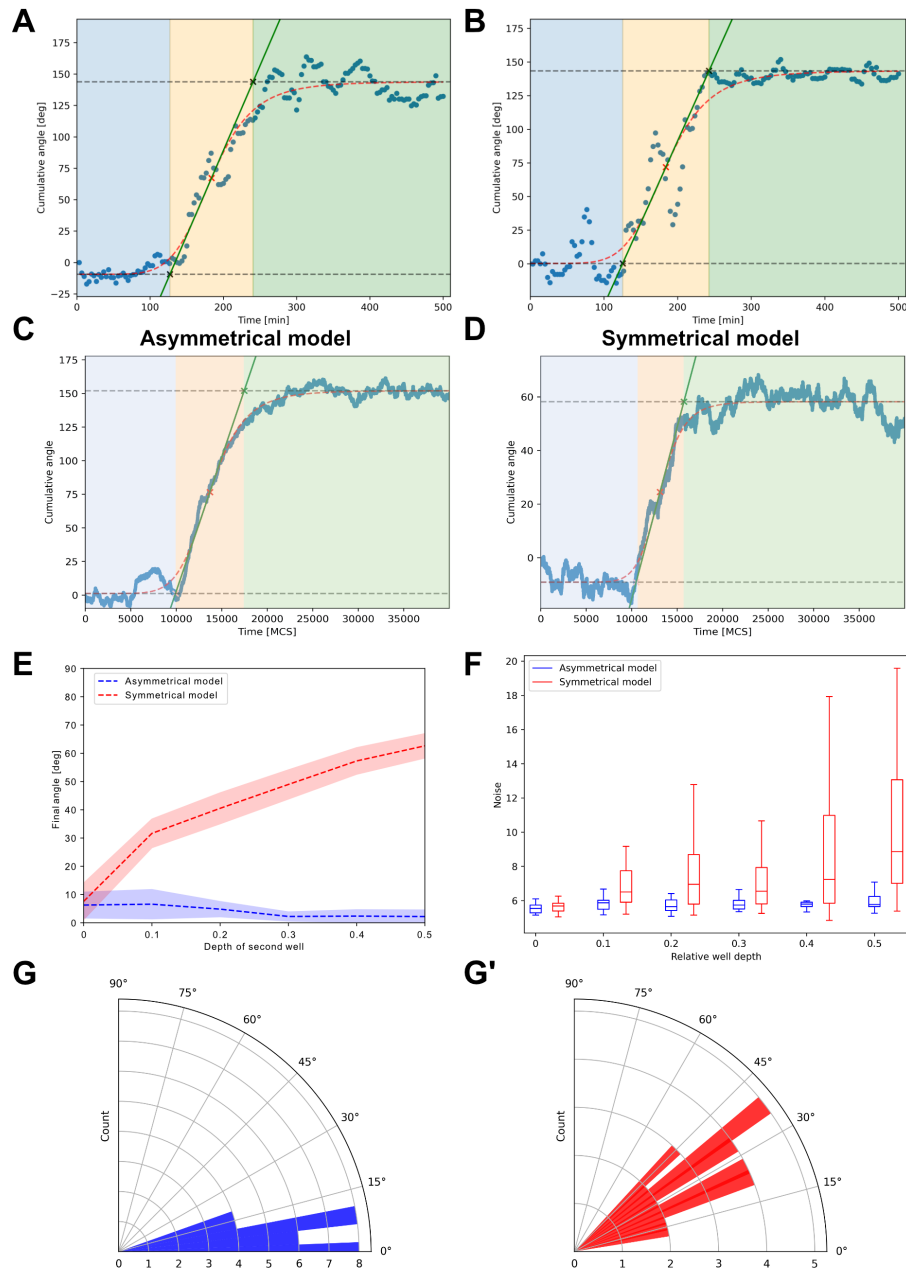


Abbildung 4.7: **Computational model relationship with the phenotypes.** (A, B) Representative cumulative angle trajectory of the inverting pair for a wild type and a *notch1a* knockout. The colored regions represent the three phases of the process: onset (blue), progression (orange), and stoppage (green). (C, D) Similarly, the asymmetrical and symmetrical models are represented in the same configuration for a depth of 50 and 0 (C) and a depth of 50 and 20 (D). (E) Final angle achieved by the inverting pair as a function of the relative depth of the wells for the symmetrical (red) and asymmetrical (blue) model. The dashed line represents the mean value, and the shadowed area is one standard deviation. (F) Noise predicted by both models as a function of the relative well depth. (G, G') final angles achieved by the asymmetrical (well depth of 50 and 0, panel G) and symmetrical (well depth of 50 and 20, panel G') models.

in the depth, I decided on the case where only one of the wells is active ($\omega_1 = 50$ and $\omega_2 = 0$), and for the symmetrical model, I chose a relative depth of $\frac{\omega_1}{\omega_2} = 0.4$ ($\omega_1 = 50$ and $\omega_2 = 20$) (Figure 4.7G and G').

The asymmetrical model is more robust to changes in the relative depth of the wells and presents less noise than its symmetrical counterpart. Moreover, cells reliably align more closely with the AP axis in the symmetrical model than in the asymmetrical model. Thus, I argue that the asymmetrical model better represents the wild-type situation, while the symmetrical one can help study the mutant's behavior.

Kapitel 5

Discussion

The aim of the present work is to understand how different agents interact to generate functional patterns in biological tissues. Throughout this thesis, I have used a dual strategy. First, I focused on the local interactions between the cells and how this cooperation can achieve the final pattern. Afterward, I characterized the Planar Cell Inversion process through careful quantitative measurements. Using this information, I proposed a phenomenological PCI model that can reproduce wild-type observations and mutant pairs qualitatively.

5.1 Inferring mechanical states through time

Different mechanical properties can be measured *in vivo*, or at least estimated. In this thesis, I have proposed a new method to infer the Mechanical State, as given by the collection of intercellular stress and intracellular pressures in a 2D tissue monolayer. In particular, I have offered a formalism that allows the dynamic information in the movement of the tricellular junctions to be incorporated into the Geometrical Stress Inference framework, allowing it to become dynamic.

We discussed at the beginning of section 2 the main ingredients that should be present in an inference model. This thesis mainly focuses on the third one mentioned: the scale relationship dilemma that arises when incorporating time to the pipeline. Usually, stress inference is performed by solving a homogeneous system of equations. Moreover, the results given by mechanical inference are values relative to an unknown scale. Together, these two statements reveal that the scale itself can be neglected. Nevertheless, when dynamic elements are incorporated, that is, some aspect of the time evolution of the system, the particular measurement scale used for space and time needs to harmonize. Currently, seven Stress Inference algorithms exist, of which only two have a temporal component: VFM [22] and ForSys [15].

By examining the form of the force at each tricellular junction and the viscoelastic approximation used for the system's dynamical behavior, I found a new number through the nondimensionalization of the system, which I conspicuously called $1/Wi$. This number

represents the relation between the viscous ($\eta\bar{v}$) and the elastic ($\bar{\lambda}$) scales of the system. There, the $\bar{\ast}$ quantities denote a representative quantity of the experimental system, such as the velocity or stress.

By fitting *in silico* known data, I found that this parameter had a value of approximately 0.1, meaning that in the *in silico* model I used, the elastic scales are an order of magnitude more significant than the viscous one, which is compatible with the expected result. Importantly, I showed that the accuracy of the inferences depends on selecting the correct parameter. Interestingly, when calculating the value it should have, from the mean of the system's tensions and the mean of the system's velocities, I found that in all examples, the observed value was bigger than the theoretical one. I then fitted the free viscosity constant η to find an optimal value $\eta \approx 2.5$ for the *in silico* simulations.

A related quantity for which no new equation was presented is the pressure. I have based the pressure estimation on the Young-Laplace equation, which is derived under equilibrium conditions. Establishing a new pressure equation, considering the dynamical aspects, is an open problem.

Therefore, I showed how time can be effectively incorporated into estimating the mechanical state of a 2D monolayer of cells. I also showed that tuning the space and time scales is critical to finding biologically relevant values effectively.

5.2 ForSys: A software to infer dynamic states

After creating a theoretical framework that allows time to come into play in stress inference models, I turned to developing a software tool. The goal was to create an easy-to-use and approachable software tool that the community could use readily. Given these requirements, I used Python, a programming language widely used in the scientific community, and I made the software Open Source through GitHub [14]. This is especially relevant, as from the seven software that exist for stress inference, only three are available to the public and are Open Source (Bayesian, DLITE, and ForSys), of which ForSys is the only one with dynamic capabilities. The package conserves the possibility of creating static inferences. Still, when presented with a time series of images, the user can let the software include the dynamic information in the inference pipeline.

We found that ForSys performs very well in *in silico* models created through Surface Evolver, even when compared in its static modality with other established methods. I also showed that in its dynamic setting, ForSys consistently outperforms static implementations. I validated static ForSys in the mucociliary epithelium of *Xenopus* embryos *in vivo* and found a good correlation between the myosin fluorescence, used as a proxy for junctional stress, and ForSys inference. It is important to point out that current stress inference methods that have used tagged myosin intensity for validation have found correlations in the same range as I, as I discussed in the corresponding section.

Significantly, to effectively generate *in silico* datasets to validate the tool, I created another Open Source software: seapipy. This software uses the well-established Surface Evolver to generate the ground truths using Python without needing to write Surface

Evolver commands. I believe this tool will significantly help catalyze the efforts to develop better methods, as it provides an easy way to generate trustworthy ground truths based on the vertex model implemented in Surface Evolver. A clear next step is to adapt seapipy ground truth generation method to allow 3D systems to be created and evolved. This would allow a systematic validation method for 3D inference techniques.

Finally, I used the ForSys software to study the biological questions that drove this work, primordium's migration through the Zebrafish lateral line, and the Planar Cell Inversion Process. For the first time, I found that proto-neuromast formation could be predicted in the basal plane by looking at the pressure gradient inferred by the tool. Epithelial rosettes form in the center of the proto-neuromast before deposition, and ForSys predicted its localization with a correlation of $R = 0.99$.

I estimated the mechanical state of cells during the Planar Cell Inversion process in the neuromasts of the developing Zebrafish. This was approached using a two-fold strategy. I first looked into the stresses of the cell-cell interfaces grouped by cell type. I found that the homotypic hair cell-hair cell interface had the highest stress in the tissue. This is consistent with the view that hair cells maintain a strong bond, localizing in the center of the circular organ. Then, I showed that the homotypic interfaces between rotating sibling hairs have a lower tension than the rotating cells with the surrounding neighbors. Importantly, due to the inverse relation between cell adhesion and cell stress, it can be interpreted that PCI occurs through a strong adhesion of sibling hair cells and a weaker adhesion to the surrounding cells.

We investigated the cell-cell mechanical interactions in the migrating primordium and the fish's neuromasts with ForSys. This gave new insights into the rosetogenesis leading up to neuromast deposition and the asymmetries present in the neuromast. These asymmetries could be involved in the PCI process, allowing sibling hairs to increase their common interface and minimize contact with their neighbors, thus enabling rotational movement.

5.3 Finding the East: Polarity Cell Inversion

In the last part of this thesis, I concentrated on analyzing the rotational movement of the hair cell pair after the unipotent hair cell progenitor's (UHCP) division. I showed that a sigmoid-like function can be used to characterize their movement and provides a valuable guide to splitting its process into three separated phases: Onset, progression, and stoppage. Thus allowing a systematic approach to classifying each part of the movement.

We analyzed PCI and found observable differences between the three genotypes studied. Notably, the *emx2* knockout mutants present a delayed initiation and termination of the PCI process without changes to the progression. Interestingly, this difference is not visible in the *notch1a* mutants, hinting that the delays might not be only due to the system's loss of a symmetry-breaking event. I also showed differences in the final angle achieved under all conditions without noticeable distinctions in the starting point. Moreover, neuromasts belonging to mutant fish presented higher noise in the rotation. These results indicate that the loss of chemical asymmetry alters the road toward the final pattern and its orientation.

I created a minimalist phenomenological model to understand the physical consequences of the genotypical differences. In this simple model, two agents representing the cells interact in a confined one-dimensional space. Each agent feels the space exclusion of the other through a soft-spheres model and is attracted to a definite position in space. I built two model variants, which differ in the relative positioning of the attraction wells. The first variant, the asymmetrical model, has each cell with an attraction well opposite to its starting position. In the symmetrical variant, both attraction wells are situated in the same position on the axis. In each case, the depth of the wells and the strength with which the cells interact with them can be explored.

We found that the asymmetrical model closely follows the wild-type observations, while the symmetrical model is similar to the mutants, especially the *notch1a* knockout. Moreover, by exploring both alternatives as a function of the relative strengths of each cell's interaction with its corresponding well, I observe that the asymmetrical model is exceptionally robust to changes in the relative strength, in contrast to the symmetrical model. The symmetrical model's final angles strongly depend on the wells' relative strength. Furthermore, they are noisier than their asymmetrical counterparts. Importantly, the simulation results show that it is not the absolute value but the relative strength of the attractors that affects the system's behavior.

Together, I could quantitatively analyze the Planar Cell Inversion phenomenon in the neuromasts of the zebrafish lateral line. Through a modeling approach, I proposed an interpretation of the role of the cells' chemical identity, working as "guides" to direct the pair's migration during the inversion. Due to the space exclusion in the model, I could not rule out the possibility that only one of the cells is pushing while the other follows due to the confinement.

An explanation of how planar cell inversion relates to the functional form of the organ is still lacking. There has been evidence that *Emx2* is involved in the positioning of the hair within the cell but not the cell's position in the organ. This might relate to the dilation in the initiation of the PCI in these mutants. Moreover, there has been no evidence of a mutant that could prevent PCI from happening, as even when the whole PCP pathway is affected by knockouts of the *vangl2* or *wnt11r* genes, the process may still occur.

5.4 Final words

In this thesis, I studied collective cell migration phenomena in the Zebrafish lateral line through different modeling approaches. I created two software packages to generate *in silico* ground truths (*seapipy*) and to study the mechanical state of tissues, specially in a dynamic setting (*ForSys*). Finally, I successfully applied this to answer pressing questions regarding the relationship between the adhesion properties of different cell types in the neuromast and during the inversion process.

In the future, I believe that an extension of *ForSys* to three dimensions will be necessary to address ever more complex questions in the rheology of tissues. Additionally, applying stress estimation to other systems, such as plants, is an underexplored avenue that might

provide interesting insights into critical questions such as crop survival in agriculture.

ForSys will continue to be developed and grown to incorporate and accommodate different algorithms. In this way, it can serve as a Mechanical State Inference toolkit instead of a standalone tool. In turn, this will benefit the community as a whole, as different algorithms could be tested on the same data and cross-checked to evaluate the robustness of the inference solutions.

Mechanical State Inference is a valuable technique that complements other stress measurement methods. It can aid in experiment planning by being used as a first inexpensive technique to evaluate the system's state before a more complex and destructive experiment is performed in the sample of interest. Moreover, another unexplored possibility lies in using AI methods to make the inference instead of a tractable system of equations. In a first approach, from the image segmentation, an AI model should be able to predict the stresses, given the training data provided. This data can originate from different proxies for stress, such as myosin fluorescence intensity, or even *in silico* ground truths.

A more advanced implementation that allows automatic real-time segmentation could even perform inference from the microscope, aiding the imaging process and cementing Mechanical State Inference as an invaluable tool for experimentalists.

Anhang A

seapiPy: Automatic generation of *in silico* tissues

To validate the stress inference software, it was necessary to generate *in silico* images of tissue monolayers with known values for the membrane stress and intracellular pressures as ground truth. Moreover, these states should be generated in evolving tissues to analyze their dynamic component. We decided to use Surface Evolver [18], which implements a vertex model [105, 49, 4].

The Vertex model is well suited to simulate evolving tissue monolayers. In this model, cells are modeled as polygons, with the edges of the polygons representing the cell membranes. At each point where two edges meet, a vertex is generated. All the forces will be acting on the vertices of the system, which can be formulated through an effective potential energy [105] or through virtual work [4].

The most common terms in an effective potential energy approach typically involve membrane constriction, cell elasticity, and cell contractility [134]. Membrane constriction, also called line tension, has an energy proportional to the size of the interface (Δr), mediated by a constant (λ) as

$$F_{\text{line}}^j = \lambda \Delta r \quad (\text{A.1})$$

for membrane j . Cell elasticity is modeled akin to Hooke's law, which rewards cells near a designated target area. Finally, cell contractility rewards smaller cell sizes. To obtain the global energy, the line tension is summed over all membranes, and cell elasticity and contractility over all the cells in the system as

$$U = \sum_{i=0}^{\text{membranes}} \lambda_i \Delta r_i + \sum_{j=0}^{\text{cells}} \frac{K_E}{2} (A_j - A_{\text{target}})^2 + \frac{K_C}{2} A_j^2 \quad (\text{A.2})$$

where K_E and K_C are the elasticity and contractility constants respectively, and A_j is the area of the j th cell. Alternatively to this representation [134], the contractility term can be

used with the perimeter instead of the area as [49]

$$E_C = \sum_{j=0}^{\text{cells}} \frac{K_C}{2} P_j^2$$

where P_j is the perimeter of cell j . Surface Evolver implements an evolution over the vertices that minimizes the energy, using a parameter, *scale*, as a time step.

To simplify the creation of multiple simulations under different conditions, we created *seapipy* [13], an Open Source software that implements a Python API to communicate with the Surface Evolver executable files. *seapipy* can create Surface Evolver-compatible files using Python scripting, removing the necessity of writing boilerplate code multiple times for each condition. The software generates a Voronoi Tessellation with a given geometry, assigning initial stress to the different membranes through the `Lattice.create_example_lattice()` function. From this point, it is possible to add different commands to create the desired conditions during the system's evolution and save snapshots of the tissue's state.

I generated four ground truth conditions to test ForSys [15] in its Static and Dynamic modality against other established tools such as DLITE [147] and CellFIT[23] Figure A.1 panel A. Three conditions generate a furrow-like distribution of stresses, and a fourth one creates a random distribution of stress values with a 50% spread. For each condition, I generated twenty-five replicates.

I generated an initial Voronoi Tessellation with random stresses taken from a normal distribution, with $\mu = 1$ and $\sigma = 0.1$, over $N = 64$ points in a rectangular, at a distance of 20 from each other. Each point in the grid was moved according to a Gaussian noise with a mean of zero and a standard deviation of 0.15. Each cell was assigned a target area value of 450 ± 5 from a normal distribution.

An initial relaxation is produced by averaging the vertices' positions in the membrane and evolving the tissue for 10000 steps with different scale values. The averaging is done three times and the evolution two times ($\text{scale} = 0.25$ and $\text{scale} = 0.1$). After this, the system relaxes for a certain number of steps following this recipe

```

1 se_object.initial_relaxing(evolve_step=10000)
2 se_object.evolve_relaxing(number_of_times=10, steps=2500)
3 se_object.add_vertex_averaging(how_many=100)
4 se_object.change_scale(new_scale=0.005)
5 se_object.evolve_relaxing(number_of_times=5, steps=5000)
6 se_object.save_one_step(parameters['save_dir'],
7                           parameters['file_name'])
8 se_object.evolve_relaxing(number_of_times=5, steps=5000)

```

The function on line 2 (repeated in lines 5 and 8) evolves the tissue the number of *steps* assigned, with a scale of 0.01, and then performs all the T1 transitions that could be needed in the system, using a maximum edge size of 0.1. This is repeated `number_of_times` times.

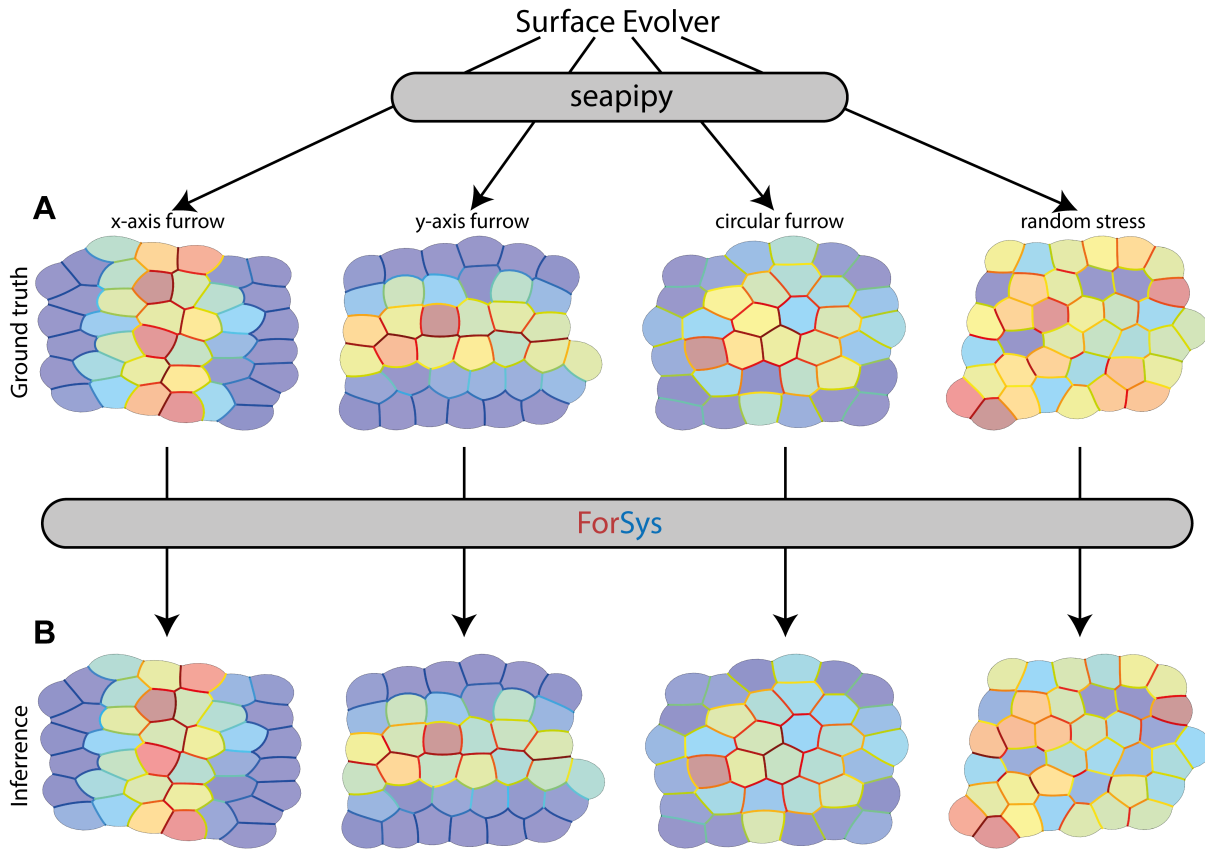


Abbildung A.1: **SeapiPy image generation.** (A) Four different conditions were generated with Surface Evolver through the seapiPy package. (B) Afterward, tissue stresses and pressures are inferred with ForSys. Figure reproduced from [15].

All four examples use the same algorithm to generate their starting geometry. Still, the initial seeding for the cells' centers in the tessellation and the stress distributions are random. We define a quantity, Surface Evolver Time (SET), as the number of steps (n) times the scale (Δt)

$$t = n\Delta t$$

The algorithm described above generates the first time point at time 3875 SET. The tissue then evolves 125 SET, marking the second time point. At that time, the stresses are assigned according to the particular recipe of the example, and each following time point is taken every 0.25 SET.

The recipes are the same in the Horizontal and Vertical Furrows; however, the Probability Density Functions (PDF) are rotated with respect to each other: Horizontal Furrows have the PDF as a function of the x position, and Vertical Furrows as a function of the y position. New tensions are created by summing the original stress of the membrane with the corresponding value of the PDF at the position of the edges centroid. The PDF's peak is in the center of the tissue, with a standard deviation of around two cellular radii. On the

other hand, the Circular Furrow uses the distance between the tissue's centroid and the edge's center, effectively making the stresses decay radially from the center. In the Random Tensions case, membrane stresses are assigned by choosing from a list of five possible values (1, 1.1, 1.2, 1.3, and 1.5) using a uniform distribution. In all cases, after the first two snapshots, the evolution continues for 23 additional steps.

seapipy allowed for an easy generation of the simulations and replicates, streamlining the *in silico* validation processes. Moreover, as the software is in Python, it would be possible to integrate it seamlessly with ForSys (Figure A.1 Panel B). As seapipy is an Open Source package, I hope that the rest of the community can take advantage of its capabilities and expand on them.

In the future, seapipy should be expanded to allow for the generation of 3D ground truths, which would allow the validation of 3D stress inference algorithms.

Anhang B

Inertia of the rotating pair

During Planar Cell Inversion (PCI), cells orchestrate their interactions to exchange positions by rotating around their contact point. To try to understand the energetic implications of the motion, we have built a toy model to represent the inertia of the movement by calculating the moment of inertia of the pair. A separate discussion might be held about the usage of this type of model in a viscoelastic material, such as the cells that are, in turn, immersed in a possibly overdamped medium [122]. However, we believe that this simple model can still allow a better understanding of the physical nature of the PCI. We illustrate our mental picture of the process in Figure B.1A. We sketch the process as two soft disks that deform as they approach their joint center of mass, ending up as one disk of twice the original mass.

From a Newtonian representation, inertia accounts for the torque necessary to produce an angular acceleration in a body, akin to mass in Newton's second law. Therefore, an equivalent statute is $\tau = I\alpha$, where τ is the torque, I is the inertia, and α is the angular acceleration. Similarly, as mass and momentum relate, the angular momentum can be expressed through the moment of inertia and the angular velocity as $L = I\omega$.

The moment of inertia is calculated as the sum of the contributions of every mass element in the system depending on its distance to the axis of rotation,

$$I = \int dm r^2 \tag{B.1}$$

The selection of the rotation axis is important for the process to be modeled. Still, it is not a definite choice, as Steiner's theorem allows the axis to be changed for any other parallel.

We intend to derive an equation for the moment of inertia as a function of the distance between the disks. The most important quantities are the bond length, shown in figure B.1B as L , and referred to in the text as l , and the total distance between the centers of the two disks, D . Then, the distances from the centers to the contact point are d_1 and d_2 for both disks, and the angle formed by the center of one of the disks and the endpoints of the mutual interface are θ . The quantities l , D , and θ can be related to each other and much of the calculations will be about these derivations.

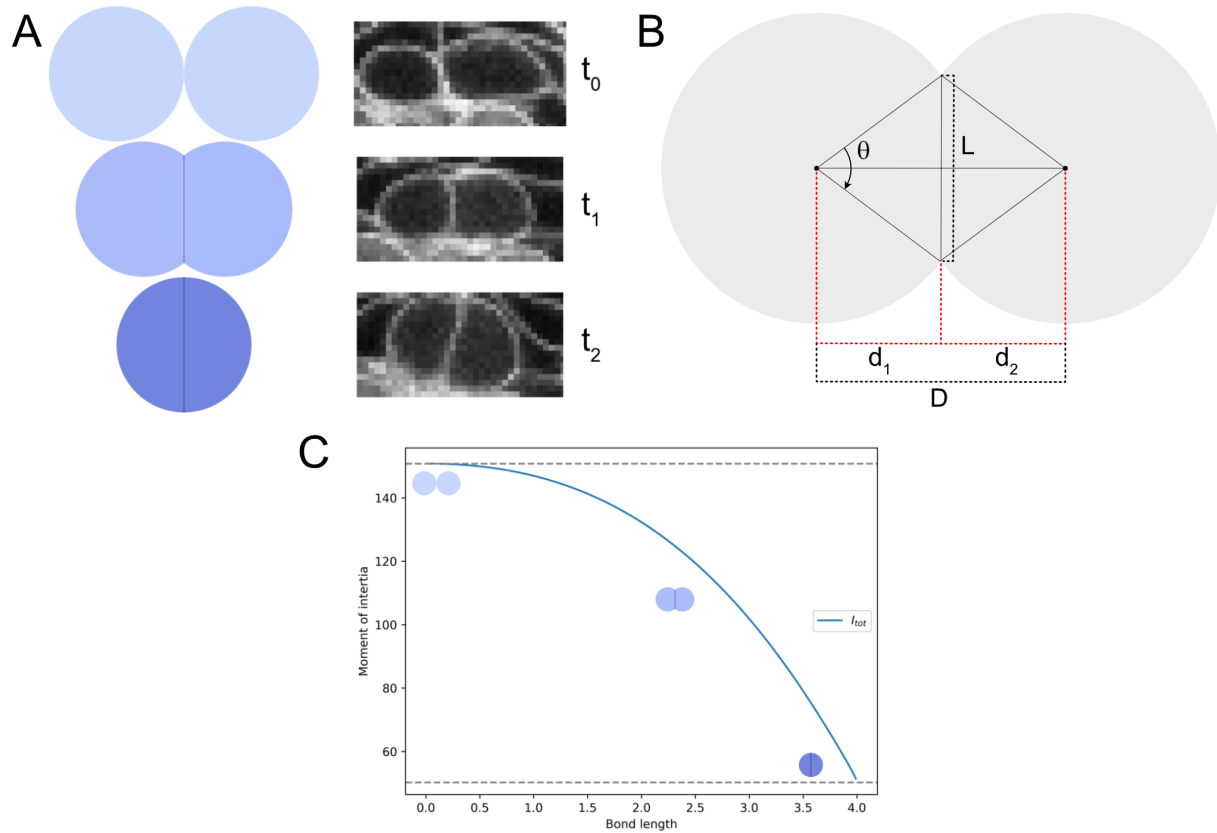


Abbildung B.1: **Moment of inertia of the rotating pair.** (A) After the Unipotent Cell Hair Progenitor division, cells separate during the onset phase, and after a small period, they start to join together. The Polarity Cell Inversion process starts around the time that a rounding appears. During the rotation, the two-cell system has the maximum circularity. The left side of the panel shows a sketch of the movement, and the right side shows a microscopy image to illustrate the step. (B) The two-cell system can be studied as the dependence of the distance D with the length of the interface l . (C) Moment of inertia of the two-cell system as a function of the bond length l . The moment of inertia for two circular bodies through their contact point is shown as the dashed line on the top of the plot. The dashed line at the bottom shows the moment of inertia for a circle in the axis through its center. In panels (A) and (C), the brightness of the circles shows their density after mass relocation.

We will assume that the mass gets redistributed uniformly between the pair while they coalesce. We will address how to calculate the distribution of mass later on. We can split the inertia into constituent parts that will be expressed as their geometrical shape. The red crosses in or beside each of the symbols will represent the axis of rotation. The moment of inertia of the general system can be written as

$$I = \textcircled{\times}_1 + \textcircled{\times}_2 - \times\})_1 - (\times)_2 \quad (\text{B.2})$$

which, after noting that $\times\}) = \times\} - \times\}$, gives

$$I = \textcircled{\times}_1 + \textcircled{\times}_2 - \left(\times\}_1 - \times\}_1 \right) - \left(\times\}_2 - \times\}_2 \right) \quad (\text{B.3})$$

Each term of equation B.3 will be calculated separately and then combined. First, the moment of inertia of a disk of radius R with homogeneous density ρ with respect to an axis through its center is $\textcircled{\times} = 2\pi\rho\frac{R^4}{4}$. In general, a segment of a disk with an angle of θ has a moment $\times\} = \rho\theta\frac{R^4}{4}$. On the other hand, for the triangles $\times\}$ and $\times\}$, an element of mass dm is going to be positioned at $r = (x, y)$, and therefore we can perform the integration

$$\times\} = \rho \iint dA r^2 = \rho \int_0^d \int_{-\frac{lx}{2d}}^{-\frac{lx}{2d}} dx dy (x^2 + y^2) = \rho \left(\frac{1}{4}ld^3 + \frac{1}{48}l^3d \right) \quad (\text{B.4})$$

where the distance d is the distance from the right-most vertex of the triangle to the center of its base, and l is the length of the base at the left. Using the parametric representation of the circles, we can find the two points at which the disk surfaces intersect (create the lens $\textcircled{\times}$) to find that

$$d_1 = \frac{D^2 + R_1^2 + R_2^2}{2D} \quad (\text{B.5})$$

$$\frac{l^2}{2} = R_1^2 - \left(\frac{D^2 + R_1^2 + R_2^2}{2D} \right) \quad (\text{B.6})$$

Using B.6, it is possible to find a relationship between the distance D and the interface length l . Let $\bar{D}(l) = D^2(l)$, then $D(l)$ is implicitly defined by

$$\bar{D}^2(l) + \bar{D}(l)(l^2 - 2(R_1^2 + R_2^2) + (R_1^2 - R_2^2)) = 0 \quad (\text{B.7})$$

Until now, the inertia has been calculated with respect to an axis that passes through the center of each disk. However, in our model, the disks jointly rotate around their center of mass. To perform the transformation, we use Steiner's theorem as

$$\begin{aligned} \textcircled{\times} &= \textcircled{\times} + m_{\textcircled{\times}}d_1^2 \\ \textcircled{\times} &= \textcircled{\times} + m_{\textcircled{\times}}d_2^2 \\ \times\} &= \times\} + m_{\times\}d_1^2 \\ \times\} &= \times\} + m_{\times\}d_2^2 \\ \times\} &= \times\} + m_{\times\}d_1^2 \\ \times\} &= \times\} + m_{\times\}d_2^2 \end{aligned}$$

These expressions all depend on d_1 (or on $d_2 = D - d_1$) that was found in equation B.6, which in turn is a function of $D(l)$ defined through equation B.7.

The final ingredient we need is the angles θ_1 and θ_2 for calculating the disk segments. This is easily found through trigonometry to be for $j = 1, 2$

$$\theta_j = 2 \arcsin \frac{l}{2R_j} \quad (\text{B.8})$$

At the start of the section, we mentioned that we suppose that the mass is redistributed to the disks uniformly when they come into contact, i.e. the radii of the disks stay constant. The change in density can be expressed as

$$\rho = \frac{m}{A} \rightarrow \rho' = \frac{m + \delta m}{A} = \frac{m}{A} + \frac{\delta m}{A} = \rho + \frac{\delta m}{A} \quad (\text{B.9})$$

The correction to the system's mass has to come from calculating the mass of the lens formed by the cells and its area: $\delta m = \rho A_{\text{cell}} = \rho(A_{\text{cell}} + A_{\text{cell}})$. The conceptual change in mass is then expressed as

$$\delta m = \rho \sum_{i=1}^2 \frac{R_i^2}{2} (\theta_i - \sin \theta_i) \quad (\text{B.10})$$

Taken together, these results give a full continuous expression for the moment of inertia of a pair of interpenetrating disks that rotate around their combined centroid. We summarized the results in figure B.1C, and using the dashed lines, we showed that the perfect circle with twice the mass, as well as the two-disk system, are special cases of the expression we have derived in the present appendix. It is interesting to entertain the possibility that the high circularity of hair cells acquired before their Planar Cell Inversion might be an energetic optimization to reduce their inertia. We believe this result is a general result for soft disks and might have a broader applicability.

Literaturverzeichnis

- [1] B. Aigouy, C. Cortes, S. Liu und B. Prud'Homme, *Development* (2020), dev.194589.
- [2] B. Aigouy, D. Umetsu und S. Eaton. In *Drosophila*, herausgegeben von C. Dahmann, Band 1478. Springer New York, New York, NY (2016), Seiten 227–239. Series Title: Methods in Molecular Biology.
- [3] U. Alon, *Nature Reviews Genetics* **8** (2007), 450.
- [4] S. Alt, P. Ganguly und G. Salbreux, *Philosophical Transactions of the Royal Society B: Biological Sciences* **372** (2017), 20150520.
- [5] E.D. Alton, Döllinger Ignaz, C.H. Pander und Royal College of Physicians of Edinburgh.: *Beiträge zur Entwicklungsgeschichte des Hühnchens im Eye*. [s.n.], Würzburg, 1817.
- [6] A. Aman und T. Piotrowski, *Developmental Cell* **15** (2008), 749.
- [7] K.E.V. Baer: *Über Entwicklungsgeschichte der Thiere. Beobachtung und Reflexion*. Bei den Gebrüdern Bornträger, Königsberg, 1828.
- [8] K. Bambardekar, R. Clément, O. Blanc, C. Chardès und P.F. Lenne, *Proceedings of the National Academy of Sciences* **112** (2015), 1416.
- [9] S.P. Banavar, E.K. Carn, P. Rowghanian, G. Stooke-Vaughan, S. Kim und O. Campàs, *Scientific Reports* **11** (2021), 8591.
- [10] C.G. Becker, B.C. Lieberoth, F. Morellini, J. Feldner, T. Becker und M. Schachner, *The Journal of Neuroscience* **24** (2004), 7837.
- [11] S. Berg, D. Kutra, T. Kroeger, C.N. Straehle, B.X. Kausler, C. Haubold, M. Schiegg, J. Ales, T. Beier, M. Rudy, K. Eren, J.I. Cervantes, B. Xu, F. Beuttenmueller, A. Wolny, C. Zhang, U. Koethe, F.A. Hamprecht und A. Kreshuk, *Nature Methods* **16** (2019), 1226.
- [12] I. Bonnet, P. Marcq, F. Bosveld, L. Fetler, Y. Bellaïche und F. Graner, *Journal of The Royal Society Interface* **9** (2012), 2614.

- [13] A. Borges. *borgesaugusto/seapipy: v0.2.0-alpha*, März 2024. Language: en.
- [14] A. Borges, A.S. Ceccarelli und O. Chara. *ForSys software*, Mai 2024. Language: en.
- [15] A. Borges, J.R. Miranda-Rodríguez, A.S. Ceccarelli, G. Ventura, J. Sedzinski, H. López-Schier und O. Chara, (2024).
- [16] A. Borges, F. Pinto-Teixeira, I. Wibowo, H.M. Pogoda, M. Hammerschmidt, K. Kawakami, H. López-Schier und J.R. Miranda-Rodríguez, *microPublication Biology* **2024** (2024).
- [17] F. Bosveld, Z. Wang und Y. Bellaïche, *Current Opinion in Cell Biology* **54** (2018), 80.
- [18] K.A. Brakke, *Experimental Mathematics* **1** (1992), 141. Publisher: Taylor & Francis
eprint: <https://doi.org/10.1080/10586458.1992.10504253>.
- [19] C. Brangwynne, S. Huang, K.K. Parker und D.E. Ingber, *In Vitro Cellular & Developmental Biology - Animal* **36** (2000), 563.
- [20] G.W. Brodland und H.H. Chen, *Journal of Biomechanical Engineering* **122** (2000), 402.
- [21] G.W. Brodland und D.A. Clausi, *Journal of Biomechanical Engineering* **116** (1994), 146.
- [22] G.W. Brodland, V. Conte, P.G. Cranston, J. Veldhuis, S. Narasimhan, M.S. Hutson, A. Jacinto, F. Ulrich, B. Baum und M. Miodownik, *Proceedings of the National Academy of Sciences* **107** (2010), 22111.
- [23] G.W. Brodland, J.H. Veldhuis, S. Kim, M. Perrone, D. Mashburn und M.S. Hutson, *PLOS ONE* **9** (2014), 1. Publisher: Public Library of Science.
- [24] D.B. Brückner, N. Arlt, A. Fink, P. Ronceray, J.O. Rädler und C.P. Broedersz, *Proceedings of the National Academy of Sciences* **118** (2021), e2016602118.
- [25] D.B. Brückner, A. Fink, C. Schreiber, P.J.F. Röttgermann, J.O. Rädler und C.P. Broedersz, *Nature Physics* **15** (2019), 595.
- [26] M. Buscaglia und D. Duboule, *The International Journal of Developmental Biology* **46** (2002), 5.
- [27] M.T. Butler und J.B. Wallingford, *Nature Reviews Molecular Cell Biology* **18** (2017), 375.
- [28] B.A. Camley, Y. Zhang, Y. Zhao, B. Li, E. Ben-Jacob, H. Levine und W.J. Rappel, *Proceedings of the National Academy of Sciences* **111** (2014), 14770.

- [29] O. Campàs, I. Noordstra und A.S. Yap, *Nature Reviews Molecular Cell Biology* (2023).
- [30] C.J. Chan, C.P. Heisenberg und T. Hiiragi, *Current Biology* **27** (2017), R1024.
- [31] S. Chanut und A.C. Martin. In *Progress in Molecular Biology and Translational Science*, Band 126. Elsevier (2014), Seiten 317–352.
- [32] H.H. Chen und G.W. Brodland, *Journal of Biomechanical Engineering* **122** (2000), 394.
- [33] K.K. Chiou, L. Hufnagel und B.I. Shraiman, *PLOS Computational Biology* **8** (2012), e1002512. Publisher: Public Library of Science.
- [34] R. Clément, B. Dehapiot, C. Collinet, T. Lecuit und P.F. Lenne, *Current Biology* **27** (2017), 3132.
- [35] C. Collinet, A. Bailles, B. Dehapiot und T. Lecuit, *Developmental Cell* **59** (2024), 156.
- [36] J.B. Collins und H. Levine, *Physical Review B* **31** (1985), 6119.
- [37] P.G. Cranston, J.H. Veldhuis, S. Narasimhan und G.W. Brodland, *Annals of Biomedical Engineering* **38** (2010), 2937.
- [38] R. Dahm und R. Geisler, *Marine Biotechnology* **8** (2006), 329.
- [39] C. Dareste: *Recherches sur la production artificielle des monstruosités, ou, Essais de tératogénie expérimentale / par Camille Dareste*. E. Reinwald,, Paris :, 1877.
- [40] C. Darwin: *The Origin of Species: By Means of Natural Selection, or the Preservation of Favoured Races in the Struggle for Life*. 6. Auflage. Cambridge University Press, Juli 2009.
- [41] P.G. De Gennes, *Reviews of Modern Physics* **57** (1985), 827.
- [42] J.M. Dealy, **79** (2010), 14.
- [43] M.R. Deans, D. Antic, K. Suyama, M.P. Scott, J.D. Axelrod und L.V. Goodrich, *The Journal of Neuroscience* **27** (2007), 3139.
- [44] S. Dijkgraaf, *Biological Reviews* **38** (1963), 51.
- [45] A. Dresden, *Bulletin of the American Mathematical Society* **26** (1920), 385.
- [46] S. Ernst, K. Liu, S. Agarwala, N. Moratscheck, M.E. Avci, D.D. Nogare, A.B. Chitnis, O. Ronneberger und V. Lecaudey, *Development* **139** (2012), 4571.

- [47] A. Erzberger, A. Jacobo, A. Dasgupta und A.J. Hudspeth, *Nature Physics* **16** (2020), 949.
- [48] R. Etournay, M. Popović, M. Merkel, A. Nandi, C. Blasse, B. Aigouy, H. Brandl, G. Myers, G. Salbreux, F. Jülicher und S. Eaton, *eLife* **4** (2015), e07090.
- [49] R. Farhadifar, J.C. Röper, B. Aigouy, S. Eaton und F. Jülicher, *Current Biology* **17** (2007), 2095.
- [50] H. Fol und S. Warynski, *CR Acad. Sci. Paris* **96** (1883), 1674.
- [51] A. Ghysen und C. Dambly-Chaudière, *Current Opinion in Neurobiology* **14** (2004), 67.
- [52] A. Ghysen und C. Dambly-Chaudière, *Genes & Development* **21** (2007), 2118.
- [53] S.F. Gilbert, Herausgeber. *A Conceptual History of Modern Embryology*. Springer US, Boston, MA, 1991.
- [54] N. Gompel, N. Cubedo, C. Thisse, B. Thisse, C. Dambly-Chaudière und A. Ghysen, *Mechanisms of Development* **105** (2001), 69.
- [55] F. Graner und D. Riveline, *Development* **144** (2017), 4226.
- [56] K.A. Grant, D.W. Raible und T. Piotrowski, *Neuron* **45** (2005), 69.
- [57] B. Guirao und Y. Bellaïche, *Current Opinion in Cell Biology* **48** (2017), 113.
- [58] M. Gómez-González, E. Latorre, M. Arroyo und X. Trepát, *Nature Reviews Physics* **2** (2020), 300.
- [59] P. Gómez-Gálvez, S. Anbari, L.M. Escudero und J. Buceta, *Seminars in Cell & Developmental Biology* **120** (2021), 147.
- [60] H. Hashimoto, F. Robin, K. Sherrard und E. Munro, *Developmental Cell* **32** (2015), 241.
- [61] W.K. Hastings, *Biometrika* **57** (1970), 97.
- [62] D. Hava, U. Forster, M. Matsuda, S. Cui, B.A. Link, J. Eichhorst, B. Wiesner, A. Chitnis und S. Abdelilah-Seyfried, *Journal of Cell Science* **122** (2009), 687.
- [63] B. Hayes, *American Scientist* **101** (2013), 92.
- [64] C.P. Heisenberg und Y. Bellaïche, *Cell* **153** (2013), 948.
- [65] A. Henfrey und T.H. Huxley: *Scientific memoirs, selected from the transactions of foreign academies of science, and from foreign journals. Natural history*. Taylor and Francis, London, 1853.

- [66] P.P. Hernández, F.A. Olivari, A.F. Sarrazin, P.C. Sandoval und M.L. Allende, *Developmental Neurobiology* **67** (2007), 637.
- [67] W. His: *Unsere Körperform und das physiologische Problem ihrer Entstehung Briefe an einen befreundeten Naturforscher / von Wilhelm His*. F.C.W. Vogel., Leipzig :, 1874.
- [68] M. Holley, C. Rhodes, A. Kneebone, M.K. Herde, M. Fleming und K.P. Steel, *Developmental Biology* **340** (2010), 547.
- [69] S. Huang, C. Brangwynne, K. Parker und D. Ingber, *Cell Motility* **61** (2005), 201.
- [70] S. Ichbiah, F. Delbary, A. McDougall, R. Dumollard und H. Turlier, *Nature Methods* **20** (2023), 1989.
- [71] S. Ishihara und K. Sugimura, *Journal of Theoretical Biology* **313** (2012), 201.
- [72] M. Iwasaki, H. Yokoi, T. Suzuki, K. Kawakami und H. Wada, *Developmental Dynamics* **249** (2020), 1440.
- [73] A. Jacobo, A. Dasgupta, A. Erzberger, K. Siletti und A. Hudspeth, *Current Biology* **29** (2019), 3579.
- [74] Y.R. Ji, S. Warriar, T. Jiang, D.K. Wu und K.S. Kindt, *eLife* **7** (2018), e35796.
- [75] Johannes Holtfreter, *Arch Exptl Zellforsch Gewebezicht* **23** (1939), 169.
- [76] C. Jopling, E. Sleep, M. Raya, M. Martí, A. Raya und J.C.I. Belmonte, *Nature* **464** (2010), 606.
- [77] A.J. Kalmijn. In *The Mechanosensory Lateral Line*, herausgegeben von S. Coombs, P. Görner und H. Münz. Springer New York, New York, NY (1989), Seiten 187–215.
- [78] R. Keller, *Science* **338** (2012), 201.
- [79] C.B. Kimmel, W.W. Ballard, S.R. Kimmel, B. Ullmann und T.F. Schilling, *Developmental Dynamics* **203** (1995), 253.
- [80] C.S. Ko und A.C. Martin. In *Current Topics in Developmental Biology*, Band 136. Elsevier (2020), Seiten 141–165.
- [81] J. Kockelkoren, H. Levine und W.J. Rappel, *Physical Review E* **68** (2003), 037702.
- [82] E.L. Kozak, J.R. Miranda-Rodríguez, A. Borges, K. Dierkes, A. Mineo, F. Pinto-Teixeira, O. Viader-Llangués, J. Solon, O. Chara und H. López-Schier, *Development* **150** (2023), dev200975.
- [83] E.L. Kozak, S. Palit, J.R. Miranda-Rodríguez, A. Janjic, A. Böttcher, H. Lickert, W. Enard, F.J. Theis und H. López-Schier, *Current Biology* **30** (2020), 1142.

- [84] C.A.M. La Porta und S. Zapperi, Herausgeber. *Cell Migrations: Causes and Functions*, Band 1146 von *Advances in Experimental Medicine and Biology*. Springer International Publishing, Cham, 2019.
- [85] D.A. Lauffenburger und A.F. Horwitz, *Cell* **84** (1996), 359.
- [86] C.L. Lawson und R.J. Hanson: *Solving Least Squares Problems*. Society for Industrial and Applied Mathematics, Januar 1995.
- [87] V. Lecaudey, G. Cakan-Akdogan, W.H.J. Norton und D. Gilmour, *Development* **135** (2008), 2695.
- [88] V. Ledent, *Development* **129** (2002), 597.
- [89] D.A. Lee, M.M. Knight, J.J. Campbell und D.L. Bader, *Journal of Cellular Biochemistry* **112** (2011), 1.
- [90] F. Leong, *Biophysical Journal* **105** (2013), 2301.
- [91] A. Lepilina, A.N. Coon, K. Kikuchi, J.E. Holdway, R.W. Roberts, C. Burns und K.D. Poss, *Cell* **127** (2006), 607.
- [92] E.B. Lewis, *Nature* **276** (1978), 565.
- [93] B. Li und S. Sun, *Biophysical Journal* **107** (2014), 1532.
- [94] S. Lo Vecchio, O. Pertz, M. Szopos, L. Navoret und D. Riveline, *Nature Physics* **20** (2024), 322.
- [95] L. Lu, T. Guyomar, Q. Vagne, R. Berthoz, A. Torres-Sánchez, M. Lieb, C. Martin-Lemaitre, K. Van Unen, A. Honigmann, O. Pertz, D. Riveline und G. Salbreux, *Nature Physics* **20** (2024), 1194.
- [96] H. López-Schier, *Current Opinion in Genetics & Development* **20** (2010), 428.
- [97] H. López-Schier und A.J. Hudspeth, *Proceedings of the National Academy of Sciences* **103** (2006), 18615.
- [98] H. López-Schier, C.J. Starr, J.A. Kappler, R. Kollmar und A. Hudspeth, *Developmental Cell* **7** (2004), 401.
- [99] A.C. Martin, M. Kaschube und E.F. Wieschaus, *Nature* **457** (2009), 495.
- [100] W.K. Metcalfe, C.B. Kimmel und E. Schabtach, *Journal of Comparative Neurology* **233** (1985), 377.
- [101] N. Metropolis, A.W. Rosenbluth, M.N. Rosenbluth, A.H. Teller und E. Teller, *The Journal of Chemical Physics* **21** (1953), 1087.

- [102] I. Mirkovic, S. Pylawka und A.J. Hudspeth, *Biology Open* **1** (2012), 498.
- [103] A. Mongera, P. Rowghanian, H.J. Gustafson, E. Shelton, D.A. Kealhofer, E.K. Carn, F. Serwane, A.A. Lucio, J. Giammona und O. Campàs, *Nature* **561** (2018), 401.
- [104] M. Montcouquiol, R.A. Rachel, P.J. Lanford, N.G. Copeland, N.A. Jenkins und M.W. Kelley, *Nature* **423** (2003), 173.
- [105] T. Nagai und H. Honda, *Philosophical Magazine B* **81** (2001), 699.
- [106] J. Navajas Acedo, M.G. Voas, R. Alexander, T. Woolley, J.R. Unruh, H. Li, C. Moens und T. Piotrowski, *Nature Communications* **10** (2019), 3993.
- [107] A. Nechiporuk und D.W. Raible, *Science* **320** (2008), 1774.
- [108] M. Newville, R. Otten, A. Nelson, T. Stensitzki, A. Ingargiola, D. Allan, A. Fox, F. Carter, Michał, R. Osborn, D. Pustakhod, Lneuhau, S. Weigand, A. Aristov, Glenn, C. Deil, Mgunyho, Mark, A.L.R. Hansen, G. Pasquevich, L. Foks, N. Zobrist, O. Frost, Stuermer, Azelcer, A. Polloreno, A. Persaud, J.H. Nielsen, M. Pompili und P. Eendebak. *lmfit/lmfit-py: 1.2.2*, Juli 2023.
- [109] K. Nishizawa, S.Z. Lin, C. Chardès, J.F. Rupprecht und P.F. Lenne, *Proceedings of the National Academy of Sciences* **120** (2023), e2212389120.
- [110] C. Nizak, S. Martin-Lluesma, S. Moutel, A. Roux, T.E. Kreis, B. Goud und F. Perez, *Traffic* **4** (2003), 739.
- [111] N. Noll, S.J. Streichan und B.I. Shraiman, *Physical Review X* **10** (2020), 011072.
- [112] C. Nüsslein-Volhard und E. Wieschaus, *Nature* **287** (1980), 795.
- [113] S. Ohta, Y.R. Ji, D. Martin und D.K. Wu, *eLife* **9** (2020), e60432.
- [114] P. Oteiza, I. Odstrcil, G. Lauder, R. Portugues und F. Engert, *Nature* **547** (2017), 445.
- [115] J. Peloggia, D. Münch, P. Meneses-Giles, A. Romero-Carvajal, M.E. Lush, N.D. Lawson, M. McClain, Y.A. Pan und T. Piotrowski, *Developmental Cell* **56** (2021), 1296.
- [116] R. Penrose, *Mathematical Proceedings of the Cambridge Philosophical Society* **51** (1955), 406.
- [117] N.I. Petridou und C. Heisenberg, *The EMBO Journal* **38** (2019), e102497.
- [118] C. Pfefferli und A. Jazwińska, *Regeneration* **2** (2015), 72.
- [119] D. Pinheiro und C.P. Heisenberg. In *Current Topics in Developmental Biology*, Band 136. Elsevier (2020), Seiten 343–375.

- [120] D. Pinheiro, R. Kardos, Hannezo und C.P. Heisenberg, *Nature Physics* **18** (2022), 1482.
- [121] F. Pinto-Teixeira, O. Viader-Llargués, E. Torres-Mejía, M. Turan, E. González-Gualda, L. Pola-Morell und H. López-Schier, *Biology Open* **4** (2015), 903.
- [122] E.M. Purcell, *American Journal of Physics* **45** (1977), 3.
- [123] M. Reimer, A. Norris, J. Ohnmacht, R. Patani, Z. Zhong, T. Dias, V. Kuscha, A. Scott, Y.C. Chen, S. Rozov, S. Frazer, C. Wyatt, S.i. Higashijima, E. Patton, P. Panula, S. Chandran, T. Becker und C. Becker, *Developmental Cell* **25** (2013), 478.
- [124] M.M. Reimer, I. Sörensen, V. Kuscha, R.E. Frank, C. Liu, C.G. Becker und T. Becker, *The Journal of Neuroscience* **28** (2008), 8510.
- [125] A.J. Ridley, M.A. Schwartz, K. Burridge, R.A. Firtel, M.H. Ginsberg, G. Borisy, J.T. Parsons und A.R. Horwitz, *Science* **302** (2003), 1704.
- [126] P. Roca-Cusachs, V. Conte und X. Trepast, *Nature Cell Biology* **19** (2017), 742.
- [127] C. Roffay, C.J. Chan, B. Guirao, T. Hiiragi und F. Graner, *Development* **148** (2021), dev192773.
- [128] P. Rørth, *EMBO reports* **13** (2012), 984.
- [129] E. Scarpa und R. Mayor, *Journal of Cell Biology* **212** (2016), 143.
- [130] A. Schauer und C.P. Heisenberg, *Developmental Biology* **474** (2021), 71.
- [131] C.H. Seo, H. Jeong, Y. Feng, K. Montagne, T. Ushida, Y. Suzuki und K.S. Furukawa, *Biomaterials* **35** (2014), 2245.
- [132] F. Serwane, A. Mongera, P. Rowghanian, D.A. Kealhofer, A.A. Lucio, Z.M. Hockenbery und O. Campàs, *Nature Methods* **14** (2017), 181.
- [133] S.S. Shen-Orr, R. Milo, S. Mangan und U. Alon, *Nature Genetics* **31** (2002), 64.
- [134] P. Spahn und R. Reuter, *PLoS ONE* **8** (2013), e75051.
- [135] M.A. Spencer, Z. Jabeen und D.K. Lubensky, *The European Physical Journal E* **40** (2017), 2.
- [136] M.B. Stein und R. Gordon, *Journal of Theoretical Biology* **97** (1982), 625.
- [137] M.S. Steinberg, *Developmental Biology* **180** (1996), 377.

- [138] M. Steps, U. Hossfeld, G.S. Levit und M. Simunek: *Wilhelm Roux's archives of developmental biology 1894-2004*, Band 24 von *Studies in the history of sciences and humanities*. 2011. Auflage. Institute for Contemporary History of the Academy of Sciences in Prague, Prague, 2011.
- [139] W.J. Stewart, G.S. Cardenas und M.J. McHenry, *Journal of Experimental Biology* **216** (2013), 388.
- [140] K. Sugimura, P.F. Lenne und F. Graner, *Development* **143** (2016), 186.
- [141] B. Tarchini und X. Lu, *Neuroscience Letters* **709** (2019), 134373.
- [142] R. Tassinari, E. Olivi, C. Cavallini, V. Taglioli, C. Zannini, M. Marcuzzi, O. Fedchenko und C. Ventura, *iScience* **26** (2023), 105875.
- [143] R.J. Tetley, M.F. Staddon, D. Heller, A. Hoppe, S. Banerjee und Y. Mao, *Nature Physics* **15** (2019), 1195.
- [144] D.W. Thompson: *On Growth and Form*. 1. Auflage. Cambridge University Press, Juli 1992.
- [145] P.L. Townes und J. Holtfreter, *Journal of Experimental Zoology* **128** (1955), 53.
- [146] L. Van Speybroeck, D. De Waele und G. Van de Vijver, *Annals of the New York Academy of Sciences* **981** (2002), 7.
- [147] R. Vasan, M.M. Maleckar, C.D. Williams und P. Rangamani, *Biophysical Journal* **117** (2019), 1714.
- [148] J.H. Veldhuis, A. Ehsandar, J.L. Maître, T. Hiiragi, S. Cox und G.W. Brodland, *Philosophical Transactions of the Royal Society B: Biological Sciences* **372** (2017), 20160261.
- [149] J.H. Veldhuis, D. Mashburn, M.S. Hutson und G.W. Brodland. In *Methods in Cell Biology*, Band 125. Elsevier (2015), Seiten 331–351.
- [150] G. Ventura, A. Amiri, R. Thiagarajan, M. Tolonen, A. Doostmohammadi und J. Sedzinski, *Nature Communications* **13** (2022), 6423.
- [151] O. Viader-Llargués, V. Lupperger, L. Pola-Morell, C. Marr und H. López-Schier, *eLife* **7** (2018), e30823.
- [152] A. Vian, M. Pochitaloff, S.T. Yen, S. Kim, J. Pollock, Y. Liu, E.M. Sletten und O. Campàs, *Nature Communications* **14** (2023), 7023.

- [153] P. Virtanen, R. Gommers, T.E. Oliphant, M. Haberland, T. Reddy, D. Cournapeau, E. Burovski, P. Peterson, W. Weckesser, J. Bright, S.J. Van Der Walt, M. Brett, J. Wilson, K.J. Millman, N. Mayorov, A.R.J. Nelson, E. Jones, R. Kern, E. Larson, C.J. Carey, Polat, Y. Feng, E.W. Moore, J. VanderPlas, D. Laxalde, J. Perktold, R. Cimrman, I. Henriksen, E.A. Quintero, C.R. Harris, A.M. Archibald, A.H. Ribeiro, F. Pedregosa, P. Van Mulbregt, SciPy 1.0 Contributors, A. Vijaykumar, A.P. Bardelli, A. Rothberg, A. Hilboll, A. Kloeckner, A. Scopatz, A. Lee, A. Rokem, C.N. Woods, C. Fulton, C. Masson, C. Häggström, C. Fitzgerald, D.A. Nicholson, D.R. Hagen, D.V. Pasechnik, E. Olivetti, E. Martin, E. Wieser, F. Silva, F. Lenders, F. Wilhelm, G. Young, G.A. Price, G.L. Ingold, G.E. Allen, G.R. Lee, H. Audren, I. Probst, J.P. Dietrich, J. Silterra, J.T. Webber, J. Slavič, J. Nothman, J. Buchner, J. Kulick, J.L. Schönberger, J.V. De Miranda Cardoso, J. Reimer, J. Harrington, J.L.C. Rodríguez, J. Nunez-Iglesias, J. Kuczynski, K. Tritz, M. Thoma, M. Newville, M. Kümmerer, M. Bolingbroke, M. Tartre, M. Pak, N.J. Smith, N. Nowaczyk, N. Shebanov, O. Pavlyk, P.A. Brodtkorb, P. Lee, R.T. McGibbon, R. Feldbauer, S. Lewis, S. Tygier, S. Sievert, S. Vigna, S. Peterson, S. More, T. Pudlik, T. Oshima, T.J. Pingel, T.P. Robitaille, T. Spura, T.R. Jones, T. Cera, T. Leslie, T. Zito, T. Krauss, U. Upadhyay, Y.O. Halchenko und Y. Vázquez-Baeza, *Nature Methods* **17** (2020), 261.
- [154] H. Wada, A. Ghysen, C. Satou, S.i. Higashijima, K. Kawakami, S. Hamaguchi und M. Sakaizumi, *Developmental Biology* **340** (2010), 583.
- [155] S. Warynski: *Sur la production artificielle des monstres a cœur double chez les poulets: quelques réflexions sur la loi qui régit la constance des formes chez l'embryon sa vérification expérimentale*. Université de Genève, Dissertation, 1886.
- [156] S. Warynski und H. Fol, *Revue médicale de la Suisse romande* **3** (1884), 395.
- [157] G. Wayne Brodland und H.H. Chen, *Journal of Biomechanics* **33** (2000), 845.
- [158] M. Westerfield: *The Zebrafish Book; A guide for the laboratory use of zebrafish (Danio rerio)*. 5. Auflage, 2007.
- [159] I. Wibowo, F. Pinto-Teixeira, C. Satou, S.i. Higashijima und H. López-Schier, *Development* **138** (2011), 1143.
- [160] M.L. Williams und L. Solnica-Krezel. In *Current Topics in Developmental Biology*, Band 136. Elsevier (2020), Seiten 377–407.

Danksagung

I sincerely thank Dr. Hernán López-Schier for his support, even during difficult times throughout my PhD. With him, I learned how to see a project to its end and communicate its results effectively. It is also thanks to him that I am now more confident in asking biologically relevant questions.

I would also like to thank Prof. Dr. Erwin Frey for his support. He has always offered advice that has directly improved the projects I worked on.

Furthermore, I am grateful to Prof. Dr. Osvaldo Chara for his ongoing mentorship for nearly a decade.

Moreover, I would like to thank all other members of the López-Schier lab: Jerónimo, Andres, Yanko, Laura, Eva, and Petra. Working with all of them taught me a great deal about doing interdisciplinary science. I want to especially thank Dr. Jerónimo Miranda-Rodriguez, who taught me basically all I know about experimentation in biology and the zebrafish.

My graduate school, QBM, recently rebranded as QMB, has been the constant that allowed me to continue this PhD despite the external context. I especially want to thank Dr. Markus Hohle and Dr. Christoph Jung for their support. I hope QMB continues to grow as the community around it has been essential for my journey.

I am also thankful to the QMB students, especially Alice, Jan, Mohammad, Pablo, and Antonia. They helped me feel welcome in the Gene Center.

Finally, I would like to thank my family, friends, and all who supported me throughout the journey, even from very far away.

RESEARCH ARTICLE

Quantitative videomicroscopy reveals latent control of cell-pair rotations *in vivo*

Eva L. Kozak^{1,*}, Jerónimo R. Miranda-Rodríguez^{1,*}, Augusto Borges^{1,2,3}, Kai Dierkes⁴, Alessandro Mineo⁴, Filipe Pinto-Teixeira⁴, Oriol Viader-Llargués¹, Jérôme Solon^{4,5}, Osvaldo Chara^{2,6,7} and Hernán López-Schier^{1,3,8,‡}

ABSTRACT

Collective cell rotations are widely used during animal organogenesis. Theoretical and *in vitro* studies have conceptualized rotating cells as identical rigid-point objects that stochastically break symmetry to move monotonously and perpetually within an inert environment. However, it is unclear whether this notion can be extrapolated to a natural context, where rotations are ephemeral and heterogeneous cellular cohorts interact with an active epithelium. In zebrafish neuromasts, nascent sibling hair cells invert positions by rotating $\leq 180^\circ$ around their geometric center after acquiring different identities via Notch1a-mediated asymmetric repression of *Emx2*. Here, we show that this multicellular rotation is a three-phasic movement that progresses via coherent homotypic coupling and heterotypic junction remodeling. We found no correlation between rotations and epithelium-wide cellular flow or anisotropic resistive forces. Moreover, the Notch/*Emx2* status of the cell dyad does not determine asymmetric interactions with the surrounding epithelium. Aided by computer modeling, we suggest that initial stochastic inhomogeneities generate a metastable state that poises cells to move and spontaneous intercellular coordination of the resulting instabilities enables persistently directional rotations, whereas Notch1a-determined symmetry breaking buffers rotational noise.

KEY WORDS: Multicellular rotations, Patterning, Regeneration, Symmetry breaking, Zebrafish

INTRODUCTION

Collective cell movement is widespread during the formation and regeneration of organs (Lecaudey et al., 2008; Norden and

Lecaudey, 2019; Dalle Nogare et al., 2020; Founounou et al., 2021; Alhashem et al., 2022; Hartmann and Mayor, 2022). This multicellular behavior is controlled at three levels: the onset, the progression and the conclusion. Each level generates the initial conditions for the next, and transition periods synchronize multiple sub- and supra-cellular processes to generate a predictable outcome (Gómez-Gálvez et al., 2021; Fredberg, 2022). At the extremes, the coordination of such processes may be deterministic and guided globally, or stochastic and canalized by local interaction and feedback between cells (Collinet and Lecuit, 2021; Hartmann and Mayor, 2022; Wibowo et al., 2011; Mirkovic et al., 2012; Tanner et al., 2012; Wang et al., 2013; Horne-Badovinac, 2014; Cetera et al., 2018; Hirata et al., 2018).


Here, we focus on a minimal model of collective cell rotations involving the positional inversion of just two cells, which was first described in neuromasts of the zebrafish lateral line (Wibowo et al., 2011). Neuromasts display largely invariant size and pattern. They consist of a radial-symmetric epithelium containing mechanosensory hair cells in the center, and two types of non-sensory supporting cells forming two outward concentric rings (Fig. 1A) (Wada and Kawakami, 2015). Hair cells are also polarized along a single axis across the apical face of the epithelium (López-Schier and Hudspeth, 2006). Hair cells undergo continuous renewal without modifying the architecture of the organ (Cruz et al., 2015; Pinto-Teixeira et al., 2015; Peloggia et al., 2021). During turnover, hair cells are produced sequentially, in pairs or dyads, from the mitotic division of facultative unipotent progenitors (UHCP) that originate from internal supporting cells (López-Schier and Hudspeth, 2006; Ma et al., 2008; Cruz et al., 2015; Denans et al., 2019; Thomas and Raible, 2019; Hardy et al., 2021; Baek et al., 2022). Local lateral-inhibitory signaling via Notch1a breaks the initial symmetry in nascent sibling hair cells by repressing the transcription factor *Emx2* in one of them (Jacobo et al., 2019; Kozak et al., 2020). The cell that activates the Notch1a receptor (Notch-on) loses *Emx2* expression, whereas its sibling (Notch-off) maintains it. Although this symmetry-breaking process is deterministic in that it always results in one of the siblings losing *Emx2* expression, it is also stochastic because it is unpredictable which cell will do so. Concurrently with this step, around half of the hair-cell pairs rotate once around their geometric center (Fig. 1B-D and Movie 1) (Wibowo et al., 2011; Mirkovic et al., 2012).

Notably, cell-pair rotations *in vivo* resemble the angular movement of mammalian cells *in vitro*, which is driven by three co-occurring processes: intrinsic cell motility and stochastic symmetry breaking (to initiate movement), strong intercellular adhesion (enabling dynamic coupling between cells for persistent directionality) and spatial confinement (so that cells cannot translocate) (Brangwynne et al., 2000; Huang et al., 2005;

¹Unit Sensory Biology and Organogenesis, Helmholtz Zentrum München, Munich D-85764, Germany. ²Systems Biology Group (SysBio), Institute of Physics of Liquids and Biological Systems (IFLySIB), National Scientific and Technical Research Council (CONICET), University of La Plata, La Plata B1900BTE, Argentina. ³Graduate School of Quantitative Biosciences, Ludwig Maximilian University, Munich 81377, Germany. ⁴Centre for Genomic Regulation, Barcelona 08003, Spain. ⁵Instituto Biofisika, Basque Excellence Research Centre, Leioa 48940, Spain. ⁶School of Biosciences, University of Nottingham, Sutton Bonington Campus, Nottingham LE12 5RD, UK. ⁷Instituto de Tecnología, Universidad Argentina de la Empresa, Buenos Aires C1073AAO, Argentina. ⁸Division of Science, New York University Abu Dhabi, Saadiyat Island 129188, United Arab Emirates.

*These authors contributed equally to this work

‡Author for correspondence (hl5251@nyu.edu)

 J.R.M.-R., 0000-0002-2775-6719; A.B., 0000-0003-0773-5352; K.D., 0000-0002-9174-3517; A.M., 0000-0002-7047-1313; J.S., 0000-0001-9967-9794; O.C., 0000-0002-0868-2507; H.L.-S., 0000-0001-7925-7439

This is an Open Access article distributed under the terms of the Creative Commons Attribution License (<https://creativecommons.org/licenses/by/4.0>), which permits unrestricted use, distribution and reproduction in any medium provided that the original work is properly attributed.

Handling Editor: Steve Wilson

Received 6 June 2022; Accepted 20 February 2023

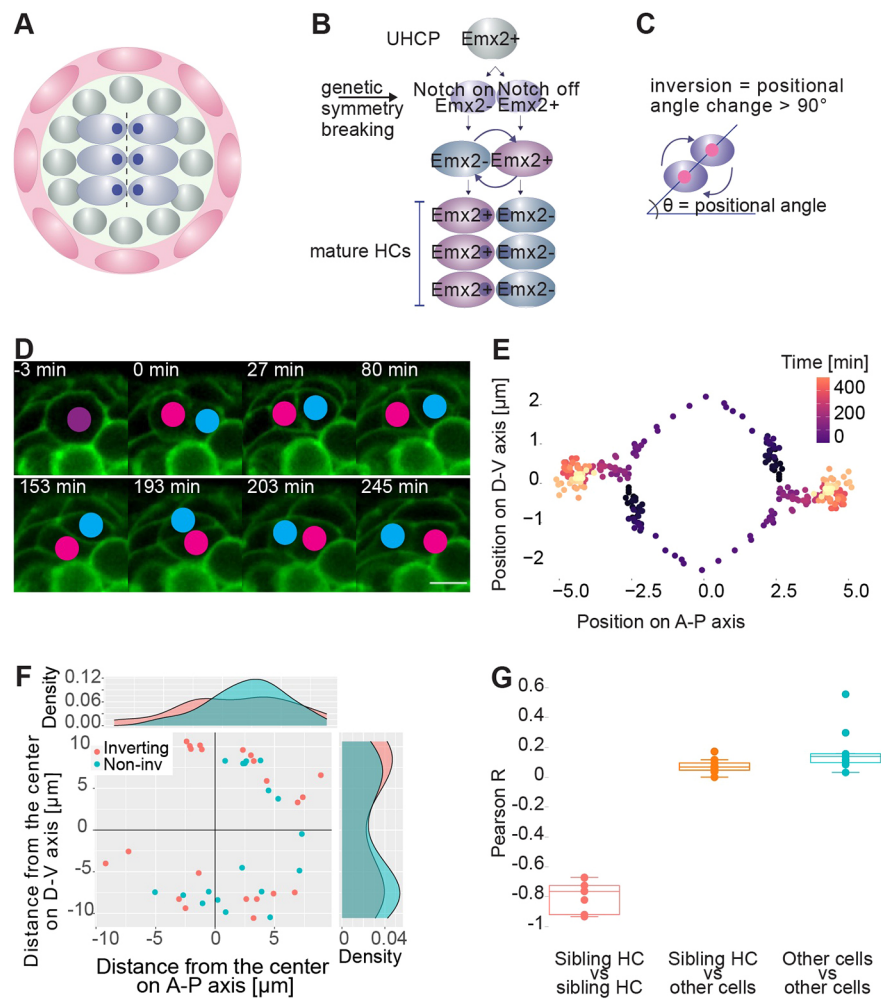


Fig. 1. Inversions are local movements of nascent sibling hair cells. (A) Scheme of a neuromast, depicting an outer ring of mantle cells (red), internal supporting cells (gray) and central hair cells (light blue) with their axis of planar polarity (dark blue dots). Dashed line indicates the midline of the organ. (B) Scheme of hair-cell development. Unipotent progenitors (UHCP) divide into two hair cells. Sibling hair cells undergo positional inversion to place Notch-on/Emx2(–) and Notch-on/Emx2(+) cells on opposite sides of the epithelium. (C) The inversion is an angular movement of at least 90°. (D) Selected frames from a time-lapse movie of cell-pair inversion in a wild-type neuromast expressing *cldnb:EGFP* and *myo6b:GFP*. The timings are relative to the mitotic division that generates the hair-cell pair. Scale bar: 5 μ m. (E) One exemplary hair-cell dyad during an inversion. The position of each cell during the inversion is depicted relative to the centroid of the pair. Time is color-coded from dark violet to yellow, where 0 is the time immediately after cell division and 400 is the upper limit of the inversion. (F) Position of the hair-cell progenitor at the time of its mitotic division. The color of the dots indicates whether the resulting hair-cell pair inverts (red) or not (blue). The center was defined as the position of all pre-existing hair cells in the neuromast. Side panels show the density of points along the dorsoventral (D-V) and anteroposterior (A-P) axes of the epithelium. It shows 22 inverting and 18 non-inverting hair-cell pairs from different neuromasts in 22 specimens. (G) Boxplots showing the Pearson correlation coefficient for the movement of cells in the neuromast along the A-P axis. Each point represents the cells during a rotation. Box plots show median values (middle bars) and first (Q1) to third (Q3) interquartile ranges (boxes); upper whisker is either 1.5 \times the interquartile range or the maximum value (whichever is the smallest) and lower whisker is either 1.5 \times the interquartile range or the minimum value (whichever is the biggest). For each neuromast, the movement was compared between the rotating hair cells (HC); the rotating hair cells and all other cells; and between all other cells. $n=9$ independent neuromasts from $N=9$ different larvae.

Camley et al., 2014; Leong, 2013; Li and Sun, 2014; Huang, 2016). Also, cell-pair rotations *in vitro* happen nearly always, have no predictable duration or extent, and do not involve intrinsic differences between cells or interactions with a surrounding epithelium. They are monotonous, exhibiting symmetrical sinusoidal trajectories with almost invariable frequency and amplitude (Huang et al., 2005). Moreover, theoretical studies have strongly influenced our thinking about multicellular rotations (Huang et al., 2005; Camley et al., 2014; Li and Sun, 2014; Leong, 2013). Yet, the mechanistic overlap between rotating cells *ex vivo* and in a natural context remains unknown. Here, we combine videomicroscopy, experimental perturbations and modeling to

quantitatively characterize cell-pair rotation *in vivo*, and reveal previously-overlooked features affecting rotational precision.

RESULTS

Cell-pair rotation *in vivo* is a discrete movement of nascent sibling hair cells

We began by acquiring a highly resolving dataset from intravital videomicroscopy of neuromasts in the posterior lateral line of larval zebrafish (Pinto-Teixeira et al., 2013). We used specimens expressing a combination of fluorescent transgenic markers to identify and visualize every neuromast cell (Haas and Gilmour, 2006; Kindt et al., 2012; López-Schier and Hudspeth, 2006; Steiner

et al., 2014). To quantify rotations at high resolution, we first defined the angle between the axis connecting the center of each cell of nascent pairs and the horizontal axis of the neuromast, which invariably runs parallel to the anteroposterior axis of the animal's body (Fig. 1C). Sibling hair cells invert positions by moving in circular arcs around their geometric center (Fig. 1E). We used a strict definition of inversion as a rotation of at least 90° of the line connecting the center of both cells at the time of their birth. Angular movements lower than 90° were considered local rearrangements rather than inversions. We confirmed results from previous studies, that ~50% of hair-cell dyads inverted, whereas the other half underwent transient rocking movements that did not result in a net positional exchange between the cells (Wibowo et al., 2011; Mirkovic et al., 2012; Ohta et al., 2020). We also found a similar frequency of inverting and stationary cell pairs in horizontal and vertical neuromasts (56.3% and 47.4%, respectively).

We did not see any significant bias from these rules when comparing inverting cell pairs at different positions along the orthogonal axes of the neuromast, suggesting that the localization of the cell-pair within the organ does not determine or tune rotations (Fig. 1F). Moreover, we never observed hair cells translocating across the tissue, indicating the inversions are a purely local collective movement. To directly test whether the rotation is an active process autonomous to the inverting cell pairs or otherwise driven by the action of neighboring cells, we assessed the movement of every cell across the entire epithelium (Fig. S1A). We segmented cellular boundaries from live imaging of neuromasts expressing a plasma-membrane targeted EGFP. Then, we quantified the displacement of each cell using particle tracking while keeping the center of the neuromast spatially fixed (Movie 2). This allowed us to compute the Pearson correlation coefficient R for the trajectories in nine independent datasets. We found that the rotation of hair-cell pairs is highly anticorrelated ($R=-0.77$), reflecting local translocation of cells. This was expected given that the trajectory of each hair cell is almost perfectly mirror-symmetric relative to the centroid of the cell pair (Fig. 1E). However, we found that epithelium-wide cellular movement is uncorrelated ($R=0.14$). This means that the movement of any one cell did not correlate with that of any other cell taken at random, indicating no coherent epithelium-wide cellular flow. Importantly, the movement of the rotating cell pairs is uncorrelated with the rest of the epithelium ($R=0.07$), indicating that rotations are not driven by any fixed anisotropic force (Fig. 1G). These data further reinforce the conclusion that cell-pair inversion is an autonomous active process of physically confined nascent hair cells.

Cell-pair inversion is triphasic and characterized by temporally correlated strong homotypic contacts and coordinated heterotypic junctional remodeling

Evolving changes in cell shape as well as junctional interphase length and shape indicate the dynamics of forces acting upon cells. This includes intrinsic intra- and inter-cellular forces as well as extrinsic forces from neighboring cells (Maire and Heisenberg, 2011; Yap et al., 2018; Lenne et al., 2021). Therefore, we decided to investigate the above morphological features during the rotations. To this end, we established a generalizable standard to benchmark this and future studies by continuously measuring the positional angle of rotating cell pairs and computing the absolute cumulative angle over time. Using a four-parameter logistic function that provided a good fit for the empirical data, we found that cell-pair rotations can be clearly split into three phases with

unique characteristics. Phase 1 is the period between the birth of the hair-cell pair and the onset of rotation, Phase 2 is the time where the main angular movement occurs and Phase 3 follows the end of active rotation until the cell pair reaches its final position (Fig. 2A).

The three phases differ in several important ways. In rotating cell pairs, the distance between the center of each cell remains constant during Phase 1, drops significantly during Phase 2 and then increases again in Phase 3 (Fig. 2B). In Phase 1, the cumulative angle of movement stays close to 0. Phase 2 starts with a rapid change in the cumulative angle, ending within a maximal rotation of 180° at Phase 3. Fig. 2C shows one example of a rotating pair. During Phase 2, the circularity of the cell pair is low in Phase 1, high throughout Phase 2, and decreases sharply at Phase 3 (Fig. 2D), revealing that both cells deform in a correlated manner (Fig. S1B). Coincidentally, there is a conspicuously fast change of the homotypic interphase (common junction) between the inverting cells, growing to a maximum during Phase 2, and shrinking again in Phase 3 (Fig. 2E). Also, the variation in circularity of the cell pair and of the length of their common junction correlate during all three phases (Fig. 2D-F; Fig. S1C). Importantly, none of these variations were observed in non-inverting pairs (Fig. 2F; Fig. S1D).

Rotating cell pairs *in vitro* display an invariant sigmoidal common junction (previously called 'Yin-Yang shape' in various *in vitro* and theoretical studies) (Brangwynne et al., 2000; Huang et al., 2005; Leong, 2013; Li and Sun, 2014). Notably, *in vitro*, the polarity of the sigmoid and the handedness of the rotations are always correlated, in that cell pairs rotate anti-clockwise upon S-shaped junctions and clockwise when junctions are 2-shaped (Huang et al., 2005). This correlation has been explained by the effect of a front-end lamellipodium of one cell wrapping the trailing edge of the other cell (Brangwynne et al., 2000), which led to the conclusion that cells neither push, nor pull one another during rotations (Brangwynne et al., 2000). However, theoretical analyses concluded that the cells must employ rear pull during rotations (Camley et al., 2014; Leong, 2013). We decided to explore this provocative idea of rotating cells *in vivo* by classifying their homotypic interphase into four categories (Fig. 3A). Two of them are non-chiral: linear shape (I), and curved shape (C). Note that the C mirrored junction is non chiral because it can be rotated back: $C \Leftrightarrow C$. The remaining two are chiral (S and 2) because they cannot be rotated into one other. By measuring interphase across focal planes in Phase 2, we found that in the majority of the cases they are symmetric and linear (I-shaped). Although we observed some S and 2 shapes, we found no correlation between their handedness and the direction of rotation (Fig. 3B; Movie 3).

Notch1a and Emx2 differentially affect cell-pair rotations

The above results led us to hypothesize that sibling hair cells interact symmetrically with the adjacent epithelial cells. This is intriguing given that sibling hair cells are distinct from one another by virtue of their asymmetric Notch/Emx2 status (Jiang et al., 2017; Jacobo et al., 2019; Kozak et al., 2020; Erzberger et al., 2020; Kindt et al., 2021). Therefore, we searched for any consistent difference between sibling cells that may indicate that this molecular asymmetry is mechanistically linked to the rotation. To this end, we employed cellular- and temporal-resolved tracking to obtain a topological and dynamic representation of rotations (Movie 2). We extrapolated junctional dynamics by quantifying the difference in the number of neighbors of each hair cell at consecutive timepoints (Fig. 3C). Importantly, because the final position of each hair cell will reveal their Notch/Emx2 status, we could also retrospectively infer

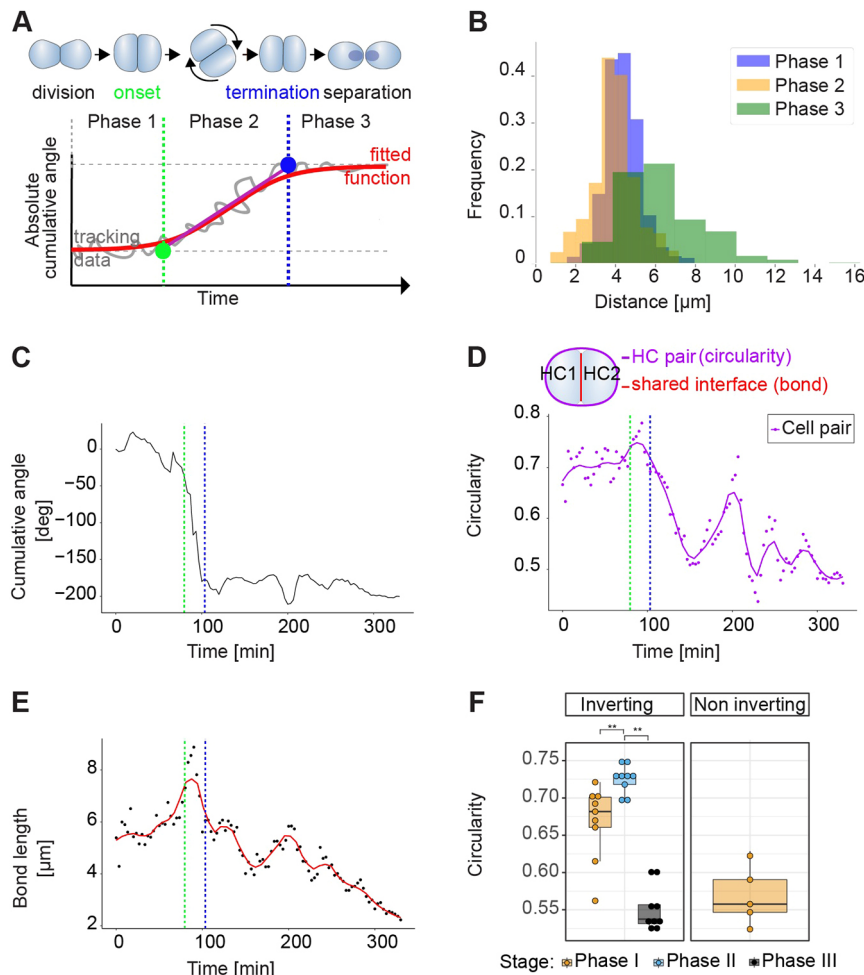


Fig. 2. Rotations are characterized by strong homotypic cell-cell interactions. (A) Scheme of an inversion (top) and fitting a four-parameter logistic function to the empiric data of the absolute cumulative angles (bottom), revealing the three phases of the inversion process. Green dot represents the transition between Phases 1 and 2, and the blue dot between Phases 2 and 3. These transitions are called onset and termination, respectively. (B) Distance between sibling hair cells (HC) during the three phases. Sibling cells are closest during Phase 2. (C) Time-resolved cumulative angular change (top) for a representative cell pair from Time 0. The two dashed vertical lines mark the beginning and end of the rotation. A negative angle change indicates a clockwise direction of rotation. (D) Circularity of the same cell pair, which, taken as a unit, reaches maximal circularity during Phase 2. The onset and termination of inversion are marked by dashed vertical lines. (E) Length of the junction between hair cell pairs, which is highest during Phase 2. (F) Comparison of mean circularity for inverting and non-inverting cell pairs during the three phases. Phase 2 is characterized by a significantly higher circularity than Phase 1, and the circularity drops dramatically in Phase 3. The circularity for non-inverting pairs is comparable to the Phase 3 of inverting pairs. Trivially, for non-inverting cells there is a single phase. $**P < 0.01$, Wilcoxon rank sum test. Box plots show median values (middle bars) and first (Q1) to third (Q3) interquartile ranges (boxes); upper whisker is either 1.5× the interquartile range or the maximum value (whichever is the smallest) and lower whisker is either 1.5× the interquartile range or the minimum value (whichever is the biggest). Each point represents the cells during a rotation.

whether a cell is Notch-off/*Emx2*(+) or Notch-on/*Emx2*(-) before the onset of inversions in Phase 1. We hypothesized that, if neighbor exchange over time was symmetric, when one hair cell loses a neighbor it immediately recovers by gaining a new neighbor and vice versa. This is true even if the exchange of neighbors were not simultaneously experienced by both hair cells. Symmetry means that the difference between the number of neighboring cells that the rotating siblings will have is always zero. Any departure from zero indicates that the contact of Notch-off/*Emx2*(+) and Notch-on/*Emx2*(-) cells with neighboring epithelial cells is consistently different (that is, invariably asymmetric). Of note, cellular proliferation and death are negligible during the recording period, effectively ruling out neighbor gain or loss via changes in cell number. As expected, we found that the difference in the number of neighbors is zero for non-inverting cell pairs because they do not exchange neighbors (Fig. 3D). For inverting pairs, the accumulated sum diverged from zero from birth, indicating that one of the hair cells (that we call ‘popular’) consistently has more neighbors than its sibling (Fig. 3D), which is maintained throughout the rotation. Importantly, however, the identity of the popular cell could not be predicted from the dynamic data, indicating that the Notch/*Emx2* status of a cell does not correlate with its popularity. These results led us to hypothesize that Notch/*Emx2* asymmetry does not determine rotations, and that neither cell drives the movement. Importantly, this idea is in partial disagreement with the current model, which states that *Emx2* is dispensable for rotations, whereas *Notch1a* is essential (Ohta et al., 2020; Erzberger et al., 2020).

Therefore, we decided to directly test it using self-consistent experimental conditions, data acquisition and analysis. We recorded rotations in fish carrying homozygous loss-of-function mutations in *Emx2* (Movie 4) or *Notch1a* (Movie 5). We first confirmed that rotations happen at normal frequency in *emx2* mutants (Fig. 3E) (Ohta et al., 2020). However, they are marginally less frequent in *notch1a* mutants (Fig. 3E). Put together, these data indicate that cell-pair rotation is characterized by co-occurring increase of hair-cell homotypic interactions and coherent heterotypic junction remodeling. Furthermore, the Notch-off/*Emx2*(+) and Notch-on/*Emx2*(-) cells participate in the rotation in an indistinguishable manner.

Intrigued by the previous results, we decided to perform a more detailed quantitative analysis of rotations across the three phases, comparing wild-type specimens with those carrying loss-of-function mutations in *Emx2* and *Notch1a* (Fig. S1E-G). We found that the rotations in the wild type were approximately equally frequent in the clockwise and anti-clockwise directions. Similarly, *emx2* and *notch1a* mutants had negligible handedness bias (Fig. 4A). Following this, we fitted a sigmoid function to each rotating trajectory with respect to time to unbiasedly define the boundaries between the three phases (Fig. 2A; Fig. S1H-J). The onset of the active rotation phase (start of Phase 2) was typically ~100 min after the birth of the hair cells, but with noticeable variability. We found that the start of Phase 2 was marginally delayed in *emx2* mutants, but significantly accelerated in *notch1a* mutants (Fig. 4B). The duration of Phase 2, however, did not differ

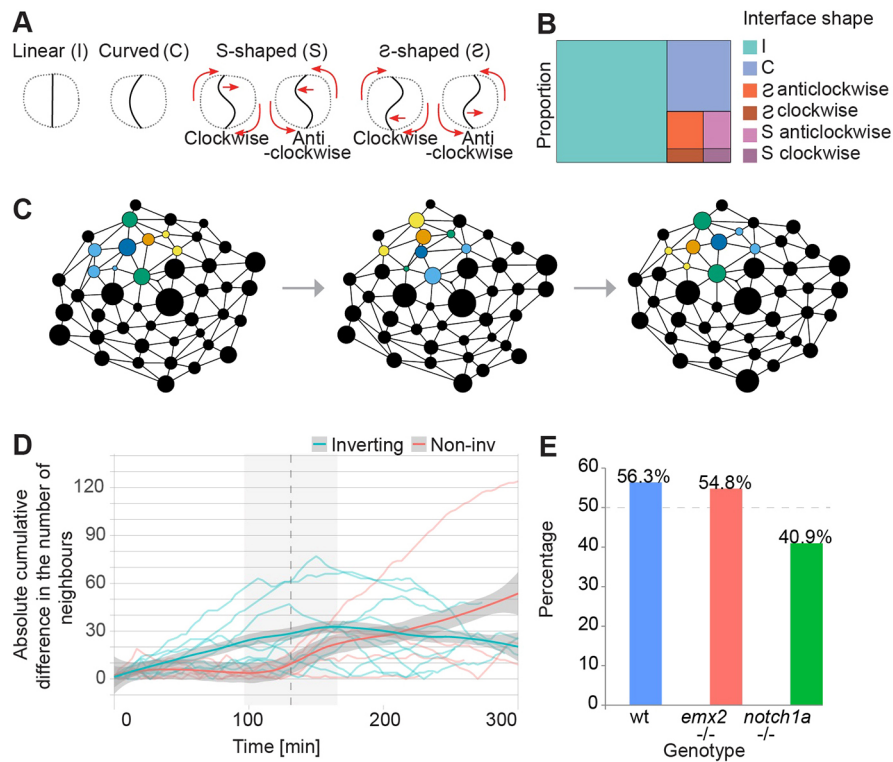


Fig. 3. Notch1a/Emx2 asymmetry is dispensable for cell-pair rotations. (A) Illustration of the cell-cell interfaces, shapes of which are classified as curved (C), linear (I), S or Z shaped. Because an Z cannot be rotated into an S, a distinction is made of the rotation direction. (B) The frequency of distinct interface shapes during inversion. The most common shape is a straight interface (63.41%), followed by curved (21.31%) and then S-shaped curves (S: 6.57% and Z: 8.7%). No shape consistently correlated with the chirality of rotation. (C) Scheme of the topological interactions between all epithelial cells during the inversion of a cell pair (representing one empirical example). Each circle is an individual cell. The area of each circle is proportional to the area of real cells from microscopy images. Straight lines (edges) represent a physical contact between any two cells. Cells are considered neighbors if there is an edge connecting them. A pair of hair cells is colored blue and orange. Neighboring cells are colored light blue if they connect only to the blue sibling in a given frame; yellow if they only connect to the other sibling; or green if they are connected to both. (D) Absolute cumulative difference in the number of neighbors for each cell of inverting (blue) and non-inverting (red) pairs. The difference of neighbors at a given time is the number of neighbors of Cell A minus the number of neighbors of Cell B. The cumulative difference at any given time T is the sum of the neighbor differences from time 1 to time N. Therefore, if there is no cell with a constantly higher number of neighbors over time, the cumulative difference remains close to zero. However, if either one of the cells constantly has more neighbors, over time the absolute cumulative difference will go up. Vertical dashed line and gray shaded areas mark the median and standard deviation of the Phase 2I for the inverting cells in this sample. Shown is the LOESS smoothing of inverting and non-inverting trajectories. (E) Fraction of hair-cell pairs that invert in wild type, *emx2* mutant and *notch1a* mutant larvae. *n* (number of cell pairs)=71 from wild type, 42 from *emx2* mutant, 22 from *notch1a* mutant larvae.

between the three genotypes (Fig. 4C). As a consequence, cell-pairs in *notch1a* mutants arrived at Phase 3 earlier than in wild-type and *emx2* mutants (Fig. 4D).

Effect of Notch/Emx2 asymmetry on the accuracy and precision of rotations

Tissue patterning is affected by both the accuracy and the precision of underlying dynamical processes (Mestek Boukhibar and Barkoulas, 2016). Importantly, although precision and accuracy are often used interchangeably, they represent non-trivial different parameters. A precise process displays a tight distribution of data points, regardless of the mean value. In other words, it has low variance. By contrast, an accurate process has a specific and consistent mean value, regardless of the actual variance of data points. It follows that loss of accuracy leads to an invariant scattering of data but with a significant deviation from mean values (akin to consistent but non-noisy changes), whereas a loss of precision will show higher scattering of data points but with non-significant changes in the mean values (akin to a noisier distribution). This distinction is important because it allows us to

better compare wild-type, *emx2* and *notch1a* mutant specimens, to shed light on the aspects of the inversion process that are influenced by genetically-determined cell identity or cell-pair asymmetry. We first focused on the transition between Phases 2 and 3. Namely, whether cell pairs arrive at their final position in one single movement or whether they overshoot and then re-align to the main axis of the organ by either a single corrective movement or multiple approximating rocking movements. As a measure of overshoot, we subtracted the final turn (the final absolute cumulative angle) from the maximal turn (the maximal absolute cumulative angle) of the cell pair. We saw rare events of cell pairs performing a double inversion or reversals, arresting in their original position. These exceptional cases were equally frequent in all three genotypes (Fig. 5A,B). In most cases, the values of the maximal turn and the final turn were very close (Fig. 5B).

When measuring the whole angular movement, it became evident that rotations are not strictly monotonous because they include small-scale and recurrent swings, which we call ‘wobbling’. To quantify wobbling, we estimated the arc-length by summing the absolute angular changes. We found high wobbling in *emx2* mutants, and even

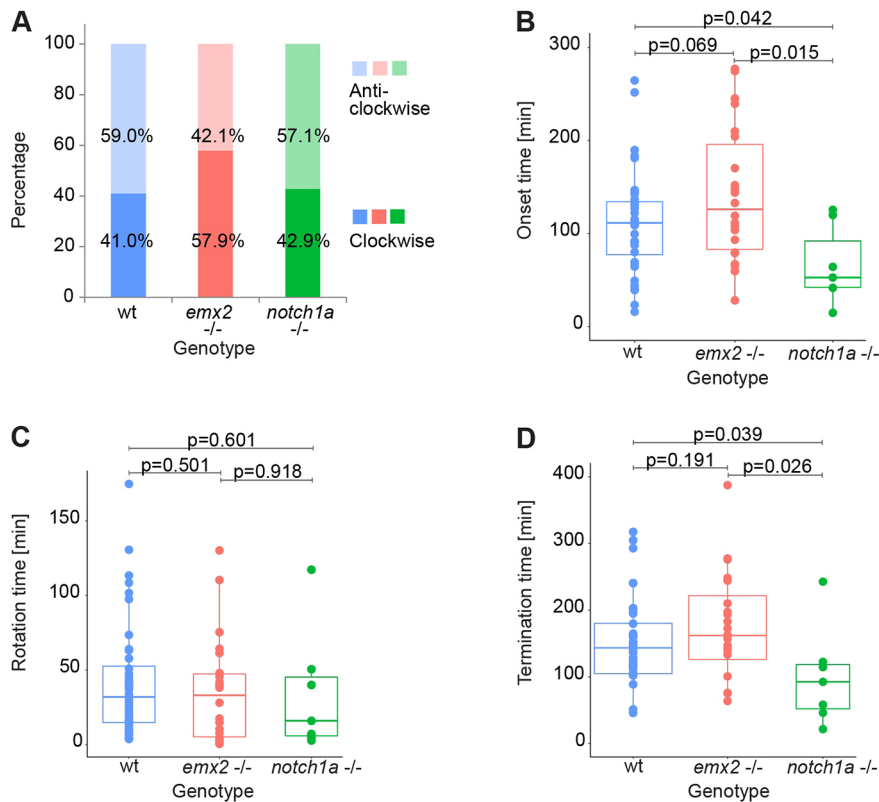


Fig. 4. Loss of Notch1a but not Emx2 impacts cell-pair rotations. (A) Handedness of cell-pair inversions in wild-type, *emx2* and *notch1a* mutant larvae. (B) Comparison of the onset (duration of Phase 1) of inverting cell pairs from wild type, *emx2* and *notch1a* mutants. (C) Comparison of the rotation duration (Phase 2) of inverting cell-pairs from wild-type, *emx2* mutant and *notch1a* mutant larvae. (D) Comparison of the termination time (Start of Phase 3) of inverting cell pairs from wild-type, *emx2* mutant and *notch1a* mutant larvae. (A-D) *n* (number of cell pairs)=40 from wild-type, 23 from *emx2* mutant, 9 from *notch1a* mutant larvae. Statistics were calculated using an unpaired two-sided Student's *t*-test. Box plots show median values (middle bars) and first (Q1) to third (Q3) interquartile ranges (boxes); upper whisker is either 1.5× the interquartile range or the maximum value (whichever is the smallest) and lower whisker is either 1.5× the interquartile range or the minimum value (whichever is the biggest). Each point represents the cells during a rotation.

higher in *notch1a* mutants (Fig. 5C). We further calculated noise as a related but unitless quantity of regularity, defined as the arc length of each trajectory normalized by the shortest path from starting to final position. The distributions for each experimental condition were statistically different (Fig. 5D), in that rotations were noisy in *emx2* mutants, and much noisier in *notch1a* mutants.

Next, we compared the initial and final positional angles (Phase 1 versus Phase 3). The initial angle corresponds to the position of the hair cells immediately after they are born. In the wild type, hair cells arise with a full spectrum of initial angles, but through rotations, the distribution of final angles becomes remarkably biphasic: either lower than 50° or higher than 150° (Fig. 6A). Note that a positional angle of either 0° or 180° means a perfect alignment with the anteroposterior axis of the neuromast. We speculated that the significant angular variability of Phase 1 (initiation) may be buffered through Phase 2 (active rotation) to reach a remarkably invariable alignment of the cells in Phase 3 (termination). The initial alignment of the cell pairs influences rotation handedness in order to undergo the lowest possible angular change (Fig. 6B). In other words, inverting cell pairs arising at 0° will tend to rotate 180°, whereas cells arising, for example at 30°, will rotate 150° rather than 210° in the opposite direction. We found the average final turn of rotating cell pairs is indistinguishable in wild type and *emx2* mutants, but larger in *notch1a* mutants (Fig. 6C). However, the final angle distributions in both mutants were significantly different from the wild type (Fig. 6D).

A computer model of the inversion suggests that intercellular asymmetry simultaneously underlies rotational and positional precision

Our understanding of the mechanism governing the robustness of cell-pair inversions *in vitro* has enormously benefited from accompanying the experimental studies with solid theory. However, a theoretical framework of inversions *in vivo* has not

yet been established. To remedy this shortcoming, we decided to develop a naïve computational model of inversions *in vivo*. We emphasized the rotational wobbling during Phase 2 and also the termination that corresponds to Phase 3. The reason behind this choice is that these events represent the main dynamic process of the inversion and are the ones experiencing the most significant deviations between the three genotypes analyzed in this study. First, we simulated the cell dyad as two particles that can freely rotate within a single plane about an orthogonal axis (Fig. 7A,B). This is appropriate because there is no evidence of anything preventing rotations once they start, and we hardly ever witnessed any off-place inversion. Of note, it is equivalent to having the rotational angle with respect to the *x*-axis as the only degree of freedom. Moreover, the *x*-axis was set to coincide with the anatomical anteroposterior axis of the neuromast. Because experimental data show that the final angle of wild-type cells falls within a narrow distribution (Fig. 6D), we reasoned that certain locations are strongly preferred. Therefore, we introduced attractive potentials into the model. Specifically, each cell is affected by an attractive potential modeled as a Gaussian well at a certain position in the circle, the depth of which represents the strength of the attraction. As our results indicate that only the inverting cell pair has a coordinated movement during the inversion process, we assumed that the role of the neighboring cells is to only confine the cell pair, with no active participation. Apart from the attraction wells, each cell of the pair interacts with each other through a soft sphere repulsion term, with an effective radius such that the cells are permanently in contact with one another, representing an effective spatial exclusion.

First, we tested a model in which each cell has its respective Gaussian well on the opposite sides of its location at the start of the inversion (Fig. 7A). Effectively, this means that a cell that appears in the anterior pole will have its minima in the posterior pole and vice versa. As each cell has its corresponding attractor in the opposite

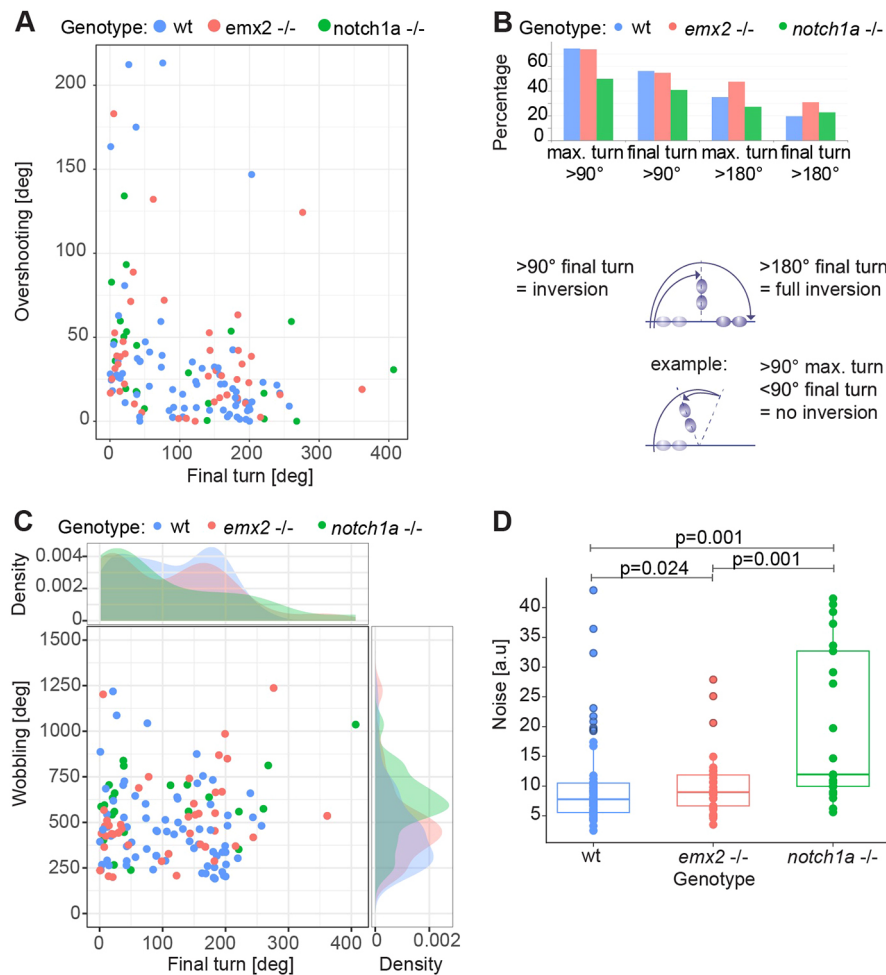


Fig. 5. Mutations in *notch1a* impact the precision of the inversion.

(A) Overshooting versus final turn in the rotations of cell pairs from wild type, *emx2* and *notch1a* mutants. We defined overshooting as the difference between the maximal turn and the final turn (absolute cumulative angle). (B) The maximal and final turns of >90° and >180° for cell pairs from wild-type, *emx2* mutant and *notch1a* mutant larvae. The sketches below illustrate the definition of categories with an example. (C) Comparison of cell pair wobbling and final turn. Wobbling was defined as the cumulative angle changes minus final turn. (D) Noise of rotating cell pairs was calculated as the arc length of each trajectory normalized by the shortest path from starting position to final position. Statistics were calculated using the Anderson-Darling test. (A-D) *n* (number of cell pairs)=71 from wild-type, 42 from *emx2* mutant, 22 from *notch1a* mutant larvae. Box plots show median values (middle bars) and first (Q1) to third (Q3) interquartile ranges (boxes); upper whisker is either 1.5× the interquartile range or the maximum value (whichever is the smallest) and lower whisker is either 1.5× the interquartile range or the minimum value (whichever is the biggest). Each point represents the cells during a rotation.

side of the anteroposterior (A-P) axis, we call this model asymmetrical. We found that the rotation that we modeled *in silico* qualitatively matches the empirical data from the wild type, in that the cell pair performs a stochastic rotation until each cell reaches its respective well (Fig. 7C; Movie 6). Notably, we also observed that if only one of the cells has an attractive well, the resulting dynamics are indistinguishable from the case where both cells have an attractive well (Movie 7). Specifically, in this case, one of the cells will be directed towards the minima, driving the inversion, whereas the other cell will passively move due to the spatial exclusion defined above. Importantly, the Notch1a/Emx2 identity of the ‘driving’ cell is irrelevant. Our experimental data show that the cell-pair rotations take place also in *emx2* and *notch1a* mutants, in which the symmetry of Emx2 expression is not broken.

Accordingly, we also generated a symmetrical model, in which both cells have attractive wells on the same side of the circle and compete to arrive at it (Fig. 7B). In this model, the cells undergo rotation until they reach a compromise between their mutual exclusion and the attraction to the minimum of the wells (Fig. 7D; Movie 8). Trivially, the particular case in which one of the wells has a depth of zero matches the one-well situation (Movie 7). After proper parametrization (see Materials and Methods), we simulated our model and quantified the final angle achieved by the cell pairs and the noise of the angular trajectory, defined as the arc length of each trajectory normalized by the shortest path from starting to final position. We found that the asymmetrical model is in best agreement with the wild-type experimental data (Fig. 7E). Most importantly,

we found that in the symmetrical model the final angle strongly depends on the relative depth between the wells, but not on the absolute strength of attraction. Thus, when one of the wells has half the depth of the other, the final angle has a deviation of ~60° with respect to the *x*-axis (Fig. 7F). We also saw that noise in the asymmetrical model was consistently lower than in the symmetrical model (Fig. 7G). Symmetry in the cell attractors results in more variability in the final angle (Fig. 7E,F), as well as higher wobbling (noisier dynamics) (Fig. 7C versus D, and Fig. 7G).

DISCUSSION

Much of our understanding of multicellular rotations derives from experimental and theoretical studies of cells *in vitro* (Brangwynne et al., 2000; Huang et al., 2005; Tseng et al., 2012; Leong, 2013; Li and Sun, 2014; Camley et al., 2014; Segerer et al., 2015; Camley and Rappel, 2017; Brückner et al., 2021). Huang and colleagues proposed three essential conditions for cell-cohort rotation *in vitro*: (1) cells must be in a confined space; (2) cells should have a long-persistence time of intrinsic motility; (3) the cell dyad must be coupled by intercellular adhesion (Huang et al., 2005). Leong used interphase morphology and rotation chirality to introduce a particle-dynamics model to explain why dynamic coupling (the third condition) is essential for rotations (Leong, 2013). Along the same line, Camley and colleagues introduced a mean-field model to identify conditions under which cells would initiate a rotation (Camley et al., 2014). They proposed a confined system where each cell has a polarity defined by the evolution of a chemical signal.

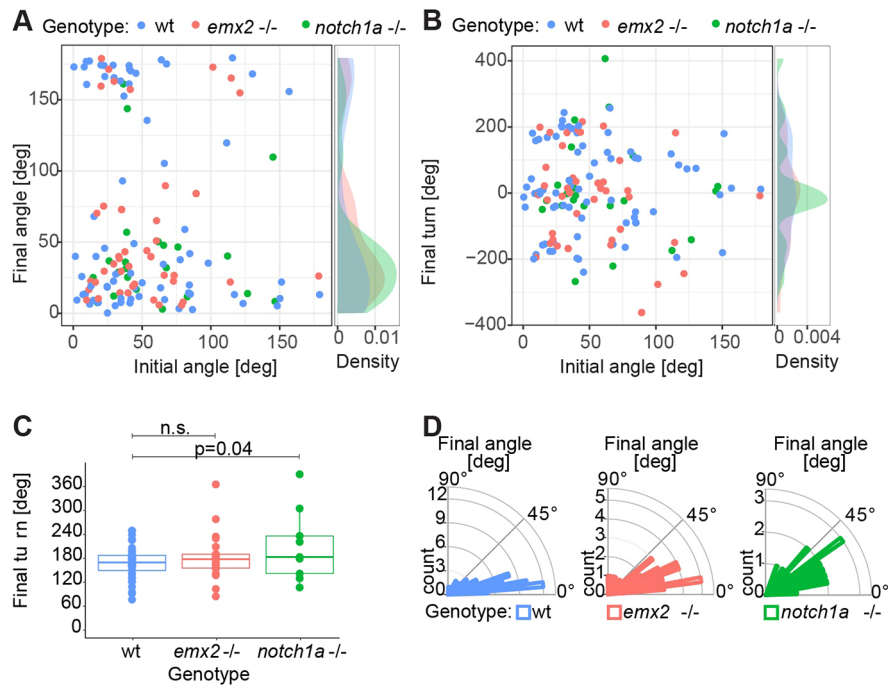
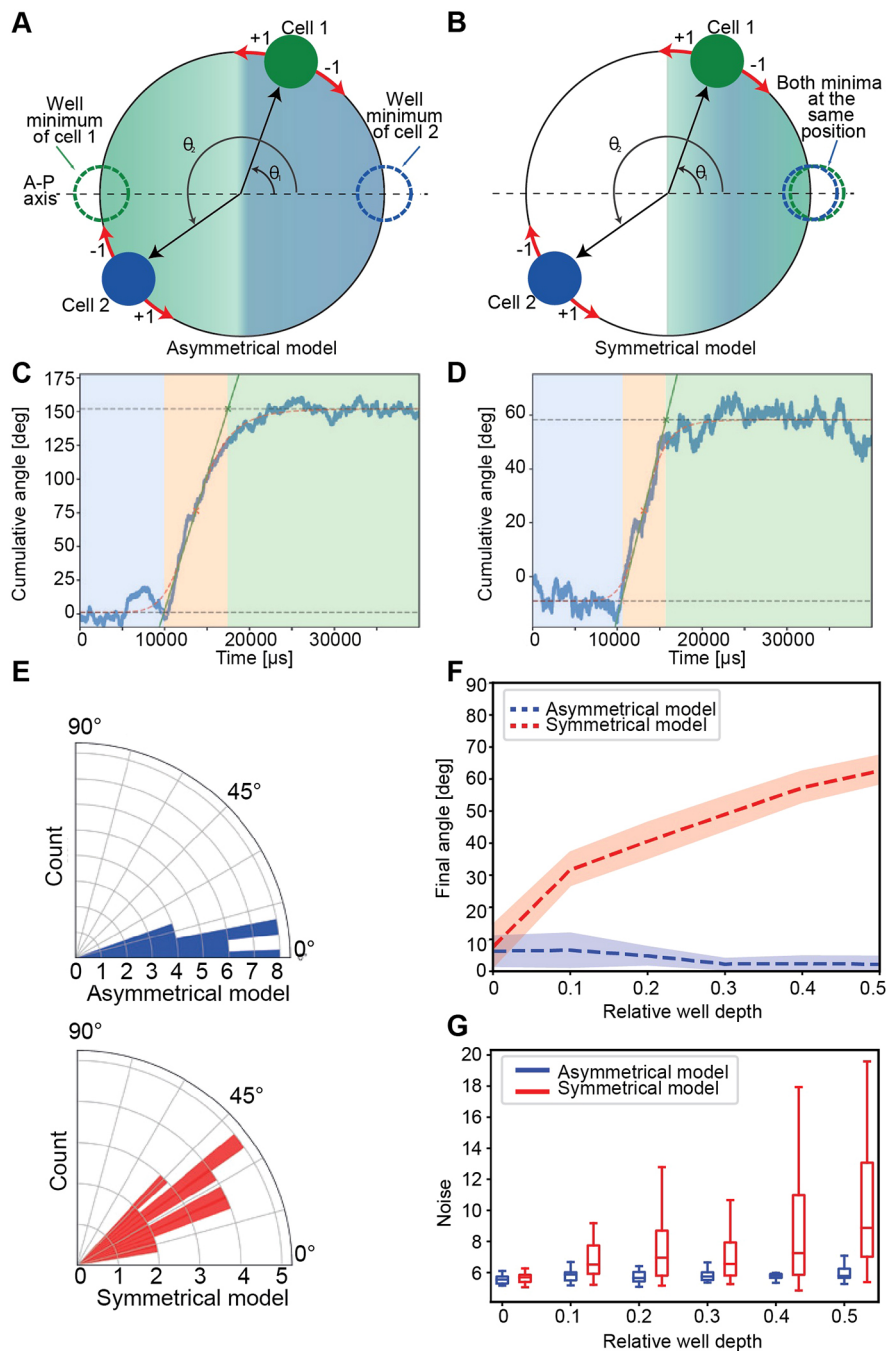


Fig. 6. Cell-pair asymmetry affects the precision and accuracy of Phase 3. (A) Relationship between the final and initial angles. The initial angle is the positional angle of the cell pair immediately after the division. The final angle is where cells come to rest (regardless of whether they have rotated). Note that both angles were normalized to 0-180° (from 0-360°). (B) Relationship between the initial angle and the final turn of cell pairs of wild type, *emx2* mutant and *notch1a* mutants. Note the initial angle was normalized to 0-180° (from 0-360°). (C) Comparison of the final turn of cell pairs from wild type, *emx2* mutant and *notch1a* mutant larvae. Statistics were calculated using an unpaired two-sided Student's *t*-test. Box plots show median values (middle bars) and first (Q1) to third (Q3) interquartile ranges (boxes); upper whisker is either 1.5× the interquartile range or the maximum value (whichever is the smallest) and lower whisker is either 1.5× the interquartile range or the minimum value (whichever is the biggest). Each point represents the cells during a rotation. (D) Final angle of cell pairs from wild type, *emx2* and *notch1a* mutants. The difference in the distribution of final angles from wild type and the two mutants are statistically significant ($P < 0.05$). Statistics were calculated using a two sample Kolmogorov–Smirnov test ($P = 0.004$ for wild type and *emx2* mutant, and $P = 0.01$ for wild type and *notch1a* mutant). (A–D) *n* (number of cell pairs) = 71 from wild type, 42 from *emx2* mutant, 22 from *notch1a* mutants.

Notwithstanding these insightful theoretical milestones, the generality and relevance of their conclusions to cells rotating in their natural context has remained unknown. In this study, we fill this gap by focusing on a minimal model of collective cell movement *in vivo* involving the coherent rotation of two cells. Combining experiment, quantitative videomicroscopy and computer simulation, we establish the first model underlying the emergence and coherence of cell-pair rotations *in vivo* (Fig. 8).

Previous studies have suggested that Notch1a-mediated symmetry breaking via *Emx2* is necessary for cell-pair inversions *in vivo* (Erzberger et al., 2020). Yet, independent work that forced symmetrical expression of the Notch1a target *Emx2* showed marginal non-significant effects on rotations (Ohta et al., 2020). We interpreted this disagreement as suggesting that either genetically-determined cell-pair asymmetry via Notch1a/*Emx2* and cell-pair inversions are epiphenomena, or that Notch1a controls rotations independently of its only known transcriptional target in neuromasts (Jacobo et al., 2019; Kozak et al., 2020). To address this discrepancy, we used a novel approach to quantitatively analyze the inversion process. We confirmed the predicted dispensability of *Emx2* but, unexpectedly, found that ~40% of hair-cell pairs inverted in specimens lacking Notch1a. We further demonstrated that neither *Emx2* or Notch1a activity, nor Notch1a/*Emx2* asymmetry between sibling cells, are essential for cell-pair rotations *in vivo*. These results allow us to consider various possibilities to explain the discrepancy of previous conclusions. First, neomorphic or gain-of-function mutant alleles in the genes

under study may produce an atypical function that affects rotations (Guichard et al., 2002; Langdon et al., 2006), which may have led to the erroneous conclusion that Notch1a activity is essential for rotations. Second, passenger mutations are not uncommon across the genome of the zebrafish strains used in nearly every laboratory. Because previous studies used a single Notch1a mutant allele, the molecular profile of which remains unknown, and no rescue experiments were reported, this possibility cannot be overlooked (Erzberger et al., 2020). To solve these issues, we have combined unambiguous high-resolution quantitative determination of inversions, comprehensive statistical tests and two independently-generated *notch1a* mutant alleles, the molecular lesion of which has been well characterized, and from which we obtained an indistinguishable phenotype (Kozak et al., 2020). We found marginal statistical differences in rotation frequency between all three genotypes. Our results are unlikely to result from partial penetrance of the two *notch1a* mutant alleles that we have used because both had a very strong effect on other previously well-characterized phenotypes: neuromast epithelial bipolarity and somitogenesis (Kozak et al., 2020). Unexpectedly, however, we found that the loss of Notch1a produces noisier rotations without changes in mean values. This suggests that neither Notch1a activity nor Notch1a-mediated asymmetry impact the active or resistive forces that underlie rotations, and reveals that both Notch(on) and Notch(off) hair cells participate equally in the movement. In addition, although rotating cells consistently interact asymmetrically with the surrounding epithelium, their Notch/*Emx2* status does not correlate

**Fig. 7. Computational modeling of cell-pair inversion.**

(A,B) Sketch of the two-cell computational model. Each cell freely rotates around a circle of a fixed radius, with its angle with respect to the x-axis (representing the A-P axis) as the degree of freedom for each cell. The arrows in each cell indicate the direction as +1 or -1 for anti-clockwise and clockwise movement, respectively. Each cell is attracted to one and only one Gaussian well. The depth of each well determines the strength with which its corresponding cell is attracted. The depth of one well can be different from the other. (A) In the asymmetrical model both cells have their attractive wells on opposite sides of the A-P axis. (B) In the symmetrical model both attractive wells lie on one side of the system, leading to a competition. (C,D) Two typical trajectories of the inverting pair in cumulative angle, as defined in Fig. 2C, for the asymmetrical and symmetrical model, respectively. The background colors indicate the phases of the process: blue (Phase 1), orange (Phase 2), green (Phase 3). (E) Distribution of final angles predicted by both models. Well depths are 0 and 50 (relative well depth=0) for the asymmetric model, and 50 and 20 (relative well depth=0.4) for the asymmetric model. (F,G) The final angle (F) and the noise (G) predicted by the asymmetric (symmetric) model are robust (sensitive) against the relative well depth. The depth of the reference well was fixed at 50 in these simulations. Asymmetric and symmetric models are represented in blue and red, respectively. Box plots show median values (middle bars) and first (Q1) to third (Q3) interquartile ranges (boxes); upper whisker is either 1.5 \times the interquartile range or the maximum value (whichever is the smallest) and lower whisker is either 1.5 \times the interquartile range or the minimum value (whichever is the biggest).

with this asymmetry. Finally, the loss of *Emx2* or *Notch1a* did not affect the speed of the rotation. Therefore, we conclude that *Notch1a* is not essential for inversions, and that both cells participate equally in the angular movement. We envision that it is not the action of *Notch1a* itself, but instead that of *Notch1a*-mediated cell-pair asymmetry which impacts rotational precision by generating a slight but persistent bias in microscopic dynamics. This leads to an increase in macroscopic coordination, with the consequent reduction of dynamic noise. Importantly, these findings reveal unanticipated latent control of rotational precision *in vivo*.

Moreover, we investigated the extent to which cell-pair inversion *in vivo* is a result of non-autonomous forces. We found no correlation between cell-pair rotations and epithelium-wide cellular flow, indicating that there are no anisotropic resistive forces from the

surrounding epithelium. Alternatively, if anisotropic forces exist, they are not stably oriented (Yap et al., 2018; Bodor et al., 2020). We found that Phase 1 is unpredictable and highly variable, and that the onset of Phase 2 is very fast, strongly suggesting that Phase 1 is marked by instability. The dynamics of Phase 2 have low variability across the arc described by the cell pair. Although wobbling is noticeable, the rotational movement is persistently directional. Inertia is unlikely to explain persistence given the extremely low Reynolds numbers of biological tissues (Hakim and Silberzan, 2017). Instead, we speculate that directionality is driven by a 'leaky' ratchet mechanism that allows persistence despite wobbling (Caballero et al., 2020). Under this scenario, persistently directional rotations will emerge by spontaneous self-generating reciprocity between cells in physical confinement. This is further supported by

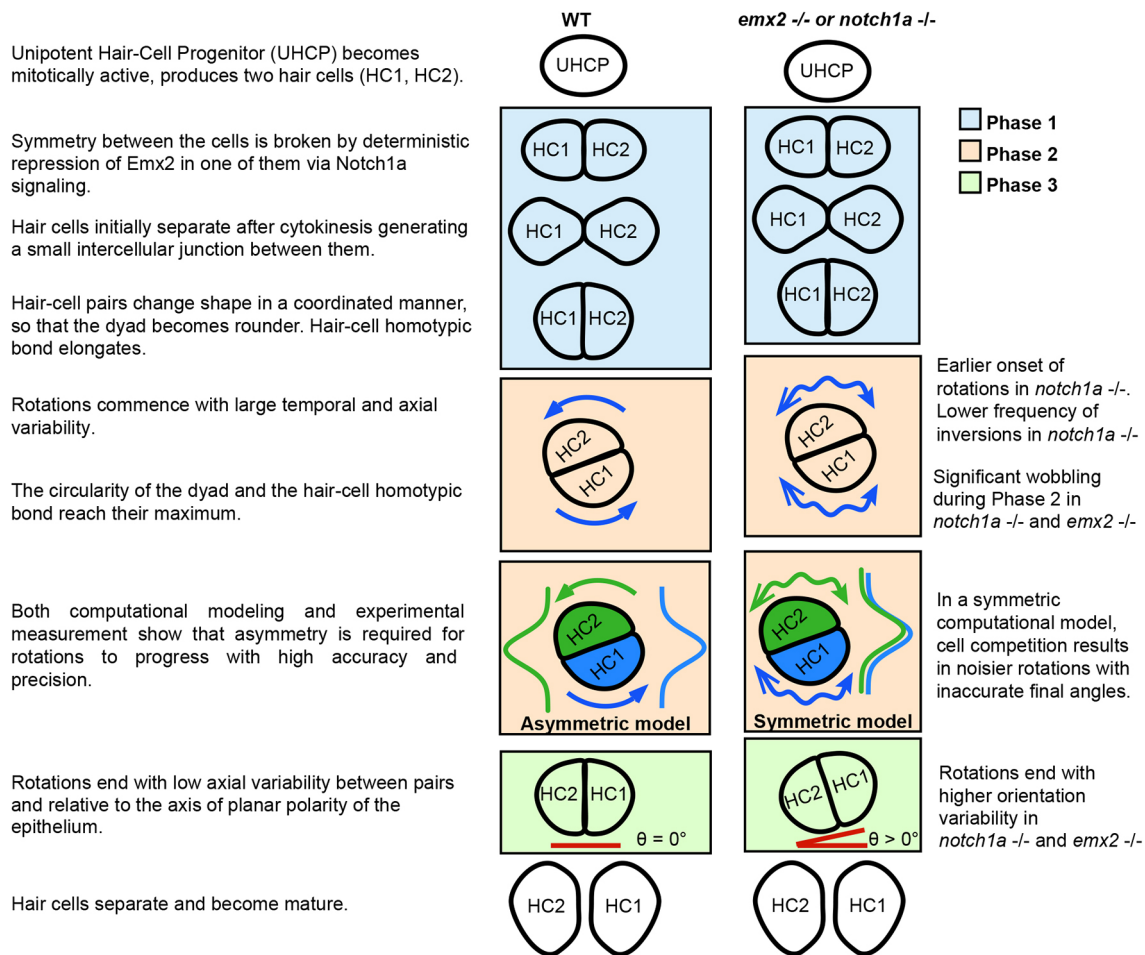


Fig. 8. A model of cell-pair rotation *in vivo*. Overview of cell-pair inversion process summarizing the key elements of the inversions in wild type on the left, and stating major differences occurring in the *notch1a*^{-/-} and *emx2*^{-/-} larvae on the right. The precision of the angular movement *in vivo* approaches that of cells *in vitro*. Phase 1 starts immediately after division of the UHCP, is characterized by a coordinated shape of the cells and expansion of the homotypic bond. Phase 2 marks the maximum of circularity of the dyad, the length of the homotypic bond and of angular velocity. Mutant rotations are characterized by significant wobbling, denoted by double-headed arrows. A computational model recapitulates this dynamic difference just by assuming that the minima of energy potentials are either symmetric or asymmetric (green and blue curves represent the Gaussian wells to which minima the respective cells are attracted in our computational model). In Phase 3 the angle between the cells and the A-P axis (blue lines) is 0 with high accuracy and precision but it is misaligned in mutants. The symmetric and asymmetric models can also explain these differences.

the observation that the interphase between inverting cells is symmetric and linear (I-shaped) in the majority of the cases. Although we did find some S and 2 shapes, their handedness did not correlate with the direction of the rotation. This suggests that rotating cells *in vivo* do not exert consistent pulling or pushing forces upon one another. Therefore, rotating cell pairs in neuromasts may represent a vertebrate example of ‘contact following’, a mechanism that has been put forward to explain the coherent motion of *Dictyostelium* cells when they form circular rotating cohorts (Umeda and Inouye, 2002).

The molecular mechanism governing the extent (discontinuity) of the rotation (Phase 3) remains enigmatic. However, we also used a naïve computational model to advance on this question. We generated two models, called symmetrical and asymmetrical. Both models include a Gaussian well of minimal energy on the opposite sides of the location of each cell of the dyad at the start of the inversion process. However, in the asymmetrical model each cell has its corresponding attractor in the opposite side of the A-P axis of the neuromast. In the symmetrical model, both cells have attractive wells on the same side of the neuromast and compete to

arrive at it. The symmetrical model best explains the experimental results of *emx2* and *notch1a* mutants, by assuming a different relative affinity for each set of potentials. By contrast, the asymmetrical model better recapitulates the robustness and final positions of the wild-type scenario. Hence, our theoretical framework suggests that the relative asymmetry of the cell attractors is the crucial element that underlies the robustness of the inversion process *in vivo*. Moreover, by testing models that recapitulate empirical data, we suggest that rotational movement will cease once the two-cell system reaches a low energy state (higher stability). Therefore, movement ceases when a ‘potential well’ or local minimum of potential energy exists, towards which the system will invariably and inevitably converge. This idea also explains another outstanding question: why do half of the cell dyads never rotate? Our model suggests that this occurs because a stable state takes hold before the coordination of local instabilities that leads to rotation can take place. Importantly, this argument would imply that the loss of *Notch1a* may not necessarily accelerate Phase 1 as we stated above, but simply prevent the late-onset rotations from taking place, coincidentally skewing the

onset towards lower values and decreasing the frequency of inversions.

We conclude that dyads of genetically equivalent cells can rotate if they are in a metastable state during which they experience persistent instabilities that enable them to move. A co-occurring spontaneous coordination of unbiased cellular motion would initiate rotations, whereas coherent homotypic interactions and heterotypic junction remodeling will enable directional persistence. Notch1a-mediated symmetry breaking between sibling cells acts as a stabilizer of the rotation. Our theoretical framework is important because it also suggests that relative asymmetry, rather than absolute attractiveness of potential wells, is the crucial element that underlies the robustness of the inversion process. This study exemplifies the power of combining high-resolution quantitative data with computational modeling to further understand the relationship between stochastic and deterministic processes underlying multicellular dynamics *in vivo*.

MATERIALS AND METHODS

Zebrafish lines and husbandry

Zebrafish larvae (*Danio rerio*) were kept under standard conditions at 28.5°C. The transgenic lines myo6b:β-actin-GFP (Kindt et al., 2012) and *Tg[-8.0cldnb:lyn-EGFP]* (Haas and Gilmour, 2006), and the *emx2*LOF mutant line (Jiang et al., 2017) have been previously described. Notch1a CRISPR mutagenesis has been described in Kozak et al. (2020). We recovered two indel alleles *hzm17* and *hzm18*. *hzm17* is an indel disrupting the *notch1a* ORF at exon 16 and is kept in the myo6b:β-actin-GFP transgenic background. *hzm18* is an indel causing the loss of part of exon 3 of *notch1a* and is kept in a myo6b:β-actin-GFP; *claudnb:lyn-EGFP* double transgenic background. Experiments were carried out either by crossing *hzm17* to *hzm18* or in-crossing *hzm18*.

Imaging, image processing and data extraction

The time-lapse movies were generated using 2-3 days postfertilization MS222-anesthetized larvae mounted in 1% low-melting point agarose in a glass-bottom Petri dish. Up to five larvae were imaged simultaneously using a Zeiss custom-built inverted spinning-disc confocal microscope with a 63× water-immersion objective. For each stage position, stacks of 16-20 z-slices 1 μm apart were acquired every 200 s. In the videographs, newborn hair cells were identified retrospectively by playing the movies backwards from the time when hair cells can be unambiguously defined using validated transgenic markers (López-Schier and Hudspeth, 2006; Kindt et al., 2012). All 4D movies were processed using FIJI software (Schindelin et al., 2012). Stacks were centered by laying point regions of interest at timeframes of significant drift and then running the Manual Drift Correction plugin. Nine inverting pairs and five non inverting pairs were selected for image segmentation and were further registered for z-slice drifts using the plugin Correct 3D drift (Parslow et al., 2014).

Comparison of cell-pair inversion

Nascent hair cells were manually tracked from the moment of division at a minimum 300 min with the MTrackJ plugin (Meijering et al., 2012). Cell tracking data (71, 42 and 22 cell pairs from wild type, *emx2* and *notch1a* knockouts, respectively) was imported into R (version 4.0.3), where all subsequent analysis was carried out. Individual cell positions were centered in pairwise fashion and observation time was limited to 500 min. For each observation time except the first, change in angle between cells relative to previous observation was calculated, positive angle denoting anti-clockwise rotation. Furthermore, for each cell pair and each observation time, cumulative angle (sum of angle changes) and absolute cumulative angle (named turn) were calculated. For each cell pair, starting angle and final angle were calculated as means of first ten or last ten observations, respectively. Final cumulative angle (final turn) and final cumulative absolute angle change were extracted as respective values at last observation. Critical angle defining planar cell inversion

was set to 90°. If final cumulative angle change was higher than this critical value, the cells were considered to perform planar cell inversion. Two-sided binomial test was used to calculate statistics on the occurrence of cell-pair rotations in different genotypes relative to wild type. For the cell pairs that did undergo an inversion, a four parameter log-logistic curve was fitted to the cumulative angle using python 'scipy.optimize' library. The form of the logistic used was:

$$f(t) = c + \frac{d - c}{1 + (t/a)^b},$$

where t is the time, and a , b , c and d are the parameters to fit. Here, a is the time of the logistic midpoint, b is the steepness, c marks the low asymptote and the high asymptote.

Start and end times of inversion (I_c and I_d) were calculated as the points where the tangent line through the inflection point and the low and high asymptote intersect, respectively:

$$I_c = \frac{c - f(a)}{\frac{b(c-d)}{4a} + a} \quad I_d = \frac{d - f(a)}{\frac{b(c-d)}{4a} + a},$$

where $f(a)$ is the fitted logistic function described above, evaluated at time a .

The noise was defined as the quotient between the real path traveled by the cell and the shortest path from start to end position according to:

$$W_j = \frac{\sum_{t=0}^{N-1} |r_j(t+1) - r_j(t)|}{|r_j(N) - r_j(0)|},$$

where $r_j(t)$ is the position of cell j at time t in the xy -plane, and N is the number of frames in the experiment. Only the first 200 frames were used for this calculation. Those experiments where one of the two sibling cells moved less than 2 μm were not taken into account for the analysis. The resulting distributions for noise, as defined above, were analyzed by pairwise comparison using an Anderson-Darling test (AD) to see whether samples could be drawn from the same underlying distribution and with a Wilcoxon-Mann-Whitney statistic (WMW) to test the alternative of the first distribution being stochastically less than the other. The P -values for the noise with both tests were: wild type versus *emx2*^{-/-}, AD $P=0.024$, WMW $P=0.022$; wild type versus *notch1a*^{-/-}, AD $P<0.001$, WMW $P<0.0001$; *emx2*^{-/-} versus *notch1a*^{-/-}, AD $P<0.001$, WMW $P<0.0001$.

Topological analysis of neuromast cells during hair cell inversion

After registration, one z-slice per time point was selected, taking 10 timepoints before division and at least 70 after. To segment membranes, we used the Autocontext workflow from *ilastik* v1.3.3 (Kreshuk and Zhang, 2019). As we used the double *cldnb:lyn-EGFP*; myo6b:β-actin-GFP transgenic, we trained in a first step, the probability of pixels to belong to one of four categories: membrane, cytoplasm, sub-membrane actin and background. In the second step, the probability of the four categories was used to train the algorithm to classify cell boundary pixels and all other pixels. The resulting probabilities were loaded in the multicut segmentation workflow to get a skeletonized segmentation of cells. These automated segmentations were loaded into Tissue analyzer (Aigouy et al., 2016) and manually corrected and semi automatically tracked. From the software Tissue analyzer, we exported two types of data: (1) cell tracking data containing x and y centroid position, cell area, perimeter (in pixels) and an ID identifying individual cells through time; (2) bond tracking data, indicating the identity of cells sharing a membrane segment, and the length of the membrane segment (in pixels). The data for each pair was fused to create a network dynamic object with the networkDynamic R package (v 0.10.1) containing information for nodes (cells) and edges (cell connections) through time as well as position, area, and perimeter.

Cumulative difference in number of neighbors is defined, for any given time T , as:

$$\sum_{t=0}^T N_t - M_t,$$

where N_t is the number of cell neighbors, at time t , of the cell that ultimately arrived at the anterior side irrespective of whether any rearrangement happened [the Notch-off/Emx2(+) cell] and M_t is the number of cell neighbors, at time t , of the cell that finishes the sequence on the posterior side irrespective of whether any rearrangement happened [the Notch-on/Emx2(-) cell].

Morphological analysis of the hair cell pairs during inversion

Circularity of the pair was calculated for all timeframes at which the nascent hair cells shared a bond, as:

$$\frac{4\pi A}{P^2},$$

where A is the sum of the area of both cells and P is the sum of the perimeter of both cells minus two times the length of their shared membrane segment. To determine the interfacial shape, the lines corresponding to the membrane interface between rotating pairs were exported as a list of xy coordinates and rotated and centered such that both ends laid on the 0 of the y -axis and equidistant to the 0 on the x -axis. A S or Z shape was assigned depending on the asymmetry of the line on the x -axis. The line was classified as a C shape depending on its asymmetry on the y -axis, if it was not previously classified as S or Z. If the interface had no notable asymmetry on either axis, it was classified as straight.

Analysis of final hair cell angle

The final angle for the three experimental conditions is defined as the angle of the vector that goes through both hair cell sibling cells with respect to the horizontal axis. Given the cartesian coordinates of each pair $v_0 = (x_0^0, x_1^0)$ and $v_1 = (x_0^1, x_1^1)$, the vector $v = v_0 - v_1$ connects both cells. As, in principle, any of the two cells can be labeled as zero or one, the orientation of the vector is not important for the calculation. Thus, the angle is calculated as:

$$\theta = \arctan\left(\frac{|x_1^0 - x_1^1|}{|x_0^0 - x_0^1|}\right),$$

which appropriately gives all angles in the first quadrant.

Then, the angle distributions were compared by pairs using a Kolmogorov-Smirnov test to evaluate whether the two samples belong to the same distribution. This was performed using SciPy's statistical package (Virtanen et al., 2020).

Computational model

In order to better understand how the *in vivo* rotations progress and stop, we decided to develop a mathematical and computational model. We chose a Monte Carlo Metropolis minimization scheme as it combines deterministic potentials to model the stop and stochastic evolution for the progression. In our model, each of the two cells is characterized by a particle in a one-dimensional space, representing the angle with respect to the A-P axis. Thus, the positions $\theta=0$ and $\theta=180^\circ$ correspond to opposing sides of that anatomical axis. The anterior region is defined as the second and third quadrant, while the posterior region is the first and fourth one (Fig. 7A). Each cell is subject to certain potentials. Cells see one another through a soft sphere repulsion, taken from the repulsive term of a Lennard-Jones potential.

$$\phi(\theta_2 - \theta_1) = \begin{cases} \left(\frac{d}{\theta_2 - \theta_1}\right)^{12}, & |\theta_2 - \theta_1| \leq d, \\ 0, & \text{otherwise} \end{cases}$$

where d is the maximum interaction distance and θ_1 and θ_2 are the positions of both cells. As the hair cell pair is bound throughout the rotation at all times in the *in vivo* experiments, parameter d is chosen as 180° to account for an interaction in the whole domain.

We also assumed that each cell is ruled by an attractor in the form of a Gaussian well,

$$\Omega(\omega_j) = -e^{-\frac{(\theta_j - \mu_j)^2}{2\sigma^2}},$$

where θ_j is the position of cell j , μ_j is the position of the attractor's minima for cell j and σ is the attractor's standard deviation. Both potentials are encoded in the system's energy, through a Hamiltonian, as:

$$H(\theta_1, \theta_2) = \rho\phi(\theta_2 - \theta_1) + \omega_1\Omega(\theta_1) + \omega_2\Omega(\theta_2).$$

The final configuration of the system is reached through an evolution, according to a Metropolis-Hasting algorithm for the phase space sampling (Metropolis et al., 1953; Hastings, 1970). The coefficients ρ , ω_1 and ω_2 allow the control of each potential's strength, representing the repulsion strength and the depth of each well, respectively. After an initial breaking time, the potential is turned on by setting ω_1, ω_2 or both to non zero values. The initial positions of the cells in the simulation are taken from a normal distribution. Its parameters are obtained through a fit of a Gaussian function to the experimental initial positions of the hair cells pairs, just after the progenitor's division, choosing $\mu_{initial} = 180^\circ \pm 50^\circ$ as an initial condition. The one-dimensional space is arbitrarily divided in a 0.25-degree interval, which is the smallest possible position change. Thereafter, cells may update their position as an anti-clockwise or clockwise movement, one cell at a time. This movement is represented by normalized velocities +1 and -1 in the discrete space, respectively. The change in energy due to the new position is then compared with the previous energy state. If the system's energy is reduced, the change is accepted with a probability of 1, otherwise it is accepted with a probability drawn from a Boltzmann distribution. When the change is rejected, the corresponding cell does not move. These calculations are performed for a fixed number of time steps for all simulations.

Acknowledgements

We thank the members of the Chara and López-Schier laboratories for their valuable comments on this study.

Competing interests

The authors declare no competing or financial interests.

Author contributions

Conceptualization: H.L.-S.; Methodology: O.C., E.L.K., J.R.M.-R., J.S.; Validation: O.C., J.R.M.-R., A.B., K.D., A.M., J.S.; Formal analysis: H.L.-S., O.C., E.L.K., J.R.M.-R., A.B., K.D., J.S.; Investigation: E.L.K., J.R.M.-R., A.M., F.P.-T., O.V.-L.; Data curation: E.L.K., J.R.M.-R., A.B., K.D., A.M., F.P.-T., O.V.-L.; Writing - original draft: E.L.K.; Writing - review & editing: H.L.-S., O.C., E.L.K., J.R.M.-R., A.B., K.D., A.M., F.P.-T., O.V.-L., J.S.; Visualization: E.L.K., J.R.M.-R., A.M., F.P.-T., O.V.-L.; Supervision: H.L.-S.; Project administration: H.L.-S.; Funding acquisition: H.L.-S.

Funding

J.R.M.-R. was funded by the European Union's Horizon 2020 research and innovation program under the HORIZON EUROPE Marie Skłodowska-Curie Actions grant agreement 840834. A.B. and O.C. were funded by Fondo para la Investigación Científica y Tecnológica (grants PICT-2017-2307 and PICT-2019-2019-03828 granted to O.C.). O.C. was funded by the Consejo Nacional de Investigaciones Científicas y Técnicas (CONICET) and by the School of Biosciences, University of Nottingham. H.L.-S. was funded by the Helmholtz-Gemeinschaft and the New York University Abu Dhabi. Open access funding provided by New York University Abu Dhabi. Deposited in PMC for immediate release.

Data availability

The codes used for the simulations can be found at <https://doi.org/10.5281/zenodo.7417603>. Data and code for Figs 2 and 3 are available at <https://gitlab.com/jeronoln/pci-topology>.

Peer review history

The peer review history is available online at <https://journals.biologists.com/dev/lookup/doi/10.1242/dev.200975.reviewer-comments.pdf>.

References

- Aigouy, B., Umetsu, D. and Eaton, S.** (2016). Segmentation and quantitative analysis of epithelial tissues. *Methods Mol. Biol.* **1478**, 227-239. doi:10.1007/978-1-4939-6371-3_13
- Alhashem, Z., Feldner-Busztin, D., Revell, C., Alvarez-Garcillan Portillo, M., Camargo-Sosa, K., Richardson, J., Rocha, M., Gauert, A., Corbeaux, T., Milanetto, M. et al.** (2022). Notch controls the cell cycle to define leader versus follower identities during collective cell migration. *eLife* **11**, e73550. doi:10.7554/eLife.73550
- Baek, S., Tran, N. T. T., Diaz, D. C., Tsai, Y.-Y., Acedo, J. N., Lush, M. E. and Piotrowski, T.** (2022). Single-cell transcriptome analysis reveals three sequential phases of gene expression during zebrafish sensory hair cell regeneration. *Dev. Cell* **57**, 799-819.e6. doi:10.1016/j.devcel.2022.03.001
- Bodor, D. L., Pönisch, W., Endres, R. G. and Paluch, E. K.** (2020). Of cell shapes and motion: the physical basis of animal cell migration. *Dev. Cell* **52**, 550-562. doi:10.1016/j.devcel.2020.02.013
- Brangwynne, C., Huang, S., Parker, K. K., Ingber, D. E. and Ostuni, E.** (2000). Symmetry breaking in cultured mammalian cells. *In Vitro Cell. Dev. Biol. Anim.* **36**, 563-565. doi:10.1007/BF02577523
- Brückner, D. B., Arlt, N., Fink, A., Ronceray, P., Rädler, J. O. and Broedersz, C. P.** (2021). Learning the dynamics of cell-cell interactions in confined cell migration. *Proc. Natl. Acad. Sci. USA* **118**, e2016602118. doi:10.1073/pnas.2016602118
- Caballero, D., Kundo, S. C. and Reis, R. L.** (2020). The biophysics of cell migration: biasing cell motion with Feynman Ratchets. *Biophysicist* **1**, 7. doi:10.35459/tp.2020.000150
- Camley, B. A. and Rappel, W.-J.** (2017). Physical models of collective cell motility: from cell to tissue. *J. Phys. Appl. Phys.* **50**, 113002. doi:10.1088/1361-6463/aa56fe
- Camley, B. A., Zhang, Y., Zhao, Y., Li, B., Ben-Jacob, E., Levine, H. and Rappel, W.-J.** (2014). Polarity mechanisms such as contact inhibition of locomotion regulate persistent rotational motion of mammalian cells on micropatterns. *Proc. Natl. Acad. Sci. USA* **111**, 14770-14775. doi:10.1073/pnas.1414498111
- Cetera, M., Leybova, L., Joyce, B. and Devenport, D.** (2018). Counter-rotational cell flows drive morphological and cell fate asymmetries in mammalian hair follicles. *Nat. Cell Biol.* **20**, 541-552. doi:10.1038/s41556-018-0082-7
- Collinet, C. and Lecuit, T.** (2021). Programmed and self-organized flow of information during morphogenesis. *Nat. Rev. Mol. Cell Biol.* **22**, 245-265. doi:10.1038/s41580-020-00318-6
- Cruz, I. A., Kappedal, R., Mackenzie, S. M., Hailey, D. W., Hoffman, T. L., Schilling, T. F. and Raible, D. W.** (2015). Robust regeneration of adult zebrafish lateral line hair cells reflects continued precursor pool maintenance. *Dev. Biol.* **402**, 229-238. doi:10.1016/j.ydbio.2015.03.019
- Dalle Nogare, D. E., Natesh, N., Vishwasrao, H. D., Shroff, H. and Chitnis, A. B.** (2020). Zebrafish Posterior Lateral Line primordium migration requires interactions between a superficial sheath of motile cells and the skin. *eLife* **9**, e58251. doi:10.7554/eLife.58251
- Denans, N., Baek, S. and Piotrowski, T.** (2019). Comparing sensory organs to define the path for hair cell regeneration. *Annu. Rev. Cell Dev. Biol.* **35**, 567-589. doi:10.1146/annurev-cellbio-100818-125503
- Erzberger, A., Jacobo, A., Dasgupta, A. and Hudspeth, A. J.** (2020). Mechanochemical symmetry breaking during morphogenesis of lateral-line sensory organs. *Nat. Phys.* **16**, 949-957. doi:10.1038/s41567-020-0894-9
- Founounou, N., Farhadifar, R., Collu, G. M., Weber, U., Shelley, M. J. and Mlodzik, M.** (2021). Tissue fluidity mediated by adherens junction dynamics promotes planar cell polarity-driven ommatidial rotation. *Nat. Commun.* **12**, 6974. doi:10.1038/s41467-021-27253-0
- Fredberg, J. J.** (2022). On the origins of order. *Soft Mat.* **18**, 2346-2353. doi:10.1039/D1SM01716K
- Gómez-Gálvez, P., Anbari, S., Escudero, L. M. and Buceta, J.** (2021). Mechanics and self-organization in tissue development. *Semin. Cell Dev. Biol.* **120**, 147-159. doi:10.1016/j.semcdb.2021.07.003
- Guichard, A., Srinivasan, S., Zimm, G. and Bier, E.** (2002). A screen for dominant mutations applied to components in the Drosophila EGF-R pathway. *Proc. Natl. Acad. Sci. USA* **99**, 3752. doi:10.1073/pnas.052028699
- Haas, P. and Gilmour, D.** (2006). Chemokine signaling mediates self-organizing tissue migration in the zebrafish lateral line. *Dev. Cell* **10**, 673-680. doi:10.1016/j.devcel.2006.02.019
- Hakim, V. and Silberzan, P.** (2017). Collective cell migration: a physics perspective. *Rep. Prog. Phys.* **80**:076601. doi:10.1088/1361-6633/aa65ef
- Hardy, K., Amariutei, A. E., De Faveri, F., Hendry, A., Marcotti, W. and Ceriani, F.** (2021). Functional development and regeneration of hair cells in the zebrafish lateral line. *J. Physiol.* **599**, 3913-3936. doi:10.1113/JP281522
- Hartmann, J. and Mayor, R.** (2022). Self-organized collective cell behaviors as design principles for synthetic developmental biology. *Semin. Cell Dev. Biol.* **141**, 63-73. doi:10.1016/j.semcdb.2022.04.009
- Hastings, W. K.** (1970). Monte Carlo sampling methods using Markov chains and their applications. *Biometrika* **57**, 97-109. doi:10.1093/biomet/57.1.97
- Hirata, E., Ichikawa, T., Horike, S.-I. and Kiyokawa, E.** (2018). Active K-RAS induces the coherent rotation of epithelial cells: a model for collective cell invasion in vitro. *Cancer Sci.* **109**, 4045-4055. doi:10.1111/cas.13816
- Horne-Badovinac, S.** (2014). The Drosophila egg chamber-a new spin on how tissues elongate. *Integr. Comp. Biol.* **54**, 667-676. doi:10.1093/icb/ucu067
- Huang, S.** (2016). Where to go: breaking the symmetry in cell motility. *PLoS Biol.* **14**, e1002463. doi:10.1371/journal.pbio.1002463
- Huang, S., Brangwynne, C. P., Parker, K. K. and Ingber, D. E.** (2005). Symmetry-breaking in mammalian cell cohort migration during tissue pattern formation: role of random-walk persistence. *Cell Motil. Cytoskeleton.* **61**, 201-213. doi:10.1002/cm.20077
- Jacobo, A., Dasgupta, A., Erzberger, A., Siletti, K. and Hudspeth, A. J.** (2019). Notch-mediated determination of hair-bundle polarity in mechanosensory hair cells of the zebrafish lateral line. *Curr. Biol.* **29**, 3579-3587.e7. doi:10.1016/j.cub.2019.08.060
- Jiang, T., Kindt, K. and Wu, D. K.** (2017). Transcription factor Emx2 controls stereociliary bundle orientation of sensory hair cells. *eLife* **6**, e23661. doi:10.7554/eLife.23661
- Kindt, K. S., Finch, G. and Nicolson, T.** (2012). Kinocilia mediate mechanosensitivity in developing zebrafish hair cells. *Dev. Cell* **23**, 329-341. doi:10.1016/j.devcel.2012.05.022
- Kindt, K. S., Akturk, A., Jarysta, A., Day, M., Beiri, A., Flonard, M. and Tarchini, B.** (2021). EMX2-GPR156-Goi reverses hair cell orientation in mechanosensory epithelia. *Nat. Commun.* **12**, 2861. doi:10.1038/s41467-021-22997-1
- Kozak, E. L., Palit, S., Miranda-Rodríguez, J. R., Janjic, A., Böttcher, A., Lickert, H., Enard, W., Theis, F. J. and López-Schier, H.** (2020). Epithelial planar bipolarity emerges from notch-mediated asymmetric inhibition of Emx2. *Curr. Biol.* **30**, 1142-1151.e6. doi:10.1016/j.cub.2020.01.027
- Kreshuk, A. and Zhang, C.** (2019). Machine learning: advanced image segmentation using ilastik. *Methods Mol. Biol.* **2040**, 449-463. doi:10.1007/978-1-4939-9686-5_21
- Langdon, T., Hayward, P., Brennan, K., Wirtz-Peitz, F., Sanders, P., Zecchini, V., Friday, A., Balayo, T. and Martinez Arias, A.** (2006). Notch receptor encodes two structurally separable functions in Drosophila: a genetic analysis. *Dev. Dyn.* **235**, 998-1013. doi:10.1002/dvdy.20735
- Lecaudey, V., Cakan-Akdogan, G., Norton, W. H. J. and Gilmour, D.** (2008). Dynamic Fgf signaling couples morphogenesis and migration in the zebrafish lateral line primordium. *Development* **135**, 2695-2705. doi:10.1242/dev.025981
- Lenne, P.-F., Rupprecht, J.-F. and Viasnoff, V.** (2021). Cell junction mechanics beyond the bounds of adhesion and tension. *Dev. Cell* **56**, 202-212. doi:10.1016/j.devcel.2020.12.018
- Leong, F. Y.** (2013). Physical explanation of coupled cell-cell rotational behavior and interfacial morphology: a particle dynamics model. *Biophys. J.* **105**, 2301-2311. doi:10.1016/j.bpj.2013.09.051
- Li, B. and Sun, S. X.** (2014). Coherent motions in confluent cell monolayer sheets. *Biophys. J.* **107**, 1532-1541. doi:10.1016/j.bpj.2014.08.006
- López-Schier, H. and Hudspeth, A. J.** (2006). A two-step mechanism underlies the planar polarization of regenerating sensory hair cells. *Proc. Natl. Acad. Sci. USA* **103**, 18615-18620. doi:10.1073/pnas.0608536103
- Ma, E. Y., Rubel, E. W. and Raible, D. W.** (2008). Notch signaling regulates the extent of hair cell regeneration in the zebrafish lateral line. *J. Neurosci.* **28**, 2261-2273. doi:10.1523/JNEUROSCI.4372-07.2008
- Maitre, J.-L. and Heisenberg, C.-P.** (2011). The role of adhesion energy in controlling cell-cell contacts. *Curr. Opin. Cell Biol.* **23**, 508-514. doi:10.1016/j.cob.2011.07.004
- Meijering, E., Dzyubachyk, O. and Smal, I.** (2012). Methods for cell and particle tracking. *Methods Enzymol.* **504**, 183-200. doi:10.1016/B978-0-12-391857-4.00009-4
- Mestek Boukhibar, L. and Barkoulas, M.** (2016). The developmental genetics of biological robustness. *Ann. Bot.* **117**, 699-707. doi:10.1093/aob/mcv128
- Metropolis, N., Rosenbluth, A. W., Rosenbluth, M. N., Teller, A. H. and Teller, E.** (1953). Equation of state calculations by fast computing machines. *J. Chem. Phys.* **21**, 1087-1092. doi:10.1063/1.1699114
- Mirkovic, I., Pylawka, S. and Hudspeth, A. J.** (2012). Rearrangements between differentiating hair cells coordinate planar polarity and the establishment of mirror symmetry in lateral-line neuromasts. *Biol. Open* **1**, 498-505. doi:10.1242/bio.2012570
- Norden, C. and Lecaudey, V.** (2019). Collective cell migration: general themes and new paradigms. *Curr. Opin. Genet. Dev.* **57**, 54-60. doi:10.1016/j.gde.2019.06.013
- Ohta, S., Ji, Y. R., Martin, D. and Wu, D. K.** (2020). Emx2 regulates hair cell rearrangement but not positional identity within neuromasts. *eLife* **9**, e60432. doi:10.7554/eLife.60432
- Parslow, A., Cardona, A. and Bryson-Richardson, R. J.** (2014). Sample drift correction following 4D confocal time-lapse imaging. *J. Vis. Exp.*, 51086. doi:10.3791/51086-v
- Peloggia, J., Münch, D., Meneses-Giles, P., Romero-Carvajal, A., Lush, M. E., Lawson, N. D., McClain, M., Pan, Y. A. and Piotrowski, T.** (2021). Adaptive cell invasion maintains lateral line organ homeostasis in response to environmental changes. *Dev. Cell* **56**, 1296-1312.e7. doi:10.1016/j.devcel.2021.03.027

- Pinto-Teixeira, F., Muzzopappa, M., Swoger, J., Mineo, A., Sharpe, J. and López-Schier, H. (2013). Intravital imaging of hair-cell development and regeneration in the zebrafish. *Front. Neuroanat.* **7**, 33. doi:10.3389/fnana.2013.00033
- Pinto-Teixeira, F., Viader-Llangués, O., Torres-Mejía, E., Turan, M., González-Gualda, E., Pola-Morell, L. and López-Schier, H. (2015). Inexhaustible hair-cell regeneration in young and aged zebrafish. *Biol. Open* **4**, 903-909. doi:10.1242/bio.012112
- Schindelin, J., Arganda-Carreras, I., Frise, E., Kaynig, V., Longair, M., Pietzsch, T., Preibisch, S., Rueden, C., Saalfeld, S., Schmid, B. et al. (2012). Fiji: an open-source platform for biological-image analysis. *Nat. Methods* **9**, 676-682. doi:10.1038/nmeth.2019
- Segerer, F. J., Thüroff, F., Piera Alberola, A., Frey, E. and Rädler, J. O. (2015). Emergence and persistence of collective cell migration on small circular micropatterns. *Phys. Rev. Lett.* **114**, 228102. doi:10.1103/PhysRevLett.114.228102
- Steiner, A. B., Kim, T., Cabot, V. and Hudspeth, A. J. (2014). Dynamic gene expression by putative hair-cell progenitors during regeneration in the zebrafish lateral line. *Proc. Natl. Acad. Sci. USA* **111**, E1393-E1401. doi:10.1073/pnas.1318692111
- Tanner, K., Mori, H., Mroue, R., Bruni-Cardoso, A. and Bissell, M. J. (2012). Coherent angular motion in the establishment of multicellular architecture of glandular tissues. *Proc. Natl. Acad. Sci. USA* **109**, 1973-1978. doi:10.1073/pnas.1119578109
- Thomas, E. D. and Raible, D. W. (2019). Distinct progenitor populations mediate regeneration in the zebrafish lateral line. *eLife* **8**, e43736. doi:10.7554/eLife.43736
- Tseng, Q., Duchemin-Pelletier, E., Deshiere, A., Baland, M., Guillou, H., Filhol, O. and Théry, M. (2012). Spatial organization of the extracellular matrix regulates cell-cell junction positioning. *Proc. Natl. Acad. Sci. USA* **109**, 1506-1511. doi:10.1073/pnas.1106377109
- Umeda, T. and Inouye, K. (2002). Possible role of contact following in the generation of coherent motion of *Dictyostelium* cells. *J. Theor. Biol.* **219**, 301-308. doi:10.1006/jtbi.2002.3124
- Virtanen, P., Gommers, R., Oliphant, T. E., Haberland, M., Reddy, T., Cournapeau, D., Burovski, E., Peterson, P., Weckesser, W., Bright, J. et al. (2020). SciPy 1.0: fundamental algorithms for scientific computing in Python. *Nat. Methods* **17**, 261-272. doi:10.1038/s41592-019-0686-2
- Wada, H. and Kawakami, K. (2015). Size control during organogenesis: development of the lateral line organs in zebrafish. *Dev. Growth Differ.* **57**, 169-178. doi:10.1111/dgd.12196
- Wang, H., Lacoche, S., Huang, L., Xue, B. and Muthuswamy, S. K. (2013). Rotational motion during three-dimensional morphogenesis of mammary epithelial acini relates to laminin matrix assembly. *Proc. Natl. Acad. Sci. USA* **110**, 163-168. doi:10.1073/pnas.1201141110
- Wibowo, I., Pinto-Teixeira, F., Satou, C., Higashijima, S. and López-Schier, H. (2011). Compartmentalized Notch signaling sustains epithelial mirror symmetry. *Development* **138**, 1143-1152. doi:10.1242/dev.060566
- Yap, A. S., Duszyc, K. and Viasnoff, V. (2018). Mechanosensing and mechanotransduction at cell-cell junctions. *Cold Spring Harb. Perspect. Biol.* **10**, a028761. doi:10.1101/cshperspect.a028761

ForSys: non-invasive stress inference from time-lapse microscopy

Augusto Borges ^{1,2}, Jerónimo R. Miranda-Rodríguez ^{1,3}, Alberto Sebastián Ceccarelli ⁴, Guilherme Ventura ⁵, Jakub Sedzinski ⁵, Hernán López-Schier ^{1,2,6} & Osvaldo Chara ^{7,8,9}

- 1) Unit Sensory Biology and Organogenesis, Helmholtz Zentrum München, Munich, Germany
- 2) Graduate School of Quantitative Biosciences, Ludwig Maximilian University, Munich, Germany
- 3) Instituto de Neurobiología, Universidad Nacional Autónoma de México (UNAM), Boulevard Juriquilla 3001, Juriquilla, México
- 4) Institute of Physics of Liquids and Biological Systems, University of La Plata, La Plata, Argentina
- 5) The Novo Nordisk Foundation Center for Stem Cell Medicine (reNEW), University of Copenhagen, Blegdamsvej 3B, 2200, Copenhagen, Denmark
- 6) Division of Science, New York University Abu Dhabi, Saadiyat Island, United Arab Emirates
- 7) School of Biosciences, University of Nottingham, Sutton Bonington Campus, Nottingham, LE12, UK
- 8) Instituto de Tecnología, Universidad Argentina de la Empresa, Buenos Aires, Argentina
- 9) corresponding author: osvaldo.chara@nottingham.ac.uk

Abstract

During tissue development and regeneration, cells interpret and exert mechanical forces that are challenging to measure *in vivo*. Therefore, stress inference algorithms have emerged as powerful tools to estimate tissue stresses. However, how to incorporate tissue dynamics effectively into the inference remains elusive. Here, we present ForSys, a Python-based software that estimates intercellular stresses and intracellular pressures using time-lapse microscopy. We validated ForSys *in silico* and *in vivo* using the well-characterized mucociliary epithelium of the *Xenopus* embryo. We applied ForSys to study the migrating zebrafish lateral line primordium. We found that stress increases during cell rounding just before cell division and predicted the onset of epithelial rosetto-genesis with high accuracy. Finally, we analyzed the development of the zebrafish neuromast and inferred mechanical asymmetries in a cell type-specific adhesion pattern. The versatility and simplicity of ForSys enhance the toolkit for studying spatiotemporal patterns of mechanical forces during tissue morphogenesis *in vivo*.

Introduction

Recent advancements in experimental techniques have reignited interest in exploring the mechanical properties of biological tissues, commonly referred to as tissue rheology. These methods have facilitated precise and quantitative measurements of tissue mechanical parameters. For example, implanted deformable magnetic droplets have been used to determine the elastic properties along the zebrafish anteroposterior axis during body elongation^{1,2} and presomitic mesoderm differentiation³. Similarly, the application of optical traps has enabled controlled deformation of cell membranes, thereby facilitating the study of viscoelastic properties during *Drosophila* development⁴. Laser ablation experiments have also been employed in various systems to probe cortical tension by measuring the recoil of cell junctions upon laser cutting⁵⁻⁷. Despite their importance, these experimental methods often come with significant drawbacks. They can be costly and necessitate specialized equipment, posing implementation challenges for many researchers. Moreover, these techniques might not be conducive to long-term imaging, potentially disrupting the normal development and, in some cases, leading to the destruction of the sample. Hence, there is a pressing need for alternative approaches to overcome these limitations while still delivering accurate and non-invasive measurements of tissue rheology.

Computational methods offer a promising solution, enabling the cost-effective and straightforward implementation of tissue mechanical characterization *in vivo*⁸. Inference techniques have emerged as powerful tools in tissue rheology, utilizing readily available microscopy images to infer the effective stress of a system based on the geometry of the cellular junctions. A key aspect of this approach centers on tricellular junctions (TJ), where three cells converge⁹. The underlying framework relies on one major assumption: mechanical equilibrium is maintained at each TJ. The strength of these models lies in their simplicity, reducing the estimation of intercellular stresses to the solution of an overdetermined system of linear equations^{10,11}. One of the first implementations of the force-inference approach is CellFIT¹⁰, which enables the estimation of stresses from microscopy images. While CellFIT provides accurate estimates in static tissues, its applicability to dynamic tissues is limited. Although recent techniques using time series data offer improvements¹², a computational tool capable of dynamic stress inference has been lacking.

Here, we introduce ForSys, an open-source Python-based inference algorithm specifically developed to tackle the complexities of dynamical stress inference from time series experiments. ForSys utilizes the local velocity of cell junctions to extract the spatiotemporal stress distribution *in vivo*, providing accurate estimations of a tissue's mechanical state.

Results

ForSys: a Python-based open-source software to infer mechanical stress in tissues.

ForSys enables the inference of intercellular mechanical stress and intracellular pressure of tissues. It takes the two-dimensional (2D) segmentation of an image, which delineates cell outlines, as its input. It then conceptualizes the entire tissue as a polygonal structure. In this structure, each polygon represents a cell, with edges connecting vertices.

ForSys operates in two distinct modes contingent upon the input (Fig. 1). When supplied with a singular segmentation of a static image, the software engages its Static mode (Fig. 1A) (see "Statical stress inference" in the Materials and Methods section). In this mode, a stress inference is applied to a single image. Conversely, if the input comprises the segmentation of a time series dataset, ForSys presents the option to function in its Dynamic mode (see "The dynamic inference case" in the Materials and Methods section) (Fig. 1B). This mode involves the extraction of temporal trajectories for vertices from the microscopy time series, thereby incorporating corresponding vertex velocities to refine stress inference.

ForSys infers *in silico* stresses accurately in static equilibrium.

To assess ForSys's performance against existing tools, we utilized as a ground truth simulations generated by a vertex model implemented in Surface Evolver via seapipy, analyzed it using our software, and compared the results with outputs from previously published methods, focusing specifically on CellFIT¹⁰ and DLITE¹². Given that both tools yield similar results (Extended data figure 3A and 3B), we opted for DLITE implementation due to its open-source nature, enabling a direct comparison with tissue stresses extracted from Surface Evolver outputs.

We selected the final time-point ($t = 24$) of simulations generated from four different conditions to compare the ground truth from the Surface Evolver output (Fig. 2A), DLITE's estimation (Fig. 2B), and ForSys in its Static modality (Fig. 2C). In all cases, the predicted intercellular stresses and intracellular pressures closely matched the ground truth. Moreover, both stress inference methods exhibited a high degree of accuracy and precision, as reflected by a low Mean Absolute Percentage Error (MAPE) (<10%) (Fig 2D) and a high saturated score function (~30) (Figure 2E and Extended Data Figure 3C). Importantly, ForSys showed a significantly lower MAPE ($p = 1e-05$; $p = 1e-8$; $p = 0.01$, for the x-furrow, y-furrow, and circular furrow, respectively), higher saturated score ($p < 0.001$; $p < 1e-4$; $p < 0.01$ for the x-furrow, y-furrow, and circular furrow, respectively) and smaller interquartile range than DLITE, for all cases except the random tensions (See the "Statistical estimator" section in Materials and Methods for details).

These results indicate that ForSys's static modality yields higher accuracy and precision estimations than DLITE while effectively capturing the *in silico*-generated ground truth spatial distributions in static equilibrium. Consequently, only ForSys in its Static modality will be used hereafter for comparison with a static solution.

ForSys stress inference in dynamical tissues outperforms static methods *in silico*

With the aim of inferring stress in dynamic tissue, we assumed that the tissue goes through a succession of quasistatic states in an overdamped regime¹³, consistent with a viscoelastic response of the cell junctions to the deformations created by the forces acting on them^{14,15}. Consequently, we incorporated a viscous term proportional to the velocity of the corresponding vertex in each junction's equation. Importantly, these velocities are not unknown: ForSys estimates them using the spatial coordinates of the vertices tracked over time. In ForSys, we call this modality of stress inference Dynamic.

Dynamic inference depends on a dimensionless parameter proportional to the reciprocal of the Weissenberg number^{16–18} (see a detailed description in the “The dynamic inference case” section of Materials and Methods). Thus, we fitted this parameter and found its optimal value for each of the examples. Our results indicate that the best dynamic results are obtained with a scale parameter of about 0.1 (see Extended Data Fig. 5 and the Materials and Methods section “Determination of the scale parameter”).

Under our prescribed conditions (Figure 3A), ForSys in its dynamical modality (Fig. 3C) outperforms static inference (Figure 3B), accurately reproducing stress and pressure distributions akin to the ground truth. Furthermore, our results indicate that dynamic modality improves static modality accuracy and precision, as indicated by MAPE ($p < 1e-09$; $p < 1e-9$; $p < 1e-7$, for the x-furrow, y-furrow, and circular furrow, respectively) (Figure 3D) and the saturated score function ($p < 1e-08$; $p < 1e-9$; $p < 1e-9$; $p = 0.03$, for the x-furrow, y-furrow, circular furrow, and random, respectively) (Figure 3E) (See the “Statistical estimator” section in Materials and Methods for details).

Interestingly, accuracy and precision (estimated with the MAPE and the saturated score function) of stress inference in each ForSys modality are damped by the increases of TJ local movements, here reflected in the norm of the velocities vector ($\|v\|_2$) (Figure 3F and G). Notably, the dynamic modality outperforms the static one for all TJ velocities, as observed by the time evolution of MAPE (Figure 3F). This can be evidenced through the ratio between dynamic and static scores (Figure 3G), where values greater than one mean that the dynamic modality outperforms the static one. The outperformance of the dynamical modality is clearer for higher TJ velocities (Figure 3F and Figure 3G).

and Extended Data Fig. 4). Thus, ForSys, in its dynamic modality, can retain a better approximation due to its use of the vertices' velocity, *i.e.*, future positions, to estimate the stress.

In this section, we have demonstrated through *in silico* validation that the dynamic modality of ForSys outperforms other methods in accurately inferring stresses in remodeling tissues.

ForSys validation *in vivo* using the mucociliary epithelium of *Xenopus* embryos

To validate ForSys in a biological setting, we used published data from the mucociliary epithelium in *Xenopus* embryos (Fig. 4A) ¹⁹. We quantified myosin II intensity using a non-muscle myosin II A-specific intrabody (SF9-3xGFP, for simplicity referred to as myosin II), which has been previously used as a proxy for active myosin II ^{20,21}. We segmented the microscopy images using Epyseg ²² (see Materials and Methods “SF9 myosin II sensor intensity measurements” for details) and compared myosin II measurements with the stress values inferred by ForSys.

As in previous sections we qualitatively compared the derived stress distribution maps with the ground truths, here given by the normalized myosin II sensor intensity (Figure 4B). We observed good qualitative agreement between inferred stress and myosin intensity, with regions of higher myosin fluorescence corresponding to higher inferred stress, most noticeable in Embryo 3 and Embryo 5 of Figure 4B. In contrast, in Embryo 4 of the same panel, ForSys can reproduce a more homogenous distribution along the tissue. On a quantitative level we found that ForSys predictions are moderately correlated with the myosin measurements for each embryo ($R=0.56 \pm 0.11$; mean \pm std) (Figure 4C). In addition, ForSys stresses predictions have a MAPE value of $(21 \pm 5)\%$ (mean \pm std). Overall, the distributions of myosin intensity and inferred stress are qualitatively similar and not significantly different (Figure 4D, $p=0.76$; Mann-Whitney U test; $N=154$).

Consequently, ForSys accurately and precisely infers the stresses present in the mucociliary epithelium of the *Xenopus* embryo, as measured by the fluorescence of the myosin II sensor.

Dynamic stress inference of collective cell behavior in zebrafish

We sought to explore ForSys inferences in an *in vivo* model that mixes TJs with low and high motility. To this end, we turned to two morphogenetic processes that occur during the development and homeostasis of the zebrafish lateral line, a mechanosensory organ formed by a collection of discrete organs called neuromasts.

We first applied ForSys to an *in vivo* model of collective cell morphogenetic behavior leading to the formation of epithelial rosettes in the lateral line primordium of developing zebrafish. The primordium is a collection of just over 100 cells that move collectively from head-to-tail of the fish embryo (Fig. 5A). During migration, groups of approximately 25 trailing cells periodically detach from

the primordium, sequentially giving rise to individual neuromasts that are then deposited at semi-regular pace²³. Although the lateral line primordium has been extensively characterized genetically^{24,25}, the mechanical forces present during migration and rosetogenesis remain unknown.

Therefore, we decided to use ForSys in its Dynamic modality to analyze time lapse data of migrating primordia, whose cells' plasma membranes were fluorescently labeled with EGFP. Migrating primordia were followed for 30 minutes with a temporal resolution of two minutes (Supplementary video 1)(Fig. 5B and 5B').

ForSys predicted the mitotic division of primordial cells by revealing high stress in the pre-dividing cellular membrane relative to the membrane of the non-dividing surrounding cells (Fig. 5C). The stresses remain partially conserved after division, mainly in the cell membrane separating the resulting cell siblings (Fig. 5C').

We then applied ForSys to predict stress tissue-wide. Apical constrictions of epithelializing cells are mechanistically associated with the formation of the rosettes that preempt neuromast morphogenesis²⁶. The apical constriction is readily detectable by morphology when looking at the apical plane of the primordium (Fig. 5D and 5D')²⁷. The relationship between apical constrictions and forces in more basal planes of the cells and how they relate to rosetogenesis remain undefined. To begin to address this possible relationship, we used time series data and aggregated the position of the cells along the anteroposterior axis of the primordium by kernel density estimation. We weighed each cell using the intracellular pressure inferred from ForSys, which results in a smoothed curve estimating intracellular pressure along the migration axis (Fig 5E). This analysis showed that the anteroposterior positions of the rosettes, manually annotated by looking at apical constriction (Asterisks in Fig. 5D' and 5E), correlate with the predicted zones of high intracellular pressure inferred by ForSys. The closeness between the predicted pressure maxima and the manually annotated rosette formation indicates a high correlation between these two quantities during primordium migration ($R=0.99$, $p<1e-51$, $N=61$; for rosettes 1 and 2 combined) (Figure 5F).

Encouraged by our previous results, we next analyzed mature neuromats. The center of this organ is occupied by mechanosensory hair cells, which are surrounded by non-sensory supporting cells (Figure 6A)²⁸. We used a plasma membrane marker to define cells, which were segmented using *ilastik*²⁹ and *epyseg*²² (Figure 6B). Then, we used the Dynamical modality of ForSys to estimate the stress at each membrane (Figure 6B') and found that membranes belonging to hair cells have higher stress on average. Homotypic interfaces between hair cells have the highest stress ($p < 1e-7$ vs. hair cell-supporting cell interfaces). On the other hand, homotypic contacts between supporting cells have the lowest stress ($p<0.006$ vs. hair cell-supporting cell interfaces) (Figure 6C).

We then focused on a still-puzzling process called planar cell inversion (PCI)^{30,31}. PCI occurs when supporting cells give rise to hair-cell progenitors, which divide once to generate a pair of hair cells. Approximately half of the resulting nascent hair-cell pairs undergo a 180° rotation around their geometric center^{30,31} (Figure 6D and 6E). The mechanical forces occurring during cell-pair inversions are not known. Therefore, we focused our analysis on the homotypic junctions between the sibling hair cells and compared them to those with the surrounding supporting cells. This allowed us to test how the stress differs between the different cell types. We found that the stress in the membranes juxtaposing the rotating hair-cell pair is significantly smaller than that between hair cells and the adjacent supporting cells ($p < 0.0005$) (Figure 6F). Because tension and adhesion are generally inversely related, PCI could be characterized by a strong adhesion within the rotating cell pair and weaker adhesion with the surrounding cells. This result suggests a cell-type and cell-state-specific adhesion pattern that underlies contact remodeling necessary for coordinated cell-pair rotations. Taken together, these results show that ForSys's dynamical implementation predicts high stresses before cell division in a migrating tissue. They also revealed that rosette formation could be prefigured by mechanical rosetogenesis changes in the cells, which allows the inference of apical constrictions during rosetogenesis using information from basal planes.

Discussion

Here, we introduce ForSys, a new software that statically and dynamically infers stresses without disrupting biological tissues. Traditional inference methods rely on geometrical information to calculate the relationship among the stresses acting on cell membranes in a static image. However, these methods generally lack the dynamical component present in a time-series microscopy. ForSys extends the applicability of inference techniques by enabling dynamic stress inference in cell membranes when tissues are in motion.

We validated our software in its static and dynamic modalities with different *in silico* spatial patterns of tissue stresses using a cell-based computational model implemented in Surface Evolver³², which we integrated into a Python package called seapipy³³. Our results show that ForSys can recover the ground truth in its static and dynamic modalities. Significantly, the dynamic modality improves the accuracy of the static modality. Unlike static inference, characterized by a unique scale contained in the stresses to be inferred, dynamic inference adds a viscous term proportional to the nodes' velocities, which introduces an additional scale to the problem. The dynamic inference can thus be reformulated in terms of the Weissenberg number^{16–18}. The optimal value found for this number *in silico* indicates that elastic forces are an order of magnitude larger than viscous forces. Strikingly,

dynamic inference outperforms static inference even when elastic forces dominate over the viscous forces, pointing to a wide applicability of the dynamic modality.

We then validated ForSys in the *Xenopus* embryonic mucociliary epithelium. We found a positive correlation between the inferred stress and cortical stress that was indirectly measured using variations in the intensity of myosin II. As the embryonic mucociliary epithelium progresses over several hours, continuous, direct probing of the mechanical forces is extremely laborious, likely to interfere with tissue development, and hardly compatible with single-cell resolution measurements. Therefore, using ForSys for non-invasive mapping of mechanical forces at the scale of an entire tissue across time could pave the way for a more comprehensive understanding of the mechanical forces that drive tissue development.

We further demonstrated the power of ForSys by studying two aspects of organ development and homeostasis using the neuromasts of the lateral line in zebrafish embryos. Specifically, we addressed two processes that involve a complex collective cell behavior. First, we applied Dynamical ForSys to the migrating lateral-line primordium. Although this process has been extensively dissected genetically, it is still unknown what forces play a role during migration and neuromast deposition^{34,35}. Therefore, this process of collective cell migration will benefit from an accessible and non-invasive method to estimate forces in a dynamical tissue. Two characteristics of this migratory primordium make it well-suited for applying ForSys: the tissue as a whole is migrating through the lateral line, and its membranes have a curved shape. We showed that ForSys can detect cell division and rosette formation. ForSys will be useful for testing various hypotheses about tissue mechanics in other dynamic cell systems, for instance, during tissue repair and organ regeneration.

We also applied ForSys to address the still mysterious process of planar cell inversion, during which sibling cells rotate around their centroid after the mitotic division of their progenitor³⁰. We discovered that homotypic contacts between rotating cells have the most stress, whereas the contacts between the rotating pair have lower stress than the contacts of each hair cell with its neighbors. This strongly suggests that adhesion dynamics during rotation are based on a strong homotypic interaction of the sibling cells and a weak heterotypic interaction with the surrounding cells, enabling contact exchange during the inversion³⁰.

ForSys provides a versatile and noninvasive tool for studying spatiotemporal patterns of mechanical stresses during tissue morphogenesis *in vivo*. This software makes stress predictions that can guide researchers in conducting further experiments, which can significantly contribute to understanding the mechanisms involved in development and regeneration. ForSys was built as open-source software in Python, thus allowing the community to participate in its development and maintenance. In our eyes, an interesting future perspective will be to extend the software to tissues

in non-equilibrium conditions and adapt the method to operate within a 3D geometry to generate 4D mechanical stress inference.

Materials and Methods

SF9 myosin II sensor intensity measurements

Images of stage 16 to stage 20 *Xenopus* embryos expressing the SF9-3xGFP myosin II sensor were acquired in using a 3i spinning disk microscope with a Plan-Apochromat x63 oil objective (N.A. = 1.4) mounted on an inverted Zeiss Axio Observer Z1 microscope (Marianas Imaging Workstation [3i—Intelligent Imaging Innovations]), equipped with a CSU-X1 spinning disk confocal head (Yokogawa) and an iXon Ultra 888 EM-CCD camera (Andor Technology). From these images we obtained maximum intensity Z projections, which were then used to extract myosin intensity values of the epithelial junctions. For all vertices constituting a membrane in the segmentation, smoothed intensity values were first obtained by taking the median over first neighbors. The intensity value for each membrane is then defined as the mean of smoothed intensities at each of its constituting vertices. Then, to allow comparison with the inferred stresses, these values were normalized to a mean value of one for each embryo.

Zebrafish primordium migration experiments

Zebrafish carrying the $Tg[-8.0cldnb:Lyn-EGFP]^{36}$ were kept under standard conditions at 28.5°C. At 40-48 hours post-fertilization, larvae were anesthetized with MS222 and mounted in 0.8% low-melting point agarose on a glass-bottom petri dish. Larvae were imaged in a custom-built Zeiss inverted spinning disk confocal microscope. 16 slices Z stacks of the migrating primordium II were acquired every two minutes with a 63X objective. Subsequently, one z-slice was manually selected from each frame, and the membrane image was segmented using Tissue Analyzer³⁷. The image segmentations were used for ForSys predictions, and the cells' centroids' X and Y coordinates, the time point (frame number), and the cell pressures were exported. The probability density function of the cell position along the anteroposterior axis was estimated via a Gaussian kernel in the R statistical software. The value of cell pressure was used as a weight in the density estimation. From this density curve, local maxima were determined through the second derivative.

The conceptual model behind ForSys

ForSys uses microscopy images as input to estimate the mechanical state of the tissue. The software extracts vertices, edges, and cells from the segmentation, which can be achieved through different software (see, for example, ^{8,22,38}). Although most vertices separate two edges, a number of them connect three or more edges and are central for stress inference. We call these pivot vertices or junctions. ForSys calculates the mechanical stresses operating on each edge while assuming mechanical equilibrium in each vertex. Conveniently, this creates a system of equations representing

the geometrical state of the tissue^{10,12}. One equation per coordinate is built from every pivot vertex using force balance at the junction.

In the dynamic modality, ForSys assumes that each vertex is in an overdamped regime, where a viscous damping force proportional to the velocity balances the mechanical stresses at that vertex. This creates a non-homogeneous system of equations where the inhomogeneity is proportional to the vertex velocity. In both Static and Dynamic modalities, the resulting system of equations is solved through a Least Squares minimization with the constraint that the average tension equals one (see “Solving the system of equations” in Materials and Methods for more details).

Finally, ForSys uses the stress inferred as an input to estimate cellular pressure within the tissue. For this, a Young-Laplace equation is built at each cell-cell membrane, and the corresponding system is solved similarly to the stresses. However, this requires that the mean pressure of the system is equal to zero (see Section Statical stress inference for details). ForSys renders intercellular stresses as a color code of the cellular outlines, specifically at the edges. Similarly, intracellular pressures are depicted in a color code within the cytoplasmic area of the cells. Moreover, the numerical values of the inference and other observables are easily exportable, facilitating further analysis of the mechanical state of the tissue.

seAPIpy: generation of *in silico* tissues to validate ForSys.

To validate the accuracy of ForSys, we compared the intercellular mechanical stresses inferred by the software with a ground truth distribution of stresses within the tissue. To establish the ground truth, we employed a cell-based computational model to simulate tissues with known intracellular pressures and intercellular stress patterns. Specifically, we employed the vertex model, which is particularly suitable for mechanically evolving epithelial tissues^{39,40}. For the implementation of the vertex model, we utilized Surface Evolver software³². To facilitate the integration and streamline the simulation process, we developed a Python-based software called seapipy³³. This open-source computational tool enables Python scripting to generate the desired initial tissue conditions and simulate them using a vertex model implemented in Surface Evolver. seAPIpy generates a Voronoi tessellation with a given geometry as a starting configuration and assigns initial stresses to the edges (Extended data figure 1). Through seAPIpy functions, the user may add Surface Evolver commands to create the desired conditions for evolution and generate the Surface Evolver-compatible file. By leveraging both ForSys and the capabilities of seAPIpy software, we implemented four conditions as examples that were later used to test ForSys stress inference in both its Static and Dynamic modalities. The first two conditions induce a furrow formation on vertical and horizontal strips, respectively. In the third condition, a central zone of elevated stress is introduced, which diminishes

radially. Lastly, a fourth condition assigns five different random stresses to edges, following a uniform distribution, with a 50 % spread in stress values. Each condition underwent twenty-five repetitions. These simulations served as the ground truths for validating ForSys *in silico*, as shown in the following two sections (Fig. 2 A, 3 A, and Extended data figure 2).

We generated four examples to validate our software *in silico*. In all four cases, tissues evolve until a time zero is defined. The stresses are modified according to a prescribed condition, and the tissue evolves for shorter periods while it relaxes.

We generated the initial condition in each example by creating a Voronoi tessellation from $N = 64$ points in a rectangular grid. Each point in the grid is moved with a Gaussian noise centered at zero. Initial cell target areas are randomly assigned as $A = 450 \pm 5$ (mean \pm std) from a normal distribution. The initial stress of each edge is also taken from a normal distribution centered at 1 with a standard deviation of 0.1. From this state, the tissue evolved through several rounds of vertex averaging and T1 swaps with varying scales.

We defined time as the number of steps elapsed, times the scale ($t = n \Delta t$), and call it Surface Evolver Time (SET). The first time point is generated after 3875 SET, after which the tissue is evolved for an additional 125 SET. At this point, membrane stresses are changed according to each condition, and each simulation snapshot is saved every 0.25 SET.

In the conditions corresponding to the horizontal and vertical furrows, the new tensions are generated by summing the value corresponding to the position of the center of an edge in the probability density function (PDF) of a normal distribution to the initial randomized value. The normal distribution has its maximum at the centroid of the tissue and a standard deviation of ~ 2 cellular radii. Vertical furrows have the PDF on the y-axis, and horizontal furrows on the x-axis. Similarly, the circular furrow uses the distance of the edge's center to the tissue's centroid to calculate the new stress. Finally, in the condition corresponding to the “random examples”, tensions are assigned from normal distributions with a 50% spread around five possible values (1, 1.1, 1.2, 1.3, 1.5) chosen uniformly.

Therefore, seapipy facilitates testing multiple *in silico* examples and has an easy integration into the analysis pipeline. seapipy offers advantages over an existing package (python-evolver)⁴¹ because it incorporates Surface Evolver syntax directly into the Python code, eliminating the need to write Surface Evolver commands manually into the input files. seapipy allows for a systematic and straightforward generation of *in silico* ground truths, enabling a better exploration of strengths and limitations in stress inference tools.

Statical stress inference

We assume a 2D tissue with C cells, representing each cell as a polygon. The system consists of V vertices and E edges in total. Each edge is composed of two vertices. We define pivot vertices as those that correspond to junctions between three cells or are at the border of the tissue. This method can be applied to junctions shared by more than three cells but at the risk of losing stability in the underlying model⁴². All vertices between two pivots are regarded as virtual, and only pivot vertices are used to compute stresses. We then use Newton's second law and assume mechanical equilibrium to assert that the sum of forces at each pivot vertex equals zero. We can calculate the force acting on each vertex as a sum of the contributions of the forces along the edges connected to it. Mathematically, the force at each pivot vertex will have an equation in the form

$$\vec{F}_i = \sum_{\langle ij \rangle} \lambda_{ij} \vec{r}_{ij} \quad (\text{Eq. 1})$$

Where i and j indicate the vertices i and j , \vec{F}_i is the force on vertex i , λ_{ij} is the edge force modulus in that edge, and \vec{r}_{ij} is the versor along the edge starting at vertex i . The sum is done over all j vertices connected to the vertex i . Note that $\lambda_{ij} = \lambda_{ji}$. The directions of the r_{ij} versor is obtained by fitting a circle to the corresponding membrane, following other authors^{10,12}.

Applying Eq. 1 to all the vertices in the tissue will translate into a homogeneous set of linear equations that have to be solved simultaneously with the edge tensions (λ_{ij}) as unknowns. Hence, we write Eq. 1 and equate it to zero for each system vertex to guarantee that all the forces are balanced. Each of these V equations will be written as

$$\lambda_1 \vec{r}_{i1} + \lambda_2 \vec{r}_{i2} + \dots + \lambda_E \vec{r}_{ij} = 0 \quad (\text{Eq. 2})$$

this equation corresponds to the i th vertex, and the edge tensions λ are the unknowns.

Similarly, it is possible to infer the pressures of each cell in the tissue by assembling a system of equations that connects the stress at each membrane with its curvature. The Young-Laplace equation relates these quantities with the pressure difference between two neighboring cells.

Symbolically,

$$P_j - P_i = \lambda_{ij} \rho_{ij} \quad (\text{Eq. 3})$$

Where P_i is the pressure of cell i , λ_{ij} is the stress of the membrane shared by cells i and j , and ρ_{ij} is the curvature of the shared membrane. This leads to a system of E equations, one per edge, and C unknowns.

The dynamic inference case

The static inference algorithm assumes that vertices do not move. To perform stress inference in a dynamic tissue where all vertices are moving, we modified the static algorithm to include vertex movement. If the system has a low Reynolds number, viscous forces dominate the dynamics over

inertial components; Eq. 1 can be modified, assuming a constant viscosity throughout the tissue, to incorporate viscous forces as

$$\vec{F}_i = \sum_{\langle ij \rangle} \lambda_j \vec{r}_{ij} - \eta \vec{v}_i \quad (\text{Eq. 4})$$

where \vec{v}_i is the velocity of vertex i and η the viscosity of the tissue. This would modify the coupled system of equations, which could be rearranged to get the i th vertex

$$\sum_{\langle ij \rangle} \lambda_j \vec{r}_{ij} = \eta \vec{v}_i \quad (\text{Eq. 5})$$

To determine the scales correctly, we proceeded to make Eq. 5 nondimensional. For this, we redefine the stresses by using an unknown reference stress $\lambda'_j = \frac{\lambda_j}{\bar{\lambda}}$. We take this reference stress as the average stress in the system. We used a reference velocity defined as the time average over all the frames of the mean junction velocity

$$\bar{v} = \frac{1}{N_{frames}} \sum_{t=t_i}^{t_f} \frac{\sum_i ||\vec{v}_i^t||}{N^{t_v}} \quad (\text{Eq. 6})$$

Combining these equations gives a nondimensional expression for the force balance at each junction

$$\sum_j \lambda'_j \vec{r}_{ij} = \left(\frac{\eta \bar{v}}{\bar{\lambda}}\right) \frac{\vec{v}_i}{\bar{v}} \quad (\text{Eq. 7})$$

Importantly, this led to the nondimensional parameter $\frac{\eta \bar{v}}{\bar{\lambda}}$. Even though the right-hand side of equation 5 is not a viscosity but rather a damping coefficient, we can interpret it as such in this context. Therefore, as the stress of each membrane represents the elastic forces in the system, this parameter can be interpreted as the relation between the elastic and the viscous forces acting on the system, which is inversely proportional to the Weissenberg number ($\frac{1}{Wi} = \frac{\eta \bar{v}}{\bar{\lambda}}$).

Solving the system of equations

In static and dynamic cases, it is necessary to solve a system of linear equations with homogeneous and inhomogeneous conditions, respectively. In both cases, we will turn the system into its matrix form, add a constraint to the unknowns through a Lagrange multiplier, and convert it into a least squares problem. Finally, we will attempt to invert the resulting matrix, and if that is not possible, we will use a numerical algorithm to find the best solution.

Given a two-dimensional tissue with V vertices and E edges, the system would have $2V$ equations, as each vertex has one equation per dimension and E unknowns, one for each edge. Following the method proposed by Brodland *et al.*¹⁰, the set of equations in Eq. 1 is then translated into matrix form as

$$M_\lambda X = B \quad (\text{Eq. 8})$$

Where M_λ is a $2V \times E$ matrix with versor coefficients, X is the unknowns column matrix of $E \times 1$, and B is a $2V \times 1$ column matrix with either all zeros under static conditions or the velocity components for

each vertex in the dynamical case. To avoid the null solution in the static case, one further condition is added: The mean value for the unknowns, *i.e.*, λ , is set equal to one, using the equation

$$\sum_{k=0}^E \lambda_k = E \quad (\text{Eq. 9})$$

where E is the number of edges and λ_k is the tension corresponding to the k th edge. In the matrix representation, this entails adding a Lagrange multiplier to the unknowns, a row and column of ones for the tension constraint, and a new row in the B matrix. Hence, the equations to be solved have $2V + 1$ equations and $E + 1$ unknowns. As this system might not always guarantee a solution, we transformed it using least squares. To this end, we apply the transpose matrix M^{tr}_λ to the equation, giving a new system

$$M^{tr}_\lambda M_\lambda X = M^{tr}_\lambda B \quad (\text{Eq. 10})$$

Symbolically,

$$M'_\lambda X' = B' \quad (\text{Eq. 11})$$

On the other hand, the B matrix in Eqs. 6 and 7 for the dynamic case has the corresponding nondimensional velocity component multiplied by the scale parameter ($1/Wi$) described in Eq. 7 in each row. Its final element has the number of edges E to enforce the constraint. To quantify the movement present in the tissue, we calculate the 2-norm of the B matrix, removing the last row, this vector is referred to as $|v|_2$. Each vertex is tracked through time to obtain the vertex velocity, and the forward velocity is calculated in all but the last step, where the backward expression is used. If a vertex cannot be followed in a frame, *i.e.*, due to significant changes in the tissue shape, it is assigned a null velocity for the frames where it cannot be tracked.

Hence, to elucidate the acting forces within the tissue, the software attempts to solve it by inverting the M'_λ matrix, thus having a solution

$$X = M'^{-1} B' \quad (\text{Eq. 12})$$

If the system is not invertible, *i.e.*, M' is singular, or if any of the edge tensions found are negative, a Least Squares algorithm can be used to find the stress values, such as a Non-Negative Least Squares, SciPy's package or `lmfit`⁴³⁻⁴⁵.

After solving the system, the calculated stresses can be used to infer the pressures of the cells. As seen from the Young-Laplace equation (Eq. 3), pressures are expressed through an inhomogeneous system of linear equations. The left-hand side is a matrix with one column per cell and one row per membrane. Each row has two entries different from zero, one +1 and one -1, representing the difference in pressure at that membrane. The right-hand side consists of a column matrix with the product of each membrane's stresses and curvatures ($\lambda_{ij}\rho_{ij}$). Then, the equations are solved analogously to the stress case using the Least Squares with the constraint that the average pressure must be zero.

Evaluating goodness of fit

We evaluated the goodness of fit of the inferred data to the ground truth using a tailored saturated score function. This score combines the Pearson correlation coefficient (p), the Mean Absolute Percentage Error (M), and the coefficient of determination (r) as

$$s(M, p, r) = \frac{\alpha}{M} + \frac{\beta}{2} \frac{1+p}{1-p} + \frac{\gamma}{1-r} \quad (\text{Eq. 13})$$

where α , β and γ are free parameters set to one. As this function is unbounded from above, we saturate the score at $s = 299.5$ for representation purposes in Figure 2, Figure 3 and Extended Data Figure 5. This value comes from an error of 1 %, *i.e.* $s(0.01, 0.99, 0.99) = 299.5$.

Determination of the scale parameter

We performed a sweep for the correct parametrization of the scale value ($1/W_i$) in the *in silico* examples, from 0 to 0.5. We calculated the score value for each of the five repetitions in the four examples at each time (Extended data figure 5A). We chose the best parameter as the median in each case (Extended data figure 5B). This value coincided with the mode in each case. We used $\frac{1}{W_i} = 0.08$ for the x-axis furrow, $\frac{1}{W_i} = 0.07$ for the y-axis furrow, $\frac{1}{W_i} = 0.13$ for the circular furrow, and $\frac{1}{W_i} = 0.18$ for the random tensions.

Comparing ForSys with other computational methods

We tested the similarity of the static implementation of ForSys with two other established software: CellFIT¹⁰ and DLITE¹². To this end, we applied the DLITE python package to solve the four *in silico* examples used throughout this work, taking advantage of its CellFIT modality. We found that the coefficient of determination is almost equal among the methods (Extended data Fig. 3A) and that the stress distributions emerging from the solution are roughly identical (Extended data Fig. 3B). Moreover, the coefficient of determination is similar for the accumulated data of all repetitions for each example at the last simulated frame (Extended data Fig. 3C).

Moreover, we generated an artificial normal distribution to measure the relative differences with a first moment of 1 and a second moment equal to 0.2. We calculated the Wasserstein Distance between the *in silico* distributions and the normal generated randomly. Given two distributions, X and Y , the Wasserstein Distance is zero if and only if the two distributions are equal. The distance between two distributions can be arbitrarily large for increasingly different shapes.

The Wasserstein Distance is almost zero in all cases, indicating that the distributions gathered from the three inference methods are similar. To compare its similarity, we used an artificially generated

normal distribution. Using this metric, we found that the methods among themselves are ~30 times closer in the x-furrow and y-furrow, 10 times closer for the circular case, and ~5 times closer in the random densities example than to the normal distribution.

Statistical estimators

To compare distributions, the Mann-Whitney U test was used with different alternative hypotheses, depending on whether we tested for stochastic ordering or whether distributions are different. In all *in silico* cases, the number of samples is twenty-five, which is the number of repetitions per condition. The Pearson correlation coefficient (R) was used when we evaluated correlations. The number of samples in each case is indicated when reporting the p -value.

Data availability

All relevant data and materials will be made available upon request.

Code availability

The seapipy³³ codebase is available on Github at <https://github.com/borgesaugusto/seapipy>.

ForSys⁴⁶ is available on GitHub <https://github.com/borgesaugusto/forsys>.

Acknowledgments

The authors thank Luis Morelli, Fabian Rost, Nicolas Aldecoa, Alice Descoeurdes and all the members of the Chara laboratory for valuable comments and suggestions. A.B. was funded by the BMBF 01GQ1904 grant. A.C. was funded by a Doctoral fellowship from CONICET, Argentina. J.S. acknowledges the support of the Novo Nordisk Foundation (grant number NNF19OC0056962) and Leo Foundation (grant number LF-OC-19-000219). The Novo Nordisk Foundation Center for Stem Cell Medicine (reNEW) is supported by a Novo Nordisk Foundation grant number NNF21CC0073729. O.C. was funded by CONICET and Fondo para la Investigación Científica y Tecnológica (PICT-2019-03828).

Author Contributions

A.B. developed the ForSys code, simulated the *in silico* results, analyzed all the inference results and wrote the manuscript. A.C. contributed to the development of the ForSys code and analyzed all the

inference results. G.V. generated the *Xenopus* images and edited the manuscript. J.M.-R. acquired the zebrafish microscopy images and analyzed the corresponding results. J.S. supervised the *Xenopus* project and edited the manuscript. H.L.S. supervised the Zebrafish project and edited the manuscript. O.C. conceived the project, contributed to the ForSys code, analyzed all the inference results, supervised A.B. and A.C as well as wrote the manuscript.

Competing Interests statement

The authors declare that they have no competing interests.

References

1. Serwane, F. *et al.* In vivo quantification of spatially varying mechanical properties in developing tissues. *Nat. Methods* **14**, 181–186 (2017).
2. Mongera, A. *et al.* A fluid-to-solid jamming transition underlies vertebrate body axis elongation. *Nature* **561**, 401–405 (2018).
3. Mongera, A. *et al.* Mechanics of the cellular microenvironment as probed by cells in vivo during zebrafish presomitic mesoderm differentiation. *Nat. Mater.* **22**, 135–143 (2023).
4. Nishizawa, K., Lin, S.-Z., Chardès, C., Rupprecht, J.-F. & Lenne, P.-F. Two-point optical manipulation reveals mechanosensitive remodeling of cell–cell contacts in vivo. *Proc. Natl. Acad. Sci.* **120**, e2212389120 (2023).
5. Bonnet, I. *et al.* Mechanical state, material properties and continuous description of an epithelial tissue. *J. R. Soc. Interface* **9**, 2614–2623 (2012).
6. Etournay, R. *et al.* Interplay of cell dynamics and epithelial tension during morphogenesis of the *Drosophila* pupal wing. *eLife* **4**, e07090 (2015).
7. Tetley, R. J. *et al.* Tissue fluidity promotes epithelial wound healing. *Nat. Phys.* **15**, 1195–1203 (2019).
8. Heller, D. *et al.* EpiTools: An Open-Source Image Analysis Toolkit for Quantifying Epithelial Growth Dynamics. *Dev. Cell* **36**, 103–116 (2016).

9. Bosveld, F., Wang, Z. & Bellaïche, Y. Tricellular junctions: a hot corner of epithelial biology. *Curr. Opin. Cell Biol.* **54**, 80–88 (2018).
10. Brodland, G. W. *et al.* CellFIT: A Cellular Force-Inference Toolkit Using Curvilinear Cell Boundaries. *PLOS ONE* **9**, 1–15 (2014).
11. Roffay, C., Chan, C. J., Guirao, B., Hiiragi, T. & Graner, F. Inferring cell junction tension and pressure from cell geometry. *Development* **148**, dev192773 (2021).
12. Vasan, R., Maleckar, M. M., Williams, C. D. & Rangamani, P. DLITE Uses Cell-Cell Interface Movement to Better Infer Cell-Cell Tensions. *Biophys. J.* **117**, 1714–1727 (2019).
13. Purcell, E. M. Life at low Reynolds number. *Am. J. Phys.* **45**, 3–11 (1977).
14. Bambardekar, K., Clément, R., Blanc, O., Chardès, C. & Lenne, P.-F. Direct laser manipulation reveals the mechanics of cell contacts in vivo. *Proc. Natl. Acad. Sci.* **112**, 1416–1421 (2015).
15. Clément, R., Dehapiot, B., Collinet, C., Lecuit, T. & Lenne, P.-F. Viscoelastic Dissipation Stabilizes Cell Shape Changes during Tissue Morphogenesis. *Curr. Biol.* **27**, 3132-3142.e4 (2017).
16. Dealy, J. M. Weissenberg and Deborah numbers—Their definition and use. *Rheology Bulletin* **79**, 14–18 (2010).
17. Poole, R. J. The Deborah and Weissenberg numbers. *Rheology Bulletin* **53**, 32–39 (2012).
18. Thompson, R. L. & Oishi, C. M. Reynolds and Weissenberg numbers in viscoelastic flows. *J. Non-Newton. Fluid Mech.* **292**, 104550 (2021).
19. Ventura, G. *et al.* Multiciliated cells use filopodia to probe tissue mechanics during epithelial integration in vivo. *Nat. Commun.* **13**, 6423 (2022).
20. Nizak, C. *et al.* Recombinant Antibodies Against Subcellular Fractions Used to Track Endogenous Golgi Protein Dynamics *in Vivo*: **Recombinant Antibodies for Cell Biology**. *Traffic* **4**, 739–753 (2003).
21. Hashimoto, H., Robin, F. B., Sherrard, K. M. & Munro, E. M. Sequential Contraction and Exchange of Apical Junctions Drives Zippering and Neural Tube Closure in a Simple Chordate. *Dev. Cell* **32**, 241–255 (2015).

22. Aigouy, B., Cortes, C., Liu, S. & Prud'Homme, B. EPySeg: a coding-free solution for automated segmentation of epithelia using deep learning. *Development* dev.194589 (2020)
doi:10.1242/dev.194589.
23. Ghysen, A. & Dambly-Chaudière, C. The lateral line microcosmos. *Genes Dev.* **21**, 2118–2130 (2007).
24. Olson, H. M. & Nechiporuk, A. V. Using Zebrafish to Study Collective Cell Migration in Development and Disease. *Front. Cell Dev. Biol.* **6**, 83 (2018).
25. Scarpa, E. & Mayor, R. Collective cell migration in development. *J. Cell Biol.* **212**, 143–155 (2016).
26. Hava, D. *et al.* Apical membrane maturation and cellular rosette formation during morphogenesis of the zebrafish lateral line. *J. Cell Sci.* **122**, 687–695 (2009).
27. Ernst, S. *et al.* Shroom3 is required downstream of FGF signalling to mediate proneuromast assembly in zebrafish. *Development* **139**, 4571–4581 (2012).
28. Hernández, P. P., Olivari, F. A., Sarrazin, A. F., Sandoval, P. C. & Allende, M. L. Regeneration in zebrafish lateral line neuromasts: Expression of the neural progenitor cell marker sox2 and proliferation-dependent and-independent mechanisms of hair cell renewal. *Dev. Neurobiol.* **67**, 637–654 (2007).
29. Berg, S. *et al.* ilastik: interactive machine learning for (bio)image analysis. *Nat. Methods* **16**, 1226–1232 (2019).
30. Kozak, E. L. *et al.* Quantitative videomicroscopy reveals latent control of cell-pair rotations *in vivo*. *Development* **150**, dev200975 (2023).
31. Wibowo, I., Pinto-Teixeira, F., Satou, C., Higashijima, S. & López-Schier, H. Compartmentalized Notch signaling sustains epithelial mirror symmetry. *Development* **138**, 1143–1152 (2011).
32. Brakke, K. A. The Surface Evolver. *Exp. Math.* **1**, 141–165 (1992).
33. Borges, A. borgesaugusto/seapipy: v0.2.0-alpha. <https://doi.org/10.5281/ZENODO.10809290> (2024).
34. Hartmann, J., Wong, M., Gallo, E. & Gilmour, D. An image-based data-driven analysis of cellular

- architecture in a developing tissue. *eLife* **9**, e55913 (2020).
35. Yamaguchi, N. *et al.* Rear traction forces drive adherent tissue migration in vivo. *Nat. Cell Biol.* **24**, 194–204 (2022).
 36. Haas, P. & Gilmour, D. Chemokine Signaling Mediates Self-Organizing Tissue Migration in the Zebrafish Lateral Line. *Dev. Cell* **10**, 673–680 (2006).
 37. Aigouy, B., Umetsu, D. & Eaton, S. Segmentation and Quantitative Analysis of Epithelial Tissues. in *Drosophila* (ed. Dahmann, C.) vol. 1478 227–239 (Springer New York, New York, NY, 2016).
 38. Merle, T. *et al.* DISSECT is a tool to segment and explore cell and tissue mechanics in highly deformed 3D epithelia. *Dev. Cell* **58**, 2181–2193.e4 (2023).
 39. Farhadifar, R., Röper, J.-C., Aigouy, B., Eaton, S. & Jülicher, F. The Influence of Cell Mechanics, Cell-Cell Interactions, and Proliferation on Epithelial Packing. *Curr. Biol.* **17**, 2095–2104 (2007).
 40. Nagai, T. & Honda, H. A dynamic cell model for the formation of epithelial tissues. *Philos. Mag. B* **81**, 699–719 (2001).
 41. Misback, E. `elmisback/python-evolver`. (2023).
 42. Spencer, M. A., Jabeen, Z. & Lubensky, D. K. Vertex stability and topological transitions in vertex models of foams and epithelia. *Eur. Phys. J. E* **40**, 2 (2017).
 43. Lawson, C. L. & Hanson, R. J. *Solving Least Squares Problems*. (Society for Industrial and Applied Mathematics, 1995). doi:10.1137/1.9781611971217.
 44. Virtanen, P. *et al.* SciPy 1.0: fundamental algorithms for scientific computing in Python. *Nat. Methods* **17**, 261–272 (2020).
 45. Newville, M. *et al.* `lmfit/lmfit-py: 1.2.2`. Zenodo <https://doi.org/10.5281/ZENODO.598352> (2023).
 46. Borges, A., Ceccarelli, A. S. & Chara, O. `ForSys` software. Zenodo <https://doi.org/10.5281/ZENODO.11282554> (2024).

Figure Legends

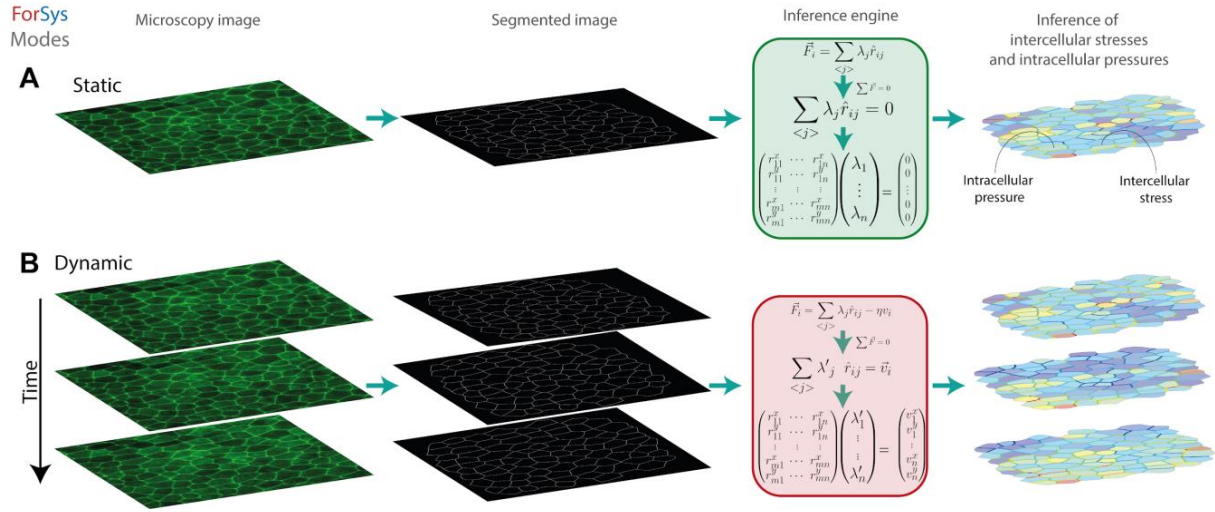


Figure 1. Force inference modalities of ForSys. (A) The static inference is performed on a microscopy image by creating a skeletonized tissue representation. Then, ForSys reads it and builds the system of equations according to the geometrical properties of the tissue, assuming that each vertex in the tissue is in mechanical equilibrium. Lastly, the system is solved, and the intracellular pressures and intercellular stresses are inferred. **(B)** Similarly, the dynamical inference uses a time series of images to add dynamical information to the system of equations used in the static case, by assuming an overdamped regime. A time mesh is generated from the succession of microscopy images, and pivot vertices are tracked through time. These are vertices at which three or more edges meet. Then, the velocity of these vertices from frame to frame \vec{v}_i is used to modify the system of equations, allowing non-static tissues to be analyzed by stress inference.

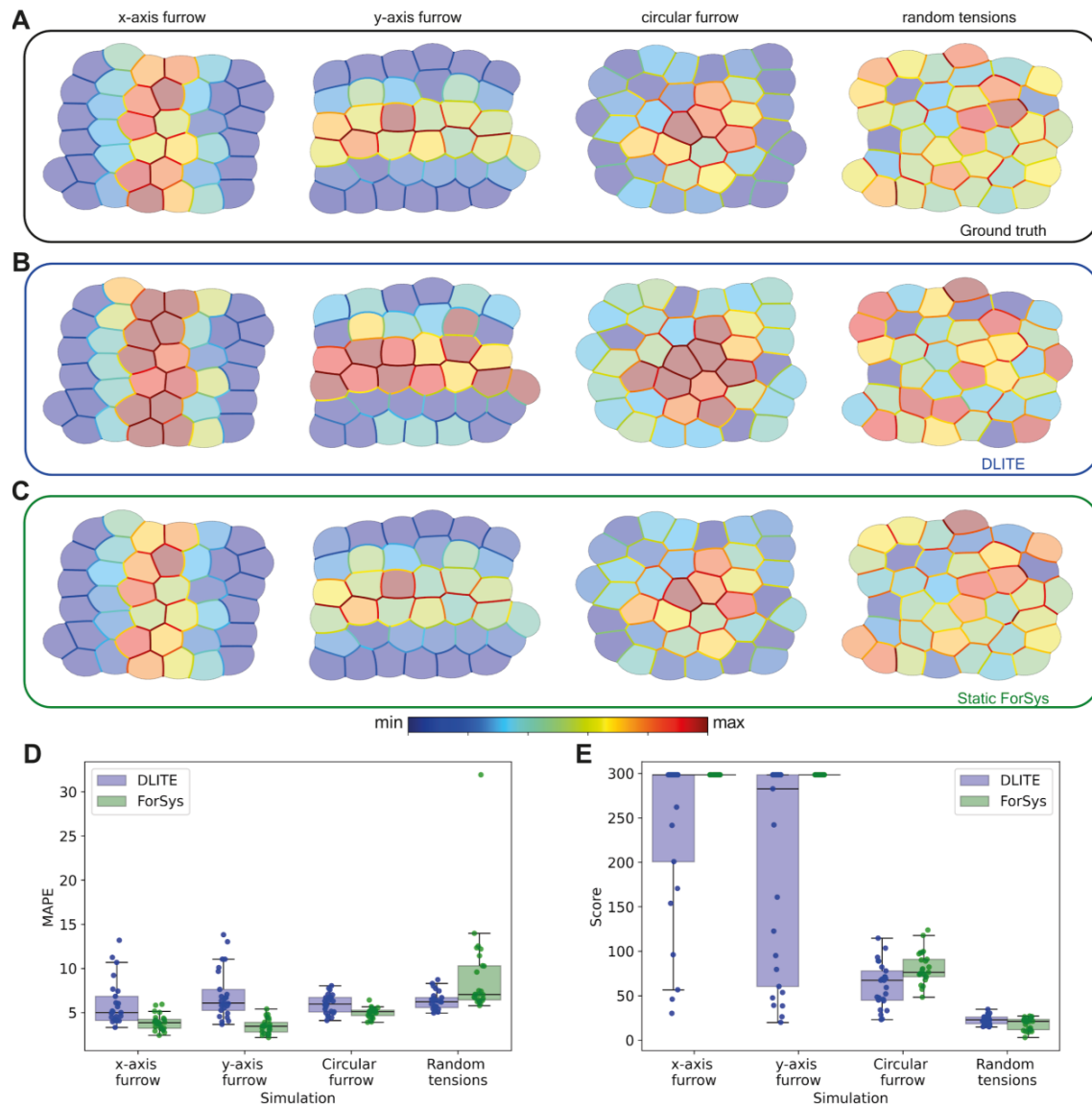


Figure 2. *In silico* validation of ForSys for tissues in static equilibrium. Four different conditions were generated with seapipy to benchmark ForSys under the static equilibrium condition. Each column shows a representative replicate per condition at the final frame ($t=24$). The ground truth (**A**) can be compared to the values for the DLITE predictions (**B**) and the Static ForSys (**C**). The three rows shown correspond to the final frame of the simulation. The color bar above the last two panels shows the order of the colormap for both the stresses and the pressures. Pressures in the cells are represented with transparency for improved visualization. The mean absolute percentage error (MAPE) (**D**) and the saturated score function (**E**) for all simulations ($N = 25$) are represented in two boxplots, DLITE and Static inference with ForSys, paired by condition. (see Materials and Methods “Evaluating goodness of fit”) Dots show the result for individual repetitions.

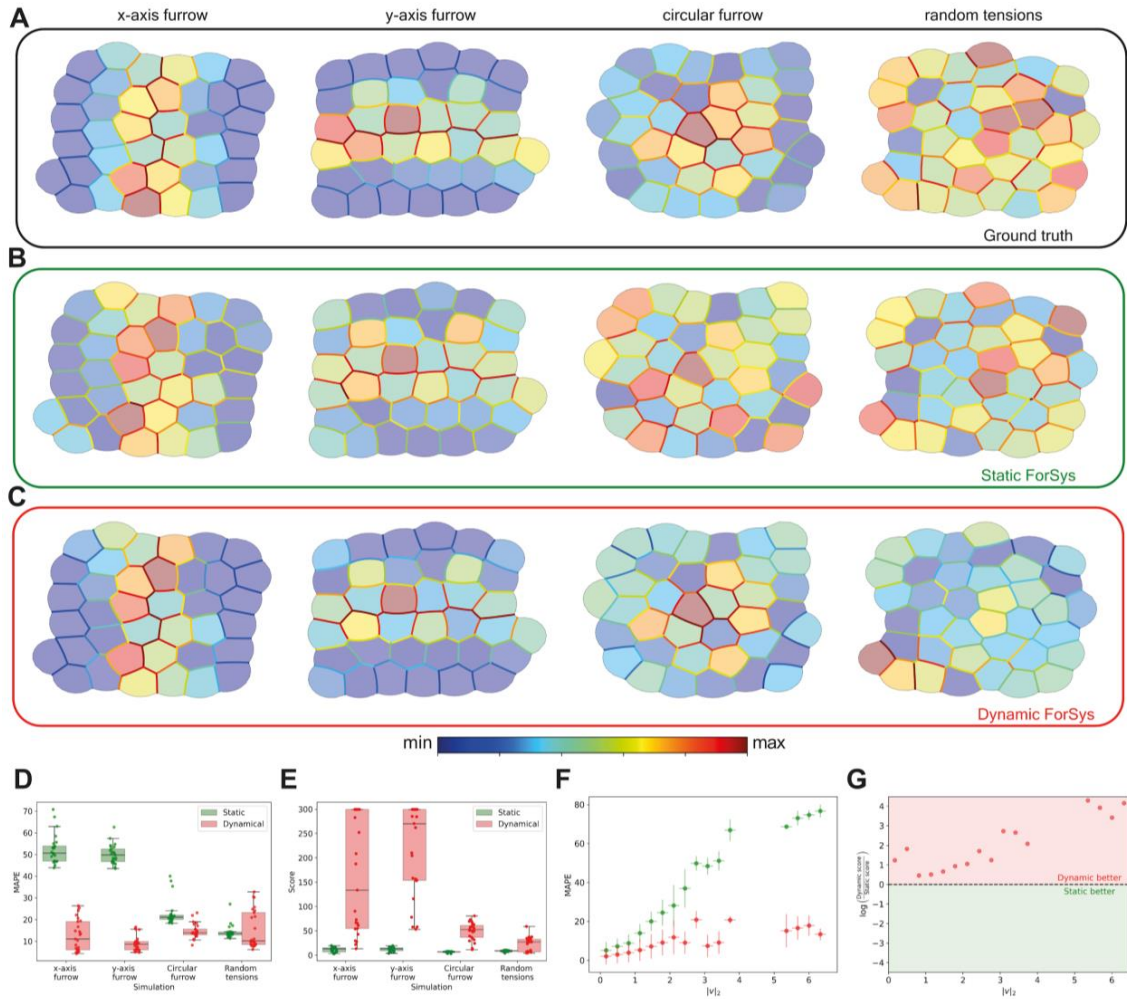


Figure 3. *In silico* validation of ForSys for tissues in dynamical equilibrium. We generated four examples with seapipy to test dynamical equilibrium conditions. Each column shows a representative repetition per example. The first row **(A)** shows the ground truth values for the stress and the pressures, the static inference made by ForSys is in the second row **(B)**, and the dynamical ForSys inference is in **(C)**. We show each example at one time point after the system's tensions changed. The color bar above the last two panels shows the order of the colormap for both the stresses and the pressures. The mean absolute percentage error **(D)** and the saturated score function value **(E)** for all simulations are represented in two boxplots, Static and Dynamical inference, paired by condition. Dots show the result for individual repetitions. **(F)** Dependence of the MAPE with the velocity $|v|_2$. The scattered dots are the median for all experiments with a velocity corresponding to the current $|v|_2$ bin. Error bars in the y-axis are one standard deviation, and error bars in the x-axis represent the size of the velocity bin. **(G)** Dynamic to static score function ratio ($r = \log(\frac{\text{dynamic}}{\text{static}})$) as a function of the $|v|_2$ bin. A ratio bigger than zero shows that the dynamic solutions performed better (Red zone), and a negative value (Green Zone) favors the static solution. The black dashed line at $y = 1$ separates both zones. All velocity bins favor the dynamic solution.

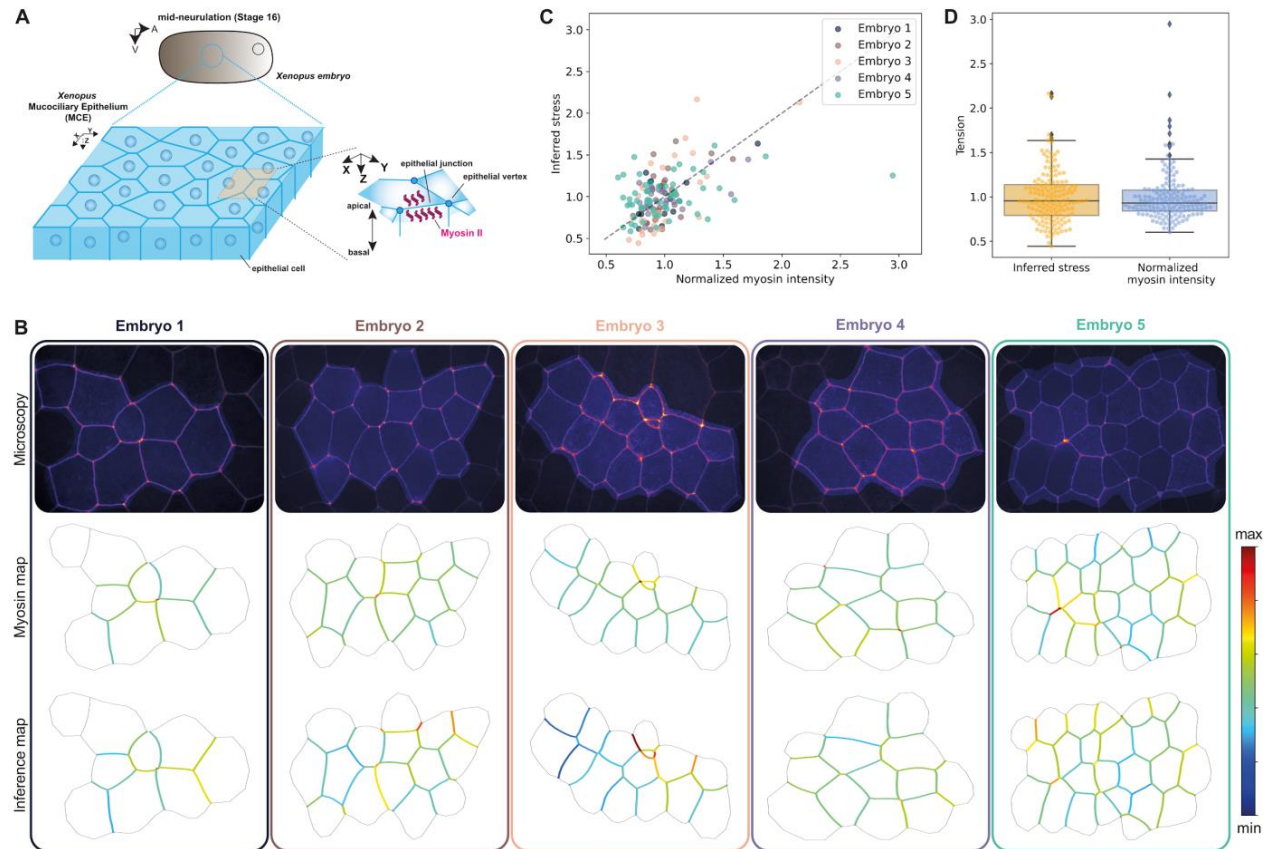


Figure 4. Comparison of ForSys-derived stress with myosin II measurements in the Xenopus embryo mucociliary epithelium. (A) Scheme of the Xenopus embryo and position of the mucociliary epithelium. **(B)** Five examples of inference in Xenopus embryos. The microscopy image is shown alongside the myosin intensity map and the ForSys inference result. The color code in the maps represents the myosin sensor intensity and the stress prediction. The scale was saturated at tension values of two. The highlighted region in the microscopies shows the area that was analyzed. **(C)** Relationship between myosin sensor intensity and stress inferred for the five examples. Each scatter point shows the value for a particular membrane in that example. The dashed black line represents the $y=x$ line. Each color coincides with the rounded rectangle around the embryo and its font color in panel (B). The average Pearson correlation coefficient is $R=0.56 \pm 0.11$; (mean \pm std) **(D)** Quantification of stresses and myosin sensor intensity for the five examples. Inferred stresses and myosin intensities are not significantly different from each other ($p=0.76$; Mann-Whitney U test; $N=154$).

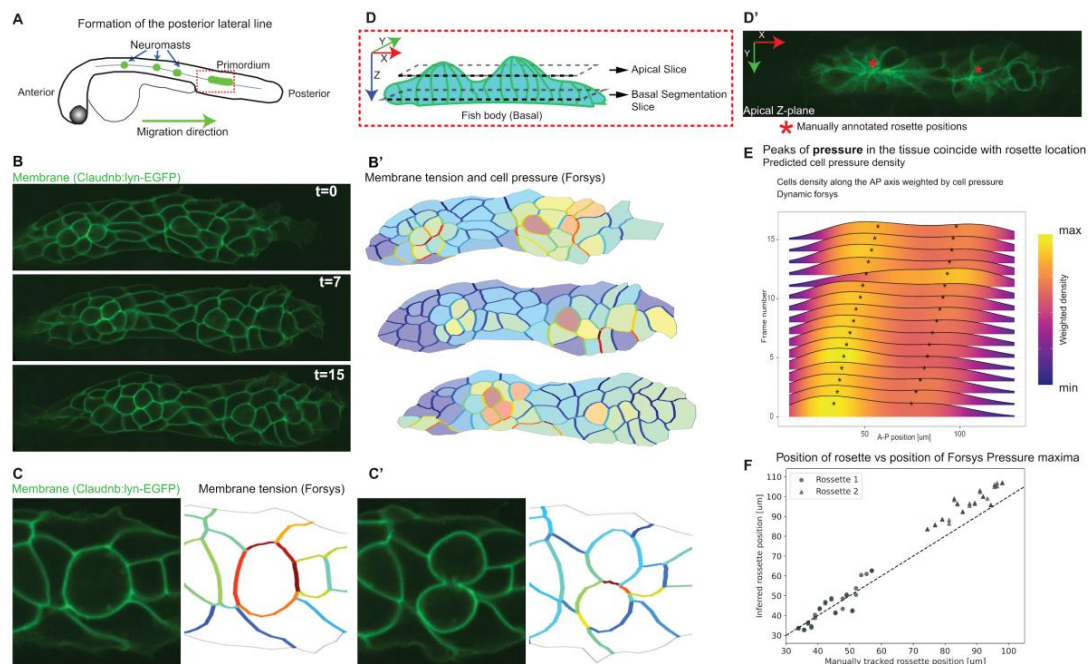


Figure 5. ForSys inference of a moving epithelium in the zebrafish lateral line at 2 dpf. (A) Schematic of the biological model. The neuromasts of the posterior lateral line are formed by detaching from a primordium that migrates from the anterior to the posterior of the fish. (B) Frames 0, 7, and 15 of the primordium migration in which cell membranes are fluorescently marked with Claudnb:lyn-EGFP. (B') The membrane signal is used for segmentation, which ForSys can use to predict cell membrane tension and intracellular pressure. (C, C') Consecutive planes show cell division. The membrane tension in the cell just about to divide is considerably higher than the surrounding membranes. After division, the dividing membrane retains a high tension. (D, D') Schematic of the primordium orientation and the position of the optical planes. Constriction of the cell membranes in rosettes is evident in the apical plane. The asterisks show the anteroposterior location of rosettes. The cell segmentation was done on a Z-plane at a more basal plane (E) Ridge line plots of Cell densities along the anteroposterior axis throughout 16 frames for a representative primordium. Time goes from bottom to top. The direction of primordium migration is to the right. The asterisks show the positions of the manually annotated rosettes. (F) Anteroposterior position of the manually tracked rosette against the inferred position by taking the local maxima of the density of pressure values from (E). The diagonal line marks $y=x$ as a reference for comparing predicted and manually annotated values.

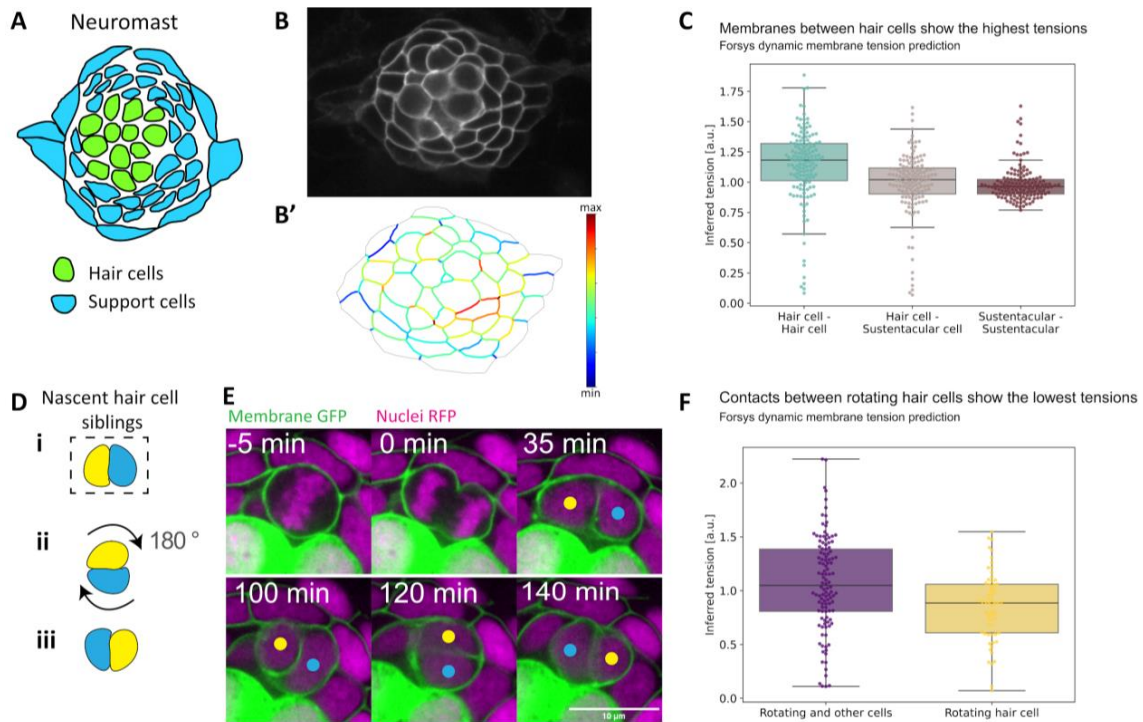
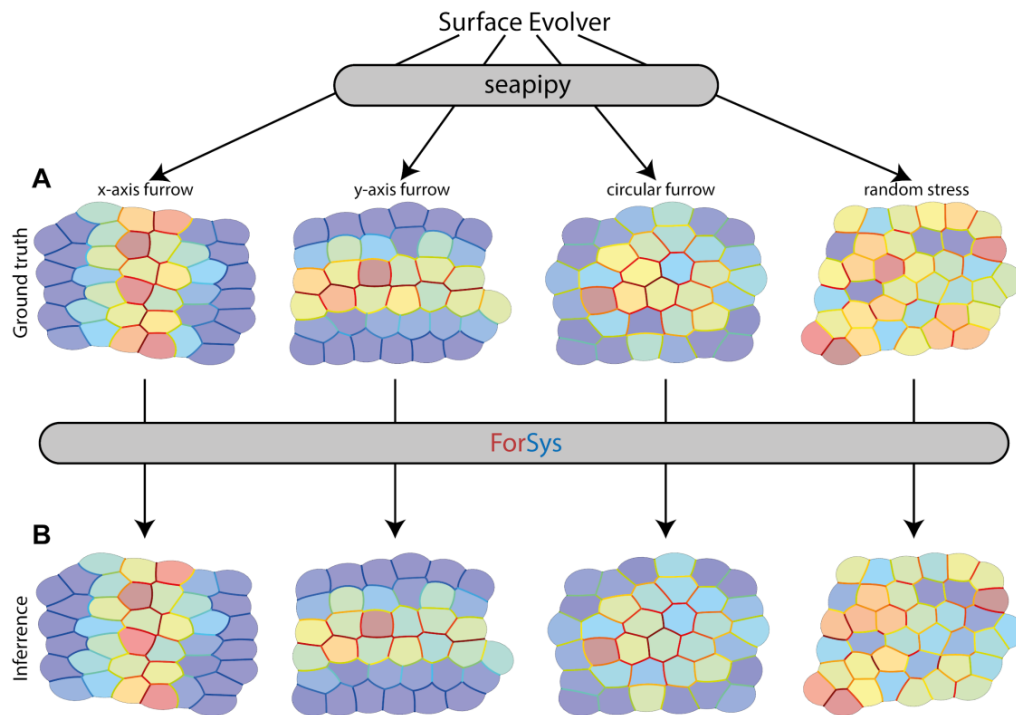
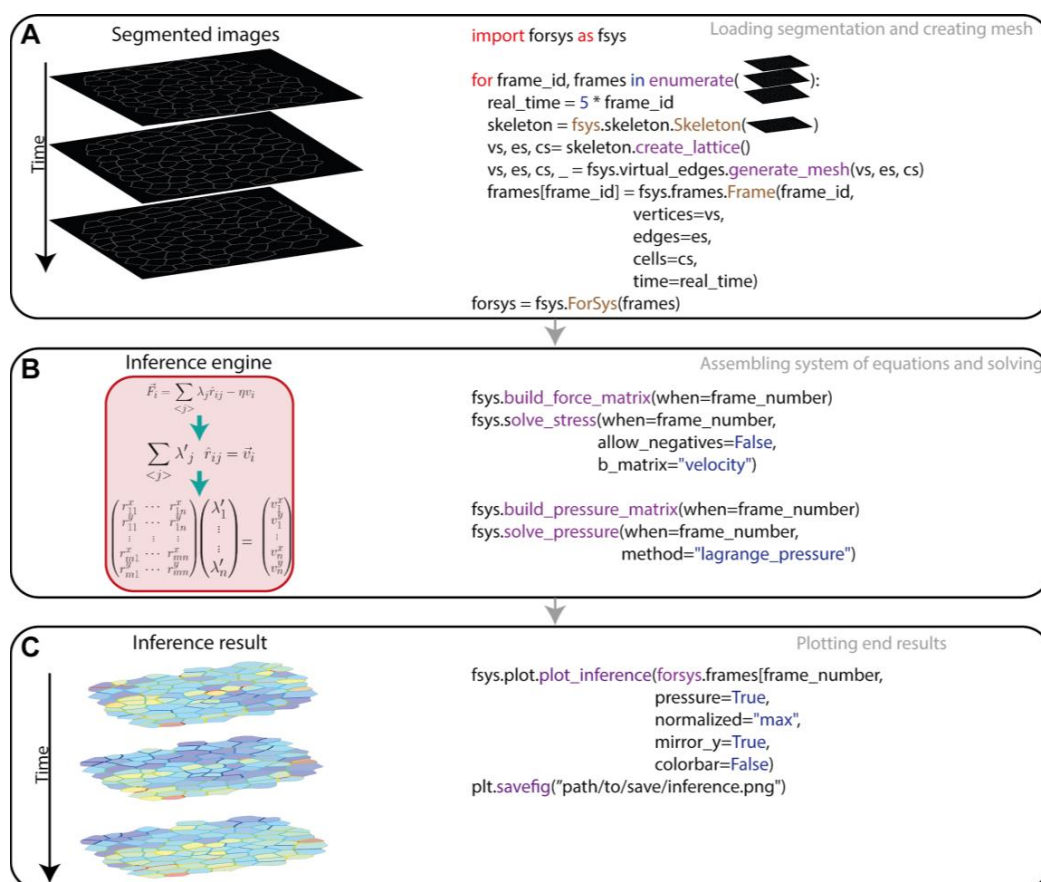


Figure 6. *in vivo* ForSys inference in an epithelium with rotating cells. (A) Schematic of cell composition in a zebrafish lateral line neuromast. Sensory hair cells are located in the center and are surrounded by support cells. (B) Image of a neuromast whose cells can be tracked by membrane-tethered EGFP. (B') ForSys tension inference after membrane segmentation. (C) The tension inferred for membranes is classified by the type of cell-cell contact. The homotypic contacts between hair cells show the highest predicted tension, while the homotypic contacts between support cells show the lowest on average. Each data point is the mean of the predicted tension values for each membrane type in one frame. The frames come from N=7 time-lapse experiments. (D) Schematic of the planar cell inversions occurring in 50% of the nascent hair cell pairs: sibling hair cells perform a 180° rotation to exchange positions along the anterior-posterior axis. (E) Time-lapse frames showing the *in vivo* rotation process: around 100 minutes after mitosis, the nascent hair cells exchange anteroposterior positions by rotating in the epithelial plane. The sibling cells remain attached to each other during the rotation, while the surrounding cells do not actively participate in the movement. (F) Homotypic tensions between the young rotating hair cells are significantly lower than their contacts with the surrounding cells.

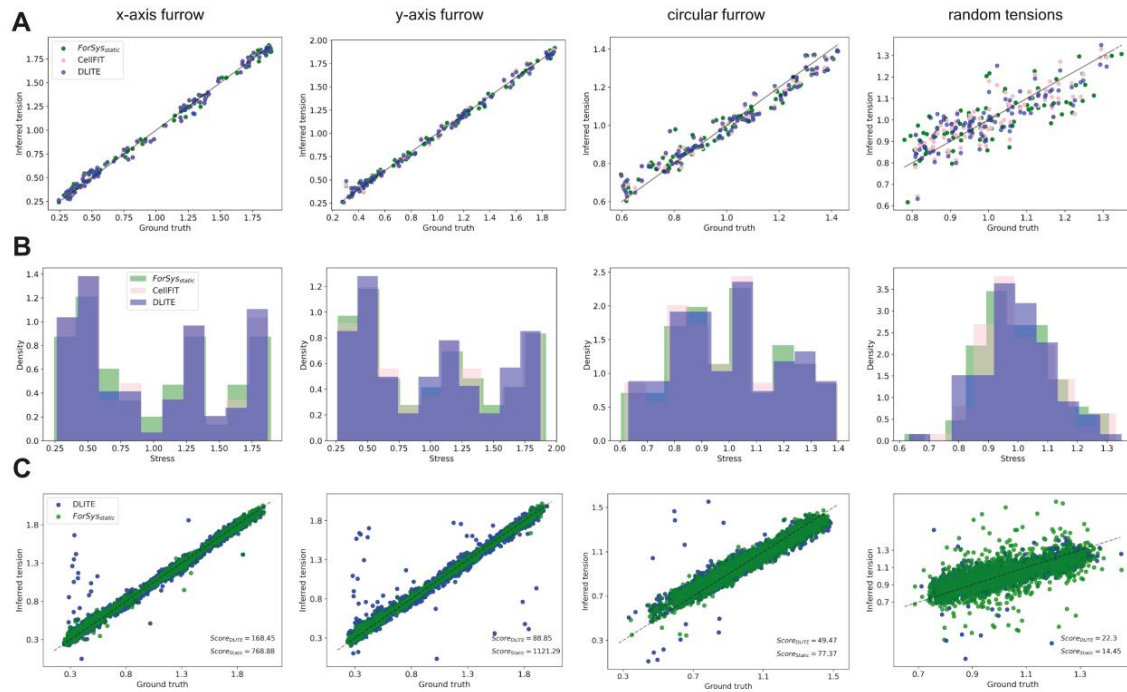
Extended data figures Legends



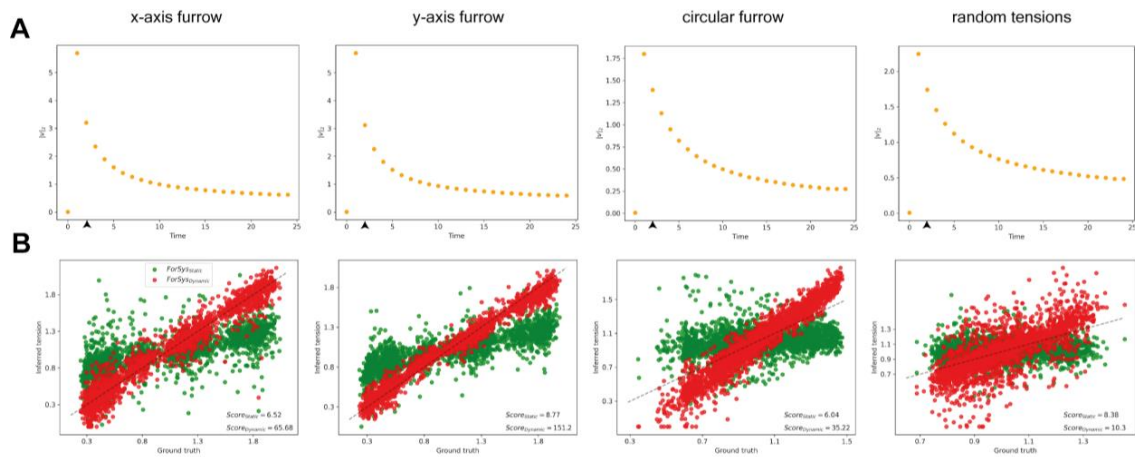
Extended Data Figure 1. ForSys pipeline for validation. We used different conditions to generate example tissues with varied stresses and pressures. All examples are created through the seapipy package, which uses Surface Evolver as a backend (A). Then, ForSys is applied in any of its modalities to infer the stresses and pressures (B).



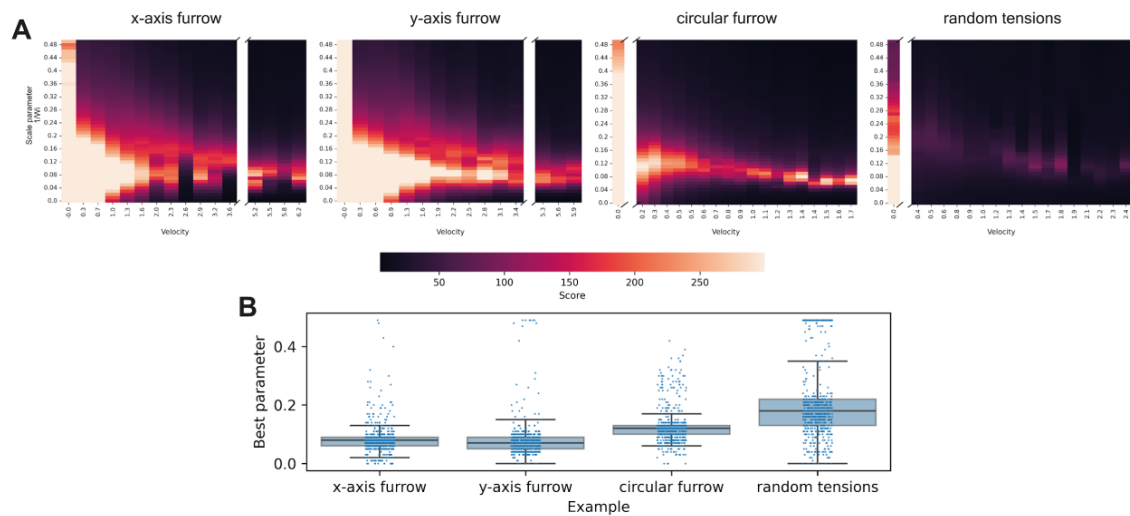
Extended Data Figure 2. ForSys general implementation. ForSys uses skeletonized images as input, which are read with the Skeleton() module of the software. Frames are collected in a dictionary and then passed to the ForSys() class to generate the corresponding mesh (A). Then, the matrices for the stresses and the pressures are built through different modules and solved individually (B). Stresses must be previously calculated to infer the pressures due to their dependence on the membrane stress. Finally, the inferred stresses and pressures are exported through the plot_inference() methods (C).



Extended Data Figure 3. Comparison between staticForSys and other force inference methods. We tested whether the static implementation of ForSys differed from the values of DLITE and CellFIT. Each column represents one of the examples. We show that the inferred stress versus the ground truth follows the $y=x$ line, plotted as a solid black line as a visual aid, for the three methods at the last simulated frame (**A**). Moreover, the distribution of stresses of all methods has similar behaviors in the histograms (**B**). Both panels (**A**) and (**B**) are for a selected representative simulation. Then, the result for all inferred tensions versus ground truth repetitions is shown for each condition at the last simulated frame. The black dashed line is the $y=x$ line and is a visual aid. The score function's values are in the lower right corner of each plot (**C**). ForSys, in its static modality, has better results in the three first examples and comparable results in the random tension case.



Extended Data Figure 4. Forsys dynamic at each example. Each column groups plots corresponding to the same prescribed conditions. **(A)** The evolution of tissue movement for each example is shown. The orange scatter dots are the mean of the 2-norm of the velocities vector, with the uncertainty being one standard deviation. In all cases, the values are derived from each example's repetitions. **(B)** The inferred tension versus ground truth is plotted for all examples. Dynamical results are plotted in red, while static ones are in green. The $y = x$ is plotted as a visual aid as a dashed black line. The score function values are in the lower right corner of each plot. In every case ForSys in its Dynamic modality gives a better score than its static counterpart.



Extended Data Figure 5. Scale parameter exploration. (A) Heatmaps show the saturated score function values for the sweep of the scale parameter proportional to the inverse of the Weissenberg number $(Wi)^{-1}$ for each example and all 25 repetitions as a function of the velocity of the frame. This velocity is defined as the norm of the vector containing the velocities in the x and y direction of each tracked junction in the tissue. The score function is calculated as described in Materials and Methods, with saturation at the corresponding value $s(0.01, 0.99, 0.99)$. **(B)** Shows the boxplots for the scale parameter corresponding to the highest score value for each time point and example. The median values of these four distributions are $m_{x-axis} = 0.08$; $m_{y-axis} = 0.07$; $m_{circular} = 0.12$; $m_{random} = 0.18$. The corresponding examples for Figures 2 and 3 use these values as scale parameters.

Supplementary video 1. ForSys dynamic inference in the migratory primordium. Top panel shows the time-lapse of the migrating primordium of figure 5 with cell membranes marked with EGFP. The primordium migrates from anterior (left) to posterior (right). The individual frames were segmented and used as input to ForSys. Bottom panel presents the corresponding values of intercellular stresses and intracellular pressures for each frame as inferred by ForSys. The color of the cell borders and cell area represent the values of the stress and pressure, respectively. Warmer colors indicate higher values and cooler colors indicate lower values.

Incoherent collective cell chemotaxis underlies organ dysmorphia in a model of branchio-oto-renal syndrome

Augusto Borges¹, Filipe Pinto-Teixeira², Indra Wibowo³, Hans-Martin Pogoda⁴, Matthias Hammerschmidt⁴, Koichi Kawakami⁵, Hernán López-Schier^{6§}, Jerónimo Roberto Miranda-Rodríguez^{7§}

¹Graduate School of Quantitative Biosciences, Ludwig-Maximilians-Universität München, Munich, Germany

²Center for Developmental Biology, Université Toulouse III - Paul Sabatier, Toulouse, France

³School of Life Sciences and Technology, Bandung Institute of Technology, Bandung, West Java, Indonesia

⁴Institute for Developmental Biology, University of Cologne, Cologne, Germany

⁵Laboratory of Molecular and Developmental Biology, National Institute of Genetics, Mishima, Shizuoka, Japan

⁶Science Division, New York University Abu Dhabi, Saadiyat Island, United Arab Emirates

⁷Department of Neurophysiology and Developmental Neurobiology, Instituto de Neurobiología, Universidad Nacional Autónoma de México, Juriquilla, México

[§]To whom correspondence should be addressed: hl5251@nyu.edu; jero.miranda.rod@gmail.com

Abstract

Mutations in *eya1* cause branchio-oto-renal syndrome (BOR) in humans and the equivalent condition in animal models. BOR is characterized by multi-organ malformations. To better understand the role of *Eya1* in organogenesis we used the zebrafish posterior lateral-line primordium. This multicellular tissue moves from head-to-tail at a constant velocity via the simultaneous action of two chemokine receptors, *Cxcr4b* and *Ackr3b* (formerly *cxcr7b*). We found that loss of *eya1* strongly reduces the expression of *ackr3b*, disrupting the coherent motion of the primordium and leading to lateral-line truncations. These findings point to abnormal collective cell chemotaxis as the origin of organ dysmorphia in BOR.

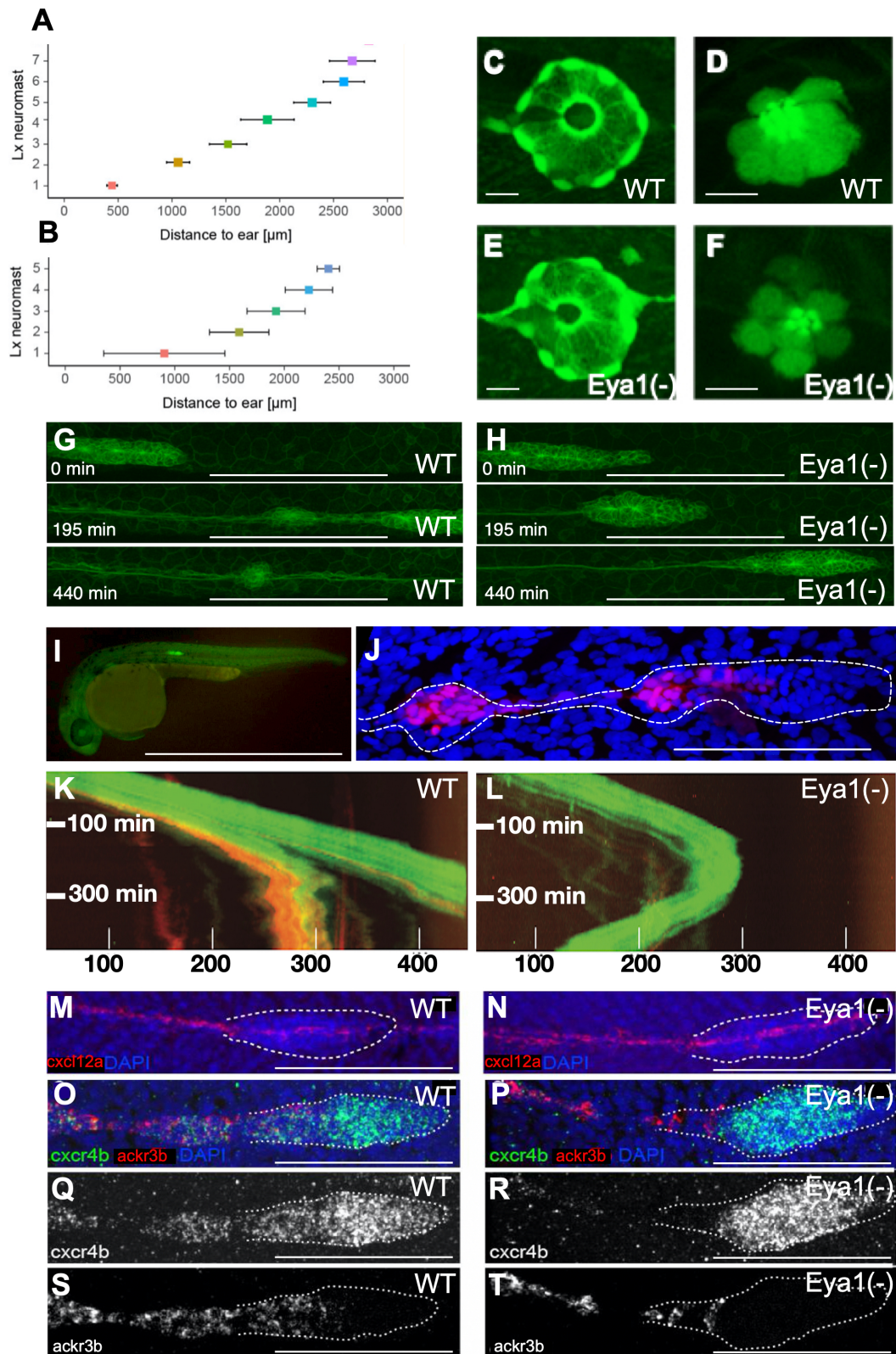


Figure 1. Loss of *eya1* disrupts lateral-line development:

(A,B) Plot of the distance (in μm) between the caudal limit of the otic vesicle and the average number of deposited neuromasts in wild-type (E) and *eya1*-mutant (F) specimens at 3 dpf (mean \pm s.d.). $N=4$ for wild type and $N=9$ for *eya1*^{-/-}. **(C-F)** Live images of neuromasts of the transgenic lines Et(krt4:EGFP)sqet20 **(C,E)** and Et(krt4:EGFP)sqet4 **(D,F)** at 6dpf in wild-type **(C,D)**, *eya1* mutants **(E,F)** revealing supporting cells **(C,E)** and hair cells **(D,F)**. **(G,H)** High magnification confocal images of a wild type **(G)** and mutant **(H)** primordium. At 195 minutes of migration, the wild-type primordium has deposited one pro-neuromast, whereas the *eya1*^{-/-} primordium failed to do so even after 440 minutes. **(I)** A transgenic gSAG181A larva at 30hpf. This line specifically expresses EGFP in the posterior lateral line primordium. **(J)** The primordium and a pro-neuromast in a SAGFF(LF)19A;UAS:RFP larva. SAGFF(LF)19A expresses a Gal4 protein in rear primordial cells, pro-neuromasts and inter-neuromast cells. **(K)** Kymograph from a time-lapse movie focusing on the migrating primordium. The trailing RFP signal driven by SAGFF(LF)19A signal is associated with pro-neuromast rosetogenesis. A few cells expressing 19A:RFP remain in the trailing edge after pro-neuromast deposition. The leading edge advances linearly with a velocity of roughly 80 microns per hour at 28°C. **(L)** Kymograph from a representative *eya1* Crispant larva in the 181A;19A:RFP transgenic background. No neuromast deposition is seen for the duration of the movie. The fish was confirmed to express 19A:RFP in older neuromasts but barely any red fluorescence is seen in the trailing edge of the primordium. The curved shape of the trajectory indicates that after stalling, the primordium performs a U-turn and starts backward migration. Black gaps in the solid green band reflect transient splitting events of the primordium. Units on the x-axis are micrometers (μm). **(M-T)** Representative fluorescent whole-mount *in situ* hybridizations **(M,N)** of *cxcl12a* (red), counterstained with DAPI (blue) to reveal the nuclei for better identification of the primordium (white dotted outline). It shows that the *cxcl12a* gene is expressed along the horizontal myoseptum in the wild type **(M)** and *eya1* mutants **(N)**. **(O-T)** *cxcr4b* (green) and *ackr3b* (red) gene-expression profiles in wild type **(O,Q,S)** and *eya1* mutants **(P,R,T)**. The *cxcr4b* gene is strongly expressed in the leading region of primordium in both in wild-type and *eya1* mutants **(O-R)**. The expression of *ackr3b*, however, is strong in the trailing region of the wild-type primordium (overlapping with *cxcr4b*) **(O,Q,S)**, but almost completely lost in *eya1* mutants, as it is restricted to the very end of the trailing region and never overlaps with *cxcr4b* **(P,R,T)**. HCR conducted in at least 10 samples. Scale bars: C-F 10 μm ; G-H 100 μm ; I 1mm; J, 100 μm ; M-T 100 μm .

Description

DESCRIPTION

The coordinated action of multiple cells governs the development of tissue shape and pattern. Consequently, mutations in genes driving collective cell behavior have profoundly deleterious effects on organogenesis. One gene of particular interest is *Eya1*, whose loss in vertebrates disrupts the formation of several organs, including the kidney, inner ear, and the lateral line (Kozlowski et al., 2005; Sahly et al., 1999; Seleit et al., 2017; Almasoudi and Schlosser, 2021). In humans, mutations in *Eya1* segregate with 40% of cases of Branchio-Oto-Renal syndrome (BOR) (Abdelhak et al., 1997; Sánchez-Valle et al., 2010; Krug et al., 2011). Standard treatments for BOR over the past 25 years have been kidney transplants, dialysis and hearing aids (Smith, 1993; Tian et al., 2022). More innovative interventions are lacking in part because the cellular mechanisms that are disrupted in BOR remain obscure (Soni et al., 2021). Here we combine forward- and reverse-genetic analyses with live imaging to study a model of BOR in zebrafish.

Alterations of the *Cxcl12a* (formerly *Sdf1a*) chemokine receptors *CXCR4b* and *Ackr3b* (formely *CXCR7b*) lead to defects in neuromast deposition during the formation of the lateral line (Venkiteswaran et al. 2013; Donà et al., 2013). Therefore, we speculated that mutations affecting the number of neuromasts will identify factors involved in chemokine signaling. Following this rationale, we analyzed zebrafish carrying a loss-of-function mutation in *eya1* (Kozlowski et al., 2005; Nica et al., 2006). Using somatic CRISPR/Cas9-mediated genome engineering we mutated *eya1* and the fluorescent enhancer-trap line SqET20 to mark non-sensory supporting cells, and SqET4 to highlight the mechanosensory hair cells in neuromasts (Parinov et al., 2004). We found that mutants produce fewer neuromasts within a truncated lateral line (Fig. 1A-B). However, the survival of mutant neuromasts over the course of 4 days after their deposition was not affected by the loss of *eya1* (Fig. 1C-F). These data indicate that the lateral-line defects in *eya1* mutants arise during development and not from post-embryonic degeneration of neuromasts. When looking at early embryos, we found that loss of *eya1* delayed the migration of primordium (Fig. 1G-H).

Next, we focused on primordium dynamics from the onset of migration by *in toto* videomicroscopy, combining two fluorescent enhancer-trap lines, Tg[gSAG181A] and Tg[SAGFF(LF)19A] (Kawakami et al., 2004). Tg[gSAG181A] is unique in that it is the only known line that expresses EGFP exclusively in the posterior lateral-line primordium (Fig. 1I). We found that Tg[gSAG181A] is an insertion near the SAM and SH3 domain containing 1a (*sash1a*) locus on chromosome 20. The Tg[SAGFF(LF)19A] is an insertion of a Gal4 transgene into *ebf3* locus (Kuriki et al., 2020). When combined with a UAS-driven RFP, it drives expression in the rear part of the primordium and in the deposited neuromasts (Fig. 1J). The combined Tg[gSAG181A;SAGFF(LF)19A;UAS:RFP] showed that wild-type primordia move at a constant velocity of around 80 $\mu\text{m}/\text{hour}$ (Fig. 1K and Supp. Movie 1), whereas *eya1*-deficient primordia undergo cycles of migration and stalling, averaging a

markedly reduced speed of 14 $\mu\text{m}/\text{hour}$ (Fig 1L). Moreover, primordia lacking *eya1* sometimes make U-turns to move back towards the head (Fig. 1L and Supp. Movie 2). Therefore, the loss of *eya1* does not block primordium migration, but instead creates pronounced defects in its otherwise coherent motion. The expression of *cxcl12a* chemokine along the migratory path, and the chemokine receptor *cxcr4b* in the front of the primordium remained normal in *eya1*-mutant fish (Fig. 1M-R). By contrast, the expression of *ackr3b* in the trailing part of the primordium was strongly diminished (Fig. 1O-P,S-T). Therefore, loss of *eya1* disrupts primordium migration due to reduced expression of *ackr3b*, which in turn may saturate the CXCR4b receptor by maintaining abnormally high levels of Cxcl12a in the trailing part of the primordium.

Based on our findings, we propose that the Eya1 protein may also govern coherent collective cell movement during otic and renal development mainly via chemokine signaling. Therefore, our results shed new light on the role of Eya1 on collective cell migration and suggest potential avenues to explore novel therapeutic strategies for human patients. Given that the causative mutation for over 50% of BOR cases is not yet known, we predict that the lateral line of zebrafish will remain a powerful model to validate genomic polymorphisms from GWAS studies of BOR patients and generate novel cellular and molecular insights with translational potential. On this regard, our findings raise the possibility that augmenting residual CXCR7 protein activity may improve the outcome of *eya1* mutations in humans (Jiang et al., 2021; Hughes and Nibbs, 2018). It also encourages the development of tissue engineering approaches to control collective cell migration aimed at clinical applications (Manivannan et al., 2012).

CONFLICT OF INTEREST STATEMENT

HL-S is scientific advisor and paid consultant for Sensorion (France). The company had no role in this study. No conflict of interests exists.

Methods

MATERIALS AND METHODS

Zebrafish animals and strains

Fish used were maintained under standardized conditions. Experiments were performed in accordance with protocols approved by the Ethical Committee of Animal Experimentation of the Helmholtz Zentrum München, the German Animal Welfare act Tierschutzgesetz §11, Abs. 1, Nr. 1, Haltungserlaubnis according to the European Union animal welfare, and under protocol number Gz.:55.2-1-54-2532-202-2014 and Gz.:55.2-2532.Vet_02-17-187 from the “Regierung von Oberbayern” (Germany). Eggs were collected from natural spawning and maintained at 28.5°C. Embryos were staged by hours post fertilization (hpf). The *eya* mutant allele used in this study is *eya1^{tm90b}* (Nica et al., 2006). Embryos were genotyped according to Kozłowski et al. (Kozłowski et al., 2005). Transgenic lines used were Et(krt4:EGFP)sqet4 and Et(krt4:EGFP)sqet20 (Pinto-Teixeira et al., 2015), Tg[Cldnb:lynEGFP]zf106Tg (Haas and Gilmour, 2006), gSAG181A (*Gt(T2KSAG)nkgsag181A*) and SAGFF(LF)19A = Et(T2KSAGFFLF)nkSAGFFLF19Aet (Kawakami et al., 2004).

Somatic CRISPR gene knock-out

Crispr somatic mutagenesis of *eya1* was done with 4 sgRNAs (Wu et al., 2018). A 1 mg/ml equimolar mixture of 4 sgRNAs, transcribed with MEGAshortscript T7 (Thermo Fischer), 5 mM Cas9 protein (Sigma), and 300 mM KCl, was injected into one-cell stage embryos. The sequences in the *eya1* gene targeted by each sgRNA are the following:
CTTCCACTTACTCGGCTGTG,TTGTCAATGTTGGGACCGTT, GACGTACCTTCAGTGCCATT,
AGAGCCGTCTGCTACAGAGG

Whole-mount *in situ* hybridization (ISH)

For ISH, antisense digoxigenin- and fluorescein-labeled riboprobes were synthesized according to manufacturer’s instructions (Roche) by using T7/SP6/T3 RNA polymerases. Probes used were: *cxcl12a*, *cxcr4b*, *ackr3b*. Whole-mount two-color fluorescence ISH was performed using anti-DIG and -fluorescein POD antibodies (Roche) and Tyramide Signal Amplification (TSA, PerkinElmer) to detect the riboprobes. Briefly, samples were fixed in 4% paraformaldehyde (PFA) for 24h at 4°C, permeabilized with methanol and cooled to 20°C. Next day, samples were rehydrated, treatment with proteinase K and post-fixed in PFA for 20 min at room temperature. The samples were washed with PBST between the steps. Probe hybridization buffer was used for the prehybridization for 30 min at 37°C and the samples were incubated in the probe solution, prepared following the manufacturer’s instructions, overnight at 37°C. After removing the probe solution, washing the samples and incubating them in the pre-amplification buffer, the samples were incubated in the hairpin mixture overnight in the dark at room temperature. Finally, after several washes with SSCT, the cell nuclei were stained with DAPI (40,6-diamidino-2-phenylindole, Sigma) 1 hour at room temperature.

Imaging and time-lapse video microscopy

For whole-mount ISH, embryos were de-yolked, flat mounted and photographed with an Olympus BX61 microscope using 20X or 40X dry objectives with transmission light. Whole embryo images were acquired on a Leica MZ10 stereomicroscope. Fluorescent images were acquired using either a Leica SP5 or SPE microscope using 20X dry objective or 40X oil immersion objective. Images were processed using Imaris and/or ImageJ software packages, and assembled with Adobe Photoshop CS2, Adobe Illustrator CS2, and Macromedia FreeHand MX. For time-lapse imaging, staged and de-chorionated embryos were anesthetized with Tricaine and mounted in 0.8-1% low-melting-point agarose on a glass-bottom culture dish (MatTek) as previously described (Torres-Mejía et al., 2020). Z-stack series were acquired every 4-10 min using a 20X dry objective of Leica SPE or SP5 confocal microscope. All movies were processed with the Imaris or ImageJ software packages. An unpaired two-tailed T test with Welch's correction was used to compare the position of neuromast L4 in *eya1* mutants and wild-type siblings. Statistics were performed using the GraphPad Prism software and Excel running QI Macros.

Acknowledgements:

Extended Data

Description: Movie 1. Resource Type: Audiovisual. File: [media-1.avi](#). DOI: [10.22002/h880t-ea128](#)

Description: Movie 2. Resource Type: Audiovisual. File: [media-2.avi](#). DOI: [10.22002/d6d9v-09443](#)

References

- Abdelhak S., Kalatzis V., Heilig R., Compain S., Samson D., Vincent C., et al., Leibovici M.. 1997. A human homologue of the *Drosophila* eyes absent gene underlies Branchio-Oto-Renal (BOR) syndrome and identifies a novel gene family. *Nat. Genet.* 15: 157.
- Almasoudi S.H., Schlosser G.. 2021. Otic Neurogenesis in *Xenopus laevis*: Proliferation, Differentiation, and the Role of *Eya1*. *Front. Neuroanat.* 15: 722374.
- Donà E., Barry J.D., Valentin G., Quirin C., Khmelinskii A., Kunze A., et al., Huber W.. 2013. Directional tissue migration through a self-generated chemokine gradient. *Nature.* 503: 285.
- Haas P., Gilmour D.. 2006. Chemokine signaling mediates self-organizing tissue migration in the zebrafish lateral line. *Dev. Cell.* 10: 673.
- Hughes C.E., Nibbs R.J.B.. 2018. A guide to chemokines and their receptors. *FEBS J.* 285: 2944.
- Jiang C., Li R., Xiu C., Ma X., Hu H., Wei L., et al., Zhao J.. 2021. Upregulating CXCR7 accelerates endothelial progenitor cell-mediated endothelial repair by activating Akt/Keap-1/Nrf2 signaling in diabetes mellitus. *Stem Cell Res. Ther.* 12: 264.
- Kawakami K., Takeda H., Kawakami N., Kobayashi M., Matsuda N., Mishina M.. 2004. A Transposon-Mediated Gene Trap Approach Identifies Developmentally Regulated Genes in Zebrafish. *Dev. Cell.* 7: 133.
- Kozłowski D.J., Whitfield T.T., Hukriede N.A., Lam W.K., Weinberg E.S.. 2005. The zebrafish dog-eared mutation disrupts *eya1*, a gene required for cell survival and differentiation in the inner ear and lateral line. *Dev. Biol.* 277: 27.
- Krug P., Morinière V., Marlin S., Koubi V., Gabriel H.D., Colin E., et al., Heidet L.. 2011. Mutation screening of the *EYA1*, *SIX1*, and *SIX5* genes in a large cohort of patients harboring branchio-oto-renal syndrome calls into question the pathogenic role of *SIX5* mutations. *Hum. Mutat.* 32: 183.
- Kuriki M., Sato F., Arai H.N., Sogabe M., Kaneko M., Kiyonari Kawakami, et al., Sehara-Fujisawa A.. 2020. Transient and lineage-restricted requirement of *Ebf3* for sternum ossification. *Development.* 147: 186239.
- Manivannan S., Gleghorn J.P., Nelson C.M.. 2012. Engineered Tissues to Quantify Collective Cell Migration During Morphogenesis.
- Nica G., Herzog W., Sonntag C., Nowak M., Schwarz H., Zapata A.G., Hammerschmidt M.. 2006. *Eya1* is required for lineage-specific differentiation, but not for cell survival in the zebrafish adeno-hypophysis. *Dev. Biol.* 292: 189.
- Parinov S., Kondrichin I., Korzh V., Emelyanov A.. 2004. Tol2 transposon-mediated enhancer trap to identify developmentally regulated zebrafish genes in vivo. *Dev. Dyn.* 231: 449.
- Pinto-Teixeira F., Viader-Llargués O., Torres-Mejía E., Turan M., González-Gualda E., Pola-Morell L., López-Schier H.. 2015. Inexhaustible hair-cell regeneration in young and aged zebrafish. *Biol. Open.* 4: 903.
- Sahly I., Andermann P., Petit C.. 1999. The zebrafish *eya1* gene and its expression pattern during embryogenesis. *Development Genes and Evolution.* 209: 399.

- Sanchez-Valle A., Wang X., Potocki L., Xia Z., Kang S.-H.L., Carlin M.E., et al., Brundage E.K.. 2010. HERV-mediated genomic rearrangement of EYA1 in an individual with branchio-oto-renal syndrome. *Am. J. Med. Genet.* 152A: 2854.
- Schumacher L.. 2019. Collective Cell Migration in Development. *Cell Migrations: Causes and Functions:* 105.
- Seleit A., Krämer I., Ambrosio E., Dross N., Engel U., Centanin L.. 2017. Sequential organogenesis sets two parallel sensory lines in medaka. *Development.* dev.142752
- Smith R.J., Adam M.P.), Mirzaa G.M.), Pagon R.A.), Wallace S.E.), Bean L.J.), Gripp K.W.), Amemiya A.. 1993. Branchiootorenal Spectrum Disorder.
- Soni U.K., Roychoudhury K., Hegde R.S.. 2021. The Eyes Absent proteins in development and in developmental disorders. *Biochem. Soc. Trans.* 49: 1397.
- Tian L., West N., Cayé-Thomasen P.. 2022. Cochlear implantation in Branchiootorenal syndrome – case report and review of the literature. *Coch. Imp. Internat.* 23: 52.
- Torres-Mejía E., Trümbach D., Kleeberger C., Dornseifer U., Orschmann T., Bäcker T., et al., Desbordes S.C.. 2020. Sox2 controls Schwann cell self-organization through fibronectin fibrillogenesis. *Sci Rep.* 10
- Vasilyev A., Liu Y., Mudumana S., Mangos S., Lam P.-Y., Majumdar A., et al., Korzh V.. 2009. Collective Cell Migration Drives Morphogenesis of the Kidney Nephron. *PLoS Biol.* 7: 1000009.
- Venkiteswaran G., Lewellis S.W., Wang J., Reynolds E., Nicholson C., Knaut H.. 2013. Generation and Dynamics of an Endogenous, Self-Generated Signaling Gradient across a Migrating Tissue. *Cell.* 155: 674.
- Wu, RS., Lam II, Clay H, Duong DN , Deo RC , Coughlin SR. (2018). A Rapid Method for directed Gene Knockout for Screening in G0 Zebrafish. *Dev. Cell* 46(1):112-125.e4.. 2018. A Rapid Method for.

Funding:

HL-S and JRM-R received funding from the European Union's Horizon 2020 research and innovation programme under the Marie Skłodowska-Curie grant agreement No. 840834, and by the New York University Abu Dhabi. KK received funding from JSPS KAKENHI JP24K02008 and NBRP from MEXT.

Author Contributions: Augusto Borges: investigation, writing - original draft, formal analysis. Filipe Pinto-Teixeira: investigation. Indra Wibowo: investigation. Hans-Martin Pogoda: resources. Matthias Hammerschmidt: resources. Koichi Kawakami: resources. Hernán López-Schier: conceptualization, formal analysis, funding acquisition, project administration, writing - review editing. Jerónimo Roberto Miranda-Rodríguez: investigation, supervision, formal analysis.

Reviewed By: Anonymous

Nomenclature Validated By: Anonymous

History: Received August 8, 2024 **Revision Received** August 28, 2024 **Accepted** September 6, 2024 **Published Online** September 23, 2024 **Indexed** October 7, 2024

Copyright: © 2024 by the authors. This is an open-access article distributed under the terms of the Creative Commons Attribution 4.0 International (CC BY 4.0) License, which permits unrestricted use, distribution, and reproduction in any medium, provided the original author and source are credited.

Citation: Borges, A; Pinto-Teixeira, F; Wibowo, I; Pogoda, HM; Hammerschmidt, M; Kawakami, K; López-Schier, H; Miranda-Rodríguez, JR (2024). Incoherent collective cell chemotaxis underlies organ dysmorphia in a model of branchio-otorenal syndrome. *microPublication Biology.* [10.17912/micropub.biology.001342](https://doi.org/10.17912/micropub.biology.001342)

Peeking into the future: Inferring mechanics in dynamical tissues

Borges Augusto^{1,2} & Chara Osvaldo^{3,4,5}

- 1) Unit Sensory Biology and Organogenesis, Helmholtz Zentrum München, Munich, Germany
- 2) Graduate School of Quantitative Biosciences, Ludwig Maximilian University, Munich, Germany
- 3) School of Biosciences, University of Nottingham, Sutton Bonington Campus, Nottingham, LE12, UK
- 4) Instituto de Tecnología, Universidad Argentina de la Empresa, Buenos Aires, Argentina
- 5) corresponding author: osvaldo.chara@nottingham.ac.uk

Abstract

Cells exert forces on each other and their environment, shaping the tissue. The resulting mechanical stresses can be determined experimentally or estimated computationally using stress inference methods. Over the years, mechanical stress inference has become a non-invasive, low-cost computational method for estimating the relative intercellular stresses and intracellular pressures of tissues. This mini-review introduces and compares the static and dynamic modalities of stress inference, considering their advantages and limitations. To date, most software has focused on static inference, which requires only a single microscopy image as input. Although applicable in quasi-equilibrium states, this approach neglects the influence that cell rearrangements might have on the inference. In contrast, dynamic stress inference relies on a time series of microscopy images to estimate stresses and pressures. Here, we discuss both static and dynamic mechanical stress inference in terms of their physical, mathematical, and computational foundations and then outline what we believe are promising avenues for *in silico* inference of the mechanical states of tissues.

Introduction

Tissue morphogenesis is driven by changes in cell numbers (in turn caused by mitoses, apoptosis, and cell extrusion), collective movements of cells, and changes in cellular mechanical properties together with alterations of the constraints imposed by the environment onto the epithelium [1–10]. Hence, tissue mechanics needs to be addressed to understand the remarkable morphogenetic processes that shape embryonic tissues during development and the outgrowth of tissues in species capable of regeneration [11].

The study of forces in embryo morphogenesis can be traced back to the *Entwicklungsmechanik* (developmental mechanics movement), which emerged during the 19th century [12]. Later, D'Arcy Thompson enlightened his time with a revolutionary concept: the size and shape of body organisms could also be interpreted as a map of the acting and driving mechanical forces [13], in the same way in which Faraday conceptualized that iron particles in his experiments were a map of the invisible magnetic fields underneath [14] (Supplementary Figure 1A-C). Thus, D'Arcy Thompson transformed our way of perceiving living organisms: The geometrical features of organisms, tissues, and cells reflect not only gene regulatory networks but also a vivid manifestation of mechanical forces at work (Figure 1A). This idea re-emerged and crystallized into a mathematical method to infer mechanical stresses in tissues during the late part of the last century.

Tissue shape is not solely a product of biochemical signalling, but results from the collective interactions between constituent cells [15–19]. Changes in the mechanical interactions between cells and their environment/substrate, reflected in tissue stiffness, can promote epithelial-mesenchymal transitions (EMT), which promote tissue repair and development [20–23]. In tumourigenesis, increased stiffness can lead to tumour progression and metastasis [21,24,25]. Spatial and temporal changes in stiffness can influence the cell-to-cell stresses that arise in tissues. Interestingly, tissue stress distribution is not temporally invariant during complex biological processes such as development [26–28]. For example, tissue stress fluctuations have been shown to play a key role in facilitating tissue reorganisation in the developing zebrafish [29]. Mechanical stress also plays a critical role in tissue regeneration by promoting cell functions such as proliferation, differentiation and migration [30–32]. Mechanical stimuli can improve bone fracture healing by promoting the growth and differentiation of bone-forming cells [30].

This mini-review¹ first describes the computational methods of static stress inference, their advantages over the standard experimental stress determination, and their limitations. Next, we discuss how these limitations lead to the alternative computational methods of dynamic stress inference, which essentially use the topology of the tissue in the "present" combined with its "future" state to predict the stresses therein. We explore the similarities and differences between the dynamic and static counterparts and highlight their advantages and disadvantages. We have summarised all stress inference algorithms that exist to the best of

¹ In the present review, we will not address continuous methods for stress inference. They include methods that rely on hydrodynamic calculations to convert cell displacements into stress maps [33–36] or using displacement from photopatterned substrates, such as Traction Force Microscopy [37,38].

our knowledge in Table 1. We conclude this review with what we believe are exciting future perspectives of stress inference in tissues.

Determining stress statically: The Geometrical Stress Inference

Computational estimation of the mechanical forces at play in biological systems was originally called Force inference, even though the calculated magnitudes are scalars. Here, as pointed out by other authors [35,39,40], we will use the term stress inference. This inexpensive technique approximates the relative stresses and pressures operating in a given system using a microscopy image as sole input, exploiting the information in the tissue topology to obtain the apparent distribution of stresses therein [35,41–46].

The contact angle among cells can serve as a proxy for cell-cell junctional tension, a concept imported from wetting phenomena to study cell interfaces [47] (Figure 1B). Thus, it can be used for stress determination between cells in monolayers, as it depends on the relative forces along the interfaces [48,49]. The cell-cell junctional tension might arise from different sources, such as actomyosin contraction due to myosin accumulation at the cortex or cell-cell adhesion through cadherin binding [2,50]. The membrane stress will be equal at a tricellular junction where all cells meet with the same contact angle ($\alpha = \beta = \gamma = 120^\circ$) (Figure 1C, upper panel). On the other hand, when there is a near-straight angle between two membranes, the stress in the third one will be almost zero (Figure 1C, lower panel). As determining the contact angles at each junction is paramount, membrane segmentation needs to be precise to avoid angle misrepresentation. New image segmentation software is appearing [51–53], and constant efforts are being made to standardize their applicability [54].

Therewith, the intracellular pressure can be inferred using the Young-Laplace Law (Figure 2A) by combining the intercellular stress and the local cell membrane curvature. Conceptually, more convex cells will have a higher pressure than concave ones (Figure 2B). Pressure differences arise from an interplay between the hydrostatic pressure in the cell's environment and the osmotic pressure due to the cell's semipermeable membrane. Only recently have the osmotic contributions to the intracellular pressure been determined *in vivo* in zebrafish [55].

Static stress inference requires the tissue of interest to be in mechanical equilibrium, allowing each cellular junction to be associated with a force balance equation. Using Newton's second law, each equation will have the sum of forces acting on a given vertex equal to zero,

$$\sum_j \vec{F}_j = 0 \quad (1)$$

where j identifies the different edges in the junction. The absence of inertial terms is justified by assuming that the system behaves as a viscous fluid. Thus, these components are negligible compared to viscous ones [56].

The precise mathematical form of the forces at each edge must also be decided. The most frequent choice is to consider the force in the direction of the edge scaled by its stress [57–60], similar to what is done in vertex models [39,44,61–63]. The force at each membrane would be associated with the vectorial equation:

$$\vec{F}_j = \lambda_j \vec{r}_j^i \quad (2)$$

Here, λ_j represents the stress of membrane j , \vec{r}_j^i the unitary vector in the direction of the edge j from junction i . Importantly, although choosing a model for the stress on the edge is necessary, it is not a unique choice [58].

Determining edge shape and estimating pressure.

The proper determination of the membrane's shape is crucial for stress inference. Noisy images might lead to numerical errors that get amplified down the pipeline, reducing the accuracy of the inference. Several methods can be used to estimate the membrane's shape contribution to the geometrical matrix defined in Equation 2. Straight edges, though easy to estimate from microscopy images, have the inconvenience of making the system less robust [35,60]. This can be visualized, for example, by taking an edge and realizing that the force will have the same components at each end, with an opposite sign (Figure 3A). On the contrary, curved edges will have a distinct value at each end of the edge, adding independent information to the system of equations (Figure 3B). In this case, each edge's direction (vector) could be determined from the tangent to the limiting angle to the cell membrane [60].

Early methods inferred cortex stresses and cell pressures simultaneously and used the straight-edge approximation [35,57,58]. These methods assume that the cell's mechanical energy will depend only on the length of the edges and the cell's area to derive the system of equations from a potential energy [39,59]. Having the pressure and stress intermixed in the same expression increases the number of unknowns per equation while maintaining only one equation for each space component. Moreover, tissue boundaries and fourfold vertices give fewer equations than unknowns, leading to an underdetermined system. Due to the constraints mentioned, this type of system has been solved using Bayesian methods [19,45,59]. These constraints are not unavoidable, as was demonstrated by the Cellular Force Inference Toolkit: CellFIT [60]. This method allows considering curved edges and makes stress and pressure inference independent. Pressure is modeled using the Young-Laplace equation. This equation relates the shape and stress of an interface with the difference in pressure between both sides (Figure 2A). As the stress in an edge is required to calculate the pressure, this inference needs to be performed subsequently, effectively decoupling both magnitudes.

Finding the solution to the inference problem

Each microscopy image (Figure 4A) is segmented (Figure 4B) and then converted to a system of equations (Figure 4C) when performing stress inference (Figure 4D). Each spatial

dimension will contribute an equation per junction and one unknown per membrane: the stress. The most common case is to have triple junctions, *i.e.*, junctions with three connecting membranes [64,65] (Figure 1B). In two dimensions, each new junction will contribute two equations and, at most, three unknowns, as some membrane stresses will be repeated.

This is commonly written in matrix form as

$$[M_\lambda][\lambda] = [b] \quad (3)$$

In the following sections, quantities that appear in brackets [] are to be interpreted as matrices. $[M_\lambda]$ in Eq. 3 summarizes all the geometrical information of a tissue, as it contains all components of the versors and their relationship to one another. Each column represents edge stress, and each row is the equation at a junction for one of the spatial coordinates (x and y in the 2D case). We call this matrix the *geometrical matrix* of the system since it reflects all the geometrical features of the edges connecting the junctions of the tissue under study (Figure 4C).

In geometrical stress inference, where no movement of the junctions is considered, the right-hand side of Eq. 3 is set to the null matrix, *i.e.*, $[b] = 0$. If all the junctions are at rest, a possible solution to the system of equations would be that no stresses are acting on the system ($\lambda_j = 0 \forall j$). Two methods are prevalent in the literature to avoid this unrealistic and trivial solution. We and other authors have included a constraint linking all the stresses in the tissue, such as a particular value for the average stress [57,58,60,66]. Fixing a value has the advantage of adding one more equation to the system without any new unknowns, thus increasing its stability. Another method consists of changing the cost function associated with the method, adding a regularizer [67] that penalizes the null solution. More generally, this could allow tailoring of the cost function to the specific needs of the problem at hand by enabling the addition of new terms, such as penalizing wider distributions of stresses.

Stress inference methods do not need to make any assumptions about the specifics of the force generation mechanism. However, stress inference may yield negative results if the inference method allows it or null stresses if not. In static stress inference, this usually means that the particular shape of a membrane is incompatible with the underlying model. Sometimes, it is possible to identify these issues and avoid problematic junctions or membranes. Typical pathological junctions include near right angles, curvy membranes, or junctions higher than three-fold [35,68,69].

Once stress is inferred, pressure can be determined by the curvature of the cell's membrane, as stated in Young-Laplace Law (Figure 2A). The equation can be made more explicit as

$$P_j - P_i = \lambda K \quad (4)$$

Here P_j and P_i are the pressures of cells j and i , respectively, λ is the membrane's stress, and K is the curvature. Therefore, an inhomogeneous system of equations can be assembled where the unknowns are each of the P_i , in matrix form

$$[M_p][P] = [b_p] \quad (5)$$

Each row of the matrix $[M_p]$ represents an interface between two cells, with a 1 at the site of the first cell and a -1 at the site of the second cell, and each column relates to one of the

rows in the $[P]$ vector of unknowns. The matrix $[b_p]$ has the corresponding curvature of the membrane and its stress in each row. As with the stresses, an additional equation is commonly incorporated as a Lagrange multiplier to set a relationship between the pressures, usually making the sum of the pressures equal zero [66,69].

A system is said to be overdetermined when there are more equations than unknowns, meaning there is no exact solution in almost all cases. Generally, stress inference pipelines encounter overdetermined systems, with some exceptions [35,59]. A popular method to address this is to find an approximate solution through the Least Squares Method, which works by creating a new system of equations using the transpose of the matrix as

$$[M_\lambda]^{Tr} [M_\lambda] [\lambda] = [M_\lambda]^{Tr} [b] \quad (6)$$

and then inverting the new square matrix $[M_\lambda]^{Tr} [M_\lambda]$. The approximate (least squares) solution to the problem is then found by minimizing the difference between both sides of the equation using a Non-Negative Least Squares or a Least Squares solver [70–72]. An alternative method to solve the system of equations is to use the Moore-Penrose pseudoinverse [39,73,74]. The generalized inverse of a matrix $[A]$ is defined as

$$[A]^\ddagger = ([A]^{Tr} [A])^{-1} A^{Tr} \quad (7)$$

Then, given a system of equations as represented by Equation 3, the stresses would be expressed as

$$[\lambda] = ([M_\lambda]^{Tr} [M_\lambda])^{-1} [M_\lambda]^{Tr} [b] \quad (8)$$

The mechanical inference pipeline is finally built as one system of equations coupling stresses and pressures, or two when decoupled, with the stresses and pressures as unknowns. Each system is built and solved for a single microscopy image (Figure 4D). However, if a specific problem has a time series of images, how can we incorporate the information about its evolution?

Dynamic Stress Inference

Tissues in a quasistatic regime may be encountered during adult tissue homeostasis or late embryonic development. However, tissues are often found in a more dynamic state in early embryonic development where cell motility and rearrangements cannot be neglected [75,76]. During development, morphogenetic flows shape the organisms into functional forms, such as in *Drosophila* [77–80] and *Zebrafish* [81–85]. Therefore, accurate prediction of mechanical forces in these tissues requires inference algorithms that work optimally in the presence of significant motion. This modality of stress inference is called Dynamic Stress Inference [35].

A key challenge in Dynamic Stress Inference is to follow the tissue's evolution reliably through time, yet not all tissue elements have to be tracked. The elements can be divided into two categories: passive elements, which dissipate energy, and active elements, which

generate work [57,58]. Brodland and colleagues suggest that the forces generated by active elements, such as the actomyosin network and cell membranes, deform the passive elements, including the cytoplasm, organelles, and extracellular matrix [58]. The inference method requires selecting an optimal level of detail, as the relevant elements need not only be the cellular cortex but could also be subcellular structures [57,58]. The selected structures must be defined in detail in the microscopy to allow tracking throughout the experiment.

The second challenge is also found in static inference and was mentioned above, the need to choose an underlying model for membrane stress: to the best of our knowledge, all currently available software uses a derived version of the stress model described by Equation 2. The choice depends on the specifics of the system of interest and the desired level of complexity. For example, in systems where the contractility of the actomyosin cortex is particularly relevant, a perimeter term may be necessary to account for the desired quantity.

Finally, the third key challenge relates to the question of the scales involved in the processes studied. In Static Inference, only the spatial scale is relevant, as it relates to the positions of the membranes among themselves and is ultimately used to find the angles. Importantly, in Dynamic Inference, the time scale comes into play, which implies that, in this formalism, the relation between scales of space and time affects the inference.

In summary, to successfully incorporate cell movement information into the inference process, the dynamic inference pipeline requires 1) faithful tracking of relevant elements of the tissue through time, 2) an underlying model for the stress at each membrane, and finally, 3) knowledge of the relationship between the scales involved in the process under study.

To the authors' knowledge, three different methods have been proposed to deal with time series of data: DLITE [67], Video Force Microscopy [57], and ForSys [66]. Only DLITE and ForSys are currently available. In the following sections, we explore the virtues and limitations of these three methods.

DLITE: Time series as an initial condition

The use of movement information, also reviewed in [35], allows tracking of the nodes through time, dealing with the first issue presented at the start of the previous section. DLITE (Dynamic Local Intercellular Tension Estimation) [67] assumes mechanical equilibrium at each junction (Eq. 1), similar to CellFIT [60]. DLITE takes membrane tensions in the direction of the edge joining the junction, with no additional terms (Eq. 2). Moreover, it uses a regularizer that penalizes small stress values to avoid the null solution. Though time series tracking of tissues is involved, as Roffay et al. [35] pointed out, this is not a dynamic inference method per se. In fact, DLITE only tracks all nodes, edges, and cells through time to use the inferred solutions of the previous time as an initial guess for the current frame (Figure 5A). Importantly, the authors show that this is sufficient to improve performance on *in silico* data and maintains better robustness over time than CellFIT [67]. Moreover, unlike CellFIT, DLITE is an open-source project, allowing users to examine the details of its implementation.

VFM: Dynamic stress inference in a mesh

Brodland and colleagues reported the first dynamical stress inference of tissues to study the mechanics of ventral furrow invagination in *Drosophila* [57]. It was called Video Force Microscopy (VFM) and previously cinemechanometry [58]. They developed this method in a series of papers spanning more than fifteen years [86–89]. VFM successfully identified stresses during ventral furrow failure due to reduced myosin II activity [57]. The authors built a finite element mesh over the tissue of interest's active landmarks (Figure 5B). This meshing need not correspond precisely with all the cell's hallmarks, namely the cell membranes, and could have subcellular details. Brodland and colleagues chose the mesh so that its nodes correspond with the elements they categorize as active. Therefore, it could be the case that the polygons enclosed by the mesh are not cells but rather subcellular domains (Figure 5B, upper panel).

They assumed that all passive elements' contributions could be subsumed in generating an effective viscosity [57]. In this model, the forces of the active components (f_t^A) are equal to the velocity of the nodes (v_t), mediated by a damping matrix (D_t) with viscosity information, so at each time-point t

$$f_t^A = D_t v_t \quad (9)$$

In contrast to the previously mentioned CellFIT method [60], VFM calculates the contribution of each force from a geometrical matrix using a straight-edge approach, which combines both the stresses and the pressures. Importantly, unlike DLITE and ForSys (discussed in the next section), VFM is not currently available.

ForSys: Dynamic inference on the vertices

Most recently, we proposed the ForSys method, which builds upon the advancements in the field and integrates them into an open-source pipeline [66]. This software allows Static and Dynamic Stress Inference in curved geometries, which is achieved by fitting a circle to the segmented edges [66], as in CellFIT and DLITE [60,67].

ForSys benefits from the viscous forces prevalent in the tissue and modified Equation 1 to include a damping term as

$$\sum_j \lambda_j \vec{r}_j^i = \eta \vec{v}^i \quad (10)$$

where η is the damping constant and \vec{v}^i the velocity of the vertex i . Implementing an overdamped regime mathematically transforms the system into an inhomogeneous system of equations, as the [B] term present in equations 3, 6, and 8 is now different from the null matrix. This matrix now includes the velocity components of all junctions in the calculation. An immediate advantage of this method is that it is no longer necessary to avoid the case where all forces in the junction are zero.

As shown in Equation 1, the left-hand side has dimensions given by the stress λ . However, in Dynamic Stress Inference, while the left-hand side still has this dimension, the right-hand side now has units of $\eta \vec{v}$, as shown in Equation 10. Thus, correctly determining the scales involved is crucial, as pointed out at the beginning of the “Dynamic Stress Inference” section. Equation 10 can be transformed into a non-dimensional form with one free parameter proportional to the Weissenberg number's reciprocal [66]. This well-known non-dimensional quantity relates the elastic and viscous forces through a reference stress $\bar{\lambda}$, velocity \bar{v} , and damping coefficient η as

$$\frac{1}{W_i} = \frac{\eta \bar{v}}{\bar{\lambda}}. \quad (11)$$

Therefore, the force at each junction is

$$\sum_j \lambda_j' \vec{r}_j^i = \left(\frac{\eta \bar{v}}{\bar{\lambda}}\right) \vec{v}^i \quad (12)$$

where $\lambda_j' = \lambda_j / \bar{\lambda}$ and $\vec{v}^i = \vec{v}^i / \bar{v}$. The scale relation introduced by this work might extend beyond the particularities of ForSys and could be used in other dynamic measurements, such as in Transverse Fluctuation (TFlux) [90,91].

When tested using *in silico* tissue movies, this method outperforms other software when the junctions move significantly and negligibly [66]. Furthermore, this method opened a window into using force inference technology in migratory structures. When applied to the mobile Zebrafish lateral line primordium, the method detected zones of high pressure/tension that indicate the presence of rosettes predating the separation of the neuromast organs [66].

Outlook

As with any technique, its falsifiability is an important aspect of stress inference. The standard for validating the inference engine in static and dynamic modalities is based on *in silico* validations, often generated using a cell-based computational model such as the Vertex model [45,67,69,92]. Various experimental validations can be performed for static inference by fluorescent measurements, such as with myosin intensity [59], antibodies staining [93,94], and flipper probes [95], or through direct manipulation with methods including laser ablation [45,59] and Atomic Force Microscopy (AFM). Complementary to hydrostatic pressure measurement [96,97], methods for osmotic pressure determination have recently emerged [55]. Pressure inference cannot distinguish between these contributing factors; however, we expect the inferred pressure to be dominated by the hydrostatic component, as osmotic pressure differences equilibrate rapidly across the tissue. In contrast, experimental validation of dynamic inference by ground truth generation is rather limited, as methods such as laser ablation or AFM irreversibly change the state of a tissue and are likely to disrupt or alter the processes of interest. Therefore, dynamic stress inference is typically calibrated using computational model simulations.

Thanks to advances in image segmentation, static stress inference can be performed in 3D, as initially reported by Broadland and colleagues [98] and more recently by the Turlier lab [92]. Incorporating the third dimension into dynamic inference will be a significant leap forward. Reliable 3D stress maps that could be used to validate an inference technique are experimentally challenging to produce, especially if the maps need to be time-dependent.

A desirable feature of future stress inference techniques is to couple the inference engine with the computational packages for simulating tissues using cell-based models that rely on mechanical information, such as the vertex model. This model requires the correct parameterisation of the line tensions needed to simulate tissues that recapitulate the phenomena they are intended to describe. In this way, the intercellular stresses obtained by stress inference could be used to parameterise a model and generate predictions embodied in model simulations.

Stress inference can uncover mechanical features of systems in various settings. It has been successfully applied to investigate cell division [40], organogenesis [66], and cell-type-specific mechanical anisotropies [39,66,99]. We expect that stress inference will expand its applications to fields such as immunology [100] and cancer biology [101,102] in the coming years, which could greatly benefit from this technique.

While stress and pressure inference allows the determination of local intracellular pressure and intercellular stress, one might expect that this information could be integrated to provide a whole tissue description of the mechanical state of the system. Recently, it was proposed that local and tissue-level mechanical information could be combined with spatial omics [103]. This will allow a deeper understanding of the connection between the mesoscopic scale and the molecular details of the interactions.

Even though a machine-learning approach has recently been used to infer forces from cytoskeletal protein distributions [104], a new avenue to explore could be using machine-learning algorithms to infer stresses. This would involve curating microscopy images and feeding them into a neural network, which in turn could learn to predict stress distribution for a given topology. To our knowledge, this exciting possibility has not been explored even in the static inference formalism.

Perspectives

- *Dynamic stress inference provides a first computational approach to determine the mechanical state of tissues and generate predictions that can guide future experiments. This family of inexpensive tools can advance the study of tissues in development and regeneration.*
- While static stress inference from microscopy images allows the characterization of a tissue's mechanical state at a single point in time, dynamic stress inference from video microscopy represents the full spatiotemporal distribution of mechanical stresses experienced by the tissue.
- *A next logical step will be to combine dynamic inference with 3D geometric inference to ultimately generate 4D stress inference. Another important step will be the coupling of inference with cell-based models, which will allow direct testing of these models in biologically relevant geometries. Finally, machine learning algorithms that allow the training of networks on specific organisms may prove helpful in recognizing specific patterns of stress distributions.*

Code availability

The *in silico* image where generated using seapipy and ForSys. The seapipy codebase is available on GitHub at <https://github.com/borgesaugusto/seapipy> and Zenodo [105]. ForSys codebase is available on GitHub at <https://github.com/borgesaugusto/forsys> and Zenodo [106].

Acknowledgments

The authors would like to thank Alice Descoeurdes, Diego Cattoni, Nicolas Aldecoa, and all the members of the Chara laboratory for their helpful comments on the manuscript.

A.B. was funded by the BMBF 01GQ1904 grant. O.C. was funded by grant PICT-2019-03828 from the Agencia Nacional de Promoción Científica y Tecnológica of Argentina and by a Biotechnology and Biological Sciences Research Council grant (grant number BB/X014908/1). The authors would like to acknowledge the two anonymous reviewers for their very constructive comments.

Author Contributions

A.B. and O.C. wrote and edited the manuscript.

Competing Interests Statement

The authors declare that there are no competing interests associated with the manuscript.

References

- 1 Lecuit, T., Lenne, P.-F. and Munro, E. (2011) Force Generation, Transmission, and Integration during Cell and Tissue Morphogenesis. *Annu. Rev. Cell Dev. Biol.* **27**, 157–184 <https://doi.org/10.1146/annurev-cellbio-100109-104027>
- 2 Heisenberg, C.-P. and Bellaïche, Y. (2013) Forces in Tissue Morphogenesis and Patterning. *Cell* **153**, 948–962 <https://doi.org/10.1016/j.cell.2013.05.008>
- 3 Godard, B.G. and Heisenberg, C.-P. (2019) Cell division and tissue mechanics. *Curr. Opin. Cell Biol.* **60**, 114–120 <https://doi.org/10.1016/j.ceb.2019.05.007>
- 4 Petridou, N.I. and Heisenberg, C. (2019) Tissue rheology in embryonic organization. *EMBO J.* **38**, e102497 <https://doi.org/10.15252/embj.2019102497>
- 5 Chan, C.J., Heisenberg, C.-P. and Hiiragi, T. (2017) Coordination of Morphogenesis and Cell-Fate Specification in Development. *Curr. Biol.* **27**, R1024–R1035 <https://doi.org/10.1016/j.cub.2017.07.010>

- 6 Gómez-Gálvez, P., Anbari, S., Escudero, L.M. and Buceta, J. (2021) Mechanics and self-organization in tissue development. *Semin. Cell Dev. Biol.* **120**, 147–159 <https://doi.org/10.1016/j.semcdb.2021.07.003>
- 7 Van Leen, E.V., Di Pietro, F. and Bellaïche, Y. (2020) Oriented cell divisions in epithelia: from force generation to force anisotropy by tension, shape and vertices. *Curr. Opin. Cell Biol.* **62**, 9–16 <https://doi.org/10.1016/j.ceb.2019.07.013>
- 8 Pinheiro, D. and Bellaïche, Y. (2018) Mechanical Force-Driven Adherens Junction Remodeling and Epithelial Dynamics. *Dev. Cell* **47**, 3–19 <https://doi.org/10.1016/j.devcel.2018.09.014>
- 9 Bailles, A., Gehrels, E.W. and Lecuit, T. (2022) Mechanochemical Principles of Spatial and Temporal Patterns in Cells and Tissues. *Annu. Rev. Cell Dev. Biol.* **38**, 321–347 <https://doi.org/10.1146/annurev-cellbio-120420-095337>
- 10 Monier, B., Gettings, M., Gay, G., Mangeat, T., Schott, S., Guarner, A., et al. (2015) Apico-basal forces exerted by apoptotic cells drive epithelium folding. *Nature* **518**, 245–248 <https://doi.org/10.1038/nature14152>
- 11 Nelson, C.M., Xiao, B., Wickström, S.A., Dufrière, Y.F., Cosgrove, D.J., Heisenberg, C.-P., et al. (2024) Mechanobiology: Shaping the future of cellular form and function. *Cell* **187**, 2652–2656 <https://doi.org/10.1016/j.cell.2024.04.006>
- 12 Keller, R. (2012) Physical Biology Returns to Morphogenesis. *Science* **338**, 201–203 <https://doi.org/10.1126/science.1230718>
- 13 Thompson, D.W. (1992) On Growth and Form. 1st ed. Cambridge University Press; 1992 [cited 2024 Jan 3]. <https://doi.org/10.1017/CBO9781107325852>
- 14 Berkson, W. (2014) Fields of Force. 1st ed. Routledge; 2014 [cited 2024 Jan 3]. <https://doi.org/10.4324/9781315779386>
- 15 Campàs, O., Noordstra, I. and Yap, A.S. (2023) Adherens junctions as molecular regulators of emergent tissue mechanics. *Nat. Rev. Mol. Cell Biol.* <https://doi.org/10.1038/s41580-023-00688-7>
- 16 Chanet, S. and Martin, A.C. (2014) Mechanical Force Sensing in Tissues. In: Progress in Molecular Biology and Translational Science. Elsevier; 2014 [cited 2024 Mar 22]. . p. 317–352. <https://doi.org/10.1016/B978-0-12-394624-9.00013-0>
- 17 Collinet, C., Rauzi, M., Lenne, P.-F. and Lecuit, T. (2015) Local and tissue-scale forces drive oriented junction growth during tissue extension. *Nat. Cell Biol.* **17**, 1247–1258 <https://doi.org/10.1038/ncb3226>
- 18 Etournay, R., Popović, M., Merkel, M., Nandi, A., Blasse, C., Aigouy, B., et al. (2015) Interplay of cell dynamics and epithelial tension during morphogenesis of the *Drosophila* pupal wing. *eLife* **4**, e07090 <https://doi.org/10.7554/eLife.07090>
- 19 Guirao, B., Rigaud, S.U., Bosveld, F., Bailles, A., López-Gay, J., Ishihara, S., et al. (2015) Unified quantitative characterization of epithelial tissue development. *eLife* **4**, e08519 <https://doi.org/10.7554/eLife.08519>
- 20 Barriga, E.H., Franze, K., Charras, G. and Mayor, R. (2018) Tissue stiffening coordinates morphogenesis by triggering collective cell migration in vivo. *Nature* **554**, 523–527 <https://doi.org/10.1038/nature25742>
- 21 Shellard, A. and Mayor, R. (2023) Sculpting with stiffness: rigidity as a regulator of morphogenesis. *Biochem. Soc. Trans.* **51**, 1009–1021 <https://doi.org/10.1042/BST20220826>
- 22 Bonnans, C., Chou, J. and Werb, Z. (2014) Remodelling the extracellular matrix in development and disease. *Nat. Rev. Mol. Cell Biol.* **15**, 786–801 <https://doi.org/10.1038/nrm3904>
- 23 Machado, P.F., Duque, J., Étienne, J., Martínez-Arias, A., Blanchard, G.B. and Gorfinkiel, N. (2015) Emergent material properties of developing epithelial tissues. *BMC Biol.* **13**, 98 <https://doi.org/10.1186/s12915-015-0200-y>
- 24 Wei, S.C., Fattet, L., Tsai, J.H., Guo, Y., Pai, V.H., Majeski, H.E., et al. (2015) Matrix stiffness drives epithelial–mesenchymal transition and tumour metastasis through a TWIST1–G3BP2 mechanotransduction pathway. *Nat. Cell Biol.* **17**, 678–688 <https://doi.org/10.1038/ncb3157>

- 25 Pickup, M.W., Mouw, J.K. and Weaver, V.M. (2014) The extracellular matrix modulates the hallmarks of cancer. *EMBO Rep.* **15**, 1243–1253
<https://doi.org/10.15252/embr.201439246>
- 26 Blanchard, G.B., Murugesu, S., Adams, R.J., Martinez-Arias, A. and Gorfinkiel, N. (2010) Cytoskeletal dynamics and supracellular organisation of cell shape fluctuations during dorsal closure. *Development* **137**, 2743–2752 <https://doi.org/10.1242/dev.045872>
- 27 David, D.J.V., Tishkina, A. and Harris, T.J.C. (2010) The PAR complex regulates pulsed actomyosin contractions during amnioserosa apical constriction in *Drosophila*. *Development* **137**, 1645–1655 <https://doi.org/10.1242/dev.044107>
- 28 Yu, J.C. and Fernandez-Gonzalez, R. (2016) Local mechanical forces promote polarized junctional assembly and axis elongation in *Drosophila*. *eLife* **5**, e10757
<https://doi.org/10.7554/eLife.10757>
- 29 Kim, S., Pochitaloff, M., Stooke-Vaughan, G.A. and Campàs, O. (2021) Embryonic tissues as active foams. *Nat. Phys.* **17**, 859–866 <https://doi.org/10.1038/s41567-021-01215-1>
- 30 Seo, C.H., Jeong, H., Feng, Y., Montagne, K., Ushida, T., Suzuki, Y., et al. (2014) Micropit surfaces designed for accelerating osteogenic differentiation of murine mesenchymal stem cells via enhancing focal adhesion and actin polymerization. *Biomaterials* **35**, 2245–2252 <https://doi.org/10.1016/j.biomaterials.2013.11.089>
- 31 Tassinari, R., Olivi, E., Cavallini, C., Taglioli, V., Zannini, C., Marcuzzi, M., et al. (2023) Mechanobiology: A landscape for reinterpreting stem cell heterogeneity and regenerative potential in diseased tissues. *iScience* **26**, 105875
<https://doi.org/10.1016/j.isci.2022.105875>
- 32 Lee, D.A., Knight, M.M., Campbell, J.J. and Bader, D.L. (2011) Stem cell mechanobiology. *J. Cell. Biochem.* **112**, 1–9 <https://doi.org/10.1002/jcb.22758>
- 33 He, B., Doubrovinski, K., Polyakov, O. and Wieschaus, E. (2014) Apical constriction drives tissue-scale hydrodynamic flow to mediate cell elongation. *Nature* **508**, 392–396
<https://doi.org/10.1038/nature13070>
- 34 Hernández-Vega, A., Marsal, M., Pouille, P., Tosi, S., Colombelli, J., Luque, T., et al. (2017) Polarized cortical tension drives zebrafish epiboly movements. *EMBO J.* **36**, 25–41
<https://doi.org/10.15252/emboj.201694264>
- 35 Roffay, C., Chan, C.J., Guirao, B., Hiiragi, T. and Graner, F. (2021) Inferring cell junction tension and pressure from cell geometry. *Development* **148**, dev192773
<https://doi.org/10.1242/dev.192773>
- 36 Blanchard, G.B. (2017) Taking the strain: quantifying the contributions of all cell behaviours to changes in epithelial shape. *Philos. Trans. R. Soc. B Biol. Sci.* **372**, 20150513 <https://doi.org/10.1098/rstb.2015.0513>
- 37 Tambe, D.T., Crutelle, U., Trepát, X., Park, C.Y., Kim, J.H., Millet, E., et al. (2013) Monolayer Stress Microscopy: Limitations, Artifacts, and Accuracy of Recovered Inter-cellular Stresses. *PLoS ONE* **8**, e55172 <https://doi.org/10.1371/journal.pone.0055172>
- 38 Marín-Llauradó, A., Kale, S., Ouzeri, A., Golde, T., Sunyer, R., Torres-Sánchez, A., et al. (2023) Mapping mechanical stress in curved epithelia of designed size and shape. *Nat. Commun.* **14**, 4014 <https://doi.org/10.1038/s41467-023-38879-7>
- 39 Chiou, K.K., Hufnagel, L. and Shraiman, B.I. (2012) Mechanical Stress Inference for Two Dimensional Cell Arrays. *PLOS Comput. Biol.* **8**, e1002512
<https://doi.org/10.1371/journal.pcbi.1002512>
- 40 Noll, N., Streichan, S.J. and Shraiman, B.I. (2020) Variational Method for Image-Based Inference of Internal Stress in Epithelial Tissues. *Phys. Rev. X* **10**, 011072
<https://doi.org/10.1103/PhysRevX.10.011072>
- 41 Sugimura, K., Lenne, P.-F. and Graner, F. (2016) Measuring forces and stresses *in situ* in living tissues. *Development* **143**, 186–196 <https://doi.org/10.1242/dev.119776>
- 42 Roca-Cusachs, P., Conte, V. and Trepát, X. (2017) Quantifying forces in cell biology. *Nat. Cell Biol.* **19**, 742–751 <https://doi.org/10.1038/ncb3564>
- 43 Campàs, O. (2016) A toolbox to explore the mechanics of living embryonic tissues. *Semin. Cell Dev. Biol.* **55**, 119–130 <https://doi.org/10.1016/j.semcdb.2016.03.011>
- 44 Gómez-González, M., Latorre, E., Arroyo, M. and Trepát, X. (2020) Measuring

- mechanical stress in living tissues. *Nat. Rev. Phys.* **2**, 300–317
<https://doi.org/10.1038/s42254-020-0184-6>
- 45 Kong, W., Loison, O., Chavadimane Shivakumar, P., Chan, E.H., Saadaoui, M., Collinet, C., et al. (2019) Experimental validation of force inference in epithelia from cell to tissue scale. *Sci. Rep.* **9**, 14647 <https://doi.org/10.1038/s41598-019-50690-3>
- 46 Ishihara, S., Sugimura, K., Cox, S.J., Bonnet, I., Bellaïche, Y. and Graner, F. (2013) Comparative study of non-invasive force and stress inference methods in tissue. *Eur. Phys. J. E* **36**, 45 <https://doi.org/10.1140/epje/i2013-13045-8>
- 47 De Gennes, P.G. (1985) Wetting: statics and dynamics. *Rev. Mod. Phys.* **57**, 827–863
<https://doi.org/10.1103/RevModPhys.57.827>
- 48 Steinberg, M.S. (1963) Reconstruction of Tissues by Dissociated Cells: Some morphogenetic tissue movements and the sorting out of embryonic cells may have a common explanation. *Science* **141**, 401–408
<https://doi.org/10.1126/science.141.3579.401>
- 49 Stein, M.B. and Gordon, R. (1982) Epithelia as bubble rafts: A new method for analysis of cell shape and intercellular adhesion in embryonic and other epithelia. *J. Theor. Biol.* **97**, 625–639 [https://doi.org/10.1016/0022-5193\(82\)90363-0](https://doi.org/10.1016/0022-5193(82)90363-0)
- 50 Beckerle, M.C., editor (2001) Cell adhesion. New York: Oxford University Press; 2001.
- 51 Aigouy, B., Cortes, C., Liu, S. and Prud'Homme, B. (2020) EPySeg: a coding-free solution for automated segmentation of epithelia using deep learning. *Development* dev.194589
<https://doi.org/10.1242/dev.194589>
- 52 Pachitariu, M. and Stringer, C. (2022) Cellpose 2.0: how to train your own model. *Nat. Methods* **19**, 1634–1641 <https://doi.org/10.1038/s41592-022-01663-4>
- 53 Stringer, C., Wang, T., Michaelos, M. and Pachitariu, M. (2021) Cellpose: a generalist algorithm for cellular segmentation. *Nat. Methods* **18**, 100–106
<https://doi.org/10.1038/s41592-020-01018-x>
- 54 Etournay, R., Merkel, M., Popović, M., Brandl, H., Dye, N.A., Aigouy, B., et al. (2016) TissueMiner: A multiscale analysis toolkit to quantify how cellular processes create tissue dynamics. *eLife* **5**, e14334 <https://doi.org/10.7554/eLife.14334>
- 55 Vian, A., Pochitaloff, M., Yen, S.-T., Kim, S., Pollock, J., Liu, Y., et al. (2023) In situ quantification of osmotic pressure within living embryonic tissues. *Nat. Commun.* **14**, 7023
<https://doi.org/10.1038/s41467-023-42024-9>
- 56 Purcell, E.M. (1977) Life at low Reynolds number. *Am. J. Phys.* **45**, 3–11
<https://doi.org/10.1119/1.10903>
- 57 Brodland, G.W., Conte, V., Cranston, P.G., Veldhuis, J., Narasimhan, S., Hutson, M.S., et al. (2010) Video force microscopy reveals the mechanics of ventral furrow invagination in *Drosophila*. *Proc. Natl. Acad. Sci.* **107**, 22111–22116
<https://doi.org/10.1073/pnas.1006591107>
- 58 Cranston, P.G., Veldhuis, J.H., Narasimhan, S. and Brodland, G.W. (2010) Cinemechanometry (CMM): A Method to Determine the Forces that Drive Morphogenetic Movements from Time-Lapse Images. *Ann. Biomed. Eng.* **38**, 2937–2947
<https://doi.org/10.1007/s10439-010-9998-1>
- 59 Ishihara, S. and Sugimura, K. (2012) Bayesian inference of force dynamics during morphogenesis. *J. Theor. Biol.* **313**, 201–211 <https://doi.org/10.1016/j.jtbi.2012.08.017>
- 60 Brodland, G.W., Veldhuis, J.H., Kim, S., Perrone, M., Mashburn, D. and Hutson, M.S. (2014) CellFIT: A Cellular Force-Inference Toolkit Using Curvilinear Cell Boundaries. *PLOS ONE* **9**, 1–15 <https://doi.org/10.1371/journal.pone.0099116>
- 61 Nagai, T. and Honda, H. (2001) A dynamic cell model for the formation of epithelial tissues. *Philos. Mag. B* **81**, 699–719 <https://doi.org/10.1080/13642810108205772>
- 62 Alt, S., Ganguly, P. and Salbreux, G. (2017) Vertex models: from cell mechanics to tissue morphogenesis. *Philos. Trans. R. Soc. B Biol. Sci.* **372**, 20150520
<https://doi.org/10.1098/rstb.2015.0520>
- 63 Farhadifar, R., Röper, J.-C., Aigouy, B., Eaton, S. and Jülicher, F. (2007) The Influence of Cell Mechanics, Cell-Cell Interactions, and Proliferation on Epithelial Packing. *Curr. Biol.* **17**, 2095–2104 <https://doi.org/10.1016/j.cub.2007.11.049>

- 64 Bosveld, F. and Bellaïche, Y. (2020) Tricellular junctions. *Curr. Biol.* **30**, R249–R251 <https://doi.org/10.1016/j.cub.2020.01.029>
- 65 Bosveld, F., Wang, Z. and Bellaïche, Y. (2018) Tricellular junctions: a hot corner of epithelial biology. *Curr. Opin. Cell Biol.* **54**, 80–88 <https://doi.org/10.1016/j.ceb.2018.05.002>
- 66 Borges, A., Miranda-Rodríguez, J.R., Ceccarelli, A.S., Ventura, G., Sedzinski, J., López-Schier, H., et al. (2024) ForSys: non-invasive stress inference from time-lapse microscopy. *bioRxiv* <https://doi.org/10.1101/2024.05.28.595800>
- 67 Vasan, R., Maleckar, M.M., Williams, C.D. and Rangamani, P. (2019) DLITE Uses Cell-Cell Interface Movement to Better Infer Cell-Cell Tensions. *Biophys. J.* **117**, 1714–1727 <https://doi.org/10.1016/j.bpj.2019.09.034>
- 68 Spencer, M.A., Jabeen, Z. and Lubensky, D.K. (2017) Vertex stability and topological transitions in vertex models of foams and epithelia. *Eur. Phys. J. E* **40**, 2 <https://doi.org/10.1140/epje/i2017-11489-4>
- 69 Veldhuis, J.H., Mashburn, D., Hutson, M.S. and Brodland, G.W. (2015) Practical aspects of the cellular force inference toolkit (CellFIT). In: *Methods in Cell Biology*. . Elsevier; 2015 [cited 2024 Feb 5]. . p. 331–351. <https://doi.org/10.1016/bs.mcb.2014.10.010>
- 70 Lawson, C.L. and Hanson, R.J. (1995) *Solving Least Squares Problems*. Society for Industrial and Applied Mathematics; 1995 [cited 2024 Jan 11]. <https://doi.org/10.1137/1.9781611971217>
- 71 Virtanen, P., Gommers, R., Oliphant, T.E., Haberland, M., Reddy, T., Cournapeau, D., et al. (2020) SciPy 1.0: fundamental algorithms for scientific computing in Python. *Nat. Methods* **17**, 261–272 <https://doi.org/10.1038/s41592-019-0686-2>
- 72 Newville, M., Otten, R., Nelson, A., Stensitzki, T., Ingargiola, A., Allan, D., et al. (2023) *lmfit/lmfit-py: 1.2.2* <https://doi.org/10.5281/ZENODO.598352>
- 73 Dresden, A. (1920) The fourteenth western meeting of the American Mathematical Society. *Bull. Am. Math. Soc.* **26**, 385–397 <https://doi.org/10.1090/S0002-9904-1920-03322-7>
- 74 Penrose, R. (1955) A generalized inverse for matrices. *Math. Proc. Camb. Philos. Soc.* **51**, 406–413 <https://doi.org/10.1017/S0305004100030401>
- 75 Scarpa, E. and Mayor, R. (2016) Collective cell migration in development. *J. Cell Biol.* **212**, 143–155 <https://doi.org/10.1083/jcb.201508047>
- 76 Rørth, P. (2012) Fellow travellers: emergent properties of collective cell migration. *EMBO Rep.* **13**, 984–991 <https://doi.org/10.1038/embor.2012.149>
- 77 Martin, A.C., Kaschube, M. and Wieschaus, E.F. (2009) Pulsed contractions of an actin–myosin network drive apical constriction. *Nature* **457**, 495–499 <https://doi.org/10.1038/nature07522>
- 78 Ko, C.S. and Martin, A.C. (2020) The cellular and molecular mechanisms that establish the mechanics of *Drosophila* gastrulation. In: *Current Topics in Developmental Biology*. . Elsevier; 2020 [cited 2024 Mar 31]. . p. 141–165. <https://doi.org/10.1016/bs.ctdb.2019.08.003>
- 79 Guirao, B. and Bellaïche, Y. (2017) Biomechanics of cell rearrangements in *Drosophila*. *Curr. Opin. Cell Biol.* **48**, 113–124 <https://doi.org/10.1016/j.ceb.2017.06.004>
- 80 Collinet, C., Bailles, A., Dehapiot, B. and Lecuit, T. (2024) Mechanical regulation of substrate adhesion and de-adhesion drives a cell-contractile wave during *Drosophila* tissue morphogenesis. *Dev. Cell* **59**, 156-172.e7 <https://doi.org/10.1016/j.devcel.2023.11.022>
- 81 Williams, M.L.K. and Solnica-Krezel, L. (2020) Cellular and molecular mechanisms of convergence and extension in zebrafish. In: *Current Topics in Developmental Biology*. . Elsevier; 2020 [cited 2024 Mar 31]. . p. 377–407. <https://doi.org/10.1016/bs.ctdb.2019.08.001>
- 82 Banavar, S.P., Carn, E.K., Rowghanian, P., Stooke-Vaughan, G., Kim, S. and Campàs, O. (2021) Mechanical control of tissue shape and morphogenetic flows during vertebrate body axis elongation. *Sci. Rep.* **11**, 8591 <https://doi.org/10.1038/s41598-021-87672-3>
- 83 Pinheiro, D., Kardos, R., Hannezo, É. and Heisenberg, C.-P. (2022) Morphogen gradient

- orchestrates pattern-preserving tissue morphogenesis via motility-driven unjamming. *Nat. Phys.* **18**, 1482–1493 <https://doi.org/10.1038/s41567-022-01787-6>
- 84 Schauer, A. and Heisenberg, C.-P. (2021) Reassembling gastrulation. *Dev. Biol.* **474**, 71–81 <https://doi.org/10.1016/j.ydbio.2020.12.014>
- 85 Pinheiro, D. and Heisenberg, C.-P. (2020) Zebrafish gastrulation: Putting fate in motion. In: *Current Topics in Developmental Biology*. Elsevier; 2020 [cited 2024 Mar 31]. . p. 343–375. <https://doi.org/10.1016/bs.ctdb.2019.10.009>
- 86 Brodland, G.W. and Clausi, D.A. (1994) Embryonic Tissue Morphogenesis Modeled by FEM. *J. Biomech. Eng.* **116**, 146–155 <https://doi.org/10.1115/1.2895713>
- 87 Wayne Brodland, G. and Chen, H.H. (2000) The mechanics of cell sorting and envelopment. *J. Biomech.* **33**, 845–851 [https://doi.org/10.1016/S0021-9290\(00\)00011-7](https://doi.org/10.1016/S0021-9290(00)00011-7)
- 88 Chen, H.H. and Brodland, G.W. (2000) Cell-Level Finite Element Studies of Viscous Cells in Planar Aggregates. *J. Biomech. Eng.* **122**, 394–401 <https://doi.org/10.1115/1.1286563>
- 89 Brodland, G.W. and Chen, H.H. (2000) The Mechanics of Heterotypic Cell Aggregates: Insights From Computer Simulations. *J. Biomech. Eng.* **122**, 402–407 <https://doi.org/10.1115/1.1288205>
- 90 Weng, S., Devitt, C.C., Nyaoga, B.M., Havnen, A.E., Alvarado, J. and Wallingford, J.B. (2023) New tools reveal PCP-dependent polarized mechanics in the cortex and cytoplasm of single cells during convergent extension <https://doi.org/10.1101/2023.11.07.566066>
- 91 Weng, S. and Wallingford, J.B. (2022) Planar polarized force propagation integrates cell behavior with tissue shaping during convergent extension <https://doi.org/10.1101/2022.11.08.515701>
- 92 Ichbiah, S., Delbary, F., McDougall, A., Dumollard, R. and Turlier, H. (2023) Embryo mechanics cartography: inference of 3D force atlases from fluorescence microscopy. *Nat. Methods* **20**, 1989–1999 <https://doi.org/10.1038/s41592-023-02084-7>
- 93 Yonemura, S., Wada, Y., Watanabe, T., Nagafuchi, A. and Shibata, M. (2010) α -Catenin as a tension transducer that induces adherens junction development. *Nat. Cell Biol.* **12**, 533–542 <https://doi.org/10.1038/ncb2055>
- 94 Mann, Z., Lim, F., Verma, S., Nanavati, B.N., Davies, J.M., Begun, J., et al. (2024) Preexisting tissue mechanical hypertension at adherens junctions disrupts apoptotic extrusion in epithelia. *Mol. Biol. Cell* **35**, br3 <https://doi.org/10.1091/mbc.E23-08-0337>
- 95 Roffay, C., García-Arcos, J.M., Chapuis, P., López-Andarias, J., Schneider, F., Colom, A., et al. (2024) Tutorial: fluorescence lifetime microscopy of membrane mechanosensitive Flipper probes. *Nat. Protoc.* <https://doi.org/10.1038/s41596-024-01027-6>
- 96 Chan, C.J., Costanzo, M., Ruiz-Herrero, T., Mönke, G., Petrie, R.J., Bergert, M., et al. (2019) Hydraulic control of mammalian embryo size and cell fate. *Nature* **571**, 112–116 <https://doi.org/10.1038/s41586-019-1309-x>
- 97 Stewart, M.P., Helenius, J., Toyoda, Y., Ramanathan, S.P., Muller, D.J. and Hyman, A.A. (2011) Hydrostatic pressure and the actomyosin cortex drive mitotic cell rounding. *Nature* **469**, 226–230 <https://doi.org/10.1038/nature09642>
- 98 Veldhuis, J.H., Ehsandar, A., Maître, J.-L., Hiiragi, T., Cox, S. and Brodland, G.W. (2017) Inferring cellular forces from image stacks. *Philos. Trans. R. Soc. B Biol. Sci.* **372**, 20160261 <https://doi.org/10.1098/rstb.2016.0261>
- 99 Petridou, N.I., Grigolon, S., Salbreux, G., Hannezo, E. and Heisenberg, C.-P. (2019) Fluidization-mediated tissue spreading by mitotic cell rounding and non-canonical Wnt signalling. *Nat. Cell Biol.* **21**, 169–178 <https://doi.org/10.1038/s41556-018-0247-4>
- 100 Huse, M. (2017) Mechanical forces in the immune system. *Nat. Rev. Immunol.* **17**, 679–690 <https://doi.org/10.1038/nri.2017.74>
- 101 Cambria, E., Coughlin, M.F., Floryan, M.A., Offeddu, G.S., Shelton, S.E. and Kamm, R.D. (2024) Linking cell mechanical memory and cancer metastasis. *Nat. Rev. Cancer* **24**, 216–228 <https://doi.org/10.1038/s41568-023-00656-5>
- 102 Clevenger, A.J., McFarlin, M.K., Gorley, J.P.M., Solberg, S.C., Madyastha, A.K. and Raghavan, S.A. (2024) Advances in cancer mechanobiology: Metastasis, mechanics, and materials. *APL Bioeng.* **8**, 011502 <https://doi.org/10.1063/5.0186042>
- 103 Hallou, A., He, R., Simons, B.D. and Dumitrescu, B. (2023) A computational pipeline

- for spatial mechano-transcriptomics <https://doi.org/10.1101/2023.08.03.551894>
- 104 Schmitt, M.S., Colen, J., Sala, S., Devany, J., Seetharaman, S., Caillier, A., et al. (2024) Machine learning interpretable models of cell mechanics from protein images. *Cell* **187**, 481-494.e24 <https://doi.org/10.1016/j.cell.2023.11.041>
- 105 Borges, A. (2024) borgesaugusto/seapipy: v0.2.0-alpha <https://doi.org/10.5281/ZENODO.10809290>
- 106 Borges, A., Ceccarelli, A.S. and Chara, O. (2024) ForSys software <https://doi.org/10.5281/ZENODO.11282554>
- 107 Brakke, K.A. (1992) The Surface Evolver. *Exp. Math.* **1**, 141–165 <https://doi.org/10.1080/10586458.1992.10504253>

Table 1. Existing stress inference methods. Details all currently existing stress inference methods, whether dynamic and/or static, 2D or 3D support and their algorithm, along with their original application and current availability.

Method	Static / Dynamic	2D/3D	Algorithm	The biological system to which it was initially applied to	Software availability	Ref. and year
VFM	Dynamic	2D	Finite element mesh; Straight edges; Stress/pressure together; Least Squares solver	Ventral furrow formation in <i>Drosophila</i> , <i>in vivo</i>	Not available	[57], 2010
Chiou <i>et al.</i>	Static	2D	Straight edges; Stress/pressure together; Inverse solution	Ventral furrow formation in <i>Drosophila</i> , <i>in vivo</i>	Not available	[39], 2012
Bayesian	Static	2D	Straight edges; Stress/pressure together; Bayesian solver	<i>Drosophila</i> pupal wing, <i>in vivo</i>	Open Source on GitHub	[59], 2012
CellFIT	Static	2D	Curved edges; Stress/pressures separated; Least Squares solver	Dorsal closure and imaginal disk in <i>Drosophila</i> , <i>in vivo</i> ; Dragonfly wing	Not available. It can be found as a binary file	[60], 2014
CellFIT-3D	Static	3D	Curved edges; Only stress; Least squares solver	Murine embryos	Not available	[98], 2017
DLITE	Static*	2D	Curved edges; Stress/pressure separated; Least Square solver	Human stem cell colonies, <i>in vitro</i> .	Open Source on GitHub	[67], 2019
VMSI	Static	2D	Fitted curved edges; Stress/pressure separated; Variational solver	<i>Drosophila</i> embryogenesis, <i>in vivo</i>	Not available	[40], 2020
foambryo	Static	3D	Curved edges; Stress/pressure separated; Least Square solver	Ascidian embryo <i>P. mammillata</i> ; <i>C. elegans</i> embryo	Open Source on GitHub	[92], 2023
ForSys	Dynamic and Static	2D	Curved edges; Stress/pressure separated; Least-square solver	Zebrafish Lateral Line, <i>in vivo</i> ; <i>Xenopus</i> Mucociliary epithelium, <i>in vivo</i>	Open Source on GitHub	[66], 2024

Figures

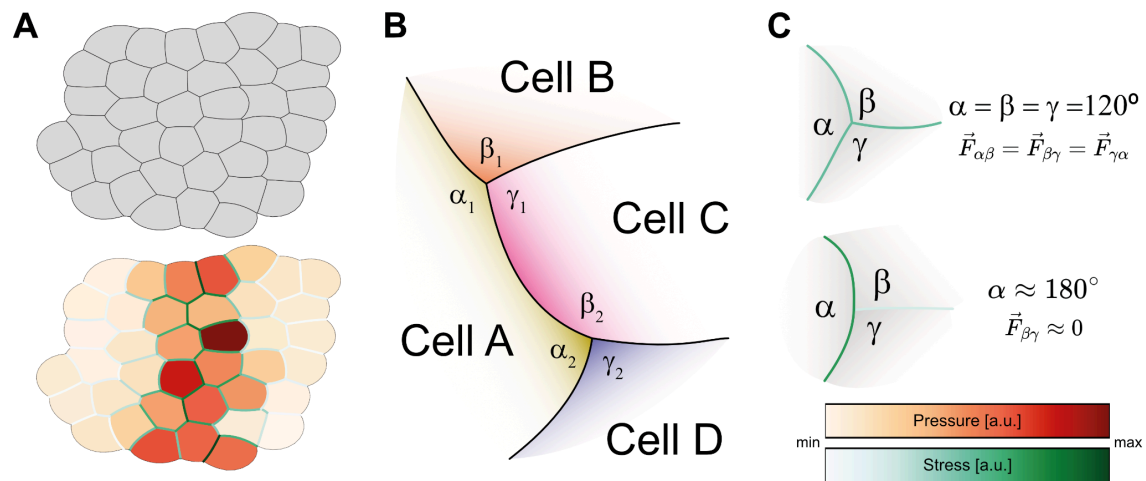


Figure 1. Stress inference, conceptually. **(A)** Stress inference uses the shape of the cells in a tissue (shown in D, upper) to estimate the stress acting on them (color code shown in C, lower). Higher values are shown in red, and smaller values in blue (color code shown in C, lower). The tissue model was generated using Surface Evolver [107] through the seapipy software, generating a high-stress furrow in the center. Stress inference was performed by using ForSys software [66]. **(B)** Cells A and C share a common edge between triple junction 1 and 2. At each of these junctions, the incoming membranes have a contact angle α_1 , β_1 , and γ_1 and α_2 , β_2 , γ_2 for the mentioned junctions 1 and 2, respectively. **(C)** Contact angles determine the relative tension of each membrane. For equal angles (upper panel), the forces and the tensions will be similar. If an angle is a straight angle, the other membrane will have a tension of zero. The color map represents the stress and pressure for panels A and C in a relative scale from minimum to maximum.

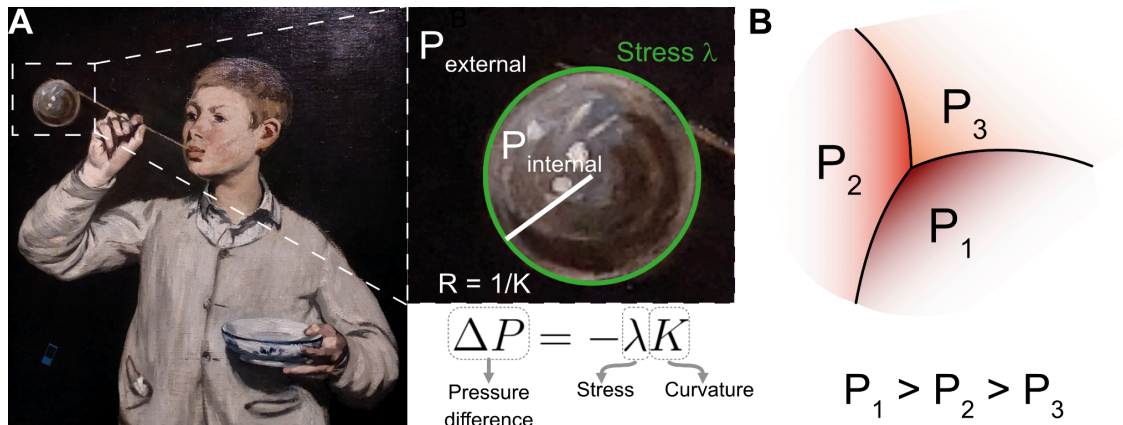


Figure 2. Stress and pressure are determined by shape. (A) The pressure on the soap bubble of the “Les Bulles de savon” (1867), Édouard Manet, Calouste Gulbenkian Museum, Lisbon (Picture acquired by OC in the exposition Manet / Degas au musée d’Orsay), can be determined by the Young-Laplace equation, relating pressure difference ($\Delta P = P_{\text{internal}} - P_{\text{external}}$) with stress on the surface (λ) and curvature of its shape ($K = 1/R$). **(B)** Scheme representing pressure differences for a given geometry. Cells with higher pressure will be more convex, while lower-pressure cells will tend to be more concave. The color intensity represents pressure values qualitatively on a relative scale from lower (orange) to larger values (red).

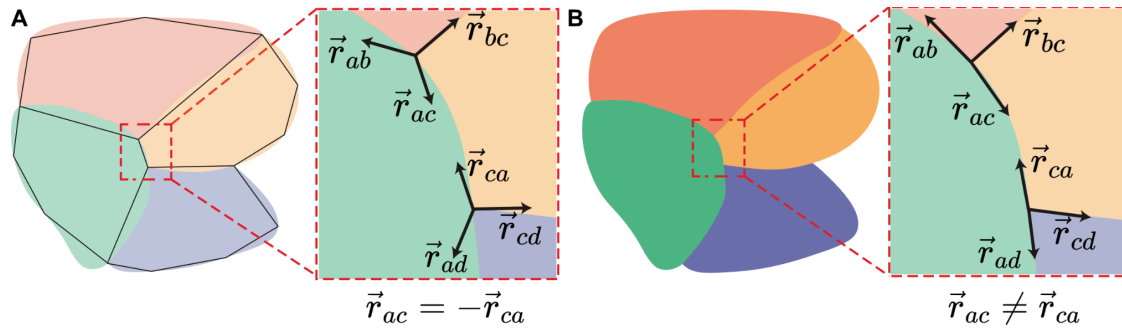


Figure 3. Approximating the shape of the membrane. **(A)** If cells are polygonal, cell membranes can be approximated in the system with straight lines joining the junctions, seen here as \vec{r}_{ab} , \vec{r}_{bc} , \vec{r}_{ac} , and \vec{r}_{ca} , \vec{r}_{ad} , \vec{r}_{cd} . In this situation, the vector joining two junctions will have the same magnitude but opposite sign at each junction. **(B)** In contrast, curved edges give a better approximation of the shape and more stability to the system of equations, as a curved shape adds more independent information to the geometric determination. Note that vectors \vec{r}_{ac} and \vec{r}_{ca} are no longer collinear in a curved shape approximation.

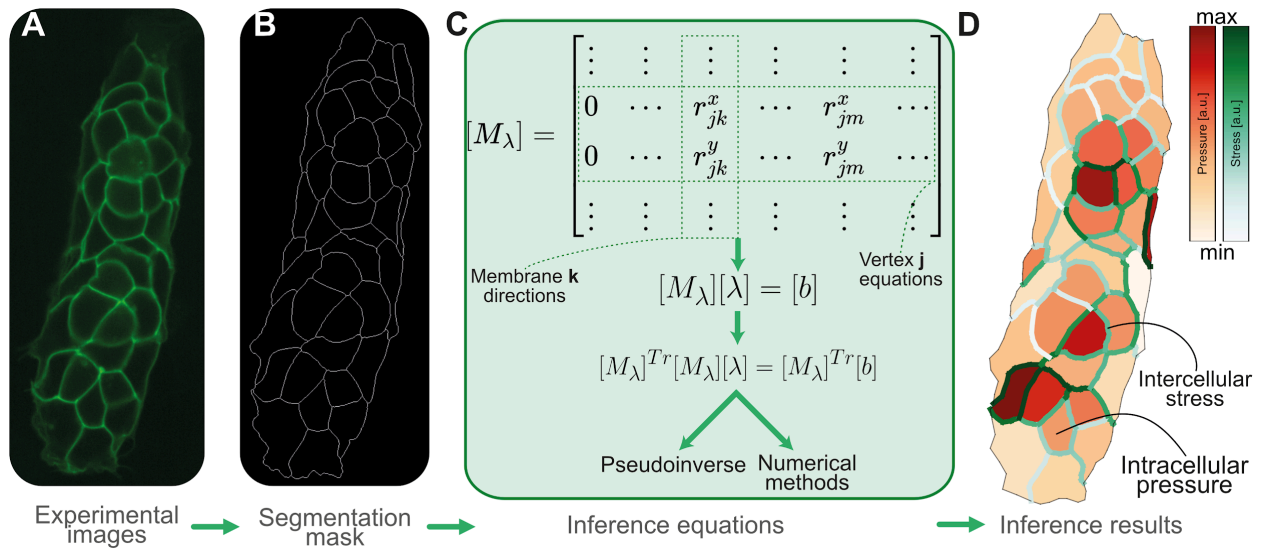


Figure 4. General stress inference pipeline. Starting from an experimental image, such as a primordium in the Zebrafish lateral line (A), a segmentation mask has to be generated (B) to construct then a Geometrical Matrix encompassing the information about the shape of cells, as described in the section “Finding the solution to the inference problem” (C). The solution can be found by inverting the system, using a pseudoinverse, or using different numerical methods. Intercellular stresses are inferred from these equations (D). The intracellular pressures are inferred using the Young-Laplace equation (see Fig. 2A). The primordium image in panel (A) was taken with a spinning disk confocal microscopy. The green fluorescence marks cell membranes in green. The primordium membranes shown in panel A were tagged using claudnb:lyn-EGFP. Stress inference was executed by using ForSys [66].

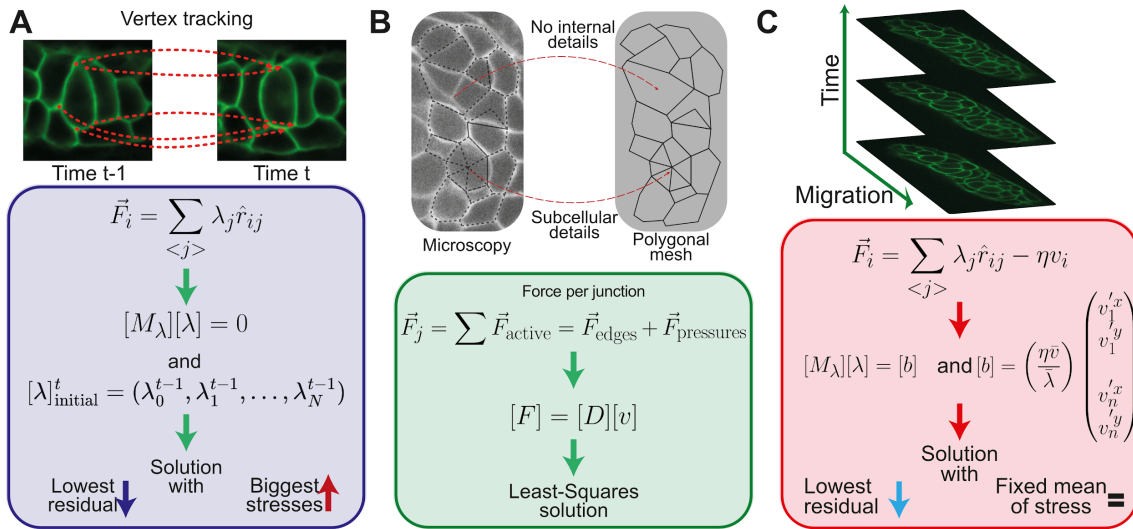
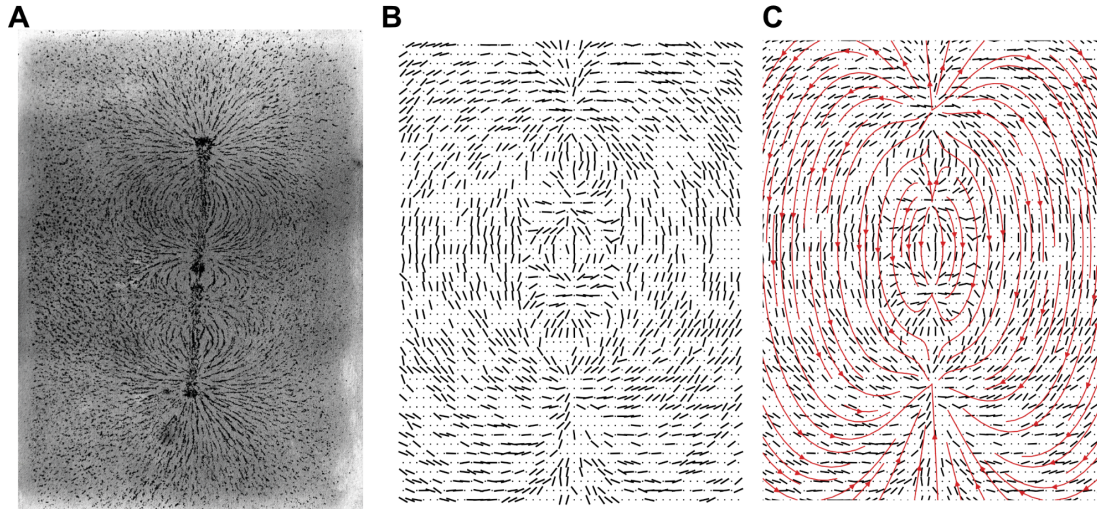


Figure 5. Dynamic stress inference. (A) DLITE is not a dynamic method *per se*. It tracks each junction of the system through time and assumes that the force (\vec{F}_i) is in the direction of the membrane (\hat{r}_{ij}) and scaled by the membranes' stress (λ). The system is compiled in a geometrical matrix ($[M_\lambda]$) and solved using the solution at the previous time point as an initial guess for the numerical algorithm. **(B)** VFM uses a Finite Element Mesh to evaluate the system's movements. The mesh does not need to coincide with the cellular details. Stresses and pressures are intertwined in the equations. The system to solve establishes a relationship between the force ($[F]$) and the velocity of the nodes ($[v]$) through a damping matrix ($[D]$). **(C)** ForSys solves the equations by considering each junction's velocity (incorporated in the $[b]$ matrix), mediated by the scale parameter ($\frac{\eta\bar{v}}{\lambda}$), which can be interpreted as the reciprocal of the Weissenberg number. Through this number, the relationship between viscous and elastic scales must be tuned. The neuromast's membranes shown in panel B and the primordium's in panels A and C were tagged using claudnb:lyn-EGFP.



Supplementary Figure1. Stress as a patterning guide. Iron filings are arranged by magnetic fields (Credit: M0000164: Michael Faraday's iron filings diagram. Wellcome Library has provided this material; GB CC BY 4.0). **(A)**, a behavior that can be modeled computationally **(B)**. This arrangement is a consequence of the underlying field **(C)**. To create this, we simulated the magnetic field of 4 charges at different positions along the y-axis. The black lines represent the direction of the field with a Gaussian noise of 10 degrees; only around 50 % of them are shown. Similarly, tissues are also shaped according to the mechanical state to which they are subjected.